University of Southampton

Faculty of Natural and Environmental Science

Ocean and Earth Science

Imaging of the Deep Galicia Margin using Ocean Bottom Seismic Data

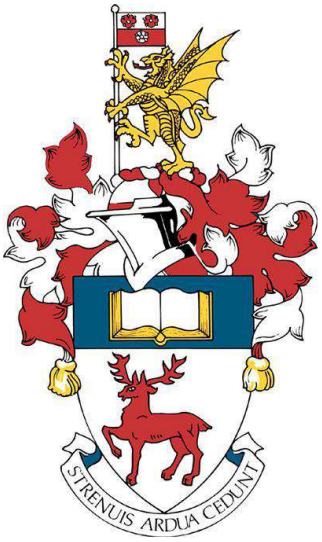

by

Bhargav Boddupalli

ORCID ID [https://orcid.org/0000-0002-4676-9056]

Thesis for the degree of Doctor of Philosophy

July 2020

University of Southampton

Abstract

Faculty of Natural and Environmental Sciences

Ocean and Earth Science

Thesis for the degree of Doctor of Philosophy

Imaging of the Deep Galicia Margin using Ocean Bottom Seismic Data

by

Bhargav Boddupalli

The Galicia margin, west of Iberia, is one of the most studied magma-poor rifted margins to understand the rifting process leading to continental breakup. Seismic imaging has been instrumental in understanding rifting in the Galicia margin. In this work, I derived a high-resolution P-wave velocity model of the Deep Galicia margin (DGM) where the final breakup of the continental crust happened. The velocity model is derived employing a 3D acoustic full waveform inversion (FWI) technique in the time domain using sparsely acquired wide-angle ocean bottom seismometer (OBS) data. The model is validated by tracking phase changes of the first arrivals during the inversion, and by comparing the predicted waveforms with the observed for all the instruments. In addition, the anomalies introduced by FWI were validated by performing synthetic inversion runs by recovering the anomalies using a synthetic dataset predicted using the final FWI model as observed dataset. The final model shows an improved alignment with the structures observed on 3D prestack time migrated multichannel seismic images compared to the starting model.

Comparison of the 3D FWI model result with 2D result derived along a profile through the 3D seismic volume highlighted the differences between the imaging methods in a real world setting. The 3D FWI result constraints better the complex faulting within the pre- and syn-rift sediments, crystalline crust and below a detachment fault, known as the S-reflector, compared to the 2D result. Below the S-reflector, 3D FWI has enhanced the pattern of serpentinisation compared to the starting model with local low velocity zones occurring around fault intersections. Based on my comparison, I conclude that the use of 3D data can partially mitigate the problem of receiver sparsity in FWI.

Using the high-resolution 3D model, I attempted to understand the nature of the crystalline crust by comparing the velocity range of the crystalline crust in the DGM with other similar tectonic settings. The velocity limits of the crystalline crust in the DGM include velocities of both the upper and lower crust observed in other similar settings, indicating that it is comprised of both the upper and lower crust. Unlike in many other settings, there is no clear evidence in the P-wave velocity profiles for a separate upper and lower crust within the crystalline crust. The high-resolution model also shows evidence for exhumation of the lower crust under the footwall of the fault blocks to accommodate the extension. I generated a serpentinisation map of the DGM at a depth of 100 ms below the S-reflector and compared the map with a map generated by training a machine learning algorithm using velocities from 2D FWI. A mean serpentinisation of ~33 % is estimated below the S-reflector using the 3D FWI model.

Seismic images of the DGM are developed in time and depth domains using the first-order multiples from the OBS data and a technique called mirror imaging. In this technique, the seafloor along with the OBS is mirror imaged with respect to the sea-surface and placed at a depth of twice the water column depth. Such an adjustment allows incorporation of the multiples in to migration algorithms just like primary reflections. I observe that mirror imaged sections show a good match within the sediment column with the multichannel images, but the quality of the images deteriorates below the top of the basement partially due to weak signal strength of the multiples. Primary reflections from the OBS illuminate very narrow sections of the subsurface, hence the quality of the image using them is poor compared to the mirror images. Mirror imaging can become a standard processing step in studies where no multichannel data are available.

Table of Contents

Table of Tables

Table of Figures

Table of Figures

Research Thesis: Declaration of Authorship

I, Bhargav Boddupalli, declare that this thesis and the work presented in it are my own and has been generated by me as the result of my own original research.

Imaging of the Deep Galicia Margin using Ocean Bottom Seismic Data

I confirm that:

This work was done wholly or mainly while in candidature for a research degree at this University;
Where any part of this thesis has previously been submitted for a degree or any other qualification at this University or any other institution, this has been clearly stated;
Where I have consulted the published work of others, this is always clearly attributed;
Where I have quoted from the work of others, the source is always given. With the exception of such quotations, this thesis is entirely my own work;
I have acknowledged all main sources of help;
Where the thesis is based on work done by myself jointly with others, I have made clear exactly what was done by others and what I have contributed myself;
Part of this work will be/has been published after/before submission

- Chapter 3 will be submitted to the journal, 'Geophysical Journal International'.
- Appendix C has been published in 'Geophysical Research Letters' in April, 2019.

Signature: ..... Date:.....

Acknowledgements

Firstly, I would like to extend my sincere gratitude to my supervisors Prof. Tim Minshull, Dr. Gaye Bayrakci and Prof. Joanna Morgan (Imperial) for their invaluable guidance, motivation, patience and support during the course of my PhD. Without their immense knowledge and experience this project wouldn't have been possible. I would like to thank them for introducing me to the cutting edge seismic imaging technology of full waveform inversion. I always enjoyed discussing with them about the project and it really helped me in developing my scientific thinking over the years.

I would like to express my grateful thanks to Dr. Juan Pablo Canales and Dr. Dirk Klaeschen. Pablo hosted me at Woods Hole Oceanographic Institution during the summer of 2018, where I learnt to process multichannel seismic reflection data and also got introduced to geodynamics of mid-oceanic ridges. Dirk hosted me at GEOMAR at the beginning of my PhD in 2017 and introduced me to mirror imaging technique. The work from GEOMAR is presented in chapter 5 of this thesis. The knowledge and experience I gained from both these visits are invaluable. Special thanks to Jeff Blundell from University of Southampton for assisting me in running big jobs on the linux clusters efficiently.

I deeply thank my parents for their love, unconditional trust and endless patience. I would like to thank my family and friends for their constant support and encouragement making my PhD journey memorable. I cannot forget to thank Sourav, Melanie, Vanessa, Utpal and Madhu for all the good and fun times.

Definitions and Abbreviations

1D	one-dimensional
2.5D	two and half dimensional
2D	two-dimensional
2DA	2D FWI result
3D	three-dimensional
3DA	2.5D FWI result
3DB	3D FWI result
CMP	Common midpoint
COT	Continent-ocean transition
CPU	Central processing unit
DGM	Deep Galicia Margin
f	mistfit function
FATT	First arrival traveltime tomography
FD	Finite difference
FWI	Full waveform inversion
G3D	Galicia-3D
GB	Gigabytes
GIB	Galicia Interior Basin
GPS	Global positioning system
Hz	Hertz
IAM	Iberian Atlantic Margins
IODP	International ocean drilling program
ISE	Iberia Seismic Experiment
km	kilometre
km/s	kilometre/second
LB	Lusitania Basin
LG	Lusigal survey
m	Model space/metre
m/s	metre/second

Moho	Mohorovicic discontinuity
ms	milliseconds
OBS	Ocean bottom seismometer
OCT	Ocean-continent transition
ODP	Ocean drilling program
PB	Porto Basin
Pg	Crustal arrivals
PML	Perfectly matched layer
PR	Peridotite ridge
RMS	Root mean square
s	seconds
SDR	Seaward dipping reflector
SIAP	Southern Iberia Abyssal Plain
Vp	P-wave velocity
Vs	S-wave velocity
ZECM	Zone of exhumed continental mantle

Chapter 1 Introduction

Continental rifting is a first-order geodynamic process that results in the surface shape of the present day continents, altering ocean circulation by opening new oceanographic pathways. Rifted margins are the passive trailing edges of the continents that are formed as an end result of rifting process. These margins are one of the largest sinks in the global carbon cycle with thick sedimentary accumulations hosting energy resources and archiving evidence of the Earth's climatic and environmental history. Despite being such important zones, most of the initial studies of these zones were concentrated in the shallow waters primarily for hydrocarbon exploration, where the crust is less stretched closer to the coast, known as proximal domain. Consequently, the proposed mechanisms of continental rifting were only based on observations in the proximal domain and intracontinental basins where the lithosphere is moderately thinned. However, with the discoveries of new hydrocarbon reserves in deep waters, known as distal domain (Figure 1.1), the focus has shifted. Facilitated by the advancements in imaging technology and the availability of drilling data from distal zones, it is now understood that distal zones have different and relatively complex crustal structure compared to the proximal zones.

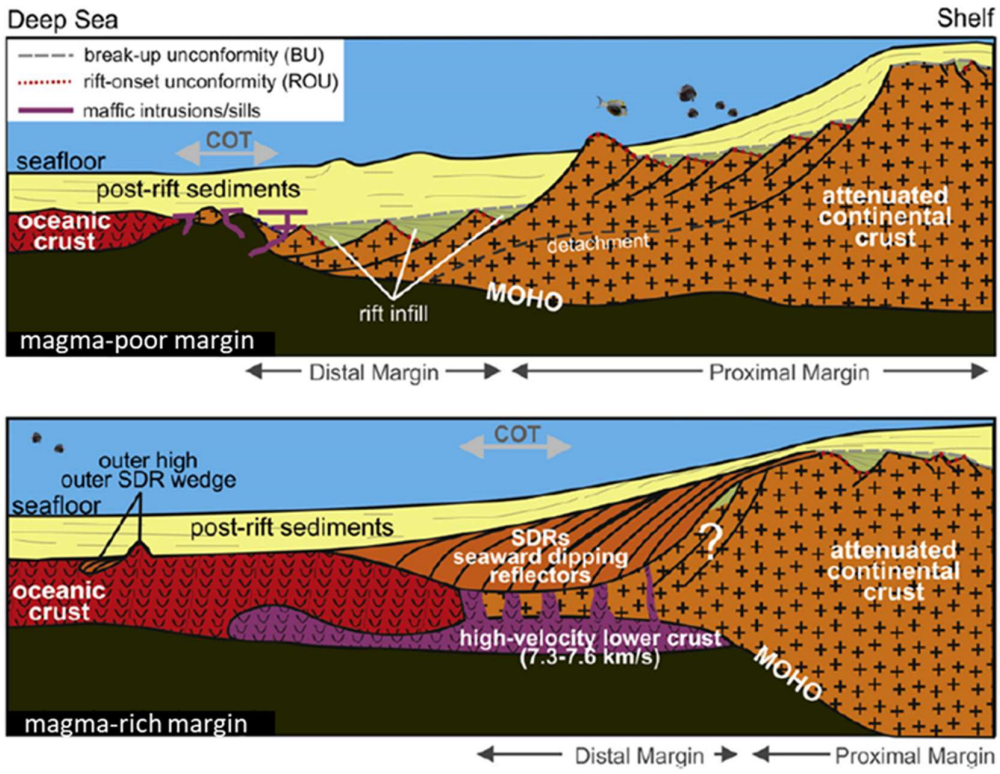

Figure 1-1 Models of magma-rich and magma-poor rifted margins highlighting the differences between the end members of rifted margin (Franke, 2013)

Early rift models were proposed based on observations in the proximal zones: tilted fault blocks with steep faults in the brittle crust and ductile deformations in the deeper crust (McKenzie, 1978; Wernicke, 1985). The 'pure shear model' was proposed by McKenzie (1978) to explain the extension of sedimentary basins. In this model, the continental lithosphere is subjected to uniform stretching involving symmetrical structures, with the extension in the upper brittle lithosphere accommodated by normal faulting, while plastic deformation occurs in the ductile lower crust. In this model, asthenosphere upwelling is directly beneath the crustal thinning zone (Figure 1.2). Though the model explains well crustal thinning and subsidence, it fails to explain asymmetry, embrittlement of crust and large scale low angle lithospheric faults observed in rift settings worldwide (e.g., De Charpal et al., 1978; Pérez-Gussinyé & Reston, 2001). In contrast to the McKenzie's pure shear model, the 'simple shear model' was proposed with low-angle detachment/shear penetrating through the entire lithosphere, introducing asymmetry to lithospheric extension (Wernicke, 1985). In the simple shear model, the crustal stretching is at an offset from the thermal upwelling under the lithosphere (Figure 1.2). The model was first proposed for the Basin and Range province of the USA, but later related to the formation of continental rifted margins (Lister et al., 1986). In addition to Wernicke's model, a number of models for rifted margins were proposed containing components from the pure and simple shear extension models, which are categorised as 'hybrid models' (e.g. Lister et al., 1986). Although these models explain the simple structures observed in the proximal parts well, they fail to explain the complex deformation in the distal parts which are comprised of more complex structures. Moreover, extending these models into distal zones predict a sharp transition between the continental and oceanic crusts contradicting the presence of transition zones between the continental and oceanic crusts.

1.1 Structure and types of rifted margins

The structure of rifted margins shows large variation in terms of the volume of magmatism, crustal architecture and sedimentation patterns. Most of the margins exhibit transitional characteristics between several end member models. These end members are magma-poor and magma-rich (Dore & Lundin, 2015; Franke, 2013), wide and narrow rifts (Brun, 1999), and symmetric and asymmetric crustal architectures (Lister et al., 1991; Ranero & Pérez-Gussinyé, 2010). The structure of rifted margins is effected by various factors. The most prominent ones are the rheology of the lithosphere, thermal structure of the lithosphere, crustal heterogeneities, anisotropies of the crust and mantle, the kinematics and obliquity of the rift system and syn-rift sediments (Brune et al., 2017). Our understanding of rifted margins evolved with access to newer and higher-resolution datasets revealing new structures in the margins, especially in the distal parts. Also, the terminology

pertaining to rifted margins has evolved in parallel with the new structural discoveries. From the unextended continental crust to the unambiguous oceanic crust, several domains with distinct

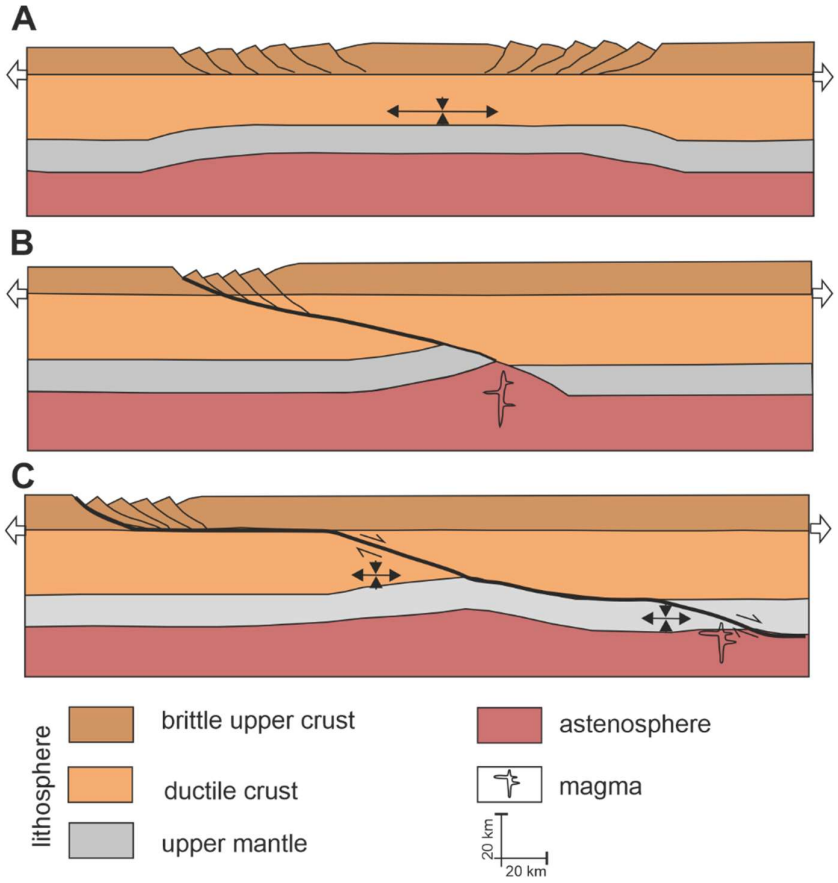

Figure 1-2 Classical rifting models for A) pure shear with symmetric extension B) simple shear with asthenosphere upwelling at an offset from the brittle faulting and C) combination of both give hybrid mechanisms. Modified from Lister et al. (1986).

structural characteristics have been identified globally. Peron-Pinvidic et al. (2013) proposed distinct domains based on structural similarities from different rifted margin settings, starting landwards and proceeding oceanwards.

The proximal domain is the first domain following the unextended continental crust towards the ocean. This zone is subjected to moderate degrees of extension that is accommodated by high-angle normal faulting. Due to the normal faulting, this zone is characterised by graben and half graben basins at the top which are filled with syn-tectonic sedimentary wedges. The normal faults in this zone terminate at mid-crustal levels where the upper crust is decoupled from the ductile lower crust (Sutra & Manatschal, 2012; Weinberg et al., 2007). Following the proximal zone towards oceanward lies the necking zone, this zone characterised by a drastic decrease in the crustal thickness from ~30 km to less than 10 km giving crust a wedge shape. This zone comprises the

coupling point at which the first brittle fault cut through the entire brittle crust and reach the mantle (Pérez-Gussinyé & Reston, 2001). The landward end of the zone is decoupled crust while the oceanward end is coupled crust with no ductile lower crust. Oceanward of the necking zone is the continent-ocean transition (COT), also known as the ocean-continent transition (OCT). Depending on the study region, this zone may also include hyperextended zone, where the crust is less than 10 km thin, and/or zone of exhumed continental mantle (ZECM) (Pérez-Gussinyé & Reston, 2001; Whitmarsh et al., 2001). Hence, the basement in the COT may comprise rocks of upper and/or lower continental crust, exhumed serpentinised mantle, oceanic crust along with possible occurrence of magmatic intrusions (e.g. Beslier et al., 1993; Dean et al., 2000). One important characteristic of the continental crust in the hyperextended zone is that completely brittle allowing normal faults to cut through the entire crust, and in a few settings occurrence of low-angle detachment fault (Pérez-Gussinyé & Reston, 2001). Following COT oceanward, the zones are 'the outer domain', a transition zone between COT and oceanic crust, and 'the oceanic domain' where the onset of unambiguous oceanic crust occurs. The outer domain is a key domain that helps in distinguishing between different kinds of rifted margins based on the volume of magma inferred in this domain. It is not straightforward to define the boundaries of these domains sharply because of the presence of ill-defined basement oceanward in the distal zone comprised of oceanic crust and/or exhumed mantle and/or continental crust.

Based on the volume of the magmatic budget identified in the distal zones, passive rifted margins are categorised between two end-members: magma-poor and magma-rich (Franke, 2013; Mutter, 1993). The main focus of this thesis is magma-poor margins.

1.1.1 Magma-poor margins

Magma-poor rifted margins are present in every ocean of the world (Figure 1.3). These margins are an end result of continental rifting process that was accompanied by less magmatism. Based on numerical modelling, magma-poor margins are associated with slower spreading rates and hyperextension (Brune et al., 2014; Lavier & Manatschal, 2006). However, observations show that hyperextension can also be associated with magma-rich margin, e.g. mid-Norwegian margins. At a global level, magma-poor margins exhibit a few common characteristics including crustal thinning, a zone of anomalous basement between the continental crust and oceanic crust, low-angle detachment faulting, serpentinisation below the thinned continental crust and exhumation of the mantle (Brune et al., 2017; Peron-Pinvidic et al., 2013; Reston, 2009b). However, not all these characteristics are necessarily present in every magma-poor rifted margin.

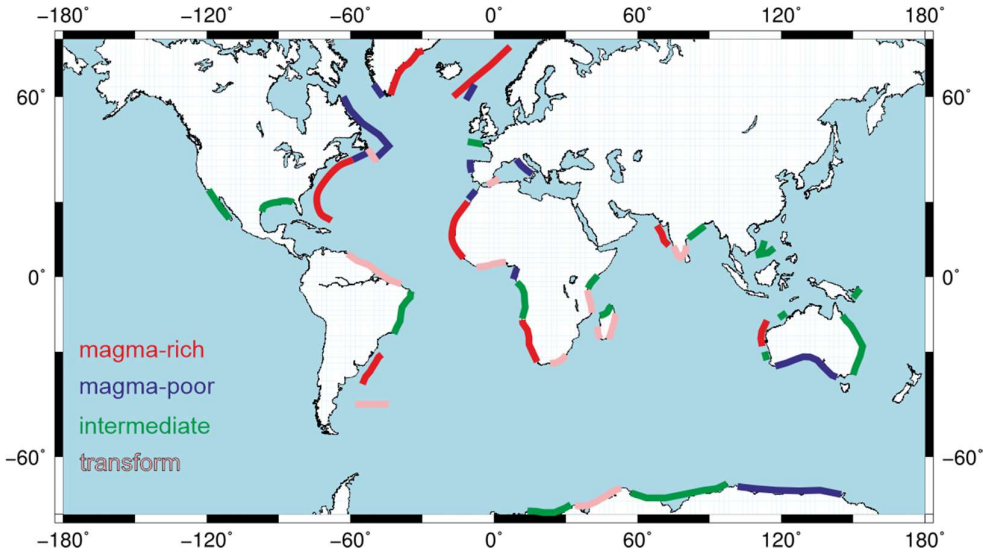

Figure 1-3 World map showing distribution of rifted margins: magma-rich, magma-poor, intermediate and transform margin. Modified from Reston (2009).

In most magma-poor margins, well-defined continental blocks are imaged, at least in the proximal domain. In the distal domain, the structures are relatively complicated and imaging these structures can become difficult with the presence of salt and pre-salt layers above the basement, for example in the Santos Basin, offshore Brazil (e.g., Evain et al., 2015). The continental crust is thinned to a few km thickness from ~30 km over a distance of 100-200 km. In the distal zone, the amount of extension accommodated by the normal faults is less than that required to explain the crustal thinning (Reston, 2005). Various mechanisms including depth-dependent stretching, sequential faulting, polyphase faulting are proposed to explain the crustal thinning in the hyperextended zone and address the 'extensional discrepancy'. Another interesting observation at several magma-poor rifted margins is the delayed post-rift subsidence, for example, South Atlantic margins, offshore Brazil, developed under a shallow water environment (Moulin et al., 2005), the South China Sea (Franke et al., 2011) and the NW Australian margin (Karner and Driscoll, 2000) demonstrate that the extremely thinned crust remained under shallow sea for considerable amount of time after cessation of extension. It is argued that upwelling of hot asthenosphere is responsible for this isostatic imbalance (Franke et al., 2014).

The shift of extension from the proximal zone to the distal zone is marked by coupling of the lower crust with the upper crust, accompanied by progressive embrittlement of the entire crust (Figure 1.1) (Pérez-Gussinyé & Reston, 2001). The normal faults that cut through the entire brittle crust act as fluid pathways, transporting seawater to the upper mantle and causing serpentinisation of the peridotites (Pérez-Gussinyé & Reston, 2001). The distribution of the serpentinisation beneath the crust can be estimated from P-wave velocities (e.g. Bayrakci et al., 2016). The velocities in the

mantle increase with depth and reach the normal mantle velocities over a few kilometres depth in the upper mantle (Bayrakci et al., 2016; Zelt et al., 2003).

Table 1-1 Comparison between end member models of rifted margins: magma-rich and magma-poor (Dore & Lundin, 2015).

Magma-rich margin	Magma-poor margin
Crustal thinning over a short distance (< 50 km)	Crustal thinning over a relatively longer distance (100 - 200 km)
Narrow necking zone	Wide necking zone
Rapid rate of extension	Slow rate of extension
Seaward dipping reflectors (SDRs)	Serpentinised mantle
Clear Moho	No Moho in exhumed zone
Subaerial breakup	Deep water breakup

At a few margins, the boundary between the highly thinned crust and serpentinised mantle can be seen as a sharp reflector on seismic images e.g. the S-reflector of the DGM (Boillot et al., 1989; Sibuet, 1992), the P reflector in the Porcupine Basin (Reston et al., 2001), the M-reflector at the Brazilian margin (Blaich et al., 2011) and the H-reflector in the Southern Iberia Abyssal Plain (Krawczyk et al., 1996). However, in a few locations, this reflector is an intracrustal reflector with lower crustal boudins trapped below the reflector for example, South China Sea (Franke et al., 2014). This reflector can also act as a detachment fault active at a low-angle (< 20°) accommodating the extension during the final stages of rifting (e.g. Reston et al., 1996, 2007).

Extension of the crust with less magma supply leads to eventual breakup and exhumation of the mantle forming a ZECM between the continental crust and the oceanic crust formed at the spreading centre (Brun & Beslier, 1996; Pickup et al., 1996). These zones show weak magnetic anomalies and drilling on the west Iberian margin recovered serpentinised mantle (Boillot & Winterer, 1988). In the ZECMs, the mantle peridotites exposed to sea water undergo serpentinisation and the degree of serpentinisation decreases with depth which is evident from increase in the P-wave velocities (Minshull, 2009). The width of ZECMs varies in range from a few tens of km to more than 100 km.

1.1.2 Magma-rich rifted margins

Majority of the rifted margins globally are magma-rich margins that are characterised by the presence of thick wedges (up to ~15 km) of volcanic flows identified on seismic reflection images as seaward dipping reflectors (SDRs) and high-velocity lower crust (Vp > 7.3 km/s) (Figure 1.1) (Menzies et al., 2002; Skogseid, 2001). The table below (Table 1.1) gives the differences between the characteristics of magma-rich margin and magma-poor margin (Dore & Lundin, 2015):

1.2 Iberia-Newfoundland rift system

The Iberia-Newfoundland system has become the type example for a magma-poor rifted margin. It has been a testing ground for concepts related to rifting tectonics including hyperextension, asymmetry in the rift structure, low-angle detachment faulting, mantle exhumation and formation of the oceanic crust. This system has been the target of various data acquisitions: geochronological, petrological, geophysical, Ocean Drilling Program (ODP) and International Ocean Drilling Program (IODP) (103,149,173 and 210) studies (Bayrakci et al., 2016; Boillot & Winterer, 1988; Reston et al., 1996; Schuba et al., 2018; Whitmarsh et al., 1996). The west Iberia margin is divided into three

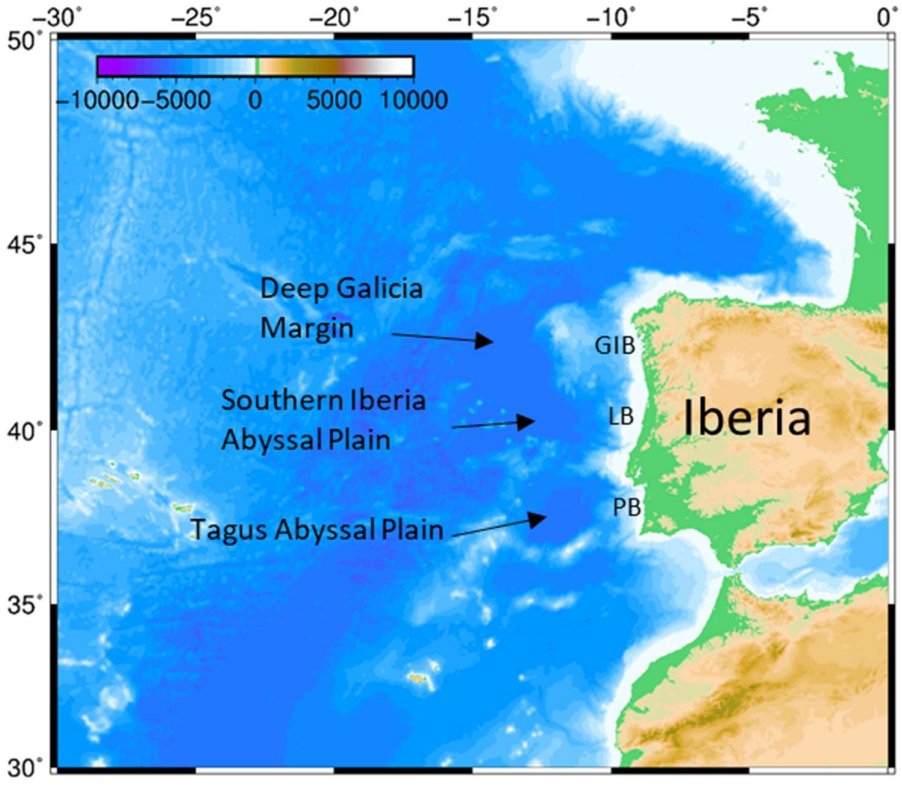

Figure 1-4 Map of the west Iberia rifted margin showing the three segments of the margin: Deep Galicia Margin (study region), Southern Iberia Abyssal Plain and Tagus Abyssal Plain. The three

basins in which initial rifting was focussed are also marked: Galicia Interior Basin (GIB), Lusitania Basin (LB) and Porto Basin (PB). Bathymetry/topography is shown metres.

segments from south to north: the Tagus Abyssal Plain, the Southern Iberia Abyssal Plain (SIAP) and the Galicia Bank (Figure 1.4). In this work, I will primarily focus on the Deep Galicia Margin (DGM) where the final breakup has occurred, west of the Galicia Bank. The timing of the continental breakup and the onset of the oceanic crust is a debated topic. Magnetic field reversal (isochrones) have been identified in a few studies to give an estimate of the timing of the breakup and the onset of oceanic crust (Bronner et al., 2011; Nirrengarten et al., 2017; Srivastava et al., 2000; Tucholke et al., 2007). (Figure 1.5). However, in the Iberia-Newfoundland system, the breakup of continental crust and the formation of oceanic crust happened during a constant polarity interval in the Cretaceous (121—83 Ma) (Gradstein et al., 2012; Sibuet et al., 1995). Another issue with identifying isochrones at this margin comes from the fact that the onset of oceanic crust was preceded by exhumation of the mantle which can also record the magnetic reversals (Sibuet et al., 2007). This makes it difficult to differentiate between the oceanic crust and exhumed mantle (Bronner et al., 2011; Russell & Whitmarsh, 2003; Sibuet et al., 2007). However, the ability of the exhumed mantle to record magnetic reversals enables the determination of the timing of basement emplacement (Bronner et al., 2011).

The isochron C34 is the first undisputed evidence for the oceanic crust on the Iberia and Newfoundland margins. C34 has an age of ~84 Ma, and is located ~280 km west of the peridotite ridge at the DGM (Figure 1.5) (Bronner et al., 2011; Gradstein et al., 2012). Another prominent anomaly is located within the COT at both on the margins, known as the J anomaly (Figure 1.5). The J anomaly has been interpreted as a pulse of magmatism that let to continental breakup before seafloor spreading or as the beginning of the seafloor spreading anomalies (M0-M3) (Bronner et al., 2011; Sibuet et al., 2007). The amplitude of the J-anomaly is strong in the SIAP and becomes weak towards the north, and is completely absent in the DGM (Figure 1.5).

The M0 magnetic anomaly (126 Ma) was interpreted as a seafloor spreading anomaly west of the peridotite ridge and also on the Flemish cap (Srivastava et al., 2000). The anomalies M2 and M3 (128—130 Ma) were interpreted as seafloor spreading anomalies within the ZECM at the SIAP, while the anomaly M1 (125—128 Ma) is interpreted as the first oceanic crust (Figure 1.5) (Minshull et al., 2014). Though the J-anomaly and M sequence anomalies have been used for plate reconstruction modelling, their consideration as the markers of the onset of oceanic crust are questioned (Nirrengarten et al., 2017; Tucholke & Sibuet, 2012).

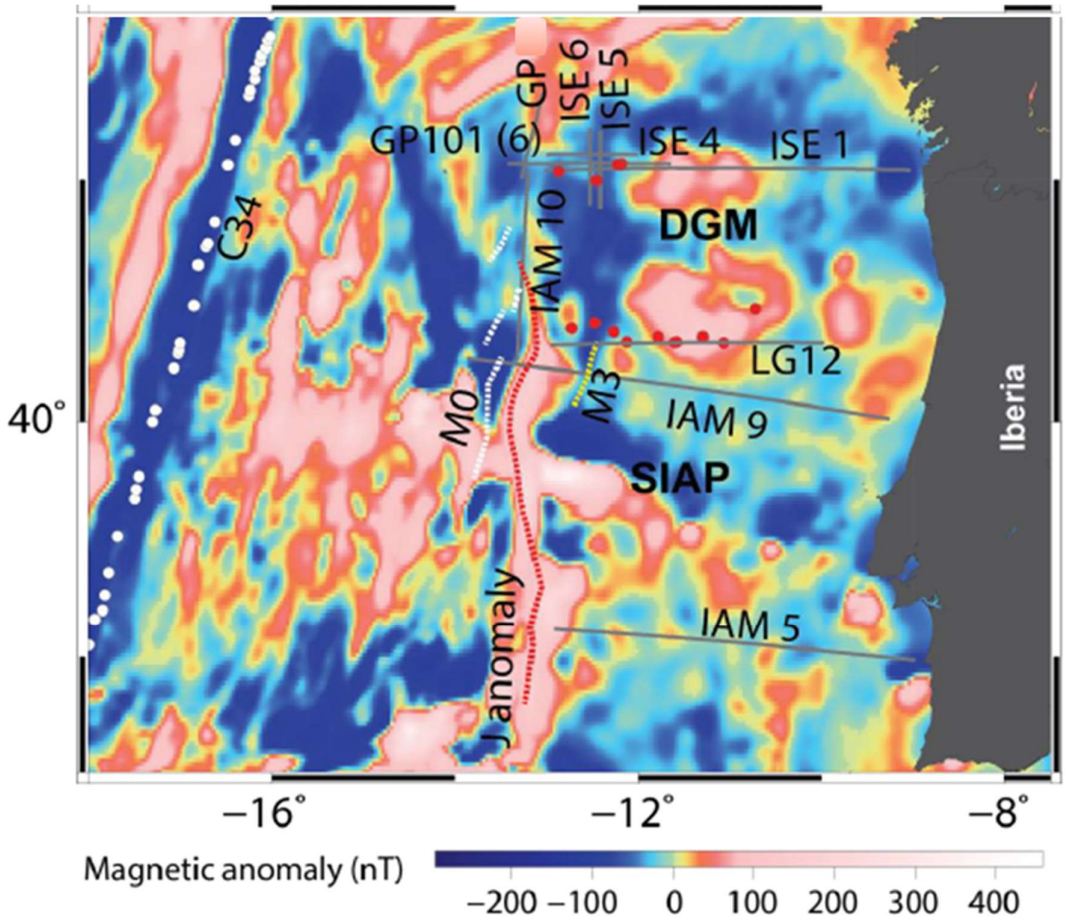

Figure 1-5 Magnetic anomaly map of the Iberia rift margin (Maus et al., 2009). Previous seismic experiments are plotted in grey lines, GP (Beslier et al., 1993a)*, ISE (Dale S. Sawyer et al., 2007), Lusigal* (Beslier et al., 1993a)*, and IAM (Pickup et al., 1996). Isochron C34 is highlighted as white dots (Klitgord & Schouten, 1986). Magnetic anomaly M0 shown as white dashed line (Srivastava et al., 2000), and yellow dashed line represents the interpreted location of magnetic anomaly M3 (Whitmarsh & Miles, 1995). Red dashed lines show the location of the interpreted J anomaly* (Beslier et al., 1993a)*. ODP Leg 103, 149 and 173 drill sites are shown as red circles (Davy et al., 2016).*

1.2.1 Rifting in the Galicia Margin

The Galicia margin is the northern segment of the west Iberia margin. It is a sediment-starved, salt-free and magma-poor margin that is extensively studied to understand the tectonics involved in the rifting process (e.g. Boillot & Winterer, 1988; Lymer et al., 2019). Crustal thinning towards zero thickness, reduced mantle velocities beneath the thinned crust and exhumed mantle were all first observed in the Galicia margin (Boillot & Winterer, 1988). The Deep Galicia margin (DGM) is the western extent of the Galicia margin where the crust is thinned to less 5 km thickness (Figure 1.6). Initial extension in the proximal zone is accommodated by listric high-angle normal faulting with

large fault-bound blocks of 10-20 km wide (Ranero & Pérez-Gussinyé, 2010). In this zone, the amount of extension explains the crustal thinning. However, a discrepancy between the amount of extension and crustal thinning exists in the hyperextended zone. As the extension progressed into the hyperextended zone, the upper and lower crust progressively became coupled and lower crust progressively became brittle (Pérez-Gussinyé & Reston, 2001).

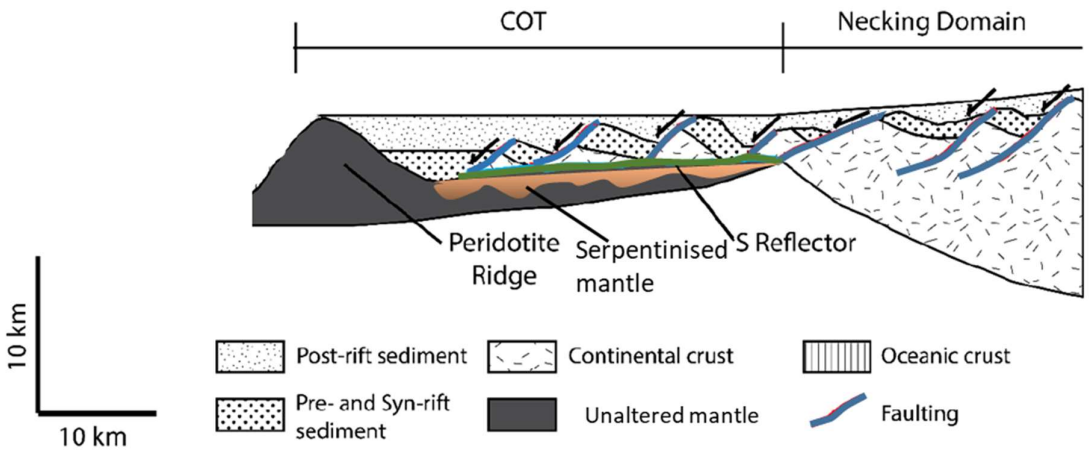

Figure 1-6 Schematic diagram of the Deep Galicia margin developed based on the 3D velocity model (Bayrakci et al., 2016).

Under the action of extensional forces, listric normal faults developed through the entire brittle crust which acted as fluid conduits transporting seawater to the upper mantle (Pérez-Gussinyé & Reston, 2001). Hydration of the mantle peridotites resulted in the formation of serpentinites beneath the crust (Bayrakci et al., 2016; Pérez-Gussinyé & Reston, 2001), which are weak and have a low friction coefficient. With continued extension, the fault blocks in the hyperextended zone slipped over a lithospheric scale detachment fault, called the 'S-reflector', active at a low-angle (< 20°) (Reston et al., 1996, 2007). The S-reflector has also been interpreted as a crust-mantle boundary and/or a brittle-ductile transition (Ranero & Pérez-Gussinyé, 2010; Reston et al., 1996, 2007; Sibuet, 1992). Slip of the crustal fault blocks along the S-reflector over a serpentinised mantle resulted in intense fracturing and brecciation in the lower parts of the crust (Reston et al., 1996). Furthermore, a low-velocity zone of ~50 m thickness, comprising highly fractured serpentinised/crustal rocks, was inferred at the S-reflector from one-dimensional full waveform inversion (Leythaeuser et al., 2005). 3D seismic reflection imaging has confirmed the presence of the "S-interval" with non-uniformly distributed fault rock material that thickens near the fault intersections with the S-reflector (Schuba et al., 2018). It was inferred, based on P-wave velocities below the S-reflector, that the mantle serpentinisation happened in a preferential manner with

lower velocities in the hanging wall side of the normal faults (Bayrakci et al., 2016; Davy et al., 2018). Bayrakci et al. (2016) proposed that the degree of serpentinisation below the S-reflector, estimated from a 3D P-wave velocity model derived using wide-angle seismic data, correlates with heaves of the normal faults, with larger heaves transporting more water than faults with smaller heaves. However, this correlation was questioned based on the serpentinisation values estimated by training a machine learning algorithm below the S-reflector (Schuba et al., 2019). During the final stages of rifting just before the continental breakup, serpentinised mantle was exhumed to the seafloor along the S reflector, and was emplaced west of the hyperextended domain, forming a structure known as the Peridotite Ridge (Figure 1.6) (Beslier et al., 1993a).

1.3 Mechanisms of rifting in the hyperextended zone

Despite gaining good understanding about the rifting process, a number of questions still remain to be answered. It is still not fully clear how the crust thins to zero thickness exposing the mantle during rifting. Different mechanisms have been proposed to explain the extensional discrepancy, the role of the lower crust, the role of detachment faults and the pattern of serpentinisation of the mantle. Out of the many proposed mechanisms, three are at the centre of the debate:

1) Depth dependent stretching: In this mechanism, the thinning varies between different depths depending on the rheology of the layers (Figure 1.7) (Driscoll & Karner, 1998). The viscous layers, being weak, require lower levels of stress, hence deform prior to brittle layers. The lower crust, which accommodates more extension compared to the brittle upper crust, is generally moving laterally either towards oceanic (proto) crust or landwards to accommodate stretching beneath the detachment fault (Davis & Kusznir, 2004; Driscoll & Karner, 1998). However, none of these is observed to explain the extent of discrepancies by this mechanism(Reston, 2009a). Using numerical modelling of the magma-poor rifted margins, it has been demonstrated that DDS occurs involves two breakup events: crustal breakup and mantle lithosphere breakup (Huismans & Beaumont, 2011). However, the order of the breakup events may vary for different rifted margin settings (Huismans & Beaumont, 2011). Evidence for this mechanism is the presence of syn-rift packages of the same age at the top of the fault blocks along the margin, indicating a single phase of extension in the upper brittle crust. In this model, the detachment zone develops during later stages of the rifting, and cuts across the base of pre-existing fault blocks that are formed in the early stages of the rifting.

2) Sequential faulting: In this mechanism, new preferential faults are cut through the thinned crust in its hanging wall (Ranero & Pérez-Gussinyé, 2010). The extension is focused on a single fault at a time and sequentially proceeds to the next fault towards the centre of the rift, explaining the

asymmetry of conjugate margins (Figure 1.7). The size of the fault blocks reduces as the extension migrates to the rift centre. The extension discrepancy in this mechanism is addressed by localised slip of the individual fault as the fault blocks rotate to lower angles over a detachment fault during the extension. Evidence for this mechanism in a margin would be systematic movement of fault blocks younging oceanward. The rolling hinge model (Buck, 1988) is a form of sequential faulting in which each fault is active individually and abandoned when a new fault cuts through the hanging wall of the previous fault, and each fault is rotated by slip on subsequent faults propagating up from a steep root zone to form a continuous sub-horizontal detachment surface. The detachment in the rolling hinge model is a rooted detachment and comprises segments of successive steep faults (Buck, 1988; Reston et al., 2007).

3) Polyphase faulting: In this mechanism, the fault blocks rotate until the faults are locked up with no further movement. Then, new faults are developed cutting the previous fault blocks, overprinting the previous faults giving rise to a complicated pattern of faulting that is below the resolution limits of seismic imaging (McDermott & Reston, 2015; Reston, 2005). This unresolvable faulting pattern explains the extension discrepancy (Figure 1.7). An evidence for polyphase faulting can be obtained from the top of the basement which in places would be the exhumed slip surface of the previous thinned fault block.

1.4 Previous seismic datasets and basement drilling

The DGM has been studied for over the past four decades for understanding the structure and tectonic processes that took place in the margin using different geophysical datasets (Figure 1.8). The earliest seismic data acquired in the margin were by Institut Francais du Petrole in 1975 and 1980 (GP profiles). The data from these experiments revealed the basic structure of the margin including post-and syn-rift sedimentary packages, titled and thinned continental crustal blocks, and a lithospheric scale detachment fault within, now known as the S-reflector (Boillot & Winterer, 1988; Mauffret & Montadert, 1987). Data from these datasets also revealed the presence of serpentinised mantle peridotites, known as the Peridotite Ridge, later confirmed by seafloor dredging, sampling via submersible and ODP drilling (ODP site 637) (Boillot et al., 1980, 1987).

Wide-angle seismic data along the GP profiles were used to derive a seismic velocity model of the COT (Whitmarsh et al., 1996). Using the velocities it was inferred that the continental crust thinned from 17 km thickness to 2 km on the east side of the peridotite ridge (Whitmarsh et al., 1996).

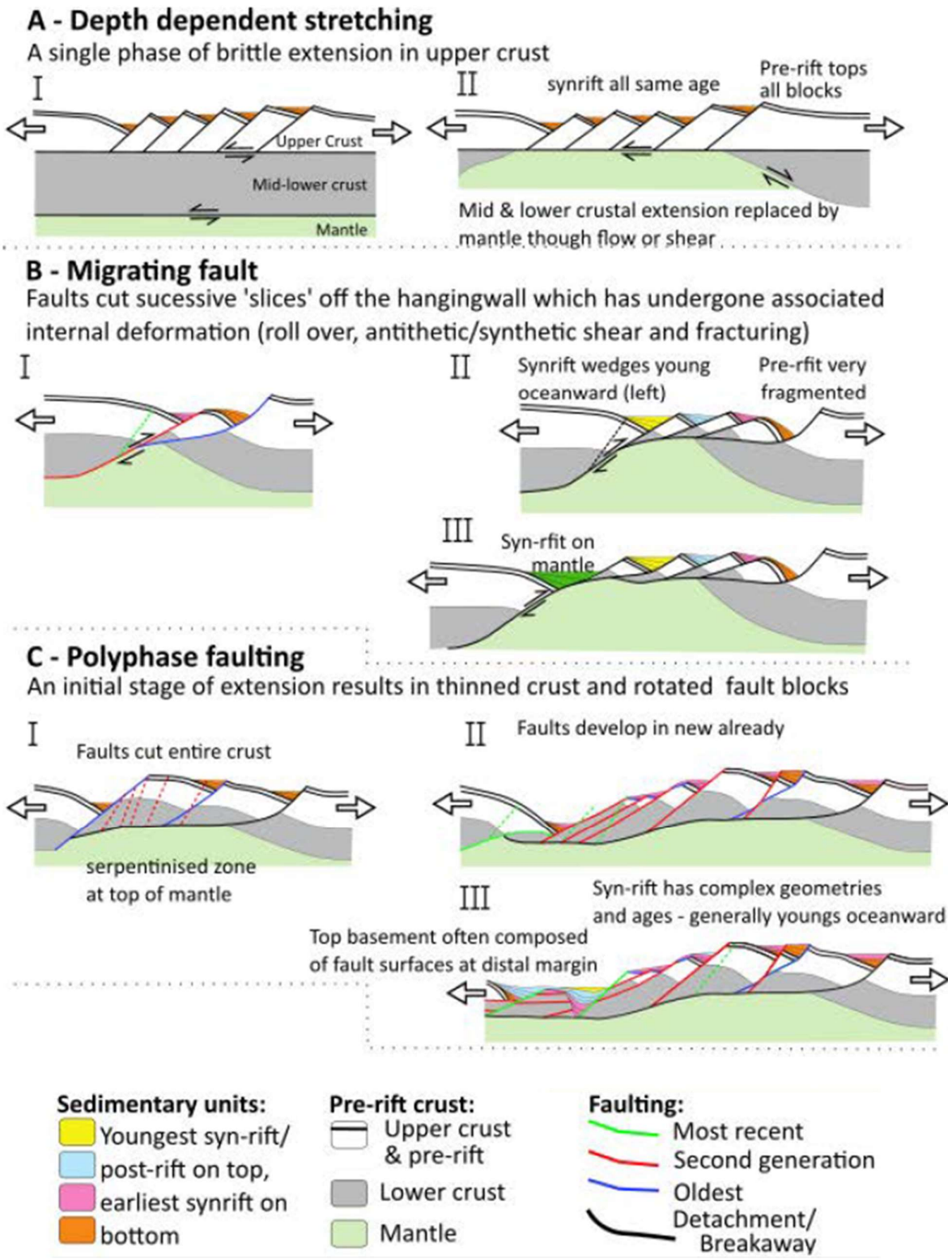

Figure 1-7 Conceptual models of the breakup of the continental crust and formation of the S reflector: Depth-dependent stretching, Sequential faulting (Buck, 1988; Ranero & Pérez-Gussinyé, 2010) and Polyphase faulting (Reston, 2005).

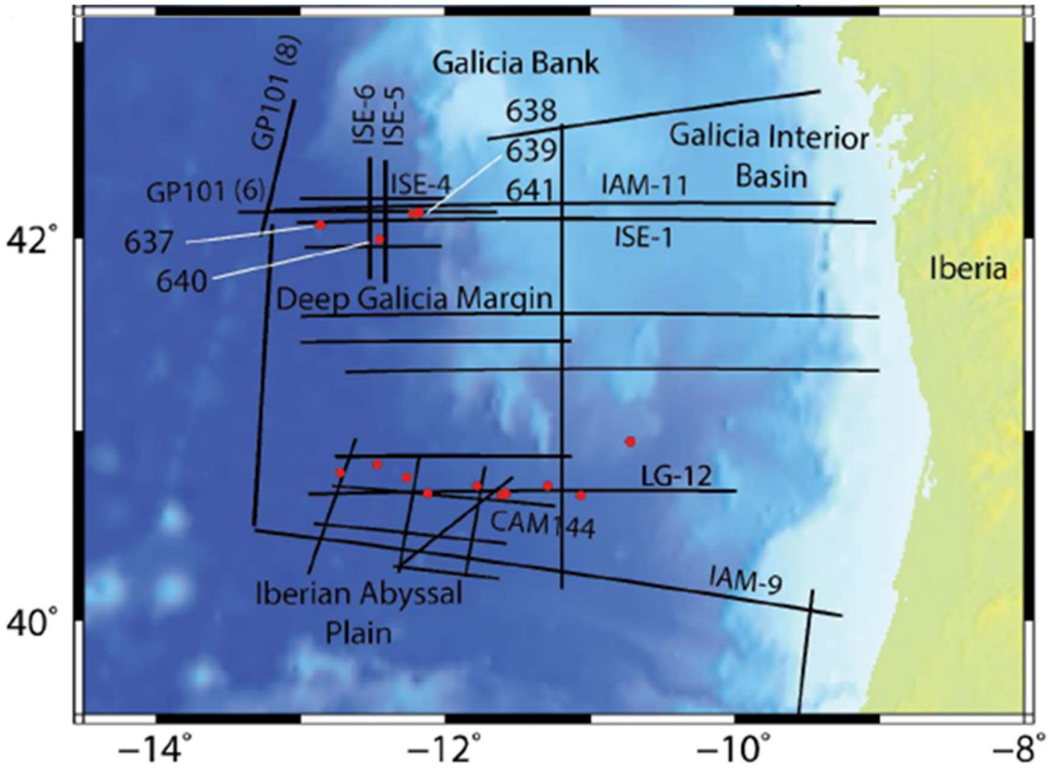

Figure 1-8 Map of the west Iberia margin showing seismic lines from previous seismic surveys in black lines: GP (Whitmarsh et al., 1996), ISE (Sawyer et al., 2007), LG (Beslier et al., 1993a), IAM (Banda & Torne, 1995) and CAM (Minshull et al., 1998). ODP drilling locations are shown in red circles.

More seismic reflection and refraction data were acquired during the Iberia Seismic Experiment (ISE) covering southern and central Galicia Bank and the DGM (Sawyer et al., 2007). The data was acquired along and across the margin during the ISE experiment. Based on interpretations from pre-stack depth migrated images of ISE lines and subsidence modelling, it was inferred that the COT in the Galicia Bank and SIAP consists of exhumed mantle that has undergone serpentinisation within the COT and also under the continental crust landwards (Henning et al., 2004). A detailed analysis of the syn-rift sedimentary units above the thinned continental crust revealed that the S-reflector is a rooted detachment active at low angles (< 20°) (Reston et al., 2007).

Other notable seismic experiments carried out on the West Iberia margin include the Lusigal (LG) survey (Beslier et al., 1993a), Iberian Atlantic Margins (IAM) (Banda & Torne, 1995) and the CAM seismic profiles (Minshull et al., 1998). All these surveys were primarily acquired to understand the structure of the COT in the SIAP, however, few have extended to include both thinned continental crust and oceanic crust in the east and west, respectively. IAM-9 seismic line is the only seismic of the all seismic lines that images the full thickness of the unambiguous oceanic crust in the west and full width of the COT in the SIAP (Dean et al., 2000). Using the wide-angle data from the CAM

profiles, velocities within the extremely thinned continental crust (2-5 km) were estimated to be 5.5-6.8 km/s (Chian et al., 1999).

ODP leg 103 has sampled the basement in number of sites in the DGM (Boillot et al., 1987; Boillot & Winterer, 1988). Site 638, 639 and 641 were drilled into the necking zone of the thinned continental crust recovering pre-rift limestone sediments from Upper Jurassic and Lower Cretaceous deposited in a shallow water depths (Figure 1.8) (Boillot & Winterer, 1988). Above this sequence, Valanginian-Hauterivian syn-rift sandstones deposited in a deep water environment were recovered. This layer was covered by a syn-rift Aptian-Barremian sediment column. On top of these syn-rift sediments, post-rift sediments were recovered from Tertiary-Aptian (Boillot & Winterer, 1988). Based on this stratigraphic record, the duration of the rifting was estimated to be ~25 M.y (Reston, 2005). At Site 637, serpentinised mantle and peridotites were sampled in the Peridotite Ridge (Figure 1.8).

The basement in the Iberia-Newfoundland margins was sampled at a few other locations. ODP legs 149, 173 and 210 have sampled at locations on both the margins (Shipboard Scientific Party ODP Leg 149, 1993; Shipboard Scientific Party ODP Leg 173, 1998; Tucholke & Sibuet, 2007). Serpentinised peridotites and minor amounts of basalt were recovered from the COTs of both margins, suggesting that mantle exhumation into shallow depths occurred on both margins preceding lithospheric breakup.

1.5 Research questions

This chapter is an introduction to the study region and to the concepts related to rifting. The main focus of the thesis is to develop a high-resolution 3D P-wave velocity model of the DGM using wide-angle seismic data and understand the rifting happened in the final stages in the DGM.

The research questions addressed in this thesis may be outlined as follows:

- Two-dimensional (2D) seismic studies are more common than 3D studies due to their cost efficiency. However, structures in the subsurface are 3D in nature and 2D imaging will distort the 3D structures to certain degree, and sometimes introduce artefacts in the images as well. Previously, a 2D high-resolution velocity model of the DGM was developed using wide-angle seismic data which resolved fine-scale structures compared to the 2D traveltime model (less resolution model; Davy et al., 2018). The wide-angle data used in for 2D imaging were a subset of 3D wide-angle data from the DGM (Bayrakci et al., 2016). Hence, developing a 3D high-resolution velocity model using the wide-angle data provides

a great opportunity to highlight the differences between 2D and 3D FWI imaging in a rifted margin setting using real dataset.

- One of the fundamental questions pertaining to the rifting process is about the crustal thinning in the distal zone. To address this question, a good understanding about the nature of the crust is required both qualitatively and quantitatively. 2D and 3D seismic reflection imaging of the DGM has provided high-resolution details regarding the structural aspects of the extension (e.g. Lymer et al., 2019; Reston et al., 1996, 2007; Schuba et al., 2018) However, a high-resolution 3D quantitative model will be a significant addition to the information archive of the DGM. A high-resolution 3D velocity model can help us to differentiate between different rock types within the crust and understand their role in the extension.
- The pattern of serpentinisation below the S-reflector can help us in understanding the relation between the fault motion and water transport process. It was proposed that the mantle is hydrated in a preferential manner with higher serpentinisation observed under the hanging wall side of the normal faults below the S-reflector (Davy et al., 2018; Pérez-Gussinyé & Reston, 2001). Generating a serpentinisation map below the S-reflector using the high-resolution 3D FWI model will enable us to check the relation between normal fault intersections and serpentinisation process.
- First-order multiples recorded in an OBS dataset contain valuable information about the subsurface. Compared to the primary reflections, the multiples continuously sample the subsurface laterally as they bounce off the same reflectors as primary reflections but at a farther distance from the receivers. The technique that uses first-order multiples for imaging is called mirror imaging. The application of this technique has been previously mostly to shallow depth targets within a few hundred metres of the seabed. The wide-angle data from the DGM has been acquired in deep water environment and is a perfect dataset to test mirror imaging at crustal scale.

1.6 Thesis outline

In this thesis work, I developed 3D high-resolution P-wave velocity model of the DGM using wide-angle seismic data. Based on the model, I look to contribute to the understanding of the rifting that happened in the DGM. I have also applied mirror imaging technique for the first time to image structures at crustal scale using a dataset that has been acquired in a deep water environment.

Chapter 2 details the acquisition of seismic reflection and refraction dataset acquired in the DGM which is used in this thesis work. Modelling methods are described which are applied to this dataset, including full-waveform inversion and mirror imaging.

Chapter 3 details the application of 3D full-waveform inversion method to the sparse spaced OBS data from the DGM. I compare the result of 3D FWI with the result from 2D FWI and highlight the difference between 3D and 2D FWI performances. I present this chapter as a stand-alone research paper that will be submitted to the journal 'Geophysical Journal International'.

Chapter 4, I present the 3D FWI result from Chapter 3 along different profiles and discuss the results based on the implications from previous studies including nature of the crust in the DGM, exhumation of the lower crust during lithospheric extension, and serpentinisation patterns below the S-reflector.

Chapter 5 details the application of 2D mirror imaging to the OBS data from the DGM. I present the results from mirror imaging in time and depth domains. I compare the results with the images developed by migrating primary reflections from the 3D seismic volume and OBS data.

Chapter 6 provides a summary of the main findings from Chapter 3 – 5, and includes suggestions for future work.

Appendix A contains two tables with the first table detailing the location of OBSs used in this study and the second table giving number shots used from each OBS in the 3D FWI in chapter 3.

Appendix B contains phase plots for all the instruments used in the Chapter 3, and plots comparing observed data and predicted data using 3D FWI model complementing results from Chapter 3.

Appendix C contains the work I did at the Woods Hole Oceanographic Institution, USA, from July to September, 2018. The aim of the study was to understand accretion of the oceanic crust at the Galapagos Spreading Centre using seismic reflection imaging. This work is published in an AGU journal, 'Geophysical Research Letters'.

Chapter 2 Data and methods

2.1 Data acquisition and survey design

The Galicia-3D experiment was conducted between May and September of 2013 in order to gain further understanding of the processes of continental rifting and lithospheric breakup at the Deep Galicia margin. Galicia-3D was a combined multichannel reflection and wide-angle seismic experiment undertaken as a collective effort between UK, US, German and Spanish research institutes. The multichannel reflection seismic volume was recorded over an area of 80 km (east-west) by 20 km (north-south) (Figure 2.1) by the RV Marcus G. Langseth operated by Lamont-Doherty Earth Observatory. The wide-angle data was recorded by 86 ocean bottom hydrophones/seismometers (OBS) from the UK Ocean Bottom Instrumentation Facility (Minshull et al., 2005) and GEOMAR Helmholtz Centre for Ocean Research. The F.S. Poseidon deployed and recovered the OBSs which concurrently recorded the signals from the seismic reflection experiment as part of Galicia-3D.

2.1.1 Multichannel reflection survey

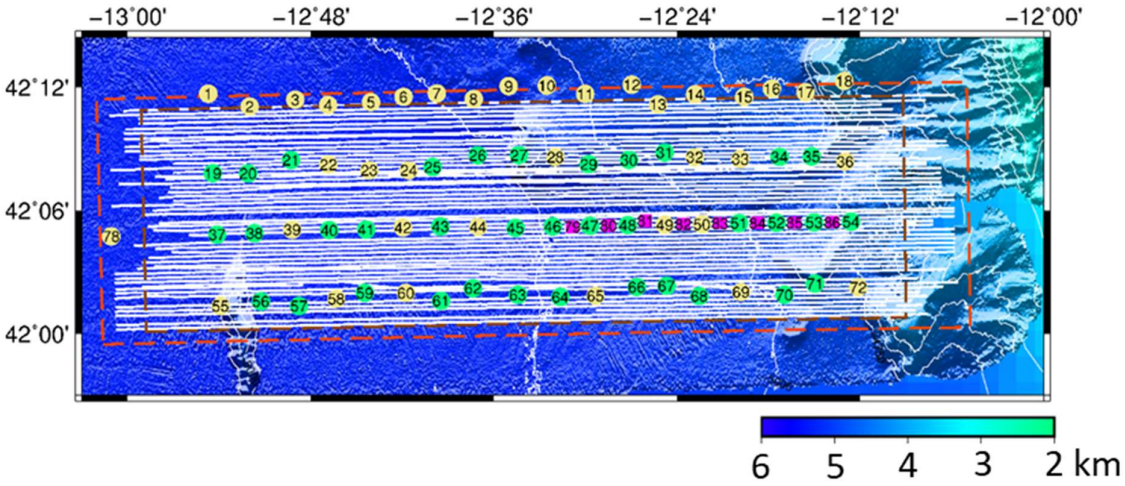

Figure 2-1 Galicia-3D seismic experiment map. The figure shows OBS locations, grids boundaries and bathymetry within the Galicia-3D experiment. The map shows multichannel seismic grid dimensions in dashed brown, named as 3D-Box and OBS grid dimensions used in this work for full waveform inversion in dashed red. The stations in green are used for the 3D FWI, stations not used are represented in yellow. Stations in pink are the high-resolution OBSs with just 2 lines of recording – 2D deployment.

The three-dimensional seismic reflection data was acquired within the 3D Box (Figure 2.1) using four 6 km streamers towed 200 m apart. Each streamer consisted of 468 hydrophones spaced 12.5 m apart, and the streamers were towed at a depth of 15 m. The survey was carried out using two air arrays each consisting of 20 airguns. The two arrays were towed 100 m apart with gun volumes between 40 cu.in. and 360 cu.in. at a depth of 9 m. The total individual volume of each airgun array was 3,300 cu.in. (Figure 2.2). Seismic shots were fired alternatively using the two source arrays every 37.5 m (a shot interval of ~ 16 s with a ship speed of 4.5 knots) enabling 8 adjacent CMP profiles, spaced 50 m apart to be recorded along the sailing lines. The survey was designed to image in three dimensions the thinned continental crust over the S-reflector and included two profiles that extended west of the peridotite ridge. These 2D seismic lines were acquired to identify the first-formed oceanic crust. These profiles are referred to as Western Extension 1 and Western Extension 2 Only one of the two seismic source arrays was fired with a distance interval of 150 m, along Western Extension 1 and Western Extension 2 (a shot interval of ~ 64 s with a ship speed of 4.5 knots).

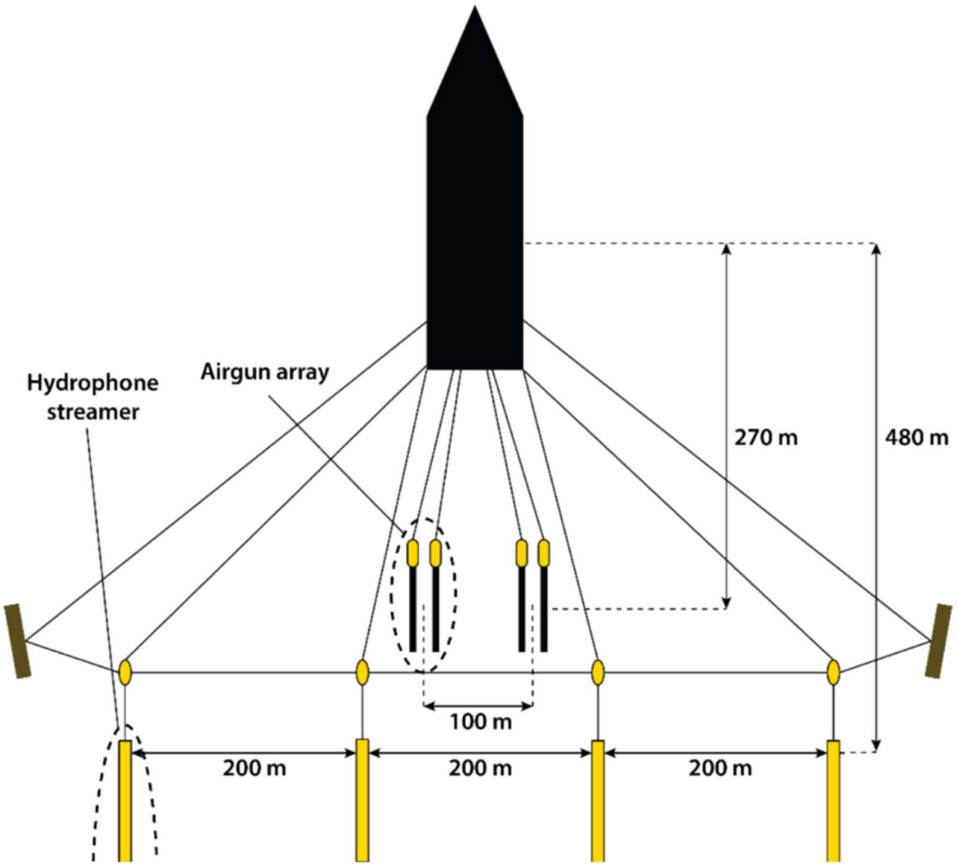

Figure 2-2 The schematic diagram of the acquisition system deployed for the acquisition of seismic data in Galicia 3D experiment (Davy, 2017). The diagram shows the distance between the center of the shipt to the airgun arrays and streamers. Also, the spacing between the airgun arrays and streamers is mentioned.

2.1.2 Ocean Bottom Seismometers and their deployment

OBS were deployed prior to the seismic reflection survey with the purpose of recording wide-angle data during the survey. UK Ocean Bottom Instrumentation Facility provided 50 OBS each of which had a three-component Sercel L-28 4.5 Hz geophone, and a High Tech HTI-90-U hydrophone . Two different types of loggers were used in these instruments either an LC2000 or an LC4x4 digital logger, which recorded seismic data at a sampling rate of 4 ms. GEOMAR provided 7 OBS with each comprising a three-component KUM 4.5 Hz geophone and a High Tech HTI-01-PCA hydrophone. Additionally, 21 OBS single High Tech HTI-01-PCA hydrophones were provided by GEOMAR. All GEOMAR instruments comprised of MLS digital loggers and recorded at a sampling rate of 5 ms.

Deployment of the OBS happened in two configurations, one within the 3D-Box as shown in Figure 2.1 and other west of the Peridotite Ridge. Within the 3D-Box the OBS were deployed along four profiles with 18 OBS in each profile. The separation between the profiles is ~6 km in the north-south direction and ~3.2 km between the instruments in the east-west direction along each profile. All the OBS were deployed for 79 days on the seafloor with 32 days of active seismic recording during the reflection experiment. Out of the 86 instruments deployed, a total of 8 OBS were not recovered and another 9 OBS did not record any usable data.

OBS are deployed on the seafloor by allowing them to free-fall through the water column. In deep waters (~5000 m), the water currents and hydrodynamic instabilities cause the instruments to move laterally before reaching the seafloor. This unavoidable lateral movement required correction from the OBS release point GPS location to know the correct location of the instrument. This correction of the location is called instrument relocation. OBS instruments in our study were relocated using the arrival times of direct waves through the water column (Appendix A-1). The relocation procedure requires knowing the sound velocity profile through the water column, bathymetry data, arrival times of the direct water waves and initial GPS location of OBS release point. A mean water velocity value of 1.52 km/s was assumed for the relocation of the instruments.

Excellent azimuthal coverage for the OBSs in the 3D-Box enabled accurate instrument relocation except the instruments along the northern most line. The relocation was carried out using the travel-time misfit between the direct-arrival times picked manually and the calculated times. All OBS were also corrected for the drifting of the internal clocks (Bayrakci et al., 2016; Davy et al., 2016). Clear crustal arrivals (Pg) can be seen on the data (Figure 2.3). First-order multiples were used in mirror imaging in chapter 5.

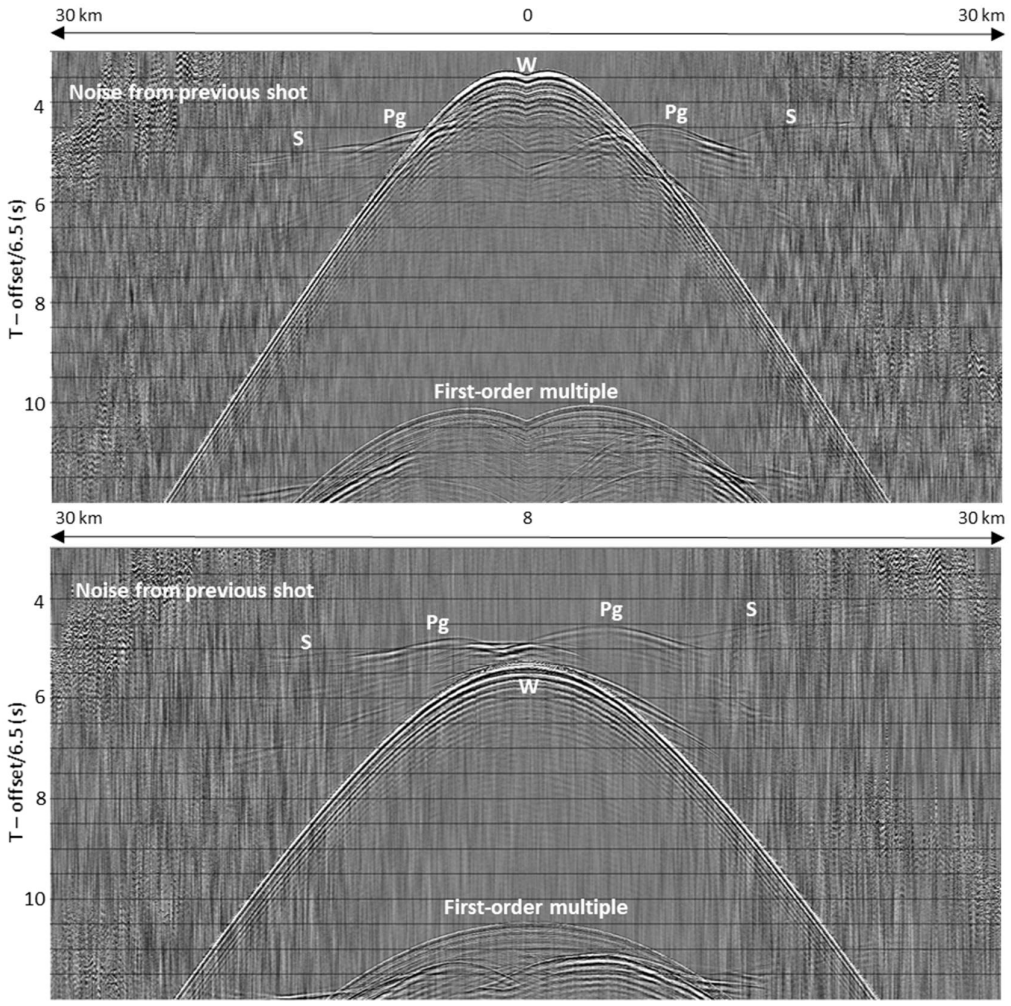

Figure 2-3 Raw OBS gather (hydrophone) showing water column arrivals (w), crustal arrivals (Pg), arrivals from the S (S) and first-order multiples along a near and far offset profiles of an OBS.

2.2 Full waveform inversion

Full Waveform Inversion (FWI) is a challenging non-linear data-fitting technique, which provides high-resolution images of subsurface physical properties. In the ideal case, FWI uses full content of the recorded data as a function of time, and models the recorded data using the complete physics of finite-frequency wave propagation. FWI works in a deterministic manner by iteratively minimizing the difference between observed and modelled datasets. With advances in data acquisition procedures and today's available computational facilities, 3D acoustic FWI application is now becoming common for industrial seismic data sets (e.g. Plessix & Perkins, 2010; Sirgue et al., 2010). In this section, I review the evolution of FWI over the years, followed by basic formulations which govern the algorithm for generating high-resolution images.

In the mid 1980s, seismic reflection surveys were limited to short-offsets and limited frequency bandwidth making the datasets poorly sensitive to intermediate wavelength causing difficulties for seismic imaging (Jannane et al., 1989). Hence, imaging became a two-step process: developing macromodel from kinematic information (low wavenumber), and then use of migration algorithms to generate images (high wavenumber) (Clærbout, 1976; Gazdag, 1978). Various methods have been proposed to iteratively achieve high-resolution images from macromodels, but all of them remained limited because of less sensitivity of data towards intermediate wavelengths. Migrated images despite having high resolution qualitatively lack in terms of quantitative information they provide. Lailly (1983) and Tarantola (1984) came up with the idea of using all phases in a single process for improving seismic imaging qualitatively and quantitatively, known as FWI. This idea of improving macromodels is based on iteratively updating the starting velocity model by cross-correlating the incident wavefields and the back-propagating residual wavefields. The first synthetic tests to demonstrate the functionality of FWI employing the acoustic wave equation was carried in 2D by Gauthier et al. (1986). Mora (1987) presented elastic inversion results using synthetic waveforms. Due to the non-availability of long-offset data and computational demands which FWI places, many researchers then believed FWI would not be particularly efficient at generating high-resolution models. However, with the advancements in computation facilities and acquisition systems made FWI a realistic method for high-resolution imaging. The first formulations for FWI were proposed for reflection seismic data only, but later studies demonstrated that inclusion of long offset wide-angle seismic recording in the input data is beneficial for FWI (e.g., Pratt & Worthington, 1990). FWI can be performed in both domains, time (e.g., Tarantola, 1984) and frequency (Pratt et al., 1998), depending on the ease of implementation mitigating the non-linearity of FWI. The frequency domain is a natural domain for implementing a multi-scale approach by starting inversion from low frequencies and progressing to higher frequencies along with the ease of inverting for attenuation. In the time domain, it is easier to add anisotropy and perform quality check of the inversion. In addition, the time domain allows time-windowing the data, and multi-scale implementation is also possible in the time domain (Bunks et al., 1995). Although, the computational time for 2D FWI in the frequency domain is less than the time domain, the performance efficiency in both the domains is comparable in 3D. In the early 1990s, FWI was mostly implemented in 1D and 2D inverse problems because of its extensive computational demands. 2D FWI became well established with the introduction of a multi-scale approach using a synthetic dataset by Bunks et al. (1995) and results were presented using 2D surface seismic data by Shipp & Singh (2002). Several studies have demonstrated that time domain modelling is well-suited for 3D FWI (Virieux & Operto, 2009; Warner et al., 2013). Štekl et al. (2007) presented the results for 3D synthetic case recovering a channel geometry, whereas Sirgue et al. (2010) presented high-resolution 3D FWI results recovering a channel system and a gas cloud using a dataset from the

Valhall field. Subsequently, many different variants of FWI were applied to field data sets e.g., Plessix & Perkins, (2010). Ideally, accounting for realistic effects in the inversion can improve the quality of the imaging significantly such as anisotropy, S-wave velocities and quality factor. However, these effects are commonly not considered due to the requirement of large computational power for visco-elastic FWI, problems arising from cross-talk between different parameter classes and complexities in the estimation of the amplitudes due to inaccuracies in density and attenuation values (Tarantola, 1986; Virieux & Operto, 2009). In the academic community, FWI application to the sparsely acquired wide-angle seismic data using OBS is gaining popularity to understand the crustal processes. Pratt et al. (1996) demonstrated the application of 2D FWI to the synthetic wide-angle data to image the crustal structures in the frequency domain. Application of 2D FWI in the frequency domain to real datasets was demonstrated by Dessa et al. (2004) and Operto et al. (2006). The first 3D application of the FWI to sparsely recorded wide-angle data was performed by Morgan et al. (2016) using the data recorded across the Endeavour oceanic spreading centre in time domain. In this PhD work, I have used the inversion software developed at Imperial College London in the FULLWAVE consortium (Warner et al., 2013). For the rest of the document, the FWI code will be referred to as FULLWAVE.

2.2.1 The wave equation

The wave equation is an important component in seismic modelling algorithms. It has wide applications in the fields of wave modelling – soundwaves, water waves etc. Mathematically, it is a second order partial differential equation involving derivatives of space and time. The solution to this equation governs the behaviour of the wave propagating through the medium as time unfolds. Computational cost involved in the calculation of the solution of the wave equation is very high, hence, it is commonly considered with approximations. I discuss the derivation of the isotropic elastic wave equation and it's simplification to acoustic form that is implemented in this work.

2.2.1.1 Elastic wave equation

The equation governing the propagation of the seismic waves through the medium can be derived by applying Newton's laws of motion. The fundamental wave equation is a partial differential equation (PDE) that is the equation of motion (Aki & Richards, 2002):

$$\frac{\partial \sigma_{ij}}{\partial x_j} + f_i = \rho \frac{\partial^2 u_i}{\partial t^2} \qquad (2.1)$$

where $\boldsymbol{\rho}$ is the mass density, $\frac{\boldsymbol{\partial}}{\boldsymbol{\partial x_j}}$ is the spatial partial derivative along the *j*th component, with *j* = 1,2,3 respectively representing the *x, y* and *z* cartesian coordinates, $\boldsymbol{t}$ is time and $\boldsymbol{u_i}$, $\boldsymbol{f_i}$ and $\boldsymbol{\sigma_{ij}}$ are

the components of the particle displacement vector, the body force vector per unit volume and the stress tensor, respectively. The relative change in the displacement field introduced by the stress is expressed by strain. The expression for strain in terms of particle displacement is:

$$\epsilon_{ij} = \frac{1}{2}\left(\frac{\partial u_i}{\partial x_j} + \frac{\partial u_j}{\partial x_i}\right) \tag{2.2}$$

The strain tensor is symmetric by definition, $\epsilon_{ij} = \epsilon_{ji}$. Stress and strain are related by a linear relationship known as constitutive law which characterises the medium. For an elastic medium, this law is called the generalised Hooke's law, which assumes no energy loss as the material deforms (Aki & Richards, 2002)

$$\sigma_{ij} = c_{ijkl}\epsilon_{kl} \tag{2.3}$$

The elastic tensor, $\boldsymbol{c}$ is a fourth-order tensor of stiffness with 81 components. Considering the symmetries of the stress and strain tensors and thermodynamic considerations, the number of independent components of the stiffness tensor are reduced to 21 (Aki & Richards, 2002). Substituting the equation (2.3) into equation (2.1) leads to the set of equations of motion for anisotropic elastic media. Assuming that the medium's physical properties are invariant with the direction of wave propagation, the number of independent parameters to define the elastic constant are reduced to two: Lamé moduli, λ and μ:

$$c_{ijkl} = \lambda\delta_{ij}\delta_{kl} + \mu\left(\delta_{ik}\delta_{jl} + \delta_{il}\delta_{jk}\right) \tag{2.4}$$

where $\boldsymbol{\delta}$ is the Kronecker delta. Substituting the above equation into the generalised Hooke's law in equation (2.3) gives the relationship between stress and strain tensors in an isotropic, elastic media:

$$\sigma_{ij} = \lambda\delta_{ij}\epsilon_{kk} + 2\mu\epsilon_{ij} \tag{2.5}$$

where $\boldsymbol{\mu}$ is defined as the shear modulus which is a measure of the resistance of a material to shear stress. The other Lamé parameter $\boldsymbol{\lambda}$ does not have physical significance. Substituting the expression for the strain tensor from equation (2.2) in the above equation gives:

$$\sigma_{ij} = \lambda\delta_{ij}\frac{\partial u_k}{\partial x_k} + \mu\left(\frac{\partial u_i}{\partial x_j} + \frac{\partial u_j}{\partial x_i}\right) \tag{2.6}$$

The above equation when coupled with the equation (2.1) gives a set of nine equations for displacement and stress whose numerical solution can model wave propagation in isotropic elastic media equation (2.7).

$$\rho\partial_{tt}u_x = \partial_x\sigma_{xx} + \partial_y\sigma_{xy} + \partial_z\sigma_{xz}$$

$$\begin{aligned}
\rho\partial_{tt}u_y &= \partial_x\sigma_{xy} + \partial_y\sigma_{yy} + \partial_z\sigma_{yz} \\
\rho\partial_{tt}u_z &= \partial_x\sigma_{xz} + \partial_y\sigma_{yz} + \partial_z\sigma_{zz} \\
\sigma_{xx} &= (\lambda + 2\mu)\partial_x u_x + \lambda(\partial_y u_y + \partial_z u_z) \\
\sigma_{yy} &= (\lambda + 2\mu)\partial_y u_y + \lambda(\partial_x u_x + \partial_z u_z) \\
\sigma_{zz} &= (\lambda + 2\mu)\partial_z u_z + \lambda(\partial_x u_x + \partial_y u_y) \\
\sigma_{xy} &= \mu(\partial_y u_x + \partial_x u_y) \\
\sigma_{xz} &= \mu(\partial_z u_x + \partial_x u_z) \\
\sigma_{yz} &= \mu(\partial_z u_y + \partial_y u_z)
\end{aligned} \tag{2.7}$$

The common method used to model wave propagation using the above set of equations is the finite difference method. This method is relatively simple to implement and is efficient to handle the complexities of the Earth. The disadvantage in this method is that it is computationally intensive and does not provide any physical insight about different wave types. Waves propagate as disturbances in a medium. In elastic media, the materials comes back to the original shape after the force is removed. This type of medium can withstand both compressional and shear deformation allowing the propagation of both compressional and shear waves through it. The velocities of these waves can be estimated by substituting the expression for stresses (2.6) into the equation of motion (2.1) and considering the force term to be equal to zero:

$$\lambda \frac{\partial u_k}{\partial x_i \partial x_k} + \mu\left(\frac{\partial^2 u_i}{\partial x_j^2} + \frac{\partial u_j}{\partial x_i \partial x_j}\right) = \rho \frac{\partial^2 u_i}{\partial t^2} \tag{2.8}$$

The above expression can be expressed in vector notation considering $\nabla . u = \frac{\partial u_i}{\partial x_i}$ and $\nabla^2 u = \nabla\nabla . u - \nabla \times \nabla \times u$

$$(\lambda + 2\mu)\,\nabla\,(\nabla . u\,) - \mu\nabla \times (\nabla \times u) = \rho \frac{\partial^2 u}{\partial t^2} \tag{2.9}$$

This is one of the forms of the seismic wave equation that ignores the gradients of the Lamé parameter terms. In the above equation, ***u*** represents the displacement vector. The expression for compressional and shear velocities can obtained by taking the divergence and curl of the above equation:

$$v_p = \sqrt{\frac{\lambda + 2\mu}{\rho}}, \qquad v_s = \sqrt{\frac{\mu}{\rho}} \tag{2.10}$$

The particle velocity associated with divergence is compressional wave velocity (Vp) and the one associated with curl is shear wave velocity (Vs). The direction of particle motion for compressional waves is the same as the direction of the wave propagation whereas for secondary wave it is

perpendicular to the direction of propagation. The compressional and shear waves are also known as Primary (P-) -wave and Secondary (S-) -wave, respectively.

2.2.1.2 Isotropic acoustic media

The wave equation can be further simplified by considering the media as an acoustic media in which waves can only propagate as compressions and rarefactions. In the isotropic acoustic case, the stress tensor is a diagonal matrix with the off-diagonal elements (shear components) equal to zero. The diagonal elements, $\sigma_{ii} = -p$, are equal to hydrostatic pressure. Since shear propagation is not possible in the acoustic case, the shear moduli $\mu = 0$. The expression for P-wave velocity becomes $v_p = \sqrt{\lambda/\rho}$. The stress tensor for acoustic media can be obtained by substituting $\mu = 0$ in equation (2.6) which yields $\sigma_{ii} = \frac{\lambda \delta_{ii} \partial u_k}{\partial x_k} = -p$. Applying the mathematical operation of divergence to the equation of motion (2.1) with force term (f) equal to zero and substituting the constitutive relation gives the wave equation for an acoustic, isotropic, non-attenuating medium:

$$\frac{1}{v_p^2}\frac{\partial^2 p}{\partial t^2} - \rho \nabla . \left(\frac{1}{\rho}\nabla p\right) = s \tag{2.11}$$

where $\boldsymbol{v_p}$ is acoustic velocity, $\boldsymbol{\rho}$ is density, **p** is pressure wavefield, **s** is source term and ***t*** is time. ∇ is the 3D del operator:

$$\nabla = \frac{\partial}{\partial x} + \frac{\partial}{\partial y} + \frac{\partial}{\partial z} \tag{2.12}$$

The wave equation describes two-way wave propagation in the medium – shot to reflector and reflector to receiver. The analytical solutions to the equation can only be obtained for simple homogenous models which is not the case in reality. Often the equation is employed with approximations to suit the case, and in discretized form using numerical methods. The forward modelling problem can be represented as below:

$$G(m) = d \tag{2.13}$$

where ***G*** is the forward modelling operator; ***m*** represents model parameters and ***d*** represents data. The above equation cannot be considered for matrix operations as it is a non-linear relationship and it is not possible to express ***G*** as a matrix. It is more convenient to pose the wave equation as a linear equation between the source and the wavefield:

$$A\varphi = s \tag{2.14}$$

where ***A*** is a wave equation operator with differential operators and model parameters, $\boldsymbol{\varphi}$ is the wavefield and ***s*** is the source. This is the discretized form of the wave equation and preferably solved by an explicit time-marching algorithm to avoid solving of linear equations (Virieux & Operto,

2009). The most common forward modelling technique used is the finite-difference (FD) method. The other methods are finite element and pseudospectral methods (Komatitsch et al., 2005).

2.2.2 Finite difference method

The finite difference scheme (FD) is one of the most common ways to solve the wave equation. In the finite difference method, the wave equation is solved by substituting approximate Taylor series expansions of the functions defined in a discretised model for partial derivatives. An approximate solution to the wave equation is obtained by discretising the model in both space and time domains. There are three types of FD implementation: forward, central and backward FD. Central FD is the most common implementation for acoustic and elastic wave equations due to its high accuracy with errors of $O(\Delta x)^2$, where Δx is the discretisation interval (Graves, 1996; Levander, 1988). The space domain expressions for first and second order partial derivatives for a one-dimensional function $\boldsymbol{v(x)}$ discretised in a grid with spacing $\boldsymbol{h}$ are (Courant et al., 1967):

$$\frac{\partial v(x)}{\partial x} \approx \frac{v(x+h) - v(x-h)}{2h} \tag{2.15}$$

$$\frac{\partial^2 v(x)}{\partial x^2} \approx \frac{v(x+h) - 2v(x) + v(x-h)}{h^2} \tag{2.16}$$

The order of the error in the above expressions is $\boldsymbol{h^2}$. Similar approximate expressions can be obtained for partial derivatives with respect to time. In seismic modelling the common practice is to employ the wave equation with fourth order approximation in space and second order approximation in time (Graves, 1996; Levander, 1988; Mufti, 1990).The fourth order approximation for the second order space partial derivative of the function $\boldsymbol{v(x)}$ is (Mufti, 1990):

$$\frac{\partial^2 v(x)}{\partial x^2} \approx \frac{-v(x-2h) + 16v(x-h) - 30v(x) + 16v(x+h) - u(x+2h)}{12h^2} \tag{2.17}$$

The above expression, along with the second-order approximation of the second-order partial derivative with respect to time, can used to solve the acoustic wave equation (equation 2.11). The source term s can be introduced into the equation as:

$$s = s(t)\delta(x - x_s)\delta(y - y_s)\delta(z - z_s) \tag{2.18}$$

where $\boldsymbol{\delta}$ is a delta function which makes the source term zero in the complete grid except at the location of the source (x_s, y_s, z_s). For an isotropic acoustic medium, the gradient of the pressure can be replaced by the particle displacement, $\nabla p = -\lambda \nabla^2 u$ where $\boldsymbol{u}$ being particle displacement. The acoustic wave equation is:

$$\nabla^2 u = \frac{1}{v_p^2}\frac{\partial^2 u}{\partial t^2} + s(t)\delta(x - x_s)\delta(y - ys)\delta(z - zs) \quad (2.19)$$

The solution to the above equation using finite difference scheme has been implemented in the FULLWAVE program to calculate the synthetic wavefield. Due to the approximate nature of the solution, the time and space sampling need to fulfil certain stability criteria to avoid numerical instability and energy dispersion. Depending on the accuracy of the FD operators and the dimensionality of the problem, the stability conditions may change. In order to reduce the dispersion of energy, a condition is placed on the length of the grid spacing in all the direction. If ***h*** represents spacing, it must obey:

$$h = \frac{v_{min}}{wf_{max}} \quad (2.20)$$

where $\boldsymbol{v_{min}}$ is the minimum velocity present in the model, $\boldsymbol{f_{max}}$ is the maximum frequency to be modelled and ***w*** is a factor that depends on the accuracy of the FD operators. For an implementation of fourth order in space and second order in time, w = 4 or 5 would be optimum, implying each wavelength must be crossed by 4-5 grid points (Alford et al., 1974; Graves, 1996; Levander, 1988). The second condition is imposed on the time sampling $\boldsymbol{dt_{max}}$ for ensuring numerical stability (Courant et al., 1967):

$$dt_{max} = \frac{\mu h}{v_{max}} \quad (2.21)$$

where $\boldsymbol{v_{max}}$ is the maximum velocity present in the model and $\boldsymbol{\mu}$ is a factor that depends on the accuracy of the FD operators and dimensionality of the problem (Lines et al., 1999). For 2D and 3D wave equation, the value of $\boldsymbol{\mu}$ is given as $\sqrt{3/8}$ and $1/2$, respectively, for a fourth-order FD operator in space (Graves, 1996; Lines et al., 1999; Mufti, 1990).

Reflections from the boundaries of the model can be avoided by applying boundary conditions. A simple way to tackle the boundary reflections problem is by extending the model at the boundaries so that the reflections are generated away (Cerjan et al., 1985). However, this solution would increase the computational burden significantly. Artificial reflections can also be reduced by attenuating the amplitudes of the wavefield within a few nodes of the boundary by multiplying the wavefield by a negative exponential function (Cerjan et al., 1985). Nevertheless, this method would require padding extra cells at the edges of the model thereby increasing the computational cost. There are several methods to address the problem of the spurious reflections at the boundaries: the paraxial approximation of the wave equation (Clayton & Engquist, 1977); projection operators and potentials (Lindman, 1975), and the perfectly matched layer (PML) method (Berenger, 1994). In FULLWAVE code, the boundary conditions are implemented mostly by using quadratic

approximations of the wave propagation to the boundary, just outside the model domain, and the reflections at the boundaries are suppressed by using the PML method (Agudo, 2018)

One of the important boundary conditions to be included into the forwarding modelling FD scheme is free-surface boundary condition between the water/land and air. In principle, it is implemented by setting the traction component to zero at the interface, ensuring numerical stability and good accuracy in the FD implementation (Chapman, 2004). However, the free-surface condition can also be implemented by setting the component of the stress σ_{zz}, = σ_{xz} = σ_{yz} = 0 at the surface and assuming symmetry for the stress components around the free-surface (Graves, 1996; Levander, 1988).

Injection of a source in to the modelling is an important step for wave propagation modelling. This can be achieved by using the stress (pressure in the acoustic media) or the velocity components. The source is injected as a time series sampled at the same interval as used in the modelling to ensure the numerical stability. The maximum frequency in the frequency content of the source must be lower than the frequency at which energy dispersion can occur according to the condition given by the equation (2.20).

2.2.3 Inverse problem

The main aim of solving inverse problems is to extract complete information about the physical properties from geophysical data. This process is opposite of the forward modelling discussed above, in which, we generate synthetic data for an assumed model.

Inverse problems can be broadly classified as probabilistic and deterministic. Our approach of inverting full waveform falls into the deterministic approach as we tackle non-linear problem iteratively in linear steps so-called length method.

The inverse problem corresponding to the forward problem is represented as below:

$$\bar{m} = G^{-1}d \qquad (2.22)$$

In the above equation, the model parameters $\bar{\boldsymbol{m}}$ are different from those involved in forward modelling because it is impossible to extract exact solution from field data sets. In most of the cases, $\boldsymbol{G}$ is not invertible and waveform inversion is not an exception. Hence, to tackle inverse problems optimisation methods are employed by defining an objective function and minimising it. Objective functions are also referred to as cost functions or functionals or misfits. The inverse problems are based on the assumption that once a global minimum is reached, the model obtained best describes the observed data.

The search for global minima can be carried out in two ways: local search and global search. Local search methods require a defined starting model that is in the vicinity of the true model. Common optimisation algorithms are steepest-descent, conjugate gradients, Newton and quasi-Newton methods. On the other hand, the global search method does not require a starting model. The model space (m) is searched for a best fitting solution. Local minima may be better avoided by using global searching schemes that search the whole solution space for the minimum, but they are too expensive computationally.

2.2.4 Local optimization

FWI minimizes the misfit function to converge the starting model to the final model. The most commonly used minimization method in large inverse problems is the least squares method. In this method, the synthetic dataset is made to match the observed data iteratively. The objective function for least squares optimization is:

$$F = \frac{1}{2}(d - d_{obs})^{\dagger}(d - d_{obs}) = \frac{1}{2}\Delta d^{\dagger}\Delta d \tag{2.23}$$

where $d = d_{mod}$, $||d - d_{obs}|| = \Delta d$ and † represents the transpose conjugate. The best solution in the model space will have the minimum value for ***F***. For linear problems, the shape of ***F***, known as a hypersurface, tends to be convex making convergence straightforward, whereas for non-linear problems it comes with local minima, increasing the chance of getting trapped in a local minima. Hence, it is essential that the starting model is relatively close to the global minimum. Several other misfit functions may be used in FWI, such as the L1 norm, the phase residual, the cross-correlation misfit, logarithmic misfit,and hybrid combinations of L1 and L2 norms (Brossier et al., 2010; Virieux & Operto, 2009; Warner et al., 2012). In the framework of elastic FWI in frequency domain, Brossier et al. (2009) demonstrated that L1 norm is less sensitive to non-Gaussian noise and maybe a good alternative to the L2 norm.

The search for an updated model in FWI relies on the Born approximation which allows to us to assume that the updated model is the sum of the starting model and a small perturbation, $m = m_0 + \Delta m$. The objective function in the vicinity of the starting model can be expanded using Taylor series assuming the updated model m has M dimensions.

$$\begin{aligned} F(m_0 + \Delta m) = F(m_0) &+ \sum_{j=1}^{M} \frac{\partial F(m_0)}{\partial m_j}\Delta m_j \\ &+ \frac{1}{2}\sum_{j=1}^{M}\sum_{k=1}^{M} \frac{\partial^2 F(m_0)}{\partial m_j \partial m_k}\Delta m_j \Delta m_k + \mathcal{O}(m^3) \end{aligned} \tag{2.24}$$

Taking the derivative of the functional with respect to the model parameter m_l gives:

$$\frac{\partial F(m)}{\partial m_l} = \frac{\partial F(m_0)}{\partial m_l} + \sum_{j=1}^{M} \frac{\partial^2 F(m_0)}{\partial m_j \partial m_l} \Delta m_j \tag{2.25}$$

Equating the gradient of the functional to zero gives an expression for model update as follows:

$$\Delta m = -\left(\frac{\partial^2 F(m_0)}{\partial m^2}\right)^{-1} \frac{\partial F(m_0)}{\partial m} \tag{2.26}$$

where $\Delta \boldsymbol{m}$ is the model update and m_0 is the starting model for the iteration. Clearly, model updates require calculating two terms: the first and second-order partial derivatives of misfit function at point m_0. The first-order derivative directs the search for model updates in the opposite direction of the steepest-ascent of the misfit function at the point m_0, it is called the "gradient". The second derivative is called the Hessian; it is a square symmetric matrix containing second-order differentials and defines the curvature of the misfit function at the point m_0. For the solution to converge towards a minimum, the second derivative should be a positive definite. The computation of the Hessian can be demanding both in terms of time and memory requirements. Hence, practical approximations are considered to the Hessian using methods like Gauss-Newton or quasi-Newton (Pratt et al., 1998). The computation burden can be further reduced by using simpler approximations – replacing the Hessian with a scalar value using the steepest-descent method.

2.2.4.1 Iterative method – Steepest-descent method

For an iterative method to converge the model m_0 to the correct solution, two conditions are required: the model m_0 should be close to the global solution and F should be monotonic in nature around the point m_0. A stopping criterion on the iteration process is required to ensure that the convergence is achieved within a finite amount of time: fixing a lower threshold value of the F and aborting the program when F's value is smaller than the threshold value or fixing a maximum number of iterations to be performed.

The basic formulations for expression of the gradient and Hessian matrices are:

$$\begin{aligned} \nabla F &= \frac{1}{2}\Re\left\{\frac{\partial}{\partial m}\left[(d - d_{obs})^{\dagger}(d - d_{obs})\right]\right\} \\ &= \frac{1}{2}\Re\left[\left(\frac{\partial d}{\partial m}\right)^{\dagger}(d - d_{obs}) + (d - d_{obs})^{\dagger}\left(\frac{\partial d}{\partial m}\right)\right] \\ &= \frac{1}{2}\Re\left[\left(\frac{\partial d}{\partial m}\right)^{\dagger}(d - d_{obs})\right] \end{aligned} \tag{2.27}$$

where d stands for the modelled data and d_{obs} is the observed data. $\Re$ is the real part of the misfit function.

$$H = \frac{\partial}{\partial m}\left\{\Re\left[\left(\frac{\partial d}{\partial m}\right)^{\dagger}(d - d_{obs})\right]\right\} \tag{2.28}$$

For computation of the gradient and the Hessian, the only unknown is the derivative of the data with respect to the model parameters. Existence of an analytical solution to the problem would have made the computation of the gradient and the Hessian simple. However, this is not the case in real-world problems, hence we depend on numerical techniques to solve it. Optimization in the FULLWAVE program uses the steepest-descent algorithm. In the steepest-descent method, the solution is searched along the steepest-ascent direction of the misfit function and the Hessian is approximated by a scalar. The perturbation update in the model using the steepest-descent method is:

$$\Delta m = \alpha \nabla F = -\alpha \Re\left[\left(\frac{\partial d}{\partial m}\right)^{\dagger}(d - d_{obs})\right] \tag{2.29}$$

The steepest-descent method efficiency depends on its ability to simplify convergence without having to calculate Hessian. A scaling parameter α in the direction of search of updated model, called step-length, is introduced replacing the Hessian. The value of α is very important as it controls the distance for searching along the line of search. Using a large value for α may increase the misfit value by missing the correct solution and using a small value for α may require too many iterations to converge to the solution. To estimate the value of α approximately, a linear relation is assumed between the data residuals and the model updates using the Born approximation. A small perturbation is added to the model in the direction opposite to the gradient and the corresponding data residual is computed Δd^0. The expression for any new data residuals assuming the linear relationship:

$$\Delta d_{\alpha} = \Delta d^0 - \alpha(\Delta d^0 - \Delta d^1) \tag{2.30}$$

where Δd^0,Δd^1 are the computed residuals for the previous iteration model and the perturbed model, respectively. We minimize L2-norm of the data residual by taking the derivative of the misfit to obtain the optimum value for α:

$$\frac{\partial F}{\partial \alpha} = \frac{\partial}{\partial \alpha}\left(\frac{1}{2}\Delta d_{\alpha}^{\dagger}\Delta d_{\alpha}\right) = 0 \tag{2.31}$$

From the above equation the value of α as follow:

$$\alpha = \frac{(\Delta d^0)^{\dagger}(\Delta d^0 - \Delta d^1)}{(\Delta d^0 - \Delta d^1)^{\dagger}(\Delta d^0 - \Delta d^1)} \tag{2.32}$$

From the above expression, it is clear that α depends on the data residuals calculated at two different points. An advantage with steepest-descent method is it does not require the calculation

of the Hessian and its inverse, thereby reduces the computational burden drastically. However, a compromise between the Newton-based methods and the steepest-descent method is achieved by incorporating a gross approximation for the Hessian by calculating only the diagonal elements (Shin et al., 2001). This inclusion of approximate Hessian for model updating is called spatial preconditioning of the gradient and is less demanding computationally. Hence, the expression for model update is:

$$\Delta m = -\alpha [H_D]^{-1} \nabla F = -\alpha \left\{ \Re \, diag \left[\left(\frac{\partial d}{\partial m} \right)^{\dagger} \left(\frac{\partial d}{\partial m} \right) \right] \right\}^{-1} \Re \left[\left(\frac{\partial d}{\partial m} \right)^{\dagger} (d - d_{obs}) \right] \qquad (2.33)$$

where H_D is the diagonal of the Hessian (spatial preconditioner); $\frac{\partial d}{\partial m}$ is also called Frechet matrix or sensitivity matrix.

2.2.5 Adjoint-state method

From the previous section, it is understood that the model update depends on the estimation of the gradient. Computation of the gradient can be highly demanding in terms of memory requirement and computational time. To mitigate the computational burden, adjoint-state approach is used in the geophysical community. This approach is based on the linear relationship between the wavefield and the source (equation 2.14). Differentiating equation (2.14) with respect to model parameters *m* gives:

$$\frac{\partial}{\partial m}(A\phi) = \frac{\partial A}{\partial m}\phi + A\frac{\partial \phi}{\partial m} = \frac{\partial s}{\partial m} = 0 \qquad (2.34)$$

Since source is independent of the model parameters the right hand side term can be equated to zero. Rearranging the terms:

$$\frac{\partial \phi}{\partial m} = -A^{-1}\frac{\partial A}{\partial m}\phi \qquad (2.35)$$

The above equation is an alternative form for the sensitivity matrix with unknowns A^{-1} and $\frac{\partial A}{\partial m}$. Calculating inverse of the forward modelling operator matrix A can be difficult whereas the second term can be easily obtained after discretising the wave equation using FD. Substituting equation (2.33) into the gradient expression given by equation (2.25):

$$\Delta d = d - d_{obs} = D(\phi - \phi_{obs}) \qquad (2.36)$$

$$\nabla F = -\Re \left\{ \left[A^{-1}\frac{\partial A}{\partial m} \right]^{\dagger} D(\phi - \phi_{obs}) \right\} \qquad (2.37)$$

The wavefield vectors are replaced by the data vectors using a diagonal matrix ***D***. ***D*** can be used to assign weights to different data points. In the above equation, it is still difficult to calculate the

inverse $\boldsymbol{A^{-1}}$ which can be avoided by using the adjoint state method. We define a new forward modelling problem propagating in the reverse direction:

$$A^{\dagger}\phi_b = s_b \tag{2.38}$$

Where $\boldsymbol{A^{\dagger}}$ is the adjoint matrix and $\boldsymbol{\phi_b}$ is the wavefield propagating in the backward direction generated by the source $\boldsymbol{s_b}$. The new source $\boldsymbol{s_b}$ is defined by the residuals obtained by subtracting the forward wavefield from the observed data:

$$s_b = D^T(\phi - \phi_{obs}), \tag{2.39}$$

where $\boldsymbol{D^T}$ is the adjoint of the $\boldsymbol{D}$ matrix. Then the new wavefield is defined as:

$$\phi_b = \left(A^{\dagger}\right)^{-1} D^T(\phi - \phi_{obs}) \tag{2.40}$$

Rearranging and replacing terms in the gradient expression following the conjugate transpose matrix rules, the expression for the gradient with adjoint-state approach is:

$$\nabla F = \Re\left\{\phi^{\dagger}\left(\frac{\partial A}{\partial m}\right)^{\dagger}\phi_b\right\} = \Re\left\{\phi_b^{\dagger}\left(\frac{\partial A}{\partial m}\right)\phi\right\} \tag{2.41}$$

where $\boldsymbol{\phi_b}$ is the back-propagated wavefield residuals. The complete residuals for each source are assembled to form residual source. The principle is similar to reverse time migration in which reflectivity image is generated by cross-correlating the incident wavefield with the back-propagated wavefield (Claerbout, 1971). The calculation of $\frac{\boldsymbol{\partial A}}{\boldsymbol{\partial m}}$ is straightforward. The Hessian is computed from the gradient as $H = \nabla^2 F$ and $H_D = diag(\nabla^2 F)$. Note that operator to compute back-propagated wavefield ($\mathrm{A}^{\dagger}$), adjoint matrix, is not same as the one used for forward modelling (A). The flow chart for the complete FWI is shown in figure 2.4.

2.2.6 Practicalities of full waveform inversion

2.2.6.1 Starting model for FWI

Building a starting model is crucial to ensure the convergence to the correct solution using FWI. There are number of methods which can be used to generate the starting model for FWI, including reflection tomography, migration-based velocity analysis, first-arrival traveltime tomography (FATT), etc. FATT is commonly used method to develop a starting model. FATT is a nonlinear inversion technique which uses first-arrival traveltimes to generate smooth models of the subsurface (e.g. Hole, 1992; Zelt & Barton, 1998). In this method, the sensitivity matrix is computed by backprojecting the traveltime residuals along the raypaths. However, the computation of the

sensitivity matrix, which is computationally demanding, can be avoided by using adjoint-state method (Taillandier et al., 2009).

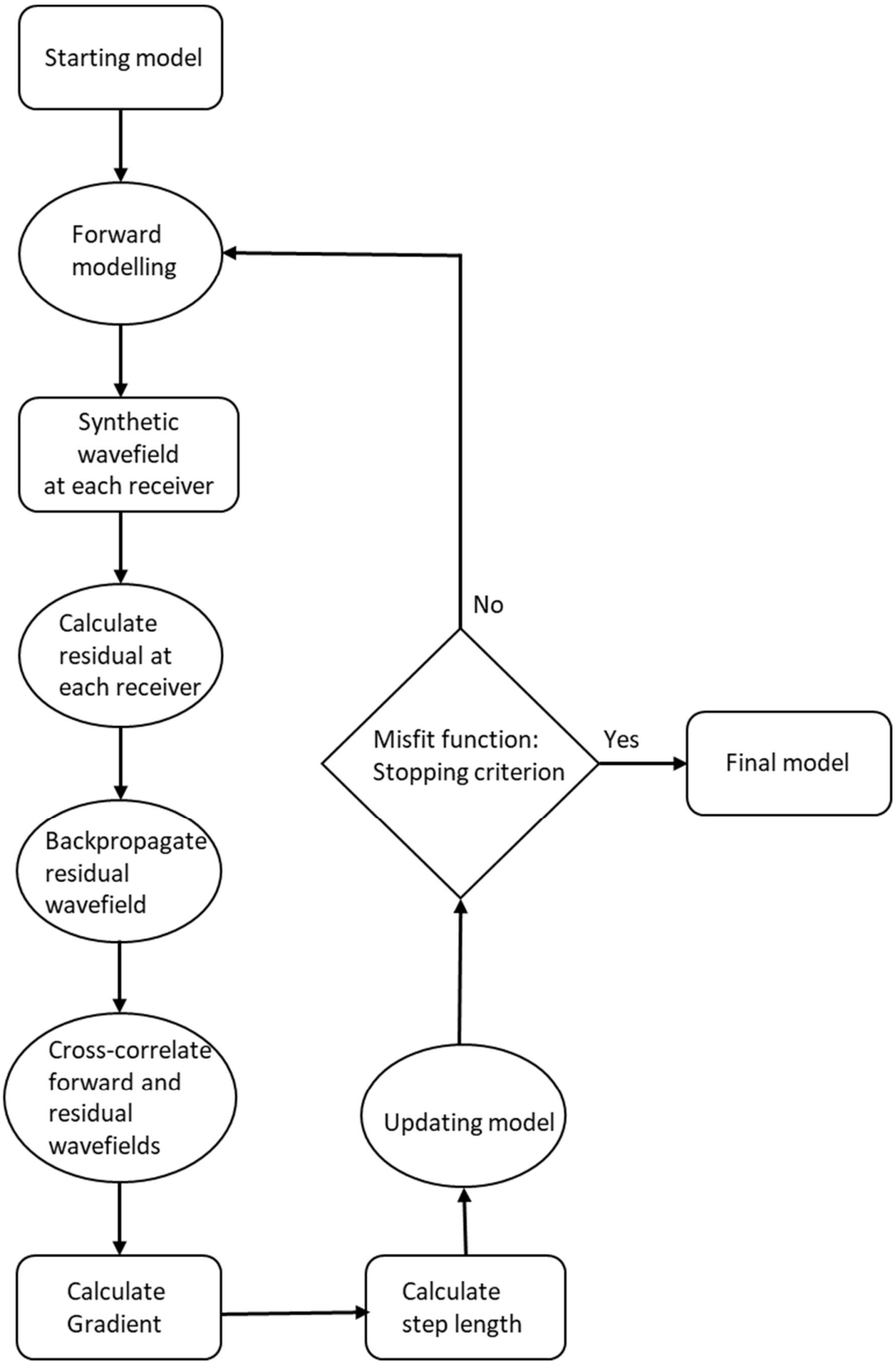

Figure 2-4 Flow chart for FWI.

FATT can also be performed as a regularised inversion solving the eikonal equation using finite difference schemes (Zelt & Barton, 1998). FATT images features within the first Fresnel zone. However, presence of low velocity zones can introduce complications in the FATT (Williamson, 1991). Good fit for the first arrivals can be achieved using FATT, however fitting the later arrivals can be challenging in some cases especially if the medium is anisotropic. An important criterion for a model to qualify as a starting model for FWI is that it should be able to predict the observed data within a half seismic wavelength. If this condition is not satisfied FWI will update the nth cycle on the synthetic data trace with n$\pm$1 cycle of the observed data trace. This mismatch is termed as cycle-skipping and will lead to convergence to a wrong final model. The problem of cycle-skipping can be avoided by inverting the data starting from low frequencies using the multi-scale approach (Bunks et al., 1995).

2.2.6.2 Source signature

The accuracy of the source is important for successful convergence of FWI. There are various methods to develop source signature for FWI. In common practice the source is an unknown parameter in FWI problems and can inverted for using the linear relationship between the wavefield and the source (Equation 2.14; Pratt, 1999). However, inverting for the source wavelet may not be straightforward as it will require to manage a trade-off between the model parameters and source parameters. Morgan et al. (2016) extracted the source from near offset direct arrivals using Wiener filter modelling. Such a modelled source requires quality control to ensure that predicted data matches the observed data. After obtaining a source wavelet, it is necessary to apply the same filters on the wavelet which were applied to the field data.

2.2.6.3 Data requirements

Commonly preferred data for performing FWI is forward-scattered data which travel horizontally in the subsurface constraining very well the low wavenumbers in the model (Sirgue, 2006). Introducing long offset data into FWI fills the gap in the wavenumber spectrum of the data by making it more sensitive to the intermediate wavenumbers of the model, which otherwise are not well constrained (Claerbout, 1971; Jannane et al., 1989). This advantage makes ocean bottom seismic datasets ideal for performing FWI compared to the streamer datasets that limit the recording of the long offset diving waves due to streamer length. However, the problem with diving waves is their shallow depth of investigation compared to the reflections. Also including long offsets in the inversion will increase the non-linearity of the inverse problem, making it difficult to model the arrivals. This problem can be tackled to certain extent by using methods like layer-stripping or multi-scale FWI depending on the data quality at the lower frequencies (Bunks et al., 1995) . Adding short offset reflections can considerably increase the depth of investigation and also add finer

structural details to the images. Modelling the back-scattered wavefield can be more challenging than the forward-scattered wavefield. The back-scattered wavefield depends on the velocity and density properties of the rocks, unlike forward-scattered field which depends mainly on the velocity (Mora, 1988). OBS data recording allows to acquire long-offset and multi-azimuth seismic data making it suitable for FWI modelling. However, the question of optimal OBS spacing to perform FWI is still outstanding

Chapter 3 Comparison of two- and three-dimensional full waveform inversion imaging using wide-angle seismic data from the Deep Galicia Margin

B. Boddupalli[1], T. A. Minshull[1], J. V. Morgan[2], G. Bayrakci[3] and D. Klaeschen[4]

[1]School of Ocean and Earth Science, University of Southampton, UK.

[2]Department of Earth Sciences and Engineering, Imperial College London, UK.

[3]National Oceanography Centre Southampton, UK.

[4]GEOMAR, Helmholtz Centre for Ocean Research Kiel, Germany.

Author contributions: This chapter will be submitted to the journal, Geophysical Journal International. This work has been carried out by BB under the guidance of rest of the authors. All authors contributed feedback on the text.

Abstract

Full waveform inversion (FWI) is a data-fitting technique capable of generating high-resolution velocity models with a resolution down to half the seismic wavelength. Application of FWI is mostly restricted to densely sampled seismic data, because such data can constrain the inverse problem well and converge to the correct solution. In this study, we applied FWI to three-dimensional (3D) wide-angle seismic data acquired using sparsely spaced ocean bottom seismometers (OBS) from the Deep Galicia Margin west of Iberia. Our dataset samples the S-reflector, a low-angle detachment present in this area. Our study aims to highlight differences between two-dimensional- (2D) and 3D-FWI performances using a real sparsely spaced dataset. We performed 3D FWI in the time domain and compared the results with 2D FWI results from one of the profiles through the 3D model. When overlaid on multichannel seismic images, the 3D FWI results constrain better the complex faulting within the pre- and syn-rift sediments and crystalline crust compared to the 2D result. We identified a new fault block and a peridotite ridge towards the end of the continental crystalline crust. We estimate variable serpentinisation of 0-45% of the upper mantle below the S-reflector along the profile. Our results highlight how 3D FWI improves imaging in the deeper parts of the model. To validate our results, we computed the model changes introduced by the FWI for both 2D and 3D cases. Based on our comparison, we conclude that the use of 3D data can partially mitigate the problem of receiver sparsity in FWI.

3.1 Introduction

Seismic imaging is one of the most widely used tools for understanding crustal processes. Advances in seismic imaging are mainly driven by the hydrocarbon exploration industry. In academia, first arrival traveltime tomography (FATT) using long offset refraction data is a widely used method to develop smooth velocity models of the crust (e.g. Hammer et al., 1994; Zelt & Barton, 1998). However, to image the main discontinuities within the crust, joint inversion of refractions and wide-angle reflections is required (e.g., Hobro et al., 2003; Korenaga et al., 2000; Zelt & Smith, 1992). A drawback of the FATT method is its resolution, which is limited at best to the width of the first Fresnel zone. In addition, the presence of low-velocity zones can pose difficulties for identifying the first arrivals in the data. To deal with such problems, seismic imaging studies are moving forward towards higher-resolution techniques like waveform inversion, which utilise complete information in the waveform record to derive finer resolution models. Advances in computational facilities and seismic data acquisition techniques have greatly supported developments in seismic imaging. The full waveform inversion (FWI) technique was proposed by Lailly (1983) and Tarantola (1984) as a linearized inverse problem using adjoint operators. Velocity models derived using FATT can be used as a starting model for performing FWI. FWI is capable of resolving structures to half the lowest seismic wavelength present in the data. Moreover, it automatically accounts for the complete waveform, avoiding the need for phase identifications. However, higher resolution comes at a cost of large computational requirement and increased non-linearity of the inverse problem. Obtaining the correct solution using FWI largely depends on how well-posed is the inverse problem.

Wide-angle seismic data are well suited for performing FWI because of their low-frequency content and sensitivity to subsurface velocity. OBS enable recording of long-offset marine seismic data, which otherwise is not possible using a limited-offset streamer. Although wide-angle acquisition using OBSs has been widely implemented for last few decades, FWI techniques have rarely been applied to these data until the last decade. In academia, the main concern in using a wide-angle dataset for FWI is the data sparsity. A sparse dataset may cause the inversion to fail to converge to the right solution due to a poorly constrained inverse problem. The first application of FWI to synthetic wide-angle data was demonstrated by Pratt et al. (1996) in 2D in the frequency domain, while real data applications were demonstrated by Dessa et al. (2004) and Operto et al. (2006). In the last few years, different variants of FWI have been applied to OBS data from different tectonic settings, restricted mostly to 2D (e.g., Davy et al., 2018; Górszczyk et al., 2017, 2019; Kamei et al., 2013). Morgan et al. (2016) demonstrated the application of 3D acoustic, anisotropic FWI to a sparse dataset from the Juan de Fuca ridge, revealing low-velocity zones interpreted as magmatic-hydrothermal reaction zones. Using a similar approach, Davy et al. (2018) presented isotropic high-

resolution models using sparsely spaced and noisy 2D OBS data from the Deep Galicia margin west of Iberia.

The Galicia margin has been a testing ground for different concepts involved in rifting including crustal thinning, reduced mantle velocities, and mantle exhumation (e.g. Boillot et al., 1987; Reston, 2009b). This margin is sediment starved and magma-poor, so allows for optimal resolution of features in and below the crust using geophysical imaging experiments. Seismic studies in this region have revealed many interesting observations over last few decades (e.g. Boillot et al., 1980; Whitmarsh et al., 2001). 3D seismic reflection imaging has enabled unique insights into the rifting tectonics in the margin, including 3D interpretation of the fault structures, identification of the coherent corrugations on the S-surface and identification of the S-interval (Lymer et al., 2019; C Nur Schuba et al., 2018). 2D and 3D tomographic models derived using wide-angle seismic data were used to identify thin oceanic crust west of the Peridotite ridge and estimate serpentinisation below the S-reflector (Bayrakci et al., 2016; Davy et al., 2016, 2018)

In this paper, we image the Deep Galicia margin (DGM) using the wide-angle data from 36 OBSs in 3D, and compare the results with 2D FWI performed using a subset of the same dataset. Our wide-angle data set from the DGM presents an ideal opportunity to compare 3D and 2D imaging. It is well known that 3D wide-angle data has the potential to improve the resolution of subsurface velocity structure, however, 2D wide-angle studies are more common than 3D studies. Hence, we aim to highlight the difference in the imaging between the 2D and 3D by comparing our 3D FWI image with the 2D FWI image. This study is the first comparison of 3D FWI images with 2D FWI images using a real sparse dataset, and illustrates the limitations in resolution of 2D FWI imaging in a rifted margin setting. The full 3D FWI results and their interpretation will be presented elsewhere.

3.2 Geological setting

The West Iberia margin is a magma-poor rifted margin where rifting is thought to have occurred in different phases (e.g. Murillas et al., 1990; Péron-Pinvidic et al., 2007; Tucholke et al., 2007). In the early stages of rifting during the late Triassic to early Jurassic, the fault bounded Lusitanian and Galicia Interior Basins were formed (Figure 3.1) (Murillas et al., 1990; Tucholke et al., 2007). During Late-Jurassic to Early Cretaceous, the Galicia Interior Basin developed further westward on the Galicia margin, thinning the continental crust to 15 km (Pérez-Gussinyé et al., 2003). In the final stages, the extension was primarily focused in the DGM, thinning the crust to less than 5 km (Murillas et al., 1990) and exhuming the subcontinental mantle lithosphere (Boillot & Winterer, 1988; Tucholke et al., 2007). The DGM is a hyperextended zone characterised by west dipping normal faults that sole into a detachment fault (Reston et al., 1996, 2007). Here, the continental

crust comprises of tilted fault blocks of crystalline basement rocks overlain by pre-, syn- and post-rift sediments. Various mechanisms are proposed to explain the faulting pattern, crustal thinning, asymmetry on the conjugate margins and role of the detachment fault in continental break-up. The detachment fault underlying the fault blocks is called the S-reflector, which is imaged as a bright reflector on seismic sections in this region (De Charpal et al., 1978; Lymer et al., 2019; Reston et al., 1996, 2007; Schuba et al., 2018). It is a boundary separating the continental crust above from the serpentinised mantle below (Leythaeuser et al., 2005; Reston et al., 1996). Westward of the continental crust lies a narrow, north-south oriented ridge with 2-4 km of relief. This ridge is interpreted as exhumed mantle and is known as the Peridotite Ridge (e.g. Beslier et al., 1993; Boillot et al., 1980). Similar ridges are identified along the strike on the West Iberia margin (Beslier et al., 1993b). At the DGM, exhumed mantle is postulated to extend seaward by at least 85 km from the Peridotite Ridge (Davy et al., 2016; Dean et al., 2015). Under the influence of continuous stretching during rifting, the entire crust was thinned to less than 10 km, making it cooler and brittle and coupling the lower- and upper-crust (Pérez-Gussinyé et al., 2003; Pérez-Gussinyé & Reston, 2001; Srivastava et al., 2000). The normal faults cut through the entire brittle crust, acting as fluid conduits, transporting seawater to the upper mantle and serpentinising the upper mantle peridotites (Bayrakci et al., 2016; Pérez-Gussinyé & Reston, 2001; Reston, 2007). Using P-wave velocities derived from wide-angle seismic data, Bayrakci et al. (2016) and Davy et al. (2018) presented the evidence for preferential hydration of the upper mantle close to the normal faults, with maximum serpentinisation of 45%.

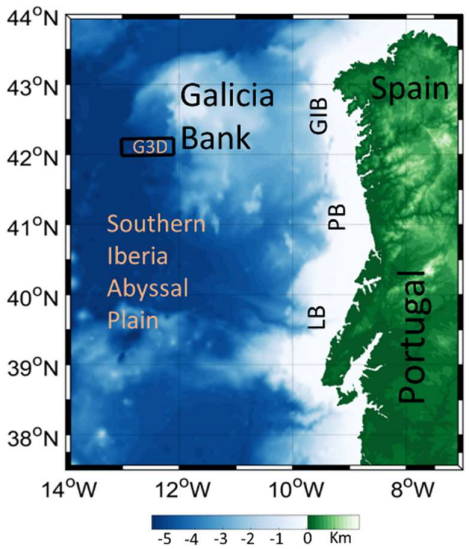

Figure 3-1 Map showing the location of the Galicia 3D (G3D) experiment in the DGM (black box). East of the DGM is the Galicia Bank, Galicia Interior Basin (GIB), Porto Basin (PB) and Lusitania Basin (LB). To the south of the study region is the Southern Iberia Abyssal Plain. Colours in the map indicate bathymetry values.

3.3 Seismic data

The Galicia-3D (G3D) experiment was performed at the DGM from June to August 2013, to acquire a multichannel reflection and coincident wide-angle seismic data. The multichannel reflection seismic volume was recorded over an area of 68.75 km (east-west) by 20 km (north-south) (Figure 3.2) by the *RV Marcus G. Langseth*. The wide-angle data were recorded within the 3D box using 80 ocean bottom hydrophones/seismometers (Figure 3.2). The *FS Poseidon* deployed and recovered the OBSs, which concurrently recorded the signals from the seismic reflection experiment. OBSs were deployed in four lines with a spacing of ~6.5 km between the lines (Figure 3.2) and at variable offset from these lines to reduce linear artefacts in 3D FWI. The mean spacing between OBSs along each line is ~3.2 km. In this study, wide-angle data recorded by the hydrophones were used because of the absence of geophones on a few instruments.

The 3D seismic reflection data were acquired using four 6 km streamers towed 200 m apart. Each streamer consisted of 468 hydrophones spaced 12.5 m apart, and the streamers were towed at a depth of 15 m. The survey was carried out using two air arrays each consisting of 20 airguns. The two arrays were towed 100 m apart with gun volumes between 40 cu.in. and 360 cu.in. at a depth of 9 m. The total individual volume of each airgun array was 3,300 cu.in.. Seismic shots were fired alternately using two source arrays every 37.5 m (shot interval of ~ 16 s with ship speed of 4.5 knots) enabling 8 adjacent CMP profiles, spaced 50 m apart, to be recorded along the sailing lines. Processing of the reflection seismic data set was performed by Repsol, who produced a 3-D pre-stack Kirchhoff time migration.

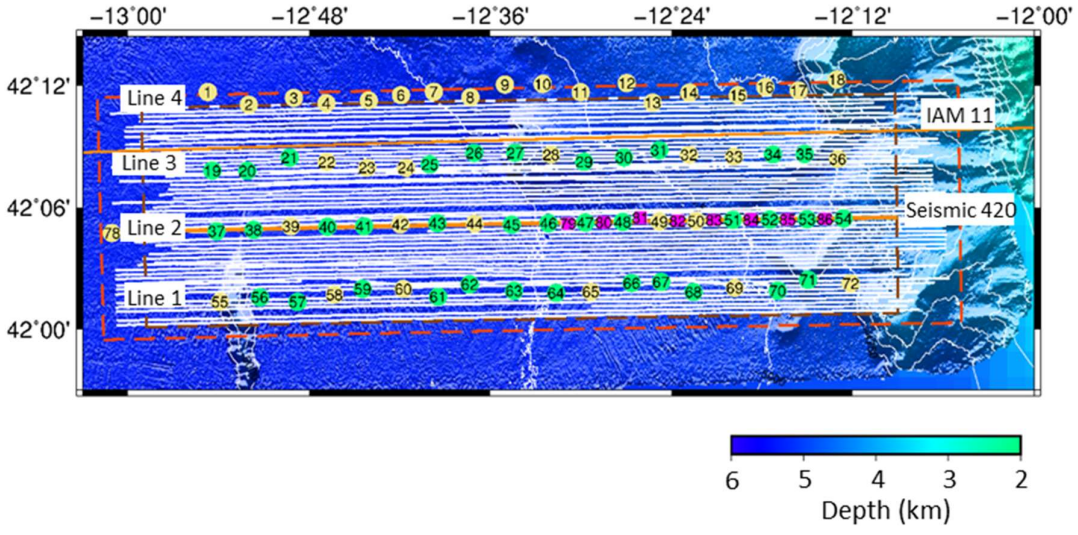

Figure 3-2 Map showing the location of the OBSs and seismic lines. The OBSs locations are aligned along four profiles from south to north: line1, line2 line3 and line4. Locations of multichannel seismic line 420 through the instruments in line2 and IAM 11 through the instruments along line3 are shown

in orange. The red-dashed box marks the area for the 3D FWI and the dashed brown box marks the multichannel seismic volume. The shot profiles recorded by the OBSs are shown in white lines. Green coloured instruments are used for 3D FWI, whereas the yellow ones have not been used in this work. The instruments in pink have only two shot profiles recorded directly above them and were not used in full 3D FWI.

3.4 Full-waveform inversion

Full waveform inversion is an advanced non-linear imaging technique capable of imaging features down to a resolution of half the seismic wavelength (Pratt et al., 1996; Tarantola, 1984). This technique involves iteratively updating a starting model using a least-squares local inversion and the Born approximation (Lailly, 1983; Tarantola, 1984). The basic equation that is solved in the FWI is:

$$\bar{m} = G^{-1} d_o \tag{8}$$

where d_o is the observed data; G^{-1} is the inverse of the forward modelling operator (G); $\bar{m}$ is the inverted model. There is no formal method to estimate G^{-1} from G. Hence, the solution to the inverse problem is achieved with an iterative approach using gradient based methods. In this study, we perform 3D FWI in the time domain using the FULLWAVE code (Warner et al., 2013). The starting model is updated in steps by reducing the residuals between the observed and predicted data generated with a forward modelling algorithm, which in our case uses the finite difference method (Warner et al., 2013). The RMS amplitude of the predicted dataset is scaled to match the RMS of the observed data trace-by-trace, and a broad sliding time-window is applied during the modelling so that different phases are normalised independently (Warner et al., 2013). The misfit (*f*) between predicted and observed datasets is calculated by summing the squares of the differences between the trace-by-trace normalised predicted (d_p) and observed (d_o) data, for every time sample:

$$f = \frac{1}{2} \left\| \frac{d_p}{\|d_p\|_2} - \frac{d_o}{\|d_o\|_2} \right\|_2^2 \tag{9}$$

Assuming a linear relationship between model perturbation and data residual, the model update is given as

$$\delta m = -H^{-1} \frac{\partial f}{\partial m} \tag{10}$$

where *H* is the Hessian matrix containing all the second-order differentials of the functional *f* with respect to model parameters, and $\frac{\partial f}{\partial m}$ is the gradient of the functional with respect to each of the model parameters. The gradient term is computed by taking a zero-lag cross-correlation between

the source generated forward-propagated wavefield and residual generated back propagated wavefield using the adjoint source (Tarantola, 1984). The density is estimated from the velocities using Gardner's law below the seafloor and is fixed during the inversion (Gardner et al., 1974).

3.5 FWI Workflow

We inverted for P-wave velocities updating the density using Gardner's law. We followed the workflows in Warner et al. (2013) and Morgan et al. (2016):

1. Generating the source wavelet
2. Starting frequency
3. Starting model
4. Pre-process the data
5. Modelling and inversion strategy
6. Quality assurance

3.5.1 Generating the source wavelet

The source wavelet was generated by developing a Weiner filter. Building the wavelet involved the following steps: 1) extracting the nearest offset direct water-wave arrivals from a few selected OBSs, muting the later arrivals; 2) aligning the direct water-wave on every individual trace to the same time (say 3.5 seconds); 3) stacking the traces to obtain a mean trace for the direct-water wave at one OBS location and resampling the trace to 1 ms; 4) generating a synthetic trace using a random guess wavelet and water column velocities for the same selected OBS (the guess wavelet should be band-pass filtered in the same way as the data and resampled to 1 ms); 5) repeating steps 1 and 2 for the synthetic trace by extracting and adjusting the direct water arrival time; 6) matching the synthetic trace with the observed trace to obtain an inverse filter using the Weiner method; 7) convolving the inverse filter with the guess wavelet to build the source wavelet; and 8) verifying the source wavelet by re-generating synthetic data and comparing it with the observed OBS data.

3.5.2 Starting frequency

Non-linearity of the inverse problem can be partially mitigated by starting the inversion from the lowest frequency available in the data and progressing towards higher frequencies – a multi-scale approach (Bunks et al., 1995). The choice of the starting frequency for our inversion is based on examining the phase of the first arrivals in the observed data with increasing offset (Figure 3.3). The phases are computed by applying a Fourier transform to each trace and extracting the phase at a particular frequency (Warner et al., 2013).. The concentric nature around the OBS of the phase

changes of the first arrival with increasing offset indicates a good signal-to-noise ratio to maximum offset of ~15 km. At ~15 km offset, the phase plots for the observed data show more chaotic behaviour indicating poor signal to noise ratio (Figure 3.3). The root-mean square (RMS) values of the phase residuals at 2.7 and 3 Hz are 1.42 and 1.44 radians, respectively. RMS values well below π radians clearly indicate that the starting model is not cycle-skipped and the starting frequency for the inversion can be 2.7 or 3 Hz. Based on the results from test runs, we choose 3 Hz as the starting frequency. Test inversion results performed using a subset of the dataset starting from 2.7 Hz and 3 Hz did not show significant differences. The RMS amplitude of the difference between the results of these test runs is equal to 36.30 m/s with the largest perturbation value equal to 236 m/s (Figure 3.4). Hence, we started the final inversion run from 3 Hz to reduce the computational time, rather than following the fundamental notion of starting the inversion from the lowest possible frequency (Sirgue, 2006).

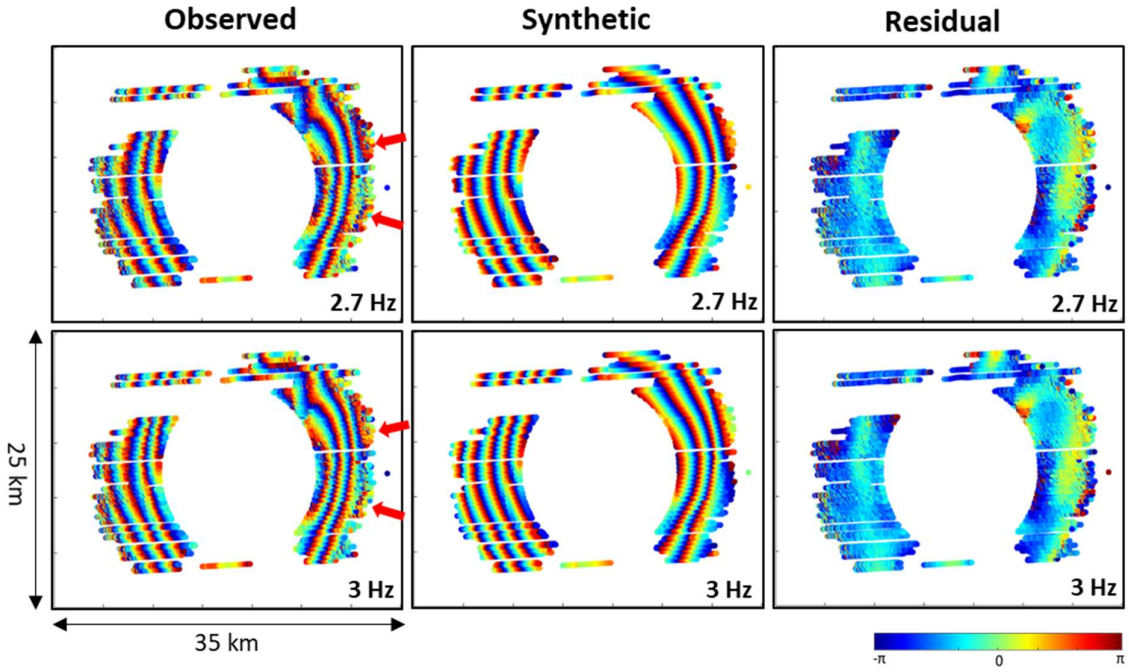

Figure 3-3 Phase residuals for OBS 46 for the starting model at frequencies 2.7 Hz and 3 Hz. Each dot represents the phase of the first arrivals extracted using a Gaussian window centred on these arrivals. The residual plot indicate that most of the data is predicted within half a cycle accuracy by the starting model. Noisy traces at far-offsets indicated by red arrows are out of phase.

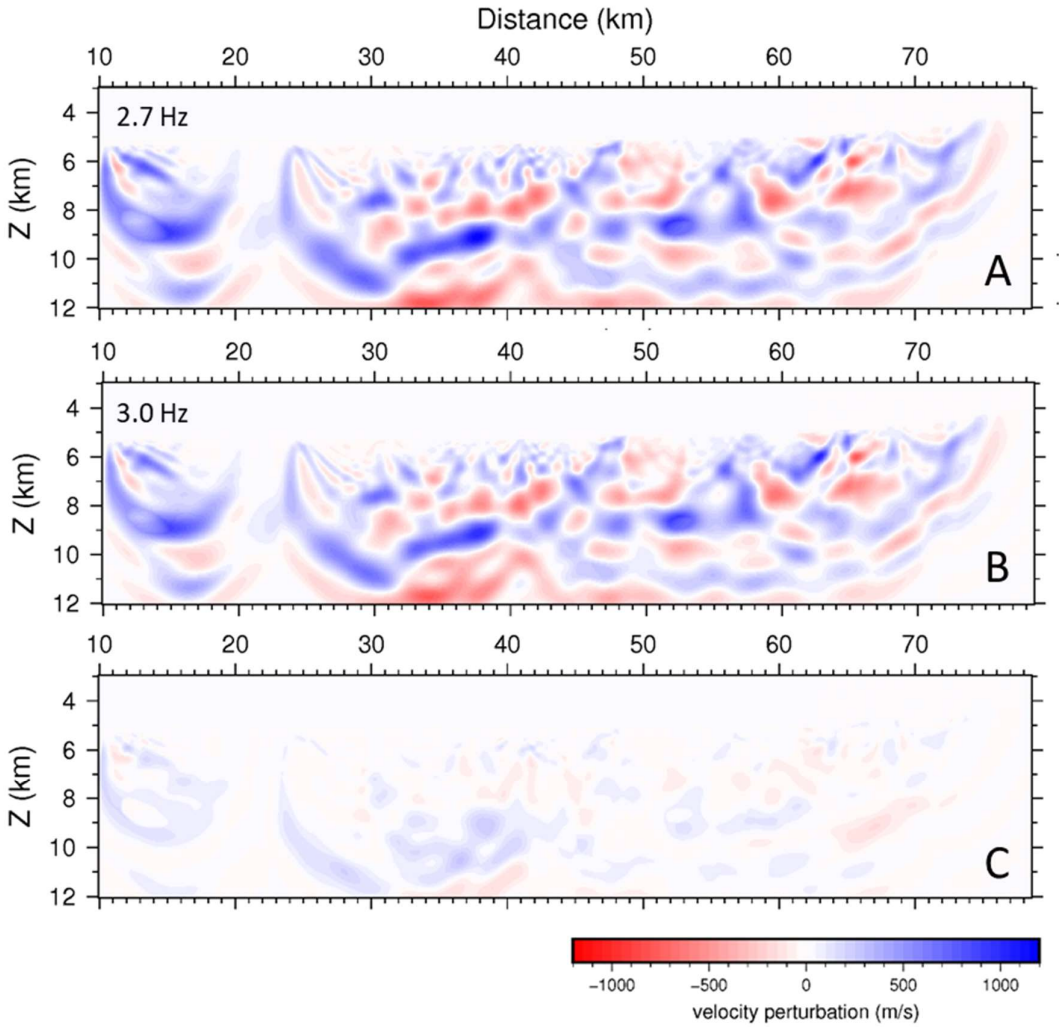

Figure 3-4 Difference between the starting model and the final model along a profile through the instruments in line 2 using the 3D inversion. A is the difference plot for inversion starting from 2.7 Hz and B is the difference plot for inversion starting from 3Hz. C is the difference between A and B.

3.5.3 Starting model

The starting velocity model is an important component of FWI. A model to qualify as a starting model for FWI should be able to predict the observed data within half a wavelength at the lowest starting frequency. The starting model used for FWI in this study was derived from FATT of the wide-angle seismic data recorded by OBSs from Galicia3D experiment (Bayrakci et al., 2016). Regularized inversion was performed using the First Arrival Seismic Tomography code, which solves the Eikonal equation using finite difference scheme and optimization using the LSQR variant of the conjugate gradient algorithm (Paige & Saunders, 1982; Zelt & Barton, 1998). The root mean square misfit for the final FATT model is 73 ms and the chi-squared value is 1 (Bayrakci et al., 2016). The starting model was modified by updating a constant water velocity of 1520 m/s to the water column

velocity profile measured during data acquisition, and linearly interpolating the grid from 500 m spacing to 50 m, ensuring an accurate and smooth seafloor. Although the final inversion runs were performed using a 50 m grid spacing, most of the test runs initially were performed using a grid spacing of 100 m to reduce computational time. 3D linear interpolation technique was used to interpolate the model from 500 m to 100 m and then further to 50 m after application of smoothing filters described below. Different interpolation techniques were tested to interpolate the data: cubic-spline, near-neighbour and linear techniques. The spline method introduced spurious values at the seafloor around the edges of the Peridotite Ridge, and the near-neighbour technique resulted in a pixelated model as it uses just the neighbouring points for calculating values at intermediate grid points. Use of a linear interpolation technique overcame these shortcomings and resulted in a smooth starting model. Smooth starting models without sharp velocity contrasts are preferred for FWI, unless such contrasts are well-constrained, such as the seafloor (Morgan et al., 2016). The smoothing process was carried out using a 2D convolutional filter applied along each profile of the 3D velocity model. Prior to the application of the filter, the velocity model was converted into a slowness model and vertically resampled to 1 m. The filter was applied over a window with dimensions 200 m vertically and 1500 m horizontally to remove any sharp velocity changes. The adequacy of the starting model was tested for its ability to predict the data within half a seismic wavelength for all instruments. Phase plots also assure the adequacy of the starting model by indicating whether the starting model is cycle-skipped (Shah et al., 2012). If the starting model, compared to the observed data, is not cycle-skipped, then the phase change is smooth and consistent with offset whereas if it is cycle-skipped there will be sudden jumps in the phase. The phase of the first arrivals of the predicted and observed data were compared to check if the predicted data were within an acceptable limit ($-\pi$ to $+\pi$) (Figure 3.3). Further verification was carried out by plotting sets of 10 traces from each dataset – observed and predicted – alternating to manually check for poor fit (Figure 3.5).

3.5.4 Pre-process the data

A minimum phase Ormsby bandpass filter with corner frequencies of 2-3 to 5-7 Hz was applied to reduce the random noise in the input data. The limits for the band-pass filter were chosen after trying different frequency ranges. The same filter was also applied to the source wavelet. Manually picked mute gates were applied to each OBS to include only the first arrivals. The data were windowed using top and bottom mute gates, which were picked manually. The window lengths were customized depending on the match of the observed traces with the synthetic traces generated using the starting model (Figure 3.5). The window length between the mute gates varied between 700 ms and 1200 ms for all the instruments. Data up to maximum offset of 15 km were

included into the inversion, beyond which the data quality degraded with arrivals from the previous shot, making it unsuitable for the FWI

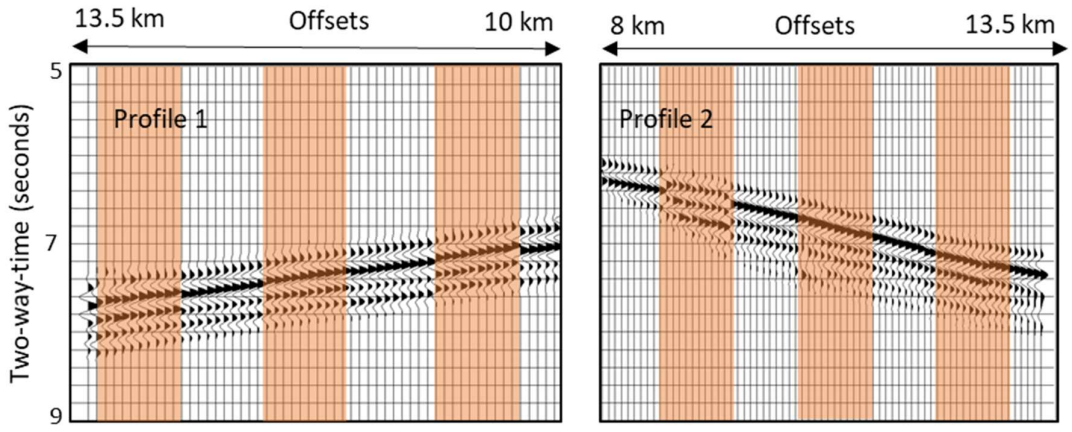

Figure 3-5 Observed (highlighted) and predicted data using the starting model plotted in sets of 10 traces from OBS 46, alternating to show the match between the arrivals along two profiles. Profile 1 is the closest profile to the OBS 46 location and Profile 2 is at a distance of ~10 km from this location. The data shown is band-pass filtered and trace-by-trace normalised.

3.5.5 Modelling strategy

We inverted only for P-wave velocities, assuming isotropic and acoustic approximations for the medium. These assumptions are based on the previous tomographic and FWI studies in this region using the same wide-angle dataset, which indicated an absence of strong elastic and anisotropic effects (Bayrakci et al., 2016; Davy et al., 2016, 2018).

Wide-angle refraction data from 36 OBSs were considered for the inversion (Figure 3.2). The number of profiles recorded by each instrument was 100. Profiles with low signal-to-noise ratio on a particular OBS were excluded from the inversion. Data from OBSs on the northernmost profile were not included because of larger uncertainty in their re-located positions, which is partly due to the lack of a shooting profile directly above the OBSs. The number of shots included from each instrument is tabulated in appendix A-2.

The maximum and minimum velocities in the starting model are 1497 and 8000 m/s, respectively. The grid spacing in the velocity model is 50 m in each of the three dimensions. To ensure that the wavefield is computed at least twice in every cell given the maximum velocity in the starting model, the sampling interval of the data should be less than 3.125 ms (0.5 * grid spacing/maximum velocity). Hence, the data was resampled to 3 ms to satisfy with this condition. The dimensions of the grid along the inline (along the shooting profiles) and crossline (across the shooting profiles)

directions are 78.5 km and 22.1 km, respectively, and the vertical dimension is 12 km. The grid dimensions in the inline and crossline directions were chosen to include all the receivers and shots within the grid. Shots falling within 1 km of the edges of the velocity grid were removed to avoid edge effects in the wave propagation. To facilitate the implementation of the code, a data reciprocity rule was applied to treat the shots as receivers and OBSs as shots. The total number of reciprocal receivers (i.e., shots) used in the inversion was 84,044. The inversion was performed following the multi-scale approach starting from low frequencies and progressing towards higher frequencies in steps (Bunks et al., 1995). During the inversion, the program applies low-pass filters rolling off at frequencies 3, 3.3, 3.9, 4.5 and 5.2 Hz to the data and the source wavelet (Warner et al., 2013). Thirty iterations were performed at each frequency to allow the misfit functional to reduce and flatten. For the final inversion run, smoothing was applied to the gradient using a Gaussian filter with correlation lengths of 2 x seismic wavelength and 1 x seismic wavelength in the horizontal and vertical directions, respectively. The smoothing parameters were adjusted to suppress the short-wavelength artefacts in the result. For the 2D inversion all the parameters were the same as for the 3D inversion except for the number of OBSs used and the grid size. For this inversion, two shot lines were used from 16 OBSs along line 2 (Figure 3.2), and the velocity model dimensions were 78.5 km x 2 km in the horizontal directions and 12 km in the vertical dimension.

FWI is a computationally demanding imaging technique, so forward modelling and inversion runs were performed on two large linux clusters: Iridis 5 (University of Southampton) and Mobilis (National Oceanography Centre). Mobilis comprises 72 computing nodes each with 64 GB of memory (DDR3 memory) and 2 x Intel Xeon E5-2650 2.6 GHz eight-core processors, giving a total of 1152 processor cores. Iridis 5 comprises of 464 compute nodes with dual 2.0 GHz Intel Skylake processors. Each compute node has 40 CPUs per node with 192 GB of DDR4 memory. Initial testing and 2D inversions were performed on Mobilis because of its smaller queue time, whereas the final 3D inversion runs were performed on Iridis 5. 2D and 3D inversion runs were performed by assigning two OBSs to each node. 2D inversion runs on Mobilis were performed using 8 nodes and one extra node for communication between the nodes. The computation time for each iteration was ~11 minutes for the final 2D inversion run. For the final 3D inversion run, 18 nodes were employed on Iridis 5, with one extra node reserved for communication between the nodes. The compute time for each iteration for the 3D run was ~45 minutes.

3.5.6 Quality assurance

We tracked the progress of the 3D inversion by monitoring the phase residuals, obtained by subtracting the phases of the predicted and observed data (Figure 3.6; Appendix B-1). We clearly observe that these phase residuals have reduced after 1 iteration at both frequencies (Figure 3.6).

Abrupt changes from one extreme phase to other (-π to + π) is indicative of cycle-skipping, which is not observed except for a few noisy traces at the far and near-offsets. Including a substantial number of cycle-skipped traces into the inversion could cause the inversion to converge to a wrong final model. However, if the number of such traces is small, the effects from cycle-skipped traces are nullified by the rest of the data driving the model towards the global minimum (Shah et al., 2012). For most of the data the phase change is gradual at 3 Hz, except a very few traces at far offsets which have poorer signal-to-noise ratio (Figure 3.6). At 4.5 Hz, there are regions that change their phases abruptly from red to blue. However, these same regions show small phase changes at 3Hz, indicating that there is no cycle-skipping. This is a clear advantage of progressing from lower frequencies to higher frequencies during the inversion. At lower frequencies, the chances of cycle-skipping are lower because the misfit function around the global minimum is devoid of local minima. To further check the convergence of the FWI, we plotted the predicted data from the traveltime model and FWI inverted model with the observed data to check the improvements resulted from FWI (Figure 3.7; Appendix B-2). The result shows clear improvement in the alignment of the FWI model synthetics with the observed data compared to the travel-time model synthetics.

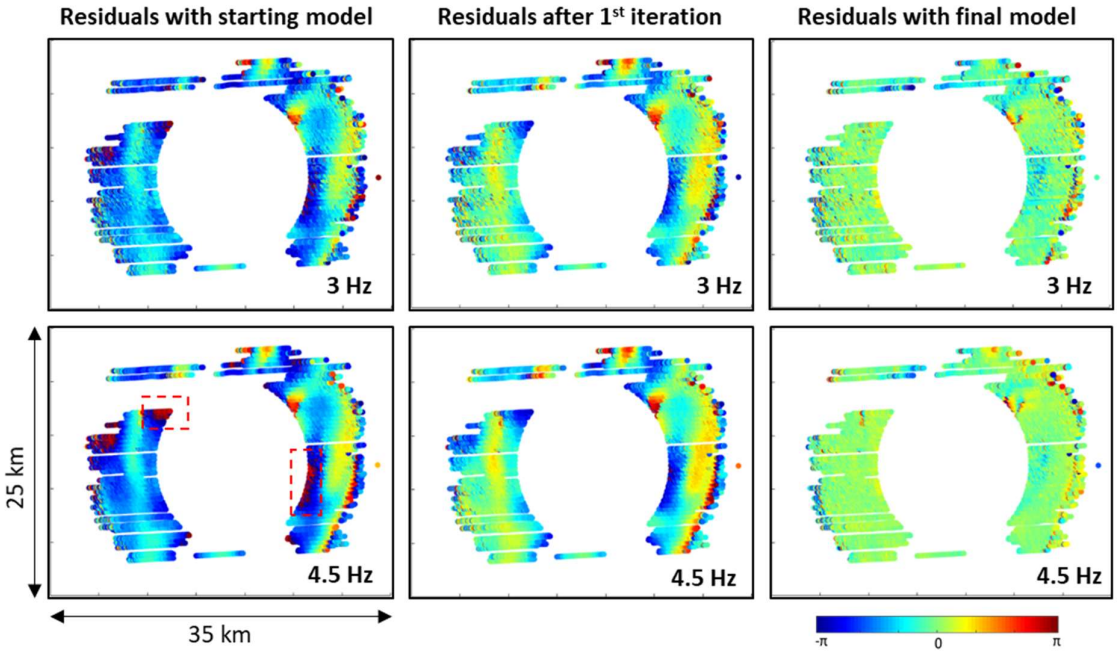

Figure 3-6 Phase plots residuals for starting model, model after 1st iteration and final models at 3 and 4.5 Hz. The phases show gradual change towards zero phase difference except at two locations highlighted in dashed red boxes at 4.5 Hz. A few lines have been excluded from the inversion because of their poor fit or poor quality, resulting in gaps in the refracted arrivals in the above plots.

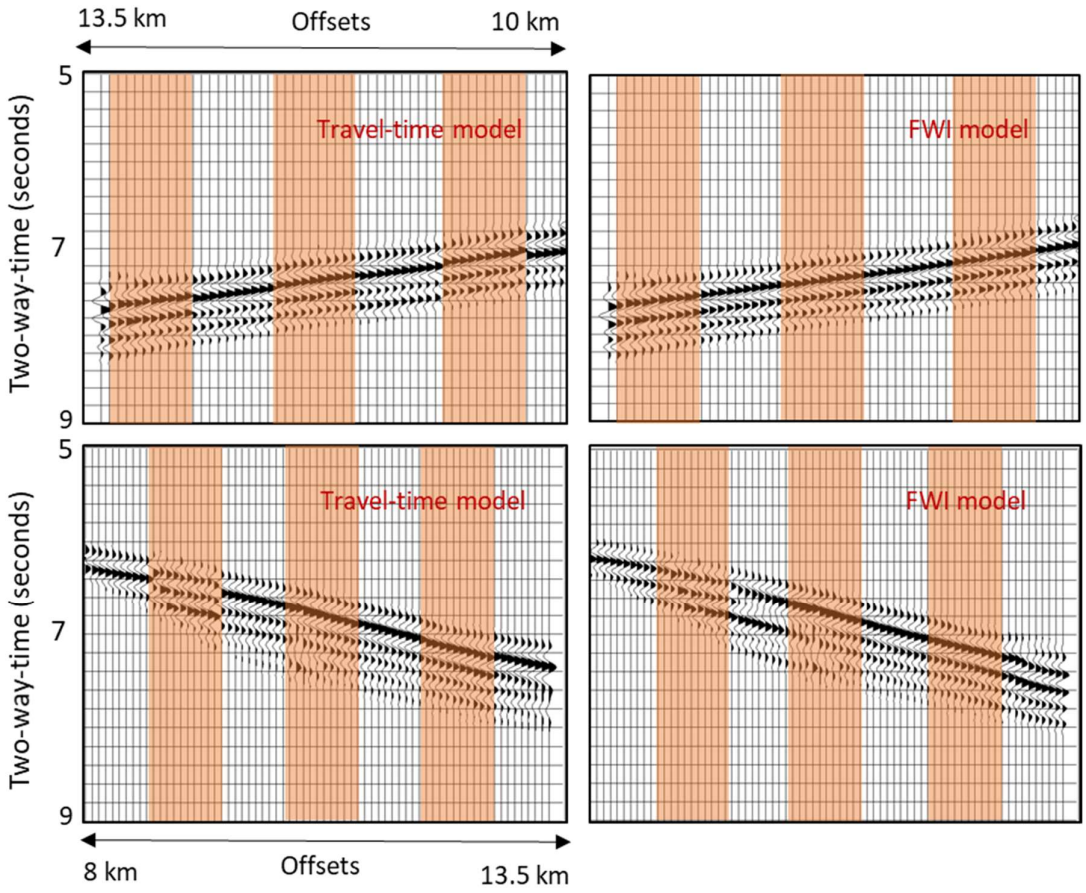

Figure 3-7 Observed and synthetic data along the same two profiles from OBS 46 as shown in Figure 3.5. Left-hand profiles are alternating sets of 10 traces from observed data (highlighted) and synthetics from the starting model. Right-hand plots show the observed data (highlighted) and synthetics from the final model.

3.6 Results and discussion

We compare the results from 2D and 3D FWI along the seismic line 420 in both depth and time domains. In our comparison, we have also included the 2D FWI result from Davy et al. (2018), which was derived along the same line using the wide-angle data from the same instruments, but from a different starting model (Davy et al., 2016). Our 2D result is derived using just two shot profiles closest to the instruments along seismic line 420 and the starting velocity model was obtained from the 3D travel-time model to include the shots and the instruments along seismic line 420 (Bayrakci et al., 2016). We present 3D inversion results from two runs, one in which only the instruments along seismic line 420 are used and the other using all the instruments indicated in Figure 3.2. The number of shot profiles included from each instrument in to the 3D inversion varied depending on the fit between the predicted and observed datasets (Appendix A-2). Only data which were

predicted by the starting model within a half seismic wavelength were included into the inversion. In order to highlight the differences between 2D and 3D imaging, we overlaid the time-converted velocity profiles on a time-migrated seismic section obtained from 3D seismic volume (Lymer et al., 2019). The interpretations used in our comparison were developed through the entire 3D seismic volume and are independent of our FWI velocity models (Lymer et al., 2019). In the text that follows, we use the following abbreviations: 2DA corresponds to 2D FWI result of Davy et al. (2018), 2DB corresponds to our 2D FWI result, 3DA corresponds to the 3D inversion using data from instruments along seismic line 420 and 3DB correspond to full 3D results.

The inversion strategy of the 2DA FWI result differs from that of the 2DB FWI result. We infer this difference to be the primary reason for the differences observed in the two sections, especially the short wavelength structures (Figures 3.8 and 3.9). The starting models used for 2DA and 2DB are derived from different studies (Bayrakci et al., 2016; Davy et al., 2016). In 2DA, the starting model was derived from 2D travel-time tomography, in which the sedimentary column velocities are constrained using the top basement depths from the multichannel images. Such a modelling approach resulted in improved fit of the top of the basement with the multichannel images, which is evident at the peridotite ridge compared to the result from 2DB. In both the results, the long wavelength structure fits the interpreted boundaries well, indicating that different starting models generated a similar background model. However, the finer details within the fault blocks and the undulations at the S-reflector differ between the images. Focusing on the differences, we notice that the 2DB model is smoother than the 2DA model. This smoothness may be due to the application of the shorter window length ~700 - 1200 ms on the input data compared to the ~1800 ms window length used for the 2DA study. Davy et al. (2018) showed that using a shorter data window resulted in a smoother model. Our choice of window length was based on the fit between the synthetic data and the observed traces. For most of the OBSs, a good fit was observed over a window length of 800 ms from the first arrival. Beyond this length, our starting model showed a poor fit with the observed data, which might result in artefacts. Another potential reason for the smooth appearance of 2DB over 2DA could be application of different smoothing parameters. We adjusted our smoothing parameters to suppress the short wavelength artefacts and we observed that the same smoothing parameters as applied in 3D did a good job for 2DB as well. Use of the same smoothing parameters facilitates comparison of 2DB, 3DA and 3DB.

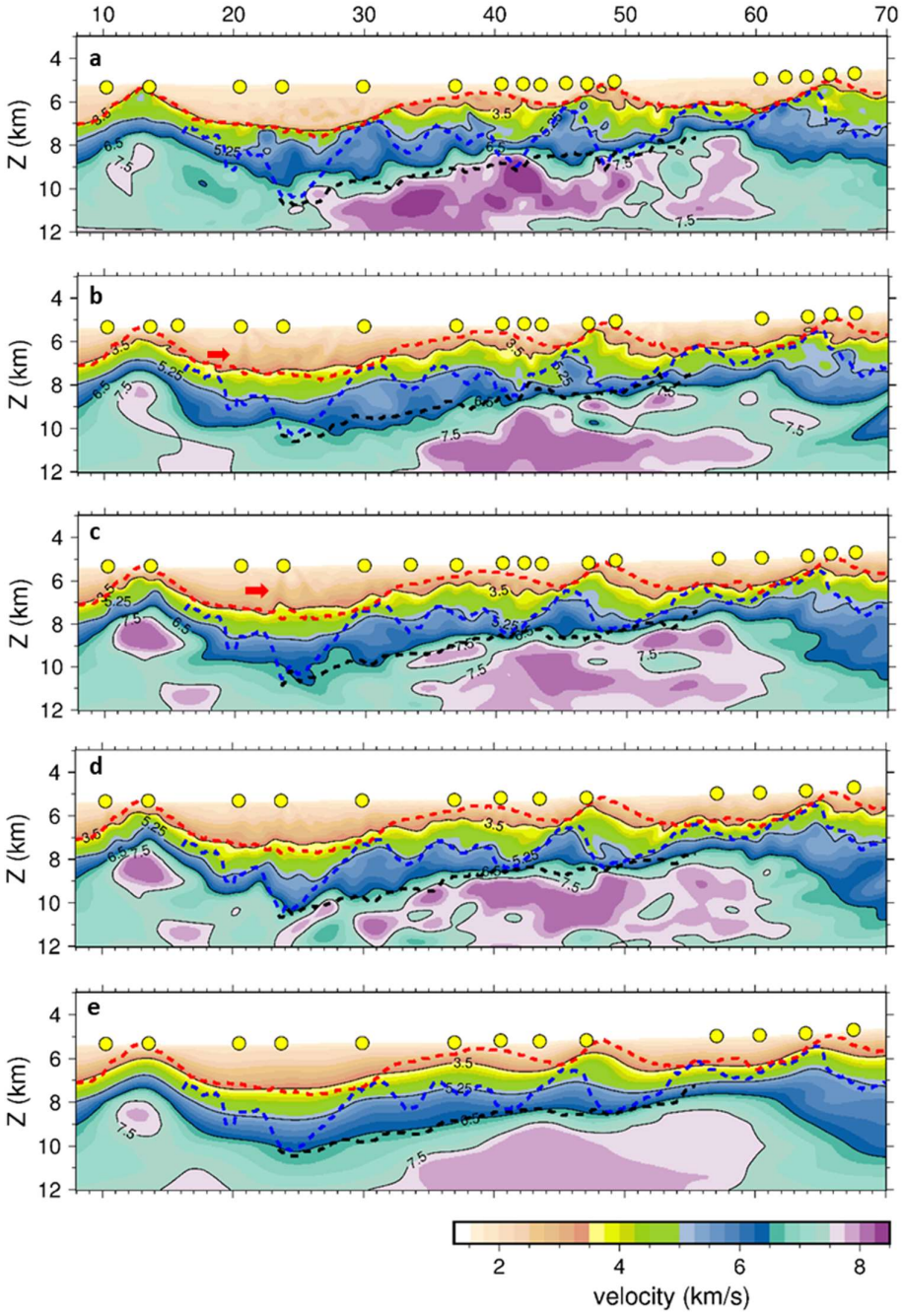

Figure 3-8 Comparing the 2D FWI and 3D FWI in depth domain. Interpretations from multi-channel seismic images (Lymer et al., 2019) are converted from time to depth using respective velocity models and overlaid on the sections along with the OBS locations in yellow circles. Profile a is the result from 2D FWI – 2DA (Davy et al., 2018), profile b is the 2D FWI from the 3D starting model – 2DB, profile c is the 3D FWI using only the instruments along line 2 – 3DA, profile d is the result from the full 3D FWI using instruments coloured in green in figure 2, and profile e is the starting model from 3D travel-time tomography (Bayrakci et al., 2016). Dashed red line marks top of the syn-rift sediments, dashed blue line is the top of the crystalline crust and dashed black line is the S-reflector. The red arrows point at the imaging artefacts.

Although both 2D FWI results show a reasonable match with the multichannel seismic image (Figure 3.9), differences in the short-wavelength structures are noticeable. Compared to the 3D starting model, the 2D results show an improved fit to the multichannel images especially along the faults. Broadly, both 2D and 3D imaging have resolved the structures that are geologically relevant. We carried out a detailed comparison of the images based on the match between the velocity models and multichannel seismic images, focusing on the pre- and syn-rift sediments, the basement blocks and the S-reflector. Compared to the 2D imaging, 3D FWI images show an improved fit between the velocity model and the multichannel images (Figures 3.8 and 3.9).

3.6.1.1 Pre- and syn-rift sediments

Pre- and syn-rift sediments are interpreted by Lymer et al. (2019) between the boundaries of the base of the post-rift sediments (dashed blue line) and top of the crystalline crust (dashed red line) (Figures 3.8 and 3.9). Both the 2D and 3D FWI results resolve the long wavelength structure in this zone well when overlaid on the multichannel interpretations. The velocities of pre- and syn- rift sedimentary packages range from ~3.5 km/s to ~5.25 km/s overlying the crystalline crust along this profile. The velocity contour of 3.5 km/s tends to oscillate in the FWI results compared to the starting model, and the pattern of the oscillations is not consistent between 2D and 3D results. This oscillatory pattern is likely to be the result of complex faulting within the pre- and syn-rift packages which has been previously interpreted in multichannel seismic images from the Deep Galicia margin (Lymer et al., 2019; Ranero & Pérez-Gussinyé, 2010; Reston, 2005). Such a fine-scale faulting pattern is beyond the resolution limits of our inversions, primarily because of the absence of high frequency content in our dataset. However, an interesting observation is that the oscillations are smaller in the 3DB result than in the 3DA and 2D results, indicating the 3D nature of this faulting.

Our final models have artefacts within the sedimentary column, which are vertical in nature and pointing towards the OBS positions (Figure 3.8). These artefacts are mainly observed in the western region of the model between the Peridotite Ridge and the crustal blocks. They arise from the inclusion of shot profiles, which are away from the OBS locations. Thus the artefacts in 3DA are stronger compared to 2DB and 3DB. Arrivals from the far-offset profiles travel through deeper parts of the model that are not well constrained by the inversion, especially when there are no other OBSs located between the far-offset shot profiles and the OBS location to locally constrain deeper parts of the model. In 3DA, only instruments along line 420 are considered with shots through the full 3D volume, resulting in the generation of stronger artefacts compared to the 3DB and 2DB. Another reason for these artefacts may be the high uncertainty of the starting model in the western part (Bayrakci et al., 2016).

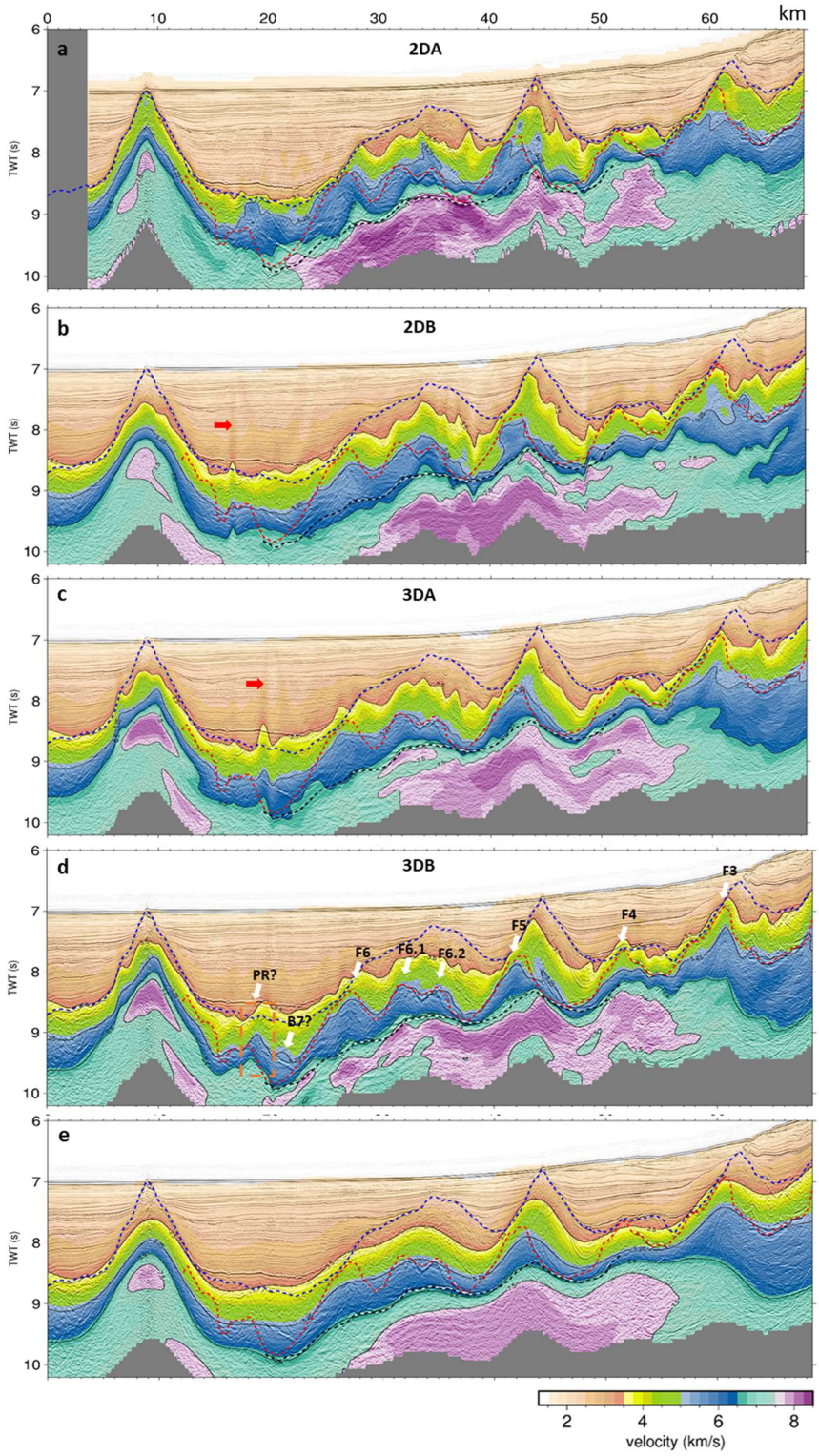

Figure 3-9 Comparison between 2D and 3D FWI results and multi-channel time sections, which are overlaid with interpretations from Lymer et al. (2019). Profiles correspond to their respective profile labels and velocity contours in Figure 3.8. Fault numbers (F-series) are marked on the FWI result (d) with fault-block (B7) landward dipping and a small peridotite ridge within the dashed orange box identified. Red arrows mark vertical artefacts.

3.6.1.2 Crystalline crust

The crystalline crustal section when overlaid on the multichannel seismic image shows significant improvement compared to the starting model (Figures 3.8 and 3.9). The velocity range for crystalline basement inferred from our results is ~5.25 km/s to ~6.5 km/s. 2D imaging shows circular velocity contours in some locations within this region, which are geologically unrealistic. Such structures can be a result of a poorly constrained inverse problem or from the assumed approximation of the wave equation as acoustic, isotropic and non-attenuating. However, these circular features would also be observed in 3D imaging if the assumed approximations of the wave equations do not fulfil the real Earth model in the study region. A good match of the 3DB velocities within the crystalline crust with multichannel images indicates the 3D nature of crustal fault-blocks.

3.6.1.3 S-reflector and serpentinisation

Previously, the 3D travel-time model has shown that velocity 6.5 km/s contour follows well the S-reflector (Bayrakci et al., 2016). However, FWI results have introduced undulations in the 6.5 km/s contour in both 2D and 3D. Although it is expected that 2DA and 2DB show similar results, 2DA shows velocities greater than 6.5 km/s and 2DB shows velocities less than 6.5 km/s at the S. The reason for this difference may be the different inversion strategies for the two cases, particularly the choice of the window lengths and offsets for the input data. To further explore the velocities below the S-reflector, we plotted average velocity values below the S-reflector over a window of 100 ms along profile 420 for all the models using the interpretations from the multi-channel seismic image (Figure 3.10). It can be seen clearly that the 2D results show poor correlation with each other. However, the pattern of 2DA shows a match with the 3DB result in certain locations. 2DB result shows a poor match along the profile until 45 km distance, beyond which the pattern matches with the patterns of 3DA and 3DB. These observations suggest that the region towards west, where the S-reflector is deeper compared to the east, 2DB has failed to generate a realistic model in the deeper parts. This poor imaging from 2DB especially in the western parts may be attributed to the sparse spacing of the OBSs and limited offset data, resulting in spurious values below the S-reflector. Moreover, the data from OBSs 38 and 40 were limited to ~11 km offset because our starting model was not able to predict the data sufficiently well beyond these offsets for these OBSs. Only 10 shot profiles closest to their locations were included from these OBSs in the 3D inversion runs.

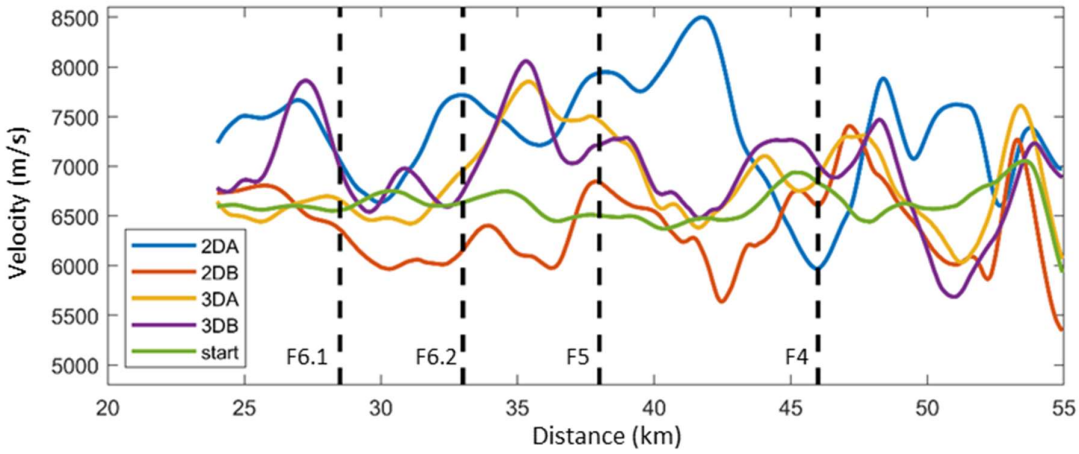

Figure 3-10 Velocities below the S-reflector averaged over a window of 100 ms for each of the FWI results. The intersection of the faults with the S-reflector are indicated by vertical dashed lines.

The effect of OBSs 38 and 40 is also evident from the poor correlation between the curves 3DA and 3DB between the distances 25 km and 30 km (Figure 3.10). In 3DB, this region has been well resolved because of the data from the instruments located in the other OBS lines of the survey. Overlaying the velocity model over a time slice through the 3D seismic volume at 100 ms below the average depth of the S-reflector (~9.1 s; Figure 3.11). Furthermore, the range of velocities resolved by the 3DB below the S-reflector indicates that 3DB has constrained the problem well with 8 km/s corresponding to unaltered peridotites with 0% serpentinisation (Carlson & Miller, 2003). Velocities higher than 8.3 km/s are unrealistic at the S-reflector and lower velocities correspond to some degree of serpentinisation of the mantle (Bayrakci et al., 2016; Davy et al., 2018). Our 3D modelling has clearly enhanced the pattern of serpentinisation below the S-reflector compared to the starting model. We observe that below the S-reflector the mantle peridotites have undergone serpentinisation with a maximum serpentinisation of 45% occurring around the fault intersections (Carlson & Miller, 2003).

Based on the 2DA, Davy et al. (2018) supported the concept of preferential serpentinisation in which the faults preferentially serpentinise the upper mantle rocks. The result from 3DB along the same profile shows a good correlation between the fault intersections with the S-reflector and occurrence of lower velocities compared to the other models along this line.

3.6.1.4 Crystalline Block 7 or Peridotite Ridge?

The final 3D model (3DB) shows significant improvement in the match with the multichannel images compared to the rest of the models, particularly within the crystalline crust and below the S-reflector. However, there are structures that correlate less well with the multichannel

interpretations. One such feature is located between the peridotite ridge and the continental crust that has been identified/interpreted in previous studies (Davy et al., 2018; Pérez-Gussinye, 2013). Based on the 2DA result, this feature was interpreted as a fault block

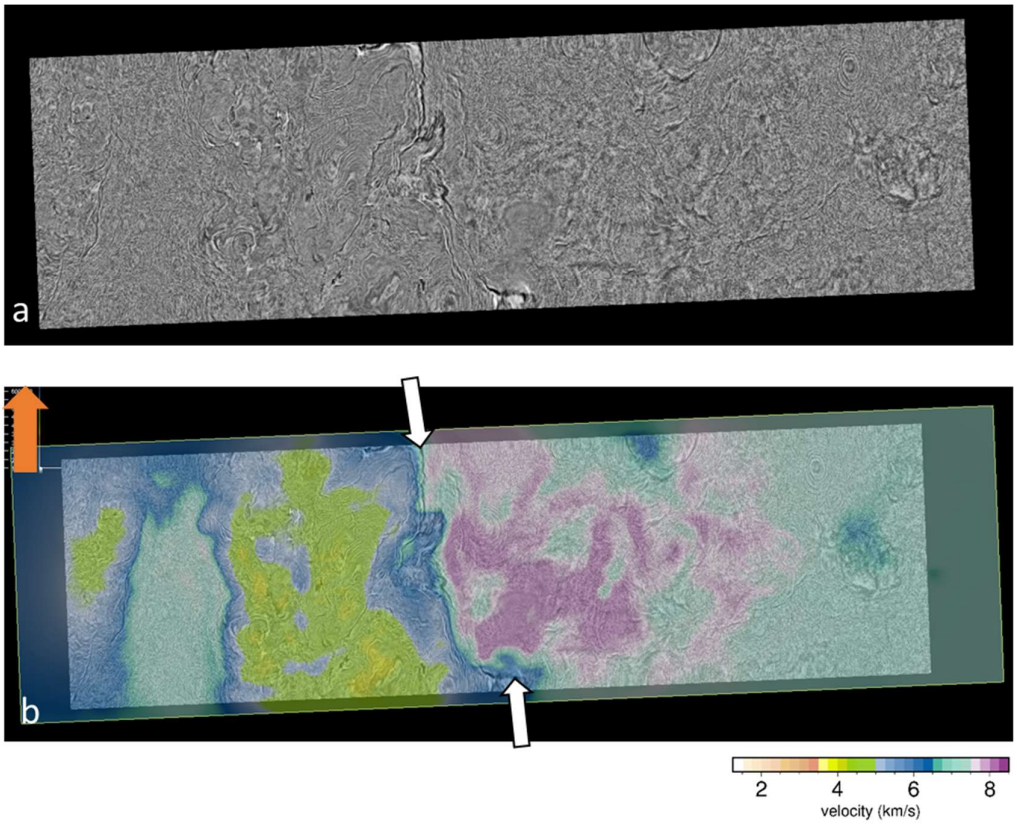

Figure 3-11 Time slice at depth 9.1 s a) timeslice from the multichannel seismic volume b) 3D FWI model overlaid on the timeslice. White arrows point to the boundary between the crust and upper mantle. North is shown by orange arrow.

because the velocities resolved within the block match crystalline crustal velocities (Davy et al., 2018). Comparing this feature in 2DA and 3DB, we observe that 3DB has introduced velocities greater than ~6.5 km/s within the feature and resulted in a pointed top, making it distinct from the other fault blocks which comprise velocities below ~6.5 km/s with flat, eroded tops (velocity contour 5.5 km/s) (McDermott & Reston, 2015; Reston, 2007). These observations support an interpretation of the feature as a small peridotite ridge rather than a fault block. Such an interpretation is further supported by the absence of the S-reflector are below this structure. Our 3DB model also indicates presence of an extra fault block (B7) at the end of the crystalline crust with its top terminating on the small peridotite ridge flank. Clear reflections from the S-reflector below it confirms its nature as crystalline crust (Figure 3.12). Pérez-Gussinye (2013) interpreted a similar structure on line IAM 11 (Figure 3.2) as a small peridotite ridge formed before or simultaneously with the formation of the Peridotite Ridge. It has been also inferred that the last

active fault terminates sub-horizontally on top of this feature following a sequential faulting mechanism (Pérez-Gussinye, 2013). Assuming that the same mechanism operated along seismic line 420 and that the small structure is a peridotite ridge in our 3DB result, we do not observe any convincing evidence for existence of a sub-horizontal structure marking the top of fault-block B7. Instead, the velocities suggest that the horizon marking the top of the pre- and syn-rift sediments terminates sub-horizontally on top of the small peridotite ridge. On this profile, fault block B7 has a landward-dipping reflector terminating on the small peridotite ridge (Figure 3.12). This observation suggests that the exhumation of the small peridotite ridge was still an ongoing process after the formation of the last fault block (B7) which has undergone further rotation after becoming sub-horizontal in the exhumation process.

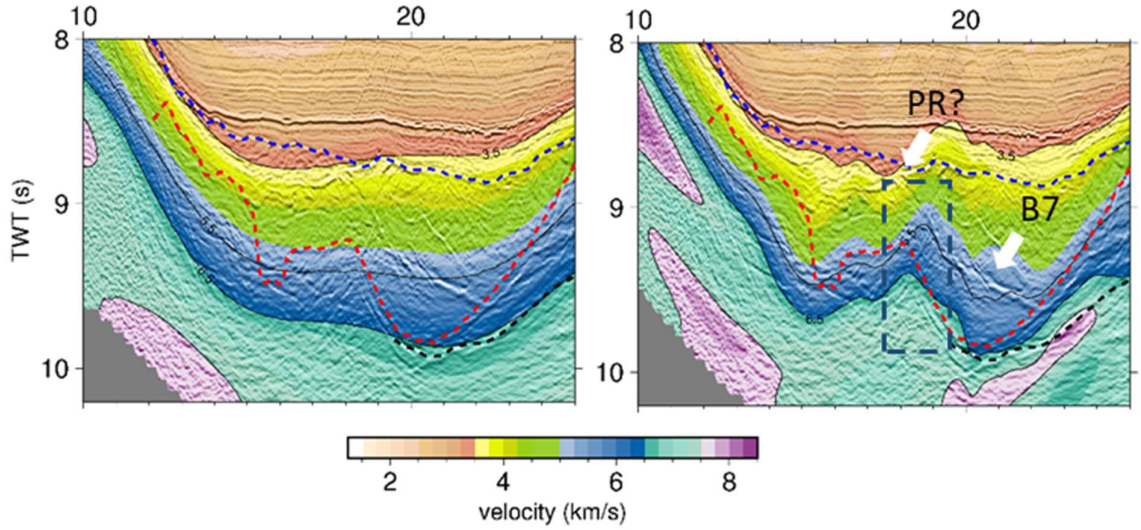

Figure 3-12 Blow up of the region around the block B7 and the small peridotite ridge from the figure 3.9(d). This blow up region is between the unambiguous continental crystalline crust towards east and peridotite ridge towards west. Using the 2D FWI, only block B7 was identified previously (Davy et al., 2018).

3.6.1.5 Data fit

Another interesting aspect to compare between the 2D and 3D FWI is the fit between the observed and predicted datasets. We generated the synthetic data for 2DB, 3DA and 3DB for the OBS 46 along one shot line and calculated the data residuals for each model by subtracting the final model predicted data from the observed data (Figure 3.13). We observe that 3DA and 3DB models fit the data better than the 2DB model. The RMS amplitude values for the scaled and trace-by-trace normalised 3D FWI results shown in Figure 3.13 are ~0.38, whereas for the 2D FWI the value is around 0.44. In the 2D FWI result, larger residual arrivals can be seen across the full offsets compared to the 3D FWI results, indicating that the 3D FWI models have better predicted the

observed data. In the 3D residual plots, the overall match is good except at the near offsets, which is probably due to poor sampling of the subsurface by OBS data in the near-offsets in general, perhaps sparse spacing between the OBS can further reduce the constraints at the near-offsets.

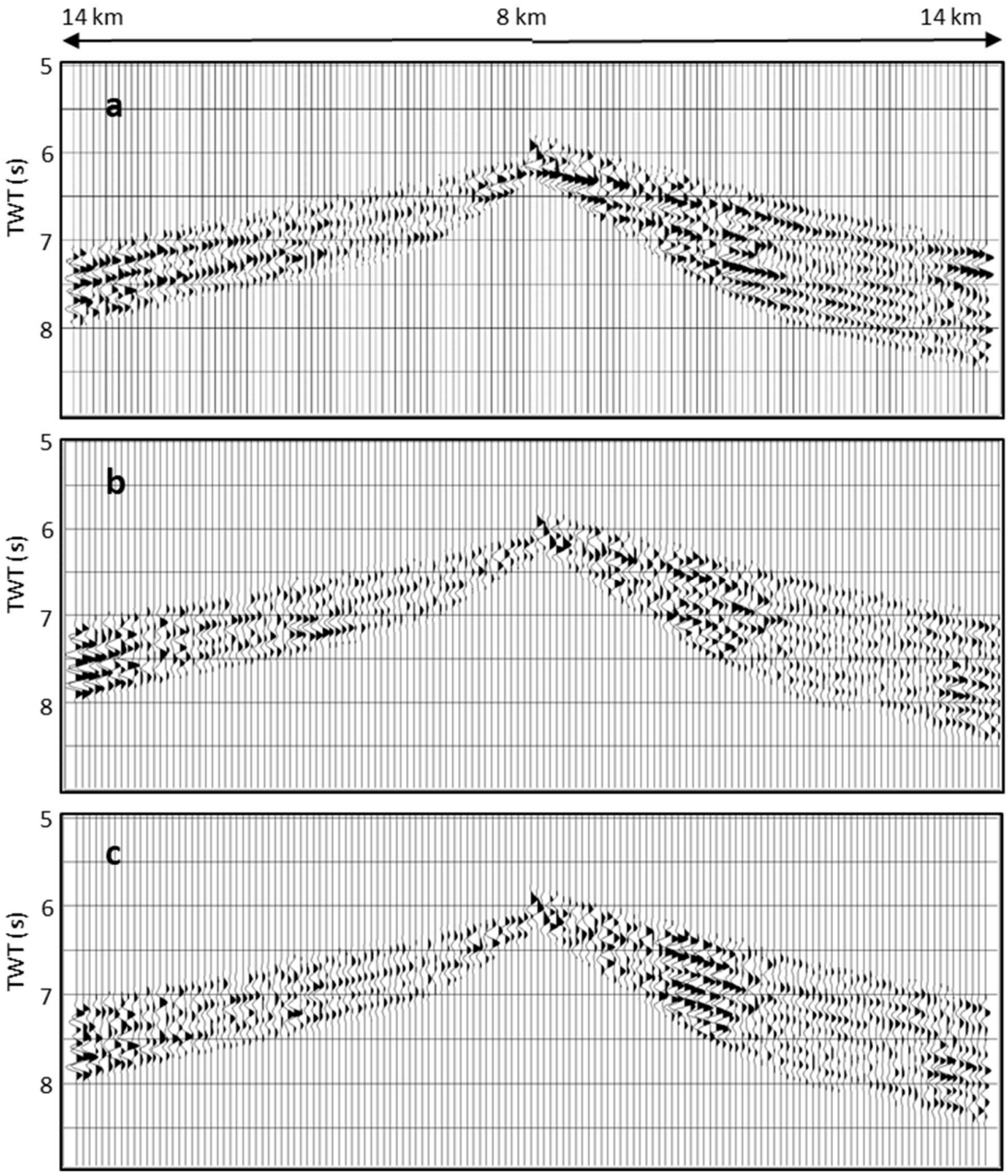

Figure 3-13 Data residual plots for the 2DB (a), 3DA (b) and 3DB (c) models for OBS 46 along the closest shooting profile to the instrument.

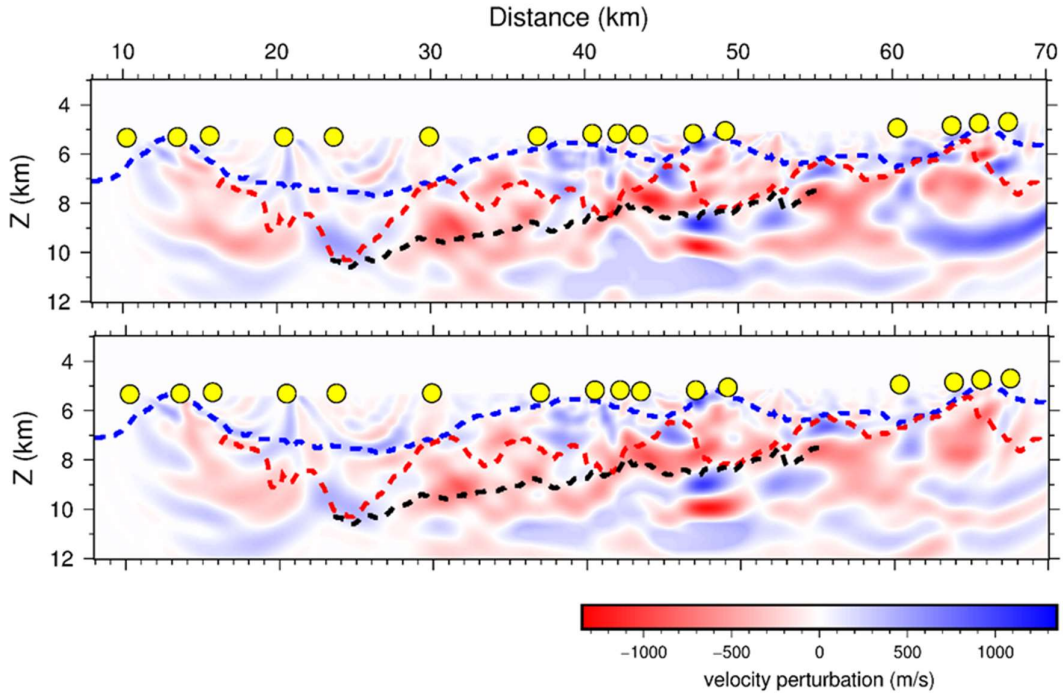

*Figure 3-14 Restoring anomaly test for 2DB A) Difference plot of the 2DB model and the starting model. B) Difference between the recovered anomaly model and the starting model. The interpretations are same as in the profile **b** in Figure 3.8.*

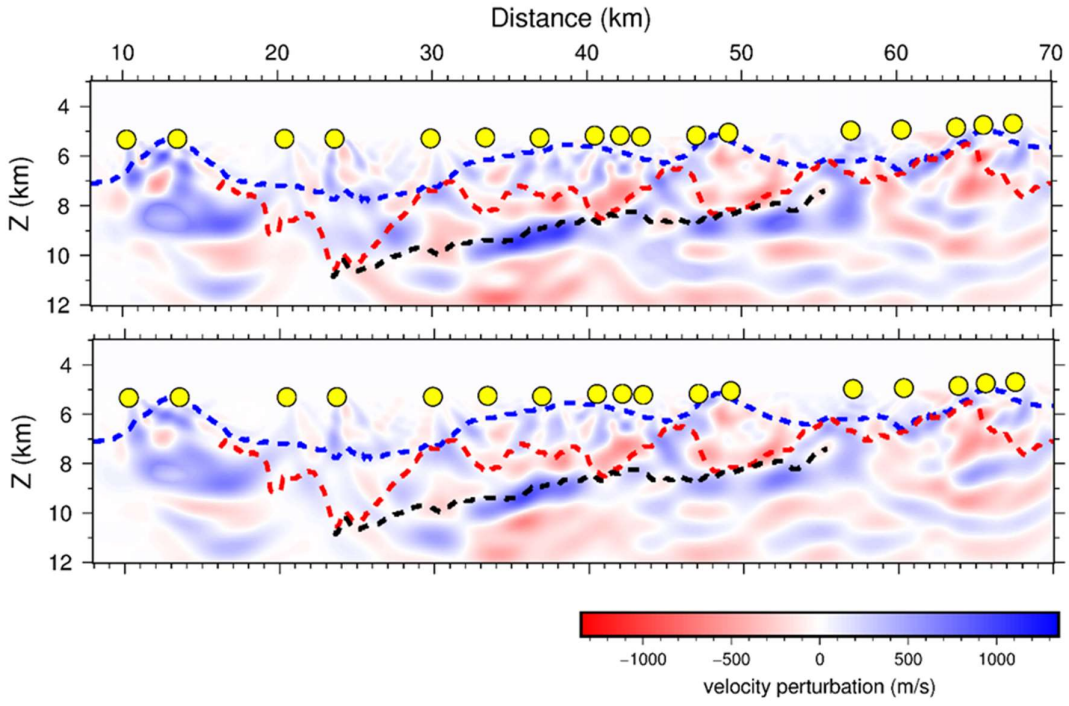

*Figure 3-15 Restoring anomaly test for 3DA A) Difference plot of the 3DA model and the starting model. B) Difference between the recovered anomaly model and the starting model. The interpretations are same as in the profile **c** in figure 3.8.*

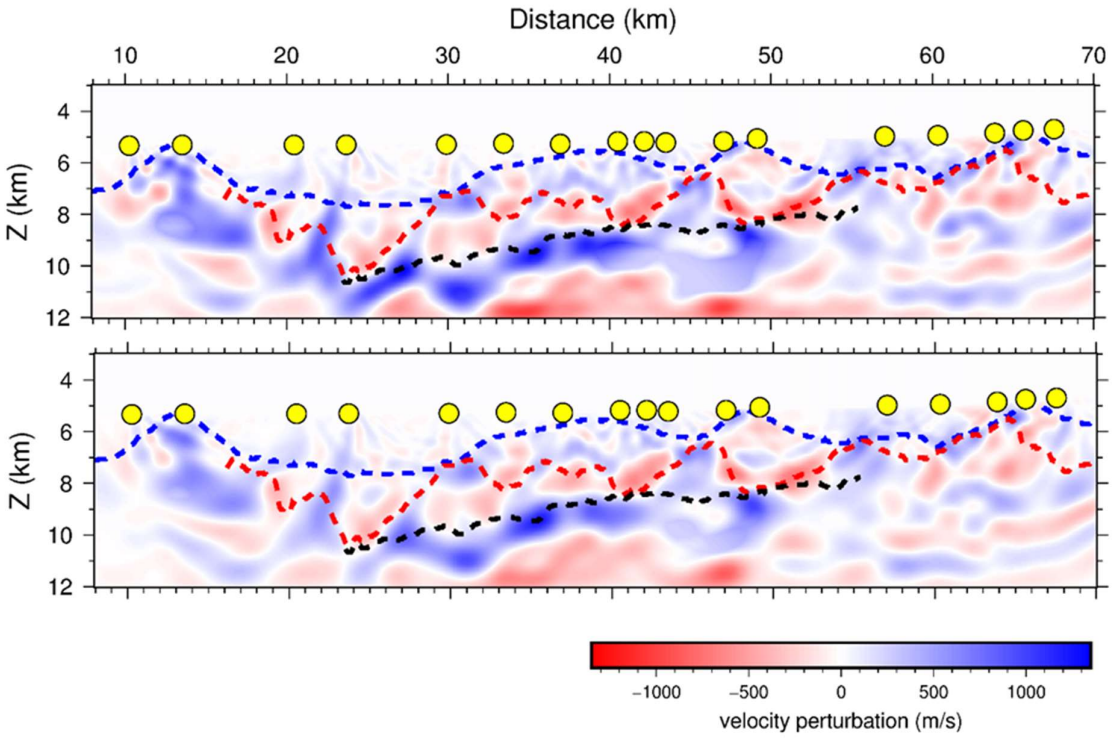

Figure 3-16 Restoring anomaly test for 3DB A) Difference plot of the 3DB model and the starting model. B) Difference between the recovered anomaly model and the starting model. The interpretations are same as in the profile ***d*** *in figure 3.8.*

3.7 Recovering the anomalies

To check whether our inversion strategies produced consistent results and to explore the size of the anomalies introduced by the FWI, we performed synthetic inversion runs using the 2DB, 3DA and 3DB models. In these tests, we generated synthetic data using the final models and used the synthetic data as observed data in the inversion runs. The starting model was the same as used in the actual runs (Bayrakci et al 2016). The results from these when subtracted from the starting should match the anomalies recovered in the actual inversion runs 2DB, 3DA and 3DB (Figure 3.14, 3.15 and 3.16). All three tests successfully recovered most of the anomalies introduced by the FWI into the final models, indicating that the anomalies recovered in the actual inversion runs are real. However, the amplitudes of the recovered anomalies are smaller in magnitude than the actual anomalies. This discrepancy may be because of the assumed approximations for the wave equation: acoustic, isotropic, non-attenuating medium. The RMS amplitudes of the differences between the anomalies introduced by FWI and the anomalies recovered are 109 m/s, 68 m/s and 83 m/s for the 2DB, 3DA and 3DB inversions, respectively. The most common way to estimate the resolution of the final inverted model is through checkerboard tests. In our case, we did not perform checkerboard tests because introducing even small anomalies in the form of checkers resulted in

changing of the arrival times, particularly far-offset arrivals, beyond the range of our mute gates applied to the input data for the actual inversion. Instead, we added the anomalies introduced by the FWI into the starting model and recovered the anomalies by performing synthetic tests.

Analysing the recovered model anomalies for these 2D and 3D tests, we observe that FWI has consistently recovered anomalies of the same polarity above the S-reflector. However, below the S-reflector, the anomaly polarity is reversed for the 2DB inversion compared to the 3DA and 3DB inversions. The anomaly below the S becomes more prominent in the 3DB compared to the 3DA indicating stronger constraints imposed in the 3DB. The polarity reversal with 2DB demonstrates that 2DB failed to resolve the velocities below the S-reflector and converged towards a wrong minimum for the deeper parts. The reason for poor performance of 2DB below the S-reflector may be that fewer first arrivals from these regions are included in the inversion. This problem may be a more general one for performing FWI on sparsely recorded datasets. Previously, most 2D FWI studies using OBS datasets have had advantage of close spacing of the OBS and long offset recording, enabling strong constraints on the deeper part (e.g. Dessa et al., 2004; Operto et al., 2006). Jian et al. (2017) demonstrated the application of 2D elastic FWI to a sparely recorded OBS dataset to image an axial magma chamber-like structure below the Southwest Indian Ridge. In that study, data from only three OBSs were used and the spacing between the OBSs were 8 km and 16 km, which is greater than in our study. However, in spite of such sparse spacing, FWI successfully converged using data from offsets up to ~50 km. Combining the experience from this and previous studies of FWI implementation using OBS data, it can be inferred that OBS spacing is an important factor for successful application of FWI, but other factors are also important, such as shot spacing, the maximum offset with usable data and the target depth of investigation. In our case, the 3D dataset has partly mitigated the problem of data sparsity, which is evident from the differences between the 2D and 3D FWI results.

3.8 Conclusions

We have performed 3D FWI in the time domain using wide-angle data recorded using sparsely spaced OBSs on the Deep Galicia margin. We compared our results with a 2D FWI result derived using a subset of the dataset through the 3D model. Our comparison revealed:

1. Both 2D and 3D FWI applications show improved alignment of the structures with coincident multi-channel seismic reflection images, compared to the travel-time model.

2. Within the pre- and syn-rift sediments, the 2D model shows an oscillatory behaviour which is reduced in the 3D model. This observation indicates that the faulting within these sediments is 3D in nature.
3. 2D FWI imaging using sparsely spaced OBS data fails to fully recover the alignment of structures due to the complex 3D nature of the faults within the crystalline crust.
4. Poor constraints on the inverse problem due to sparse data and/or our assumed approximation of the wave equation results in circular velocity contours which are geologically unrealistic. 2D FWI images resulted in more such features than 3D, indicating that they arise mainly from the data sparseness.
5. The occurrence of lower velocities below the S-reflector correlates with overlying fault intersections at the S-reflector. The maximum degree serpentinisation that we resolved was ~45% corresponding to a velocity of ~6.5 km/s.
6. We have identified a new fault block (B7) and small peridotite ridge towards the end of the crystalline crust and before the peridotite ridge.
7. Anomaly recovery tests recovered the anomalies introduced by the FWI in both 2D and 3D. These tests highlighted that the 2D inverse problem is poorly constrained in the deeper parts of the model.

Chapter 4 Nature of the crust and upper mantle in the Deep Galicia Margin

4.1 Introduction

In this chapter, I present a 3D high-resolution seismic velocity model of the DGM derived from 3D FWI using ocean bottom seismic data (Chapter 3). Based on the velocity model, I discuss the nature of the crystalline crust and present an evidence for a lower crustal exhumation under the footwall of the normal faults. I also present a serpentinisation map below the S-reflector at a depth of 100 ms and compare the map with a previous proposed map generated by training a machine learning algorithm (Schuba et al., 2019). My interpretations are primarily focused on the crystalline crust and S-reflector as these sections are best resolved by the 3D FWI model, which at these depths shows a good match with the 3D multichannel seismic images (Chapter 3).

4.2 Data and method

Please refer to chapter 2. The map below shows the location of the ocean bottom seismometers (OBS), shots and velocity grid used for 3D-FWI (Chapter 3) along with the locations of the profiles used in this chapter.

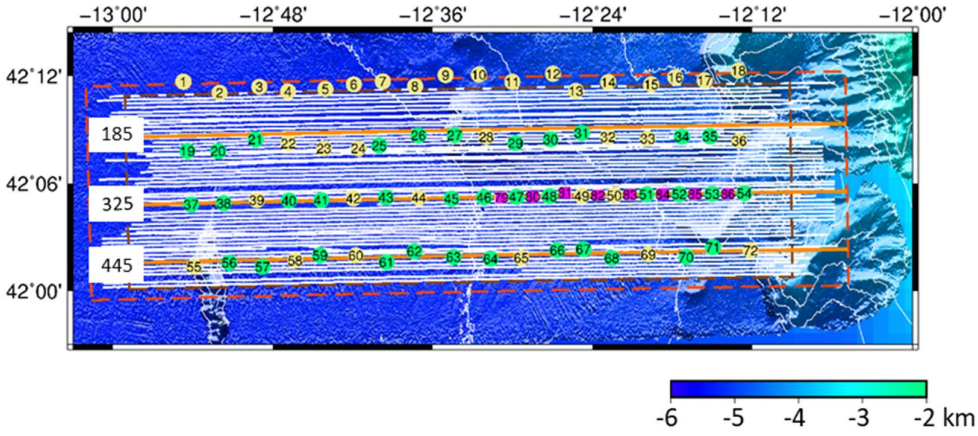

Figure 4-1 Map showing the location of the OBSs and seismic lines. Velocities along three profiles are presented in this chapter: 185, 325 and 445. The red-dashed box marks the area for the 3D FWI and the dashed brown box marks the multichannel seismic volume. The shot profiles recorded by the OBSs are shown in white lines. Green coloured instruments are used for 3D FWI, whereas the yellow ones have not been used in this work. The instruments in pink have only two shot profiles recorded directly above them and were not used in full 3D FWI.

4.3 Further analyses of the 3D FWI model

The top of the crystalline crust surface picked throughout the time-migrated multichannel seismic volume varies between ~4.3 km to 10.7 km with a broad trend of increasing depth towards west (Figure 4.2) (Lymer et al., 2019). In the central region, the depth of the top of the crystalline crust decreases at the locations of thick crystalline crust beneath (Figure 4.2). In the 3D FWI model, the velocities at the top of the crystalline crust lie between 1.5 and 5.7 km/s with a mean of 4.75 km/s and standard deviation of 0.945 km/s (Figure 4.2). The top of the crystalline crust in a few locations almost reaches the seafloor, hence the lower velocity limit is closer to the water column velocity. The velocities at the top of the crystalline crust show a similar pattern to the topography of the top of the crystalline crust, with lower velocities occurring at the locations where the top of the crystalline crust is shallow. The thickness of the crystalline crust is calculated by subtracting the depth of the top of the crystalline crust from the depth of the S-reflector. The depths of the top of the crystalline crust and the S-reflector are obtained by converting two-way-times (Lymer et al., 2019) into depths using the 3D FWI model. The thickness changes between 0 and 3.6 km with thick sections occurring at the locations of the fault blocks (Figure 4.2). The mean velocity of the crystalline crust in the FWI model is 6.01 km/s with a standard deviation of 0.44 km/s (Figure 4.2). The mean velocity of the crystalline crust tends to decrease in the regions where the thickness of the crystalline crust increases.

Velocities from the 3D FWI are presented at the S-reflector and below the S-reflector. The velocities were extracted from the velocity model using the S-reflector two-way-times picked from the 3D time migrated seismic volume by Lymer et al. (2019) and the S-surface was converted to depth using the 3D FWI (Figure 4.3). The depth of the S-reflector varies between ~7 and ~12 km with deeper reflections in the south-west and shallow reflections in the south-east and central north (Figure 4.3). Results from the anomaly restoring test along the S-reflector are presented to validate the 3D FWI derived velocities, in which synthetic dataset generated using the FWI model is used as observed data and inverted for the anomalies using the starting model derived from 3D traveltime tomography (Figure 4.4; Bayrakci et al., 2016; Chapter 3). The shapes of the anomalies are well recovered without much smearing, validating the anomalies introduced by 3D FWI (Chapter 3), but the amplitudes of the recovered anomalies are slightly lower than then actual anomalies (Figure 4.4). Further validation comes from a good match between the FWI model and multichannel seismic time slice at an average S time of 9s (Figure 4.5). The FWI model follows very well the demarcation between the crustal rocks and upper mantle rocks, indicating that the model has resolved features at this depth (Figure 4.5). There are no clear reflections observed in the mantle side of the demarcation (east), but towards the west, the velocity model shows match with the reflections from the crust (Figure 4.5). In the FWI model, the mean velocity at the S-reflector is 6.74 km/s with

a standard deviation of 0.486 km/s, which is higher than the mean velocity from the traveltime model of 6.53 km/s (Bayrakci et al., 2016). The difference between the FWI and traveltime model velocities at the S-reflector suggests that FWI has introduced finer variations at the S-reflector that match the topography of the S-reflector (Figure 4.3). The minimum and maximum velocities at the S-reflector from the 3D FWI model are 4.92 km/s and 8.2 km/s, respectively.

A map of velocities at a depth of 100ms below the S-reflector is generated by extracting velocities from the 3D FWI model. I compare this map with the velocity map generated by training a machine learning algorithm (Schuba et al., 2019; Figure 4.6). In the machine learning approach, a single 2D refraction profile was a used for full-waveform inversion studies to resolve the variations in seismic velocity within the survey area (Davy et al., 2018). Schuba et al. (2019) used these velocities from the 2D refraction profile and project them at a depth of 100 ms (~400 m) beneath the S-reflector employing an artificial neural network architecture. The inputs for the neural network were geologic and geophysical features taken from both 3D seismic reflection volume and the 2D wide-angle profile data sets (dominant frequency, and reflection amplitude of the S-reflector; the time-thickness of the major layers overlying the S-reflector; the ratios of these time-thicknesses to the total time-depth of the S-reflector; and full-waveform inversion velocities 100 ms above and 100 ms below the S-reflector). The neural network parameters were optimized to have low errors (<2% of absolute velocities). The maximum and minimum velocity predicted by the machine learning algorithm are ~9.3 km/s and ~4.3 km/s, respectively, while the FWI derived values are 8.2 km/s and ~5.3 km/s, respectively. The mean and standard deviation of the machine learning predicted velocities are higher than the FWI predicted velocities (Figure 4.6). Using the velocities, degrees of serpentinisation below the S-reflector are estimated using a linear relationship between the P-wave velocities and volume percent serpentine in peridotites (Christensen, 2004). Christensen (2004) presented the following equation:

$$S = 0.119474 * (3314 - ((v/1000) + 4.9587)/0.0039) \quad (4.1)$$

where v is P-wave velocity in m/s. and S is percent serpentinisation. This equation was based on Christensen's (2004) compilation of data for serpentinites formed at 200 MPa and 200°C. Using this equation, velocity ~4.7 km/s and 8 km/s correspond to ~100 % and ~0 % serpentinisation, respectively. I considered regions with velocities greater than 8 km/s correspond to 0 % serpentinisation. The degree of mantle serpentinisation from the 3D FWI model ranges from 0 to 84% (Figure 4.6). The average serpentinisation over the entire map area is ~34%, with a standard deviation of less than ~14% (Figure 4.6). The standard deviation of the serpentinisation values predicted by the machine learning algorithm is higher than the FWI model estimates, at ~22%. In the central northern region, the machine learning algorithm predicts high serpentinisation along

the fault intersections 5.3 and 5.4 which is not observed in the FWI estimated serpentinisation map (Figure 4.6).

I present velocities along profiles 185, 325 and 445 that are closest to the OBS locations in depth and two-way-time domains (Figure 4.1, 4.7 and 4.8). The velocity model along these profiles shows a good match with the interpretations from the 3D pre-stack time-migrated multichannel seismic volume (Lymer et al., 2019). Results from the restoring anomaly test along these profiles suggest that anomalies introduced by 3D FWI are real (Figure 4.9). However, the velocities within the sediment column are less reliable due to sparse OBS spacing, hence are not included in the discussion.

4.4 Discussion

4.4.1 Nature of the crystalline crust

I discuss the nature of the crust in the DGM based on the velocities derived from the 3D FWI and compare my results with the velocity models from other similar tectonic settings. I also present evidence for the lower crust exhumation during crustal extension that may have occurred in the DGM during the final stages of the rifting.

In the locations where the thickness of the crystalline crust is less than 2 km (thin), the velocity tends to be around 6 km/s and higher, while in the locations where the thickness is high, the velocity varies between ~4.75 km/s and the average velocity of the S-reflector (~6.7 km/s). The average velocity of the crystalline crust in the DGM is 6.01 ± 0.44 km/s, which is less than (but within error of) the global velocity average of the continental crust, including velocity models from a diverse tectonic settings, of 6.45 ± 0.21 km/s (Figure 4.2; Christensen & Mooney, 1995). However, the mean velocity is close to the global means for extended crust (6.05 ± 0.18 km/s) and rifts (6.02 ± 0.14 km/s) at 10 km depth (Christensen & Mooney, 1995). It is important to note that these global estimates do not include velocity models from hyperextended zones. Comparing to a velocity model from a similar tectonic setting, the velocity limits of the crystalline crust in the DGM agree well with the thinned continental crust in the northern part of the Southern Iberian Abyssal Plain (SIAP) where the velocity ranges between 5.0 and 6.6 km/s (Chian et al., 1999). This comparison is worthwhile because the thickness of the crystalline crust in the SIAP is in the same range (2-5 km) as in the DGM, and the northernmost line of Chian et al. (1999) is only ~170 km from the southern limit of our study area.

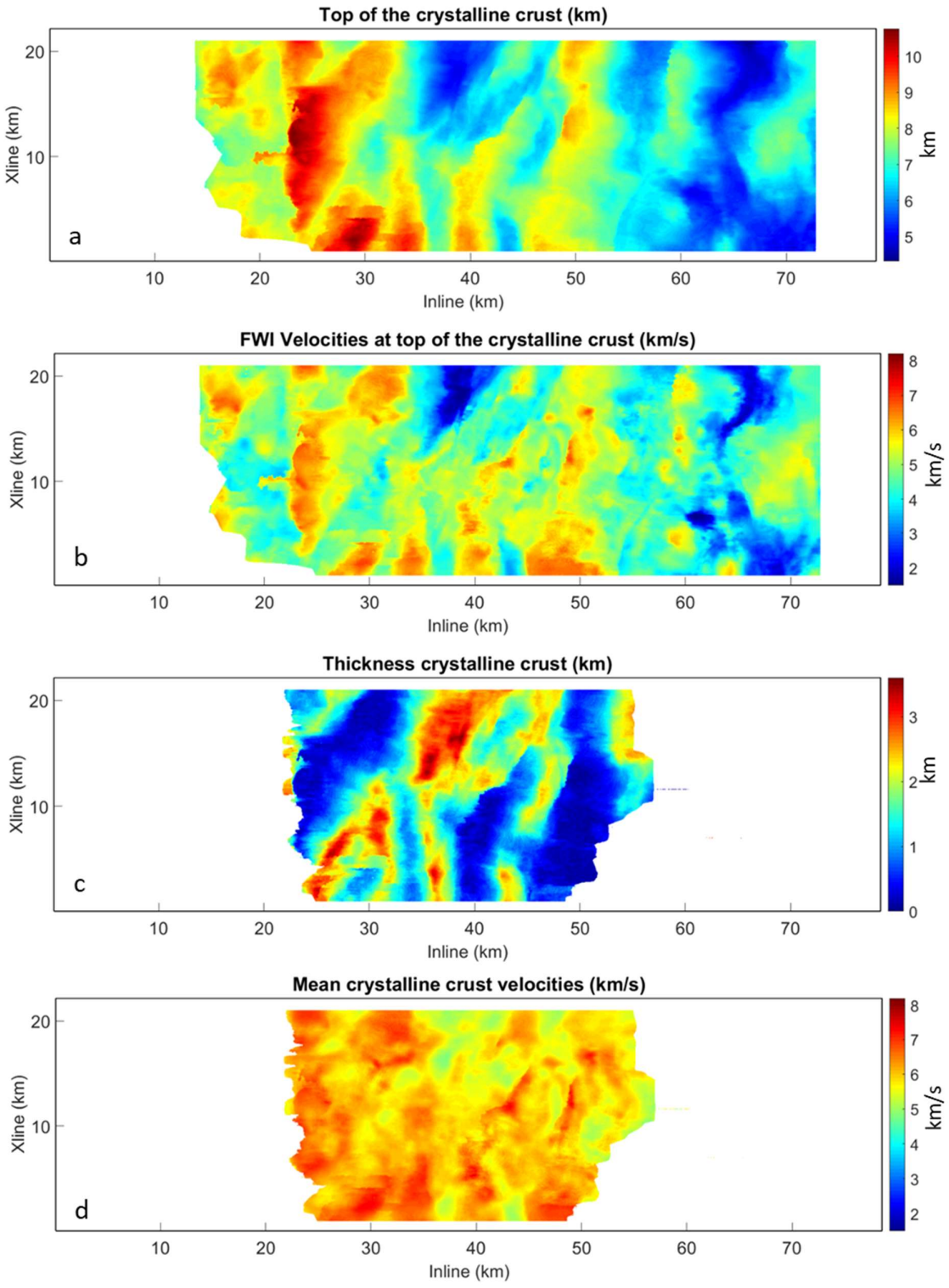

Figure 4-2 Surface of the top of the crystalline crust a) The top of the crystalline crust converted to depth using the 3D FWI model (km) b) velocities along the top of the crystalline crust from the 3D WI model (km/s) c) thickness of the crystalline crust in km d) mean velocity of the crystalline crust (km/s).

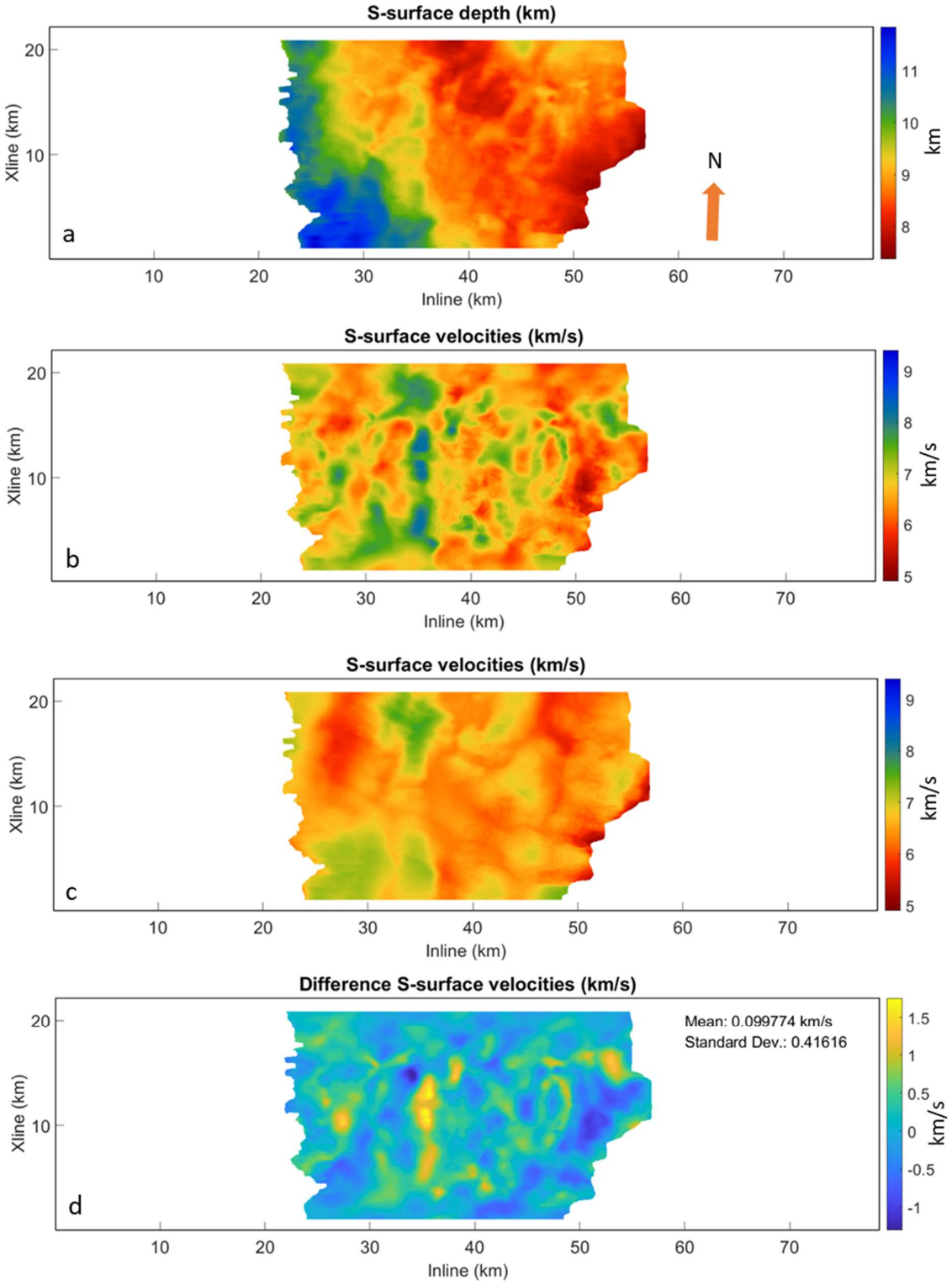

Figure 4-3 Surface of the S a) S-reflector map converted to depth (km) using the 3D FWI model b) velocities at the S-reflector from the 3D FWI model averaged over an interval of 100m across the S (km/s) c) velocities at the S-reflector from the 3D traveltime model (km/s) d) difference between the 3D FWI and traveltime model at the S-reflector (km/s).

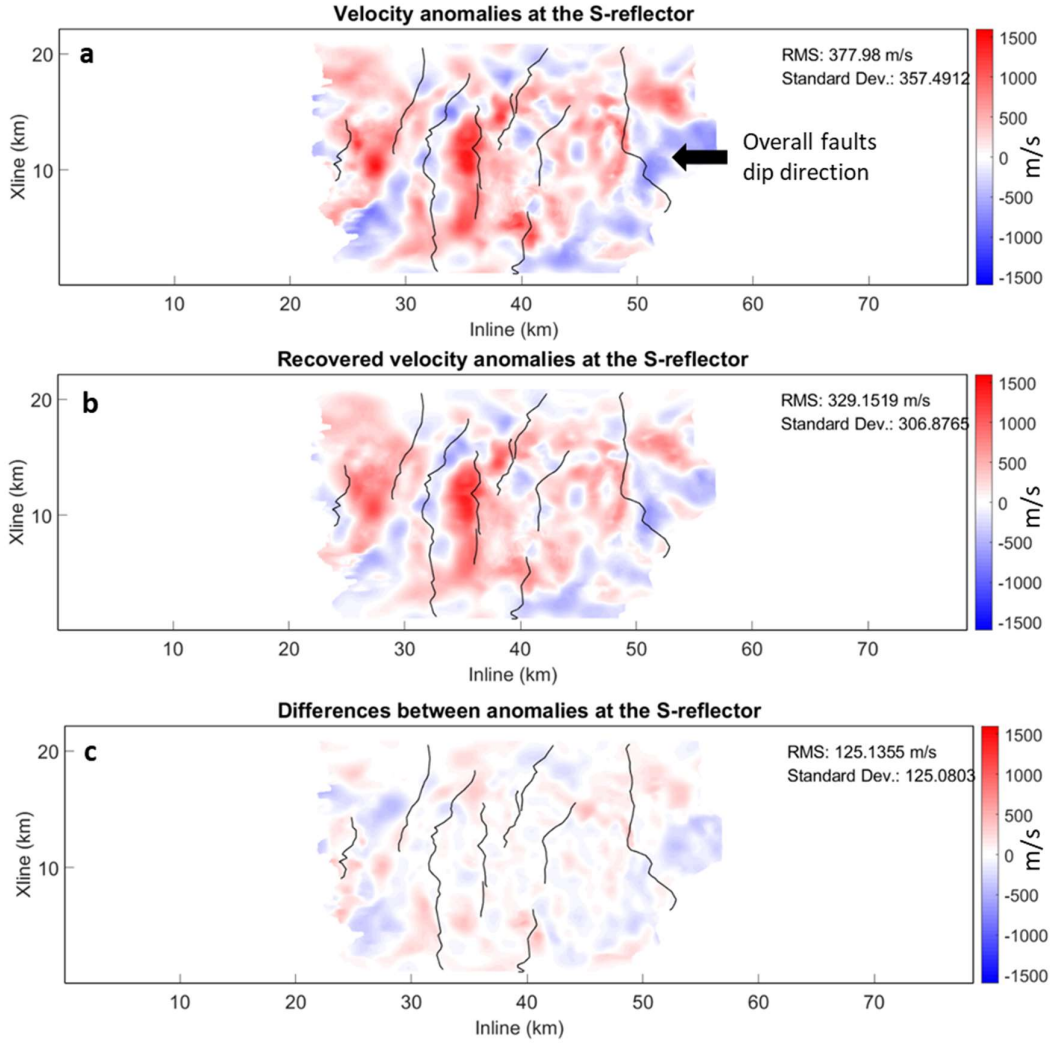

Figure 4-4 Result from restoring anomaly test at the S-reflector. a) actual anomalies introduced by the 3D FWI b) recovered anomalies c) difference between actual and recovered anomalies. The black lines are the fault intersections with the S-reflector. The black arrow shows the overall dip direction of the faults i.e. east to west.

Another interesting comparison is with the crustal velocities of the Galicia Interior Basin (GIB). GIB serves as an intermediate case between hyperextended crust further seawards (the DGM) and unextended crust landwards, providing insights into earlier stages of extension of the lithosphere. In the GIB, the crystalline crust thickness is minimum in the centre of the basin at ~7-8 km with the upper and lower crust identified as distinct layers (Pérez-Gussinyé et al., 2003). The velocity limits for the upper and lower crust obtained from wide-angle seismic data are 5.3-6.4 and 6.6-6.9 km/s, respectively (Pérez-Gussinyé et al., 2003). These limits together encompass the velocity limits of the crystalline crust in the DGM, suggesting that the crystalline crust is comprised of both the upper and lower crust rocks.

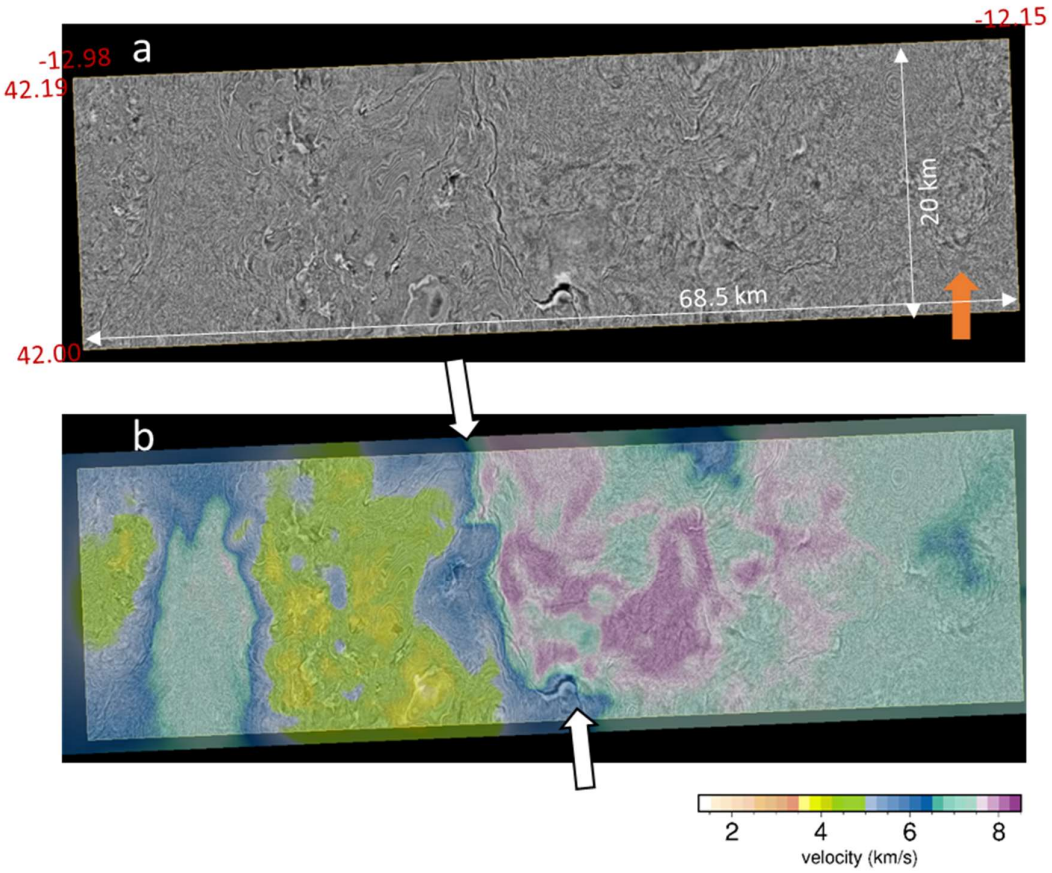

Figure 4-5 Time slice from the 3D multichannel seismic volume a) at 9 s (average time of the S-reflector) b) 3D FWI model overlaid on the time slice at 9 s. The velocity model shows a good match with the reflector at the crust-mantle boundary pointed by the white arrows. The geographic locations of the multichannel slice are indicated along with its dimensions.

It is extremely difficult to differentiate between the crustal and upper mantle rocks occurring using just compressional seismic velocities because serpentinised upper mantle rocks can show a wide-range of velocities (~5-8.3 km/s), depending on the degree of serpentinisation, practically spanning the velocity limits of crystalline crust (Christensen, 2004). Previously, based on seismic images and high-resolution velocity models, the lower regions of the crystalline crust have been interpreted as fractured and brecciated serpentinised peridotites and/or crustal rocks (Reston et al., 1996). Also, a low-velocity zone, which is not resolved in my inverted model, was inferred at the S-reflector from one-dimensional FWI result using multichannel seismic data (Leythaeuser et al., 2005). Schuba et al. (2018) identified a zone of a few tens of metres thickness above the S-reflector in the 3D multichannel seismic volume, termed it as “the S-interval”, comprising non-uniformly distributed fault rock material. Imaging of the S-interval is beyond the capability of my inversion strategy adopted for this study (Chapter 3). Hence, based on my velocity model and interpretations from

the 3D volume (Lymer et al., 2019), the velocity range of the crystalline crust in the DGM from the top of the crystalline crust to the base of the S-interval (the S-reflector) is ~4.75 – 6.7 km/s.

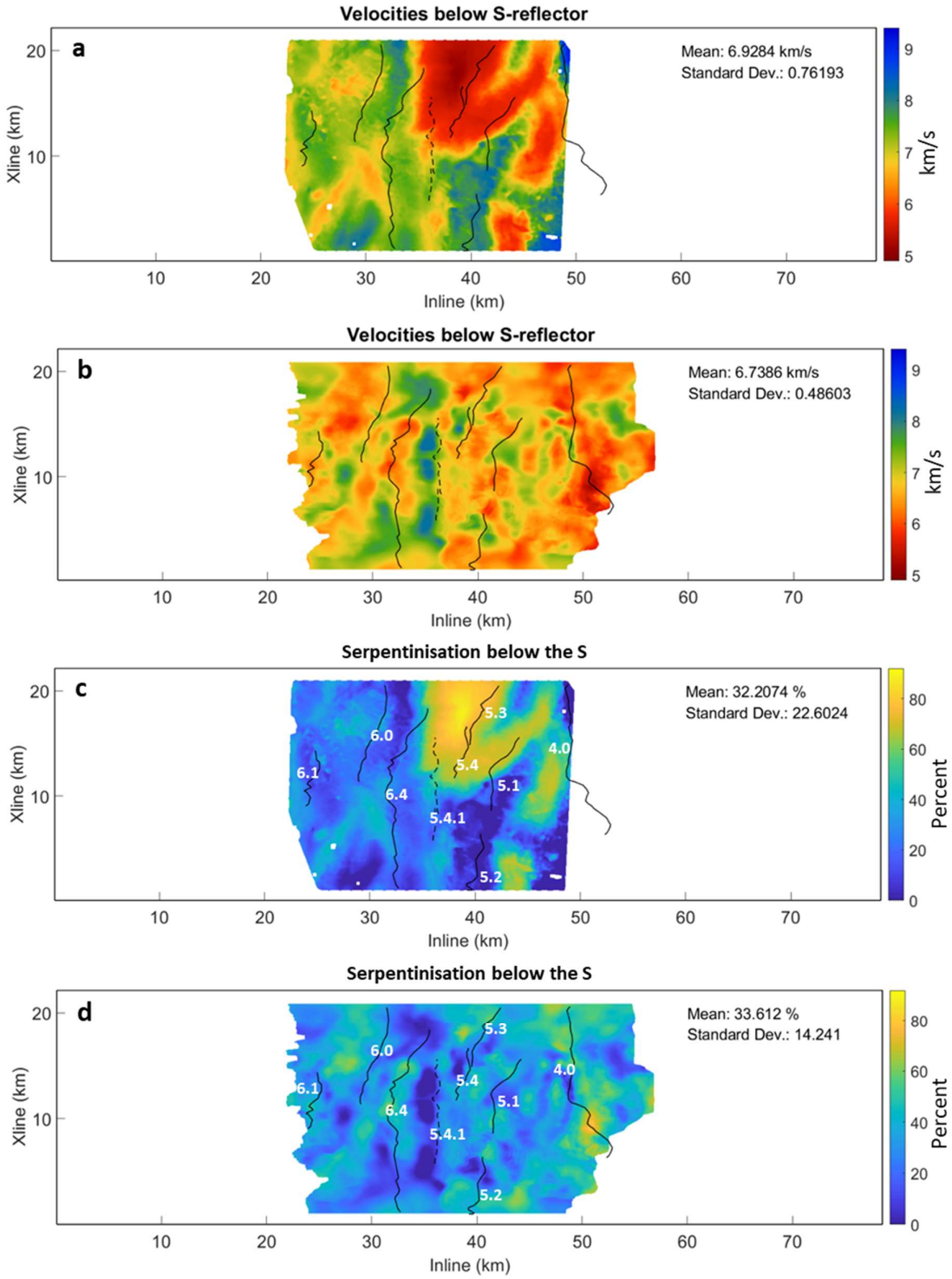

Figure 4-6 Velocities and serpentinisation below the S-reflector a) at 100 ms estimated by training a machine learning algorithm (Schuba et al., 2019) b) velocities (km/s) below the S-reflector at 100 ms from the 3D FWI model c) serpentinisation map (percentage) generated by training a machine

learning algorithm algorithm at a depth of 100 ms below the S-reflector b) serpentinisation map (percentage) derived from the 3D FWI velocities. Black lines indicate the intersections of the faults with the S-reflector and their numbers are indicated in white. Fault 5.4.1 (dashed black line) doesn't clearly cut the S-reflector.

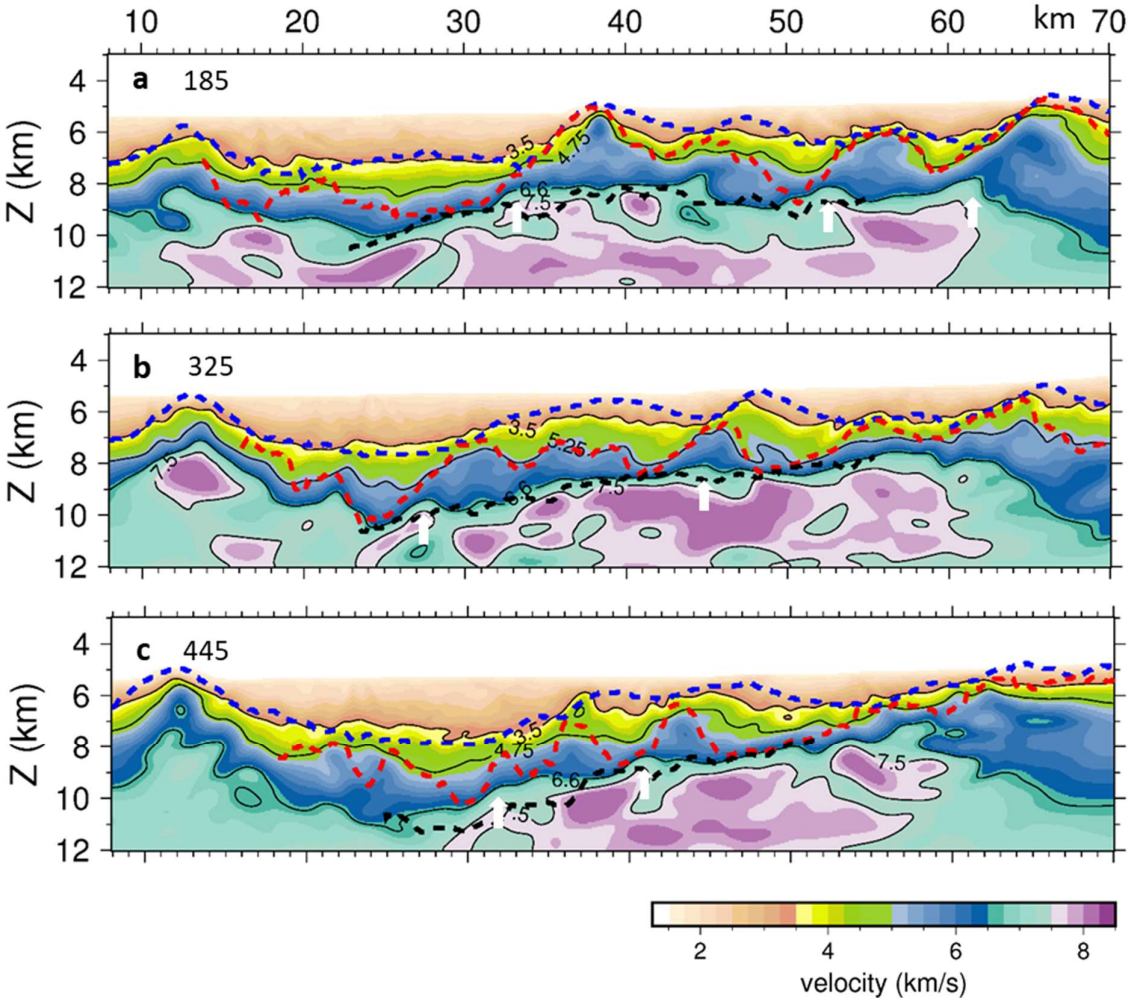

Figure 4-7 Velocity sections along profiles 185, 325 and 445 in depth with interpretations from the multichannel seismic volume overlaid. Dashed blue line indicates the top of the syn-rift sediment, dashed red line indicates the top of the crystalline crust and dashed black line indicates the S-reflector (Lymer et al., 2019). White arrows point towards the regions where the 6.6 km/s velocity contour shallows. In the profile 325, contour 5.25 km/s shows good match with the top of the crystalline crust.

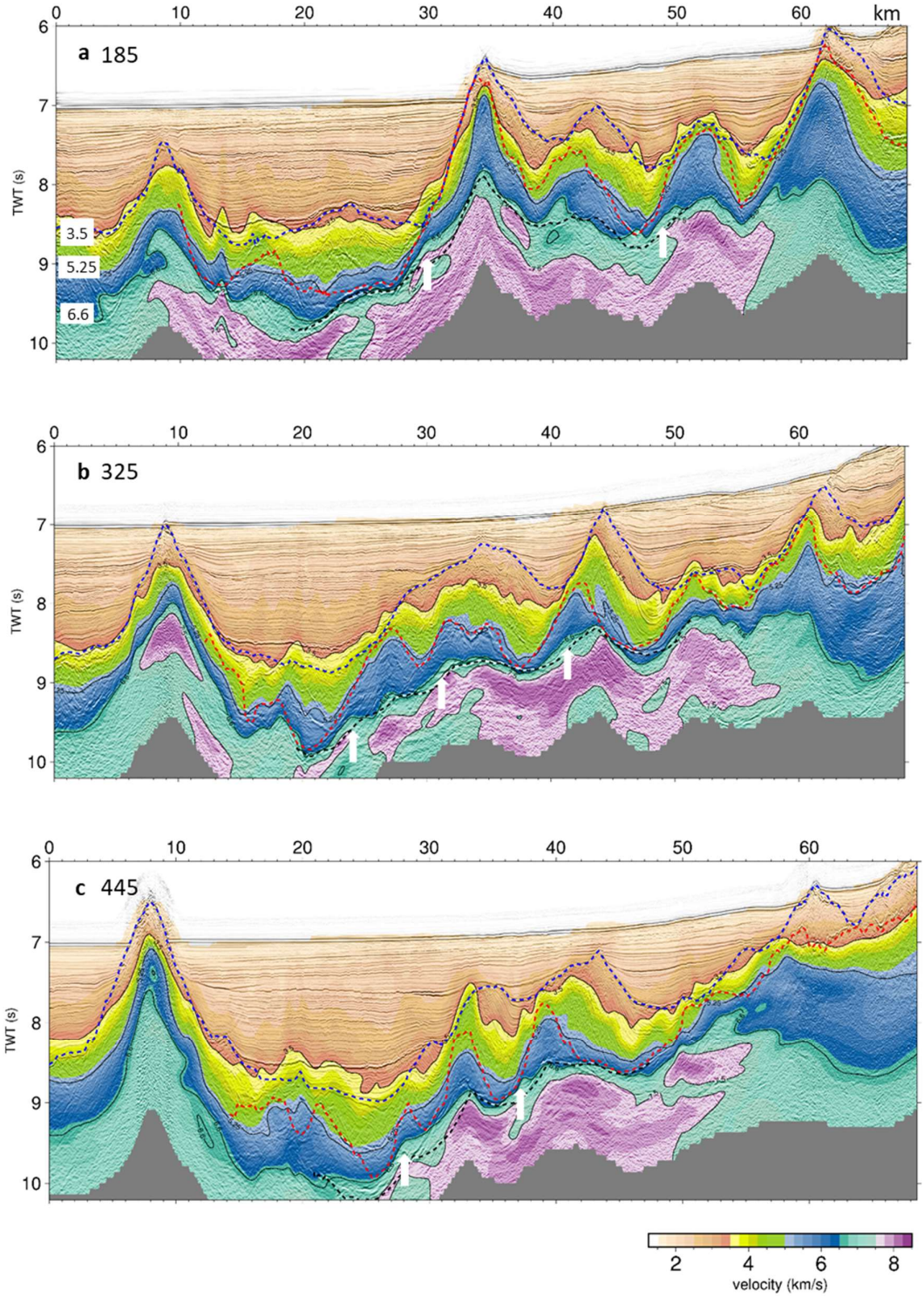

Figure 4-8 Velocity sections overlaid on 3D multichannel seismic images along profiles 185 (a), 325 (b) and 445 (c) in two-way-time (s) with interpretations. Dashed blue line indicates the top of the syn-rift sediment, dashed red line indicates the top of the crystalline crust and dashed black line

indicates the S-reflector (Lymer et al., 2019). White arrows point towards the regions where the velocity contour 6.6 km/s shallows. Same contours as figure 4.7 are plotted.

4.4.2 Two-layered model?

In a few locations along the profiles presented in this work, the crystalline crust can be divided into a higher-gradient upper part and a lower-gradient lower part (Figure 4.10). To investigate further this subdivision, velocity profiles were plotted every 1 km between 25 and 35 km along profile 325 across one fault block (Figure 4.11). Here it can be clearly observed that as the crystalline crust thickens, the velocity structure within the crystalline crust assumes two-layer model with different velocity gradients. This layering is only observed in locations where the thickness of the crystalline crust is greater than ~2 km (Figure 4.10). The upper layer has a higher velocity gradient (0.2-0.3 s^{-1}) with the velocity ranging between ~4.75 and 5.3 km/s, and the lower layer shows velocity range between ~5.3 and 6.7 km/s with a lower velocity gradient (Figure 4.11). These layers are not consistent throughout the model and their velocity ranges vary across the volume. In the following text, the upper and lower layers are referred as layer 1 and layer 2, respectively. Correlating the velocity profiles with the velocity section, it can be inferred that the layer1 at the top of the crystalline crust between 25 and 35 km (Figure 4.11). This layer is the top of the crystalline crust that has been subjected to fracturing and related mechanisms. A similar observation has also been reported at top of the basements in the GIB and the Porcupine basin with reduced velocities than crystalline crust due to fracturing and related mechanisms (Pérez-Gussinyé et al., 2003; Watremez et al., 2018). In the DGM, this layer thickens towards the centre of the fault block where the thickness of the crystalline crust is maximum (Figure 4.11), indicating that the fracturing processes were mainly active over the top of the fault blocks. Moreover, this zone correlates well with the previous interpretation using seismic images that at the top of the fault blocks the crests are flattened as a result of mass wasting or subaerial erosion during rifting (Reston et al., 2005; Reston et al., 2007). Hence, I conclude that layer 1 is the top of the crystalline crust that is subjected to fracturing and other related mechanisms. This layering observed within the crystalline crust is not an inherent layering pattern of the crystalline crust that has been preserved from the less extended crust.

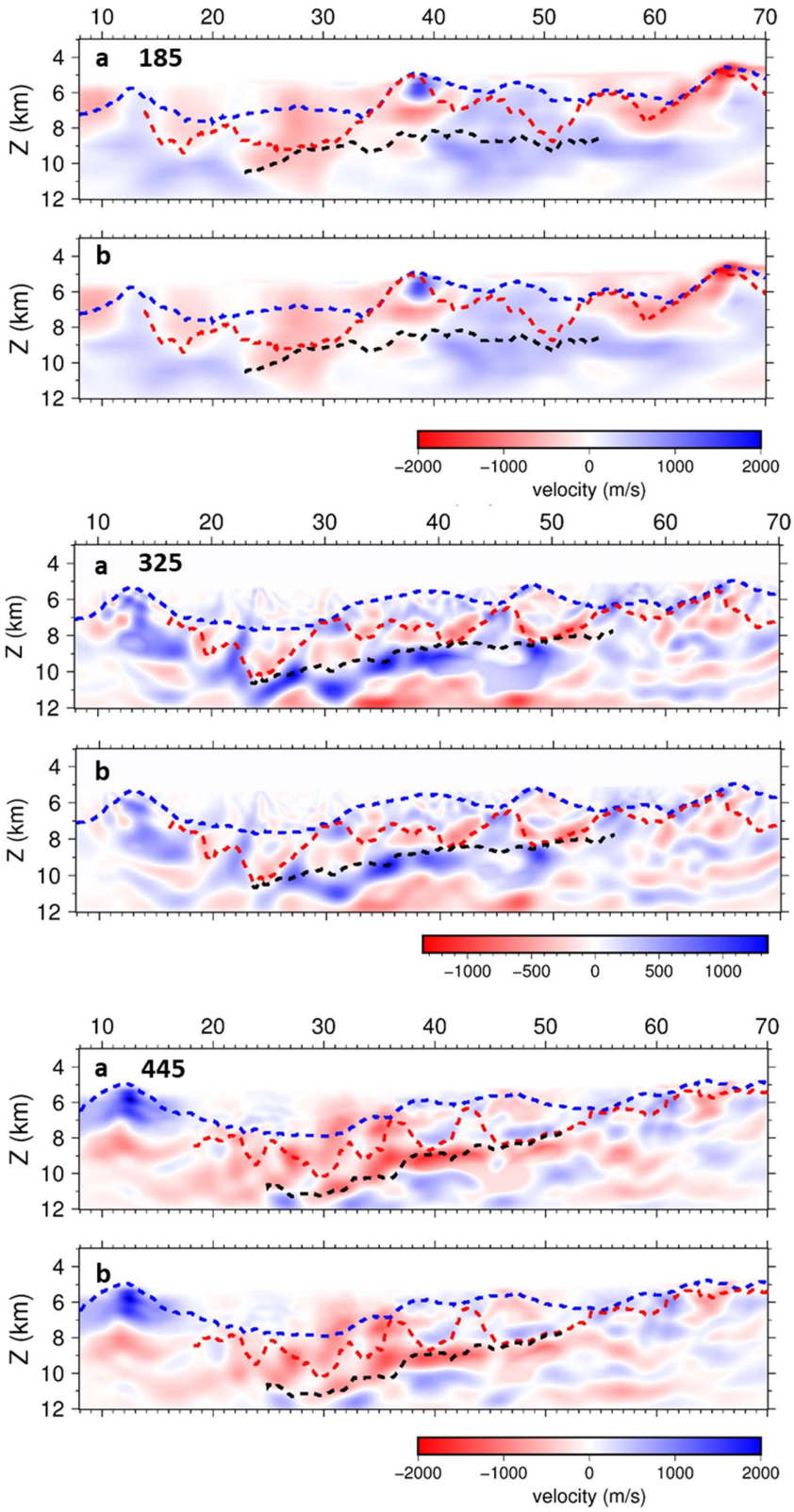

Figure 4-9 Result of the restoring anomaly test along profiles 185, 325 and 445. a) profiles are the actual anomalies b) profiles are the recovered anomalies. Colour scale for each profile are given below.

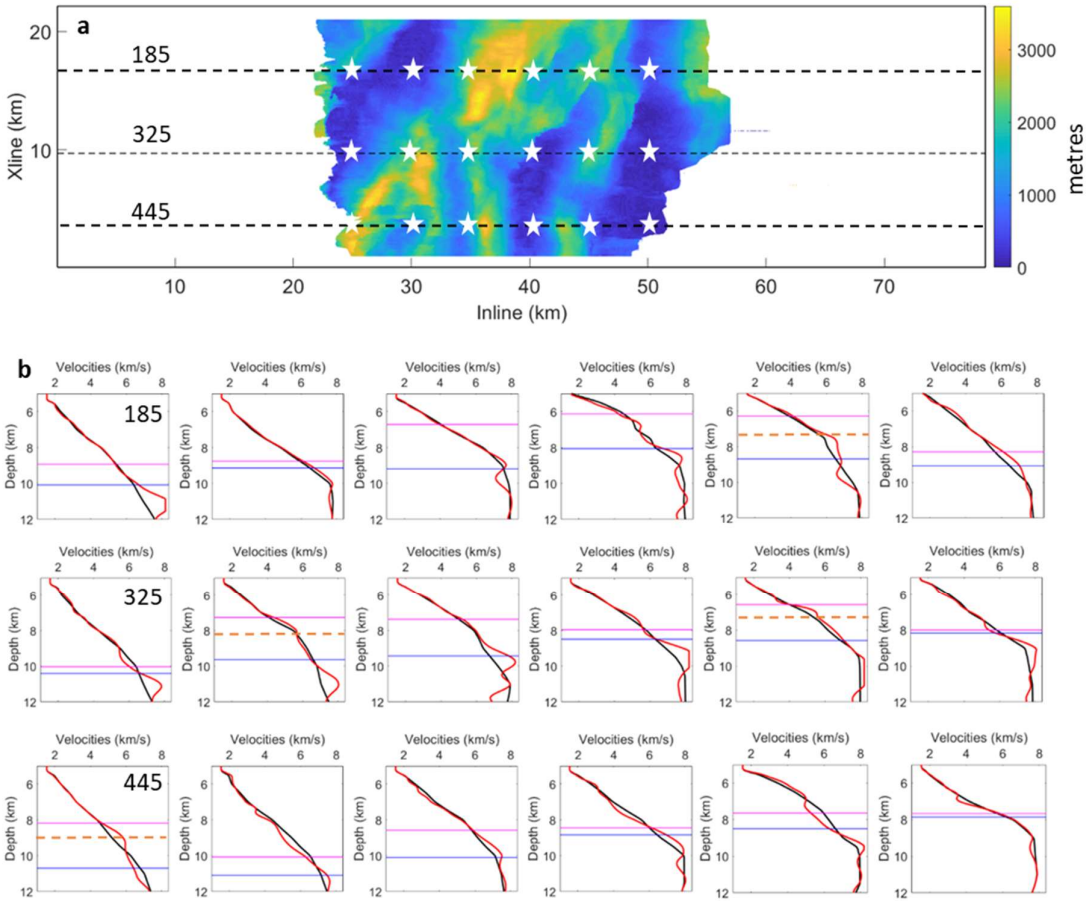

Figure 4-10 1D velocity profiles from the 3D FWI model a) Crystalline crust thickness (metres) map with white stars showing the locations of the 1D velocity profiles extracted from the 3D FWI model along profiles 185, 325 and 445 b) 1D velocity profiles from the starting (black) and 3D FWI model (red) with profile location following the same order as the order of the white stars on the profiles. Pink and violet colours in each profile mark the top of the crystalline crust and S-reflector depths, respectively. The dashed orange line indicates the boundary between two distinct layers within the crystalline crust.

4.4.3 Exhumation of the lower crust

During the late stages of rifting at magma-poor rifted margins, the upper and lower crust are tightly coupled and embrittlement of the lower crust happens progressively (Pérez-Gussinyé & Reston, 2001). Thermo-mechanical modelling predicts that the lower crust is exhumed along an "exhumation channel" under the footwall of the active normal faults and becomes brittle eventually during the extension (Brune et al., 2014). In the GIB, towards the centre of the basin, as the extension increased, it is inferred that the normal faults cutting through the brittle upper crust progressively cut into the lower crust, bringing high-velocity lower crust rocks within their footwalls to accommodate for the fault offsets (Pérez-Gussinyé et al., 2003). Interestingly, I observe evidence

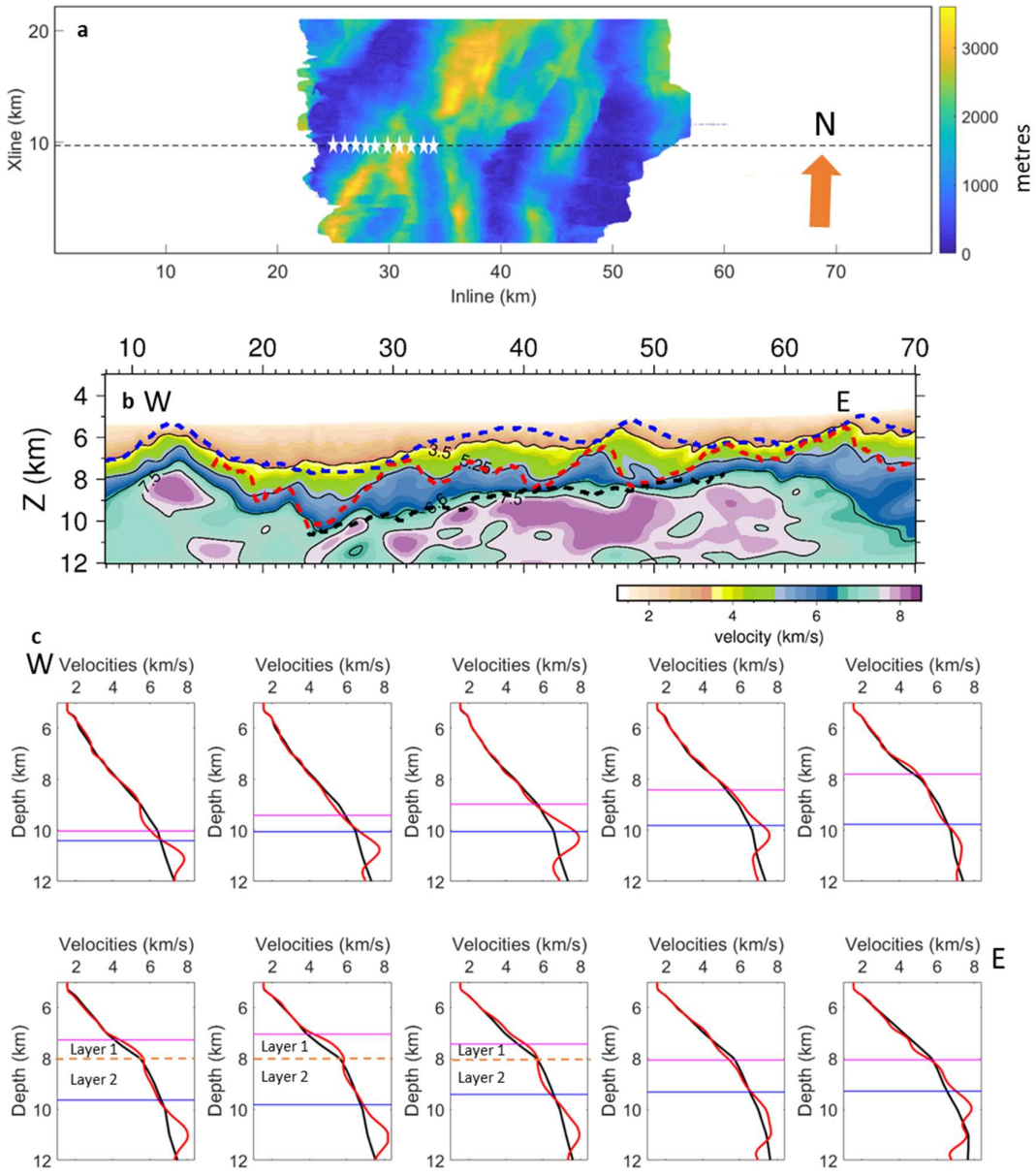

Figure 4-11 1D velocity profiles along profile 325 a) A map of the thickness of the crystalline crust with black dashed black line showing the profile 325 location; white stars indicate the locations of the 1D velocity profiles shown in (c) between 25 and 35 km (west to east) b) velocity profile 325 with interpretations as in figure 4.7 c) 1D velocity profiles from the 3D FWI model at the locations indicated by the white stars in (a), between 25 and 35 km distance in b). As the crustal thickness increases, the 1D velocity model shows two distinct layers.

for this process in the 3D FWI model of the DGM. I observe that the 6.6 km/s velocity contour, which corresponds to the top of the lower crust in the GIB, shallows under the footwall of the faults (Figure 4.7 and 4.8). Although the undulations on the 6.6 km/s contour in a few locations are small,

the actual deformation in the lower regions of the crystalline crust is over a broader thickness (Figure 4.7 and 4.8). I consider the 6.6 km/s velocity contour as a representation of lower regions of the crystalline crust to highlight the deformation. There is no evidence for the 6.6 km/s contour as the boundary between the upper and lower crust in the DGM. Assuming the crust in the DGM has undergone similar initial extension stages as in the GIB, I infer that the exhumation of the lower crust under the footwalls of the overlying fault blocks must have occurred when the lower crust was still ductile in nature, accompanied by cooling and decompression processes. In the late stages, there was no large-scale (>100 km) lower crustal flow out of the centre of the rift and the lower crustal rocks were locally displaced to accommodate for the extension (Pérez-Gussinyé et al., 2003). As the extension progressed further into the distal parts, the lower crust the beneath footwall progressively became brittle, and became coupled with the upper crust. In my velocity model, there is no clear evidence for a separate upper and lower crust within the fault blocks like in the GIB, indicating that the crust is may be coupled. Lower crustal exhumation forms a component of all the lithospheric extension mechanisms that are proposed for the final stages of rifting: the polyphase model, sequential faulting, rolling hinge model (Buck, 1988; Lymer et al., 2019; Ranero & Pérez-Gussinyé, 2010; Reston, 2005).

4.4.4 Velocities at and below the S-reflector

The velocity pattern at the S-reflector show a good correspondence with the topography of the S-surface (Figure 4.3). The deep and shallow features correlate with the high and low velocities locally, respectively (Figure 4.3). It is arguable that such a correspondence is a result of general increasing trend of velocities with depth in the subsurface. However, such a correlation is not observed on the velocity surface derived from the traveltime tomography model indicating that it is not a result of general increasing of velocities with depth (Figure 4.3). In the central region, the model shows high velocities (> 8 km/s) indicating the presence of unaltered peridotites in the central region (Figure 4.3). These high velocity locations are prone to higher uncertainty in the velocity estimation by the inversion due to significant anisotropy that can be associated with unaltered peridotites (Christensen, 2004) and my inversion strategy does not account for anisotropy (Chapter 3). In a few locations the velocity value reaches 8.2 km/s which is the maximum velocity allowed by the inversion strategy (Chapter 3). However, a validation for the presence of these high velocities comes from the anomaly restoration test indicating that the velocities derived from FWI are correct (Figure 4.4). Further, a good match between the multichannel time slice with the velocity model at an average S-reflector depth (~9 s) provides support for the velocities from the 3D FWI model (Figure 4.5).

The 3D FWI result also shows a good match with the multichannel seismic image time slice sections at a depth of 100 ms below the average S-reflector depth (Chapter 3). Based on this good match, I infer that the velocity map from the 3D FWI is more accurate than the map generated using the machine learning. The idea of training an algorithm to predict velocities over the 3D volume is an elegant approach, especially in terms of computational requirement compared to the 3D FWI problem. However, such an implementation can have a few pitfalls that are difficult to address. I suspect that the observed differences between the two maps are primarily due to the input features used for training the algorithm and limitations of the machine learning method (Schuba et al., 2019). In the chapter 3, I demonstrated that the 2D FWI result, which was used to train the machine learning, did not fully resolve the velocities below the S. Hence, using it as an input feature into the machine learning has resulted in an inaccurate velocity map below the S. Additional issues are limited data availability along the 2D line and the probable presence of wider lithological variations across the whole 3D volume that could not be modelled by the machine learning accurately (Schuba et al., 2019).

4.4.5 Serpentinisation map of the DGM

In the serpentinisation map, the regions with higher percentage of serpentinisation correspond to lower velocities in the velocity map below the S-reflector and vice-versa (Figure 4.3). The map generated by machine learning shows a match between the orientation of the crustal blocks and the alignment of the serpentinised areas (Schuba et al., 2019). Although I observe an overall alignment between the fault intersections and serpentinised areas in the FWI serpentinisation map, it is less evident compared to the machine learning map. I infer that the machine learning predictions could be biased by features from the 3D multichannel seismic data used for training the algorithm (Figure 4.2 and 4.3).

The fault intersections show an overall alignment with the eastern edges of the serpentinised areas which agrees well with the interpretation that the crustal faults acted as conduits for sea water infiltration to the mantle (Bayrakci et al., 2016; Pérez-Gussinyé & Reston, 2001). To further investigate the variation in the serpentinisation across the fault intersections, I plotted mean serpentinisation under the footwall, at the fault intersection and under the hanging wall for each fault intersection over a length of ~2km along the arbitrary lines (Figure 4.13) plotted in the direction of the corrugations (Figure 4.12; Lymer et al., 2019). All fault intersections except 5.4 show that the serpentinisation values observed below the hanging wall and at the fault intersections are higher than beneath the footwall of the fault blocks (Figure 4.12).

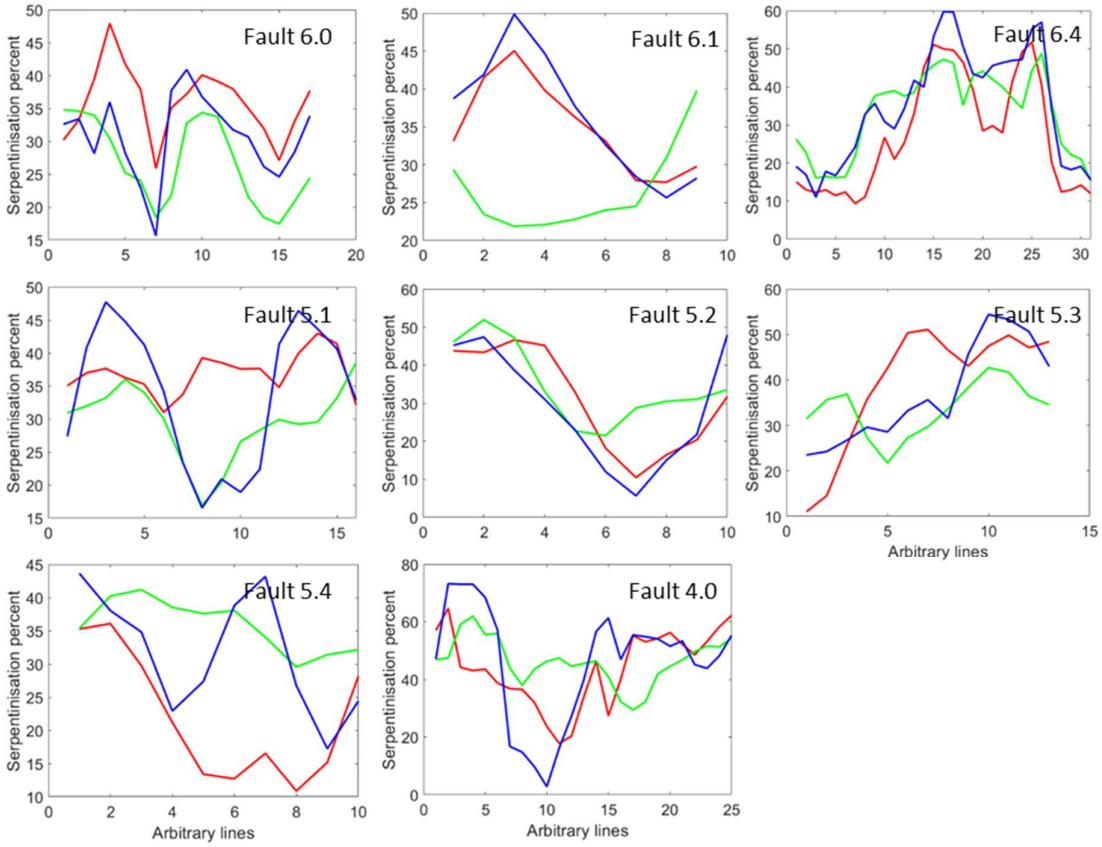

Figure 4-12 Serpentinisation estimation averaged over a length of ~1 km along the arbitrary lines from the point of fault intersection (blue) in the hanging wall (red) and foot wall (green) directions for each fault intersection. The x-axis represents number of arbitrary lines intersected by fault intersections from south to north.

At fault intersection 5.4, low serpentinisation occurs towards the hanging wall side indicating less infiltration of sea water occurred along this fault. Across fault intersection 6.4, serpentinisation estimates do not change significantly from the footwall side to the hanging wall side, indicating nearly constant water supply occurred along the fault during the hydration process. In the central region, fault intersection 5.4.1 aligned on the eastern edge of the unaltered peridotites (Figure 4.6) suggests that no water reached the mantle along the fault. Moreover, fault 5.4.1 does not show clear reflections reaching the S-reflector on the vertical sections of the 3D seismic volume, e.g., between 30 and 40 km along profile 325 (Figure 4.8). Apart from the water infiltration factor along the faults, several other factors may have also contributed in the serpentinisation process out of which the most important are the temperature, porosity and permeability of the medium (Bayrakci et al., 2016; Emmanuel & Berkowitz, 2006; Macdonald & Fyfe, 1985; Schuba et al., 2019). The changes in serpentinisation along the fault intersections may be explained by variations in these factors.

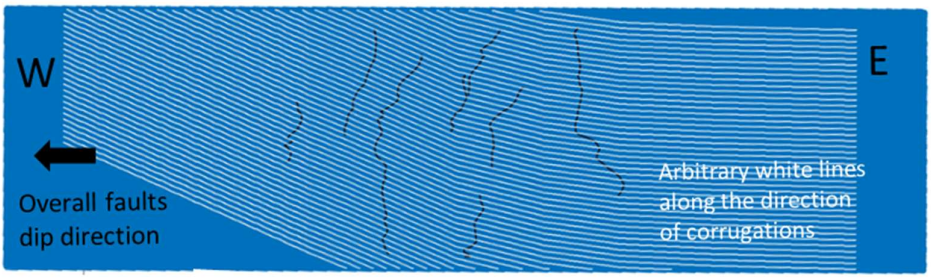

Figure 4-13 Arbitrary lines (white) plotted over the 3D FWI velocity grid (blue) along with the fault intersections in black. The arbitrary lines are drawn in the direction of the corrugations identified in the 3D time-migrated seismic volume (Lymer et al., 2019).

The pattern of serpentinisation shows a correlation with the topography of the S-reflector with deeper features showing lower serpentinisation locally (Figure 4.6). This correlation suggests that the serpentinisation process has affected the topography of the S-surface. One of the factors that may have resulted in these localized high and low relief features on the S-reflector is the change in the volume of the peridotites due to hydration (Graham, 1917), especially given the heterogeneous serpentinisation pattern (Figure 4.6). Serpentinisation of the peridotites can increase the volume of the rocks by ~40 %, and such a large increase could result in changes in the structure of a bounding surface (Germanovich et al., 2012; Lister, 1974). Regional tectonic activity may have also contributed in the formation of these relief features, however considering a good match between the S-surface topography and serpentinisation pattern, I believe serpentinisation process has been a major controlling factor. Schuba et al. (2019) reported this observation using the serpentinisation map generated using machine learning. However, their map shows a match that is limited to broader regions while on the 3D FWI map the relief features can be identified very easily (Figure 4.6). Based on my result, I infer that the serpentinisation process played an important role in the topography of the S-reflector in the DGM. However, to better understand the role of serpentinisation process in controlling the topography of the S-reflector requires quantification of the serpentinisation over a broader zone below the S starting from the S-reflector to completely unaltered peridotites in the mantle. The velocities in the FWI model are reliable to a two-way-time of ~10 s, beyond which no crustal reflections are available to validate the model. At this depth, the velocities corresponding to the upper mantle rocks are less than ~8 km/s in a few regions indicating that the rocks have undergone serpentinisation (Figure 4.14). Hence, it is not possible with my model to completely quantify the serpentinisation below the S-reflector.

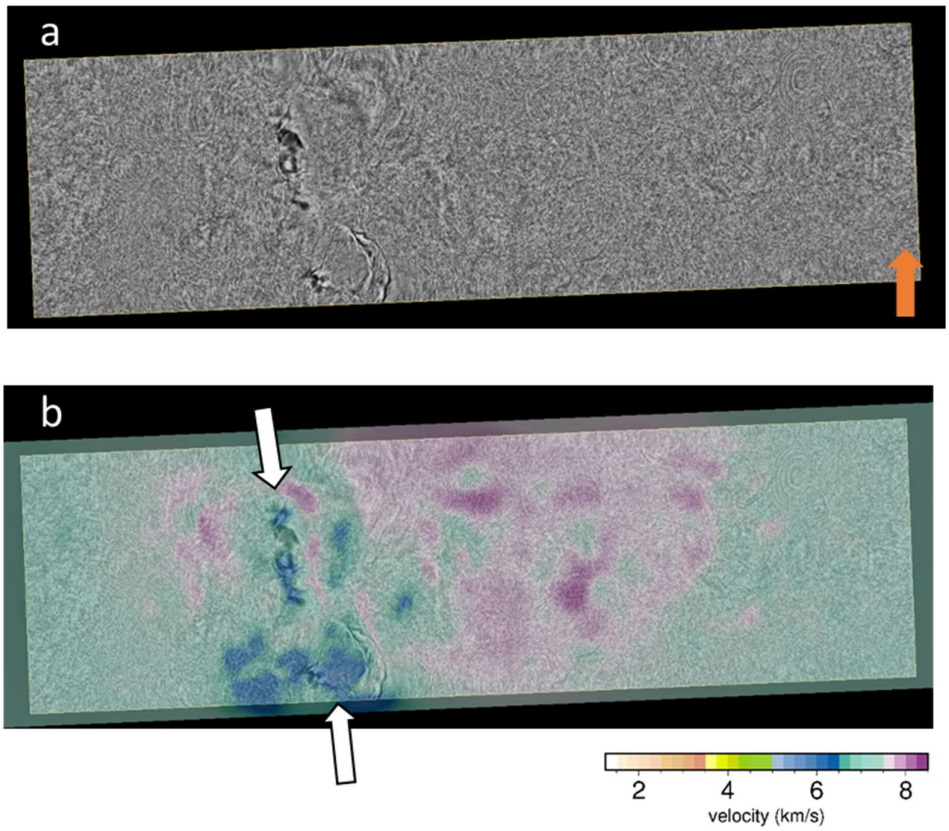

Figure 4-14 Time slice from the 3D multichannel seismic volume a) at 10 s two-way-time b) velocity model overlaid on the time slice with white arrows pointing towards crustal reflections. Velocities below 8 km/s correspond to serpentinised mantle rocks.

4.5 Conclusions

In this chapter, I present the 3D FWI model along three profiles 185, 325 and 445 oriented in the East-West direction and discuss the nature of the crust and exhumation of the LC during the extension. I also present the velocities at the top of the crystalline crust, the S-reflector and below the S-reflector at 100 ms depth. Based on my results, I conclude the following:

1. The mean velocity of the crystalline crust in the DGM (~ 6 km/s) matches closely with global averages for extended continental crust at a depth of 10 km. The velocities in the crystalline crust vary between ~4.75 and 6.7 km/s matching closely with the velocity limits of the crystalline crust in the SIAP and GIB. Within the crystalline crust, no evidence for the upper crust and lower crust as distinct layers is observed using the P-wave velocities.
2. At the top of the crystalline crust a layer with high velocity gradient is identified on the velocity profiles in the locations where the crystalline crust thickness is greater than 2 km

indicating fracturing and related mechanisms were operative at the top of the crystalline crust.

3. The velocity contour 6.6 km/s shallows under the footwall of the faults suggesting exhumation of the lower crust under the footwall of the normal faults to accommodate motion along the normal faults during the extension.
4. A map of velocities at a depth of 100 ms below the S-reflector is generated from the 3D FWI model and compared with a map generated by training a machine learning algorithm. The 3D FWI map shows a better match with the S-reflector topography in depth than the machine learning generated map with local high and low velocities corresponding to local low and high relief features on the surface.
5. The distribution of serpentinisation below the S-reflector is very heterogeneous and does not match well the serpentinisation pattern obtained by training a machine learning algorithm. A correlation between the local high and low relief features with the local high and low serpentinisation suggests that serpentinisation plays a major role in the topography of the S-reflector surface by causing volume changes in the peridotites during the hydration process.

Chapter 5 Mirror imaging in two-dimensions using the first-order multiple

5.1 Introduction

Wide-angle seismic data in marine environments is commonly acquired using ocean bottom seismometers (OBSs) or ocean bottom cables deployed on the seafloor. Generally, travel-time information of the wide-angle data from OBSs is used to develop smooth velocity models of the subsurface (e.g. Korenaga et al., 2000; Zelt & Smith, 1992). OBS data acquisition has several advantages over conventional near-surface recording: for example, OBS data are less affected by water column disturbances, enable wide-azimuth and long-offset recording, and four-component recording including shear waves. However, OBS data acquisition has its own share of practical difficulties, such as sparse spacing owing to high cost of acquisition, and the possibility of poor coupling with the seafloor. Large OBS spacing has barred the usage of OBS data for imaging due to poor illumination of the subsurface using migration algorithms for primary waves. This problem can be exaggerated in the case of a missing OBS or recording failure by an OBS in the survey. To overcome this problem, first-order multiples in the OBS data can be used for imaging, which traverse extra paths in the water column and have wider illumination compared to the primaries (Dash et al., 2009; Godfrey et al., 1998; Reiter et al., 1991; Ronen et al., 2005).

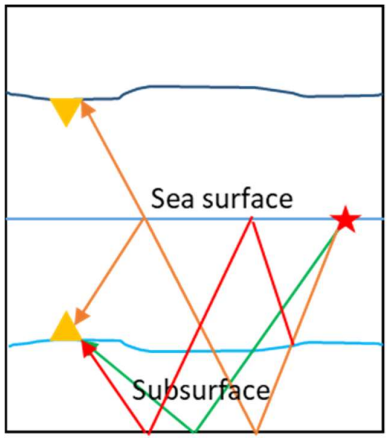

Figure 5-1 Depiction of ray paths for primary reflection (green), receiver-side first-order multiple (orange) and source-side first-order multiple (red). The seafloor (light blue) is mirror imaged (dark blue) with respect to sea-surface. The yellow triangle and red star represent OBS and shot location, respectively. Inverted yellow triangle is the mirror image of the OBS sitting on the seafloor.

Traditionally, multiples in the seismic data are considered as noise and are eliminated in the processing of the data. However, in deep water seismic data, water column multiple reflections are coherent signals separated from the primary reflections. These reflections contain valuable information as they originate from the same source as primaries but follow different paths. These multiples can be used for migration by assuming the signal is recorded on a sea surface twice as high as the seafloor depth. This simple assumption, with sources at the actual sea surface, allows for accommodation of the first-order multiples in to a migration algorithm just as primary signals. This technique of using first-order multiples to generate a seismic image is called mirror imaging (Dash et al., 2009; Godfrey et al., 1998; Grion et al., 2007; Ronen et al., 2005). In an ocean bottom seismic recording, there are two types of first-order water column multiples that are recorded in seismic surveys: one which approaches OBS from below the seafloor called “source multiple”; another is a reflection from the free surface above the receiver, called “receiver multiple” (Figure 5.1). These two multiples have slightly different arrival times which may require some processing to separate them. However, in deep water OBS data, the receiver multiples are the dominant reflections with significantly higher amplitudes, at least in the settings where the impedance contrast at the seabed is low, and wider lateral coverage of the medium than the source multiples (Reiter et al., 1991). If properly modelled, downgoing multiples can generate a qualitative image of the subsurface (Dash et al., 2009; Godfrey et al., 1998; Ronen et al., 2005). However, the resolution of the imaging will also depend on the signal strength and accuracy of the velocity model used for the migration.

In this chapter, I present seismic images of the DGM generated by applying mirror imaging to the OBS data acquired in the deep-water environment (seafloor depth ~5,000 m) of the DGM. I compare these images with the images from the coincident three-dimensional (3D) seismic volume and highlight the differences between them. Previous authors have successfully imaged receiver multiples recorded by ocean bottom hydrophones (Godfrey et al., 1998), vertical seismic profile (Jiang et al., 2005) and OBS (Dash et al., 2009; Ronen et al., 2005). All of the mirror imaging applications were applied to data that shallow depths of investigations primarily for hydrocarbon exploration and were limited to basement depths. In this case, I attempted to apply mirror imaging for the first time to a crustal scale problem to assess its performance compared to the conventional multichannel seismic imaging.

5.2 Seismic data

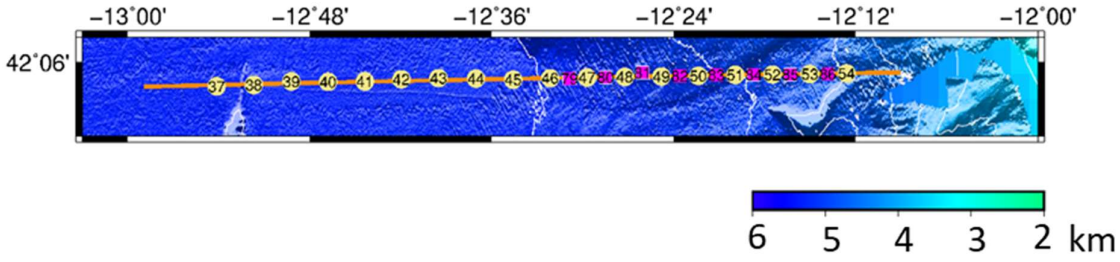

Figure 5-2 Map showing OBS locations used for 2D mirror imaging, and bathymetry within the Galicia-3D experiment (G3D). The location of the multichannel seismic line 420 is shown in orange. Stations in pink are the high-resolution OBSs. The OBSs which were not used for mirror imaging are 39, 44, 49, 50, 83, 84.

Please refer to chapter 2 in this thesis about the survey details. For mirror imaging, only data recorded by OBSs along the seismic line 420 are used (Figure 5.2). The dense shot spacing, the long shot profile lengths and adequate OBS spacing enabling continuous sampling of the subsurface laterally, combined with the seafloor depth of ~ 5,000 km allowing the multiples to cover large distances makes this dataset very suitable for performing mirror imaging.

5.3 Processing and results

I performed two-dimensional (2D) mirror imaging using data from a few OBSs using velocities derived from traveltime tomography (Bayrakci et al., 2016). Only data recorded by hydrophones were used for mirror imaging. Prior to using the data for imaging, a few quality control checks and preprocessing was done: checking for time shifts by applying moveout corrections to the direct arrivals using a constant water velocity of 1520 m/s; applying a random noise attenuation filter with an operator width of 7 traces, time window 100 ms and prediction window 28 traces (Abma & Claerbout, 1995); a low cut butterworth filter was applied with cutoff frequency 4 Hz and cutoff slope 6 db/octave. Mirror imaging was performed in both time and depth domains using the pre-stack data in 2D (Figure 5.3 and 5.4). The algorithms used for migration were the Kirchhoff time and depth algorithms with maximum offsets of 6500 m. Two shooting profiles which are closest to the OBS locations were used and projected onto an imaging line of the 3D reflection volume which is closest to the OBS locations for comparison. The post-migration processing, for time and depth sections, included applying zero phase frequency filters with low cut at 8 Hz and 3 Hz, respectively, and cut off slopes 18 db/octave and 3 db/octave, respectively. The mirror imaging is able to

illuminate features well up to ~8 km deep below the sea surface. Migration of the primary reflections from the OBSs was also carried out (Figure 5.5).

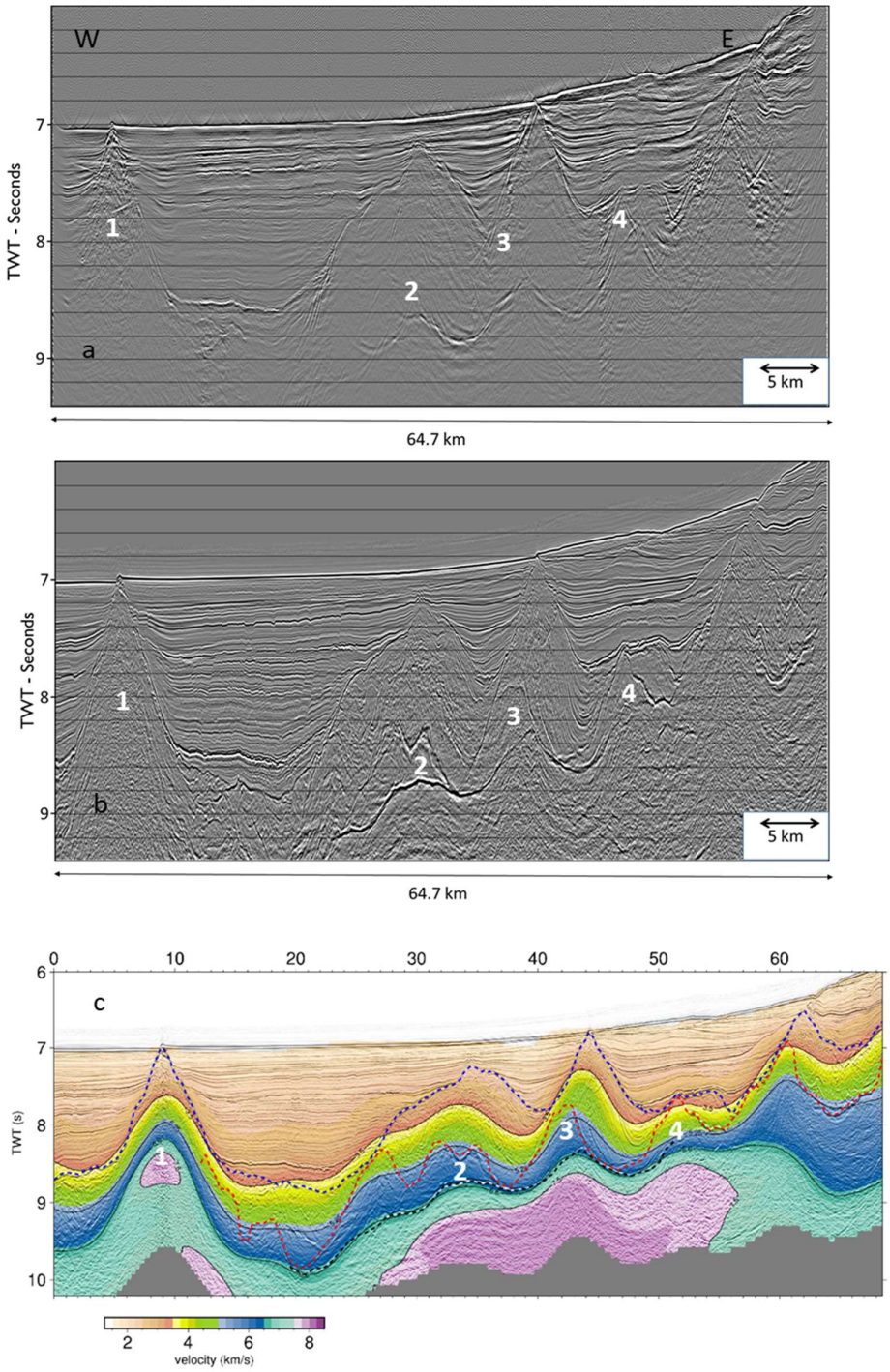

Figure 5-3 Mirror image in time a) Seismic image of the seismic line 420 from mirror imaging using the first-order multiples from the OBS data after application of gain (multiplying the trace amplitude by a scalar value, 35) b) seismic line 420 from the 3D seismic reflection volume with numbers indicating the corresponding features in the velocity model in (c). c) 3D traveltime model along the seismic line 420 overlaid on the seismic line 420 with the interpretation from Lymer et al. (2019).

The dashed blue, red and black lines correspond to the top of the syn-rift sediments, top of the crystalline crust and S-reflector, respectively. The horizontal and vertical scales are different for c) hence, same features are assigned numbers in a, b & c as 1, 2, 3 and 4.

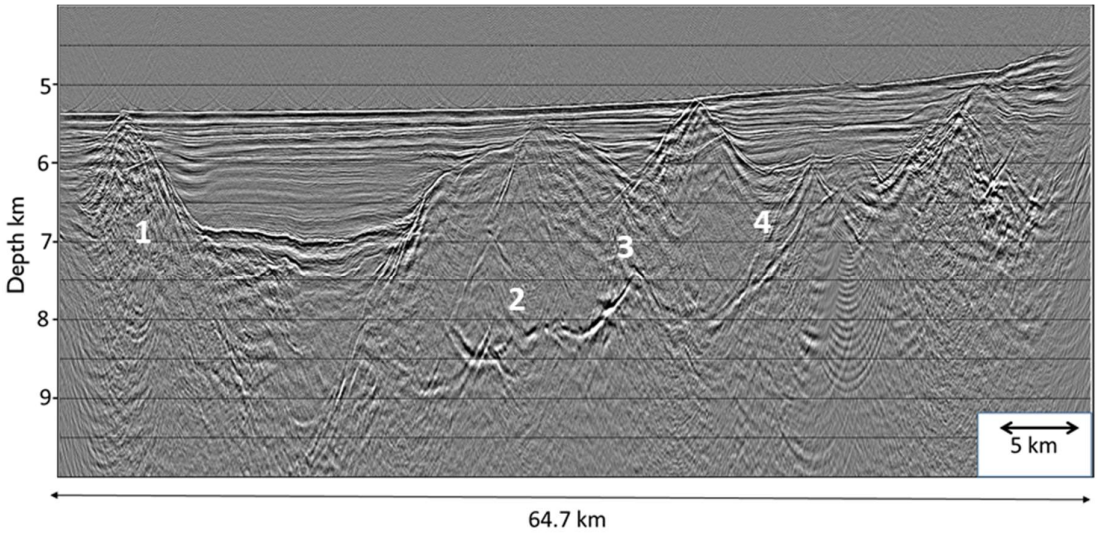

Figure 5-4 2D mirror image section using the Kirchhoff pre-stack depth migration algorithm along seismic line 420. The numbers correspond to the same regions as marked on the time sections in figure 5.3.

5.4 Discussion

Mirror imaging has imaged structures that show a match with the multichannel seismic images from the 3D volume (Figure 5.3). However, the mirror imaged section lacks in the resolution observed on the multichannel seismic images. The mirror imaging has imaged shallow targets up to ~8 s TWT well compared to the deeper sections partly due to attenuation of the multiples reflected from deeper regions. Although the deeper regions of the post-rift sedimentary column do not show clear reflections, the top of the basement reflector is clearly imaged across the complete section indicating that for a reflector to be imaged in mirror imaging sufficient impedance contrast is required across the boundary (Figure 5.3). From within the basement, there is no significant seismic energy reflected in the form of first-order multiples (Figure 5.3). The crystalline crustal reflections are completely absent in the mirror imaged sections, both in time and depth (Figure 5.3 and 5.4), and the S-reflector is imaged discontinuously with the reflector becoming weaker towards west. Based on these observations, it can be inferred that the performance of mirror imaging has drastically reduced below the basement due to weak signal strength of the multiples.

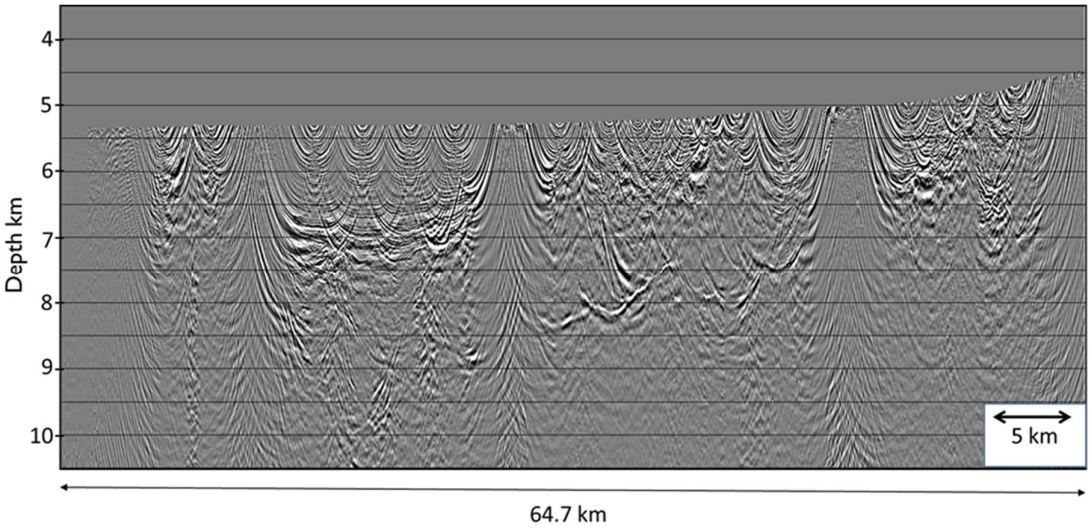

Figure 5-5 2D depth migration of the primary reflections from the OBS. Narrow illumination of the subsurface by the primary reflections results in a laterally discontinuous image.

Depth migration is more sensitive to the errors in the velocity model which can be observed on the depth section showing more noise compared to the time section (Figure 5.3 and 5.4). Also, the bubble effect is prominent in the depth section (Figure 5.4). The migrated image of the primary reflections from OBS even failed to image the seafloor and reflectors from the sedimentary column below it. Compared to the image using the primary reflections from the OBS data, mirror imaging of the multiples have better imaged the structures in the subsurface (Figure 5.5). The main reason for improved imaging of mirror imaging over the migration of the primary reflections is the wider illumination of the receiver multiples (Dash et al., 2009; Grion et al., 2007; Ronen et al., 2005). The receiver multiples bounce off from the same reflectors as the primaries but at a farther distance away from the receiver covering the medium laterally better than the primary reflections (Figure 5.1). Wider illumination of the first-order multiples comes at an expense of reduced fold. However, the illumination fold is sufficient to generate good quality images making mirror imaging computationally less demanding technique for 3D seismic imaging compared to the 3D multichannel seismic imaging. In addition, the receiver multiples are less susceptible to velocity variations just below the seabed. The location of the OBS on the seafloor causes scattering, amplitude variations, and seafloor-associated statics in the primary reflections, whereas the multiples travel through the water twice after going through the seabed anomalies. The longer travel through the water results in less seabed-associated statics than for ocean-bottom and surface recorded data (Grion et al., 2007). Another reason for better imaging using the multiples over the primary reflections is their close to vertical traverse paths, having reduced propagation angles making them more suitable for migration application. Despite having these advantages, mirror imaging is not yet a standard processing technique mainly because of the weak signal

strength of the multiples limiting the imaging to only shallow targets. However, in studies where there is no multichannel seismic data available, mirror imaging can be a useful tool to generate qualitative subsurface image using only OBS data.

5.5 Conclusions

In this study, I applied mirror imaging technique to the first-order multiples from the OBS data to develop seismic images of the DGM in 2D. The images compare well with the multichannel images, except that the signal strength is weak. Mirror imaging has imaged the prominent reflectors with strong impedance contrast, like the seafloor, top of the basement and S-reflector. However, the images lack details about syn- and pre-rift packages and crystalline crust, which is due to weak signal strength and lower impedance contrast within these sections compared to the prominent reflections.

Chapter 6 Conclusions and future work

6.1 Conclusions

The Galician margin is one of the most studied magma-poor passive margins in the world. With relatively low sediment thicknesses, and the absence of known igneous bodies and salt layers indicates that high-resolution seismic imaging is possible. Previous seismic imaging studies have revealed the presence of syn- and pre-rift sedimentary packages, the presence of tilted fault blocks of continental crust at least partially underlain by the S-reflector, corrugations along the direction of extension, the 'S-interval' above the S and preferential serpentinisation of the upper mantle by the normal faults (Lymer et al., 2019; Reston et al., 2007; Schuba et al., 2018). A 3D traveltime model developed using the wide-angle seismic data from the DGM resolved structures well at a broad-scale, however the model does not show finer details (Bayrakci et al., 2016). In this thesis, I developed a 3D high-resolution velocity model of the DGM employing 3D FWI technique using wide-angle seismic data and 3D traveltime model as the starting model. Based on the 3D FWI model, I attempted to address questions regarding the difference between 2D and 3D FWI imaging in the DGM using the OBS data, nature of the crust, exhumation of the lower crust during the extension, and serpentinisation below the S-reflector. In addition, I have developed a 2D image of the DGM using the first-order multiples employing mirror imaging technique. Below are the answers to the research questions posed in chapter 1:

1. **Differences between 2D and 3D FWI imaging for a rifted margin setting using sparsely acquired OBS data**

   2D wide-angle surveys using OBS are more common than 3D surveys in academia, mostly acquired to generate smooth velocity models of the subsurface by performing traveltime tomography. Using such datasets for performing FWI can be challenging primarily due to sparse sampling of the subsurface, resulting in the problem of an ill-posed inverse problem. Using the sparse OBS data from the DGM, I highlighted the difference between 2D and 3D FWI results and my results suggest that 3D datasets can mitigate the effects of data sparsity. With the 3D FWI model, a new fault block and small peridotite ridge towards the seaward end of the crystalline crust have been identified. Although the differences between 2D and 3D FWI have been presented using a case study of the DGM, some of the results have broader implications pertaining to the general question of differences between 2D and 3D FWI from other tectonic settings.

2. Understanding the nature of the crust in the hyperextended zone of the DGM using a high-resolution P-wave velocity model

I tried to understand the nature of the crust by comparing the velocities of the crystalline crust from SIAP and GIB to velocities from the 3D FWI, and looked for evidence to differentiate between the upper and lower crust based on P-wave velocity profiles. The velocities in the crystalline crust of the DGM vary between ~4.75 and 6.7 km/s, matching closely the velocity limits of the crystalline crust in the SIAP and GIB. Comparison with the GIB suggests that the crystalline crust in the DGM comprises of both the upper and lower crust. No clear evidence was found on the P-wave velocity profiles for the upper crust and lower crust as distinct layers within the crystalline crust. The velocity contour 6.6 km/s shallows under the footwall of the faults suggesting exhumation of the lower crust under the footwall of the normal faults to accommodate for the extension along the normal faults. At the top of the crystalline crust, a layer with high velocity gradient has been identified in a few locations where the crust is thicker than 2 km, which I interpret to have been subjected to fracturing.

3. P-wave velocities and serpentinisation below the S-reflector

A map of velocities at a depth of 100 ms below the S-reflector was generated from the 3D FWI model and compared with a map generated by training a machine learning algorithm using 2D FWI model and multichannel seismic images. A mean serpentinisation of ~33 % was estimated using P-wave velocities below the S-reflector. The distribution of serpentinisation below the S-reflector is very heterogeneous from the 3D FWI model and does not match well the serpentinisation pattern obtained by training a machine learning algorithm. The 3D FWI map shows a better match with the S-reflector topography in depth than the machine-learning generated map with local high and low velocities corresponding to local low and high relief features on the surface. This match suggests that serpentinisation plays a major role in the topography of the S-reflector surface by causing volume changes in the peridotites during the hydration process. Normal fault intersections show an overall alignment with the eastern edges of the serpentinised areas suggesting that the crustal faults acted as conduits for sea water infiltration to the mantle.

4. Mirror imaging using the first-order multiples of the OBS data

First-order water-layer multiples in OBS data can be used for mirror imaging. Using mirror imaging, I developed 2D images of the DGM in time and depth domains. When compared to the 3D seismic reflection image, mirror imaging is able to image structures to the depths

of top of the basement beyond which the structures are not well-defined. Compared to the image generated using primary reflections from the OBS, first-order multiples generate better images because of their wider illumination and are less affected by near seafloor variation. Mirror imaging is computationally less demanding compared to the conventional migration of the multichannel seismic data and can be very useful in studies where there are no multichannel data available.

6.2 Recommendations for future work

Galicia-3D dataset is a spectacular dataset with both multichannel and OBS recording coincidentally giving opportunity to test different advanced imaging techniques and, at the same time, understand rifting process in more detail. The following are a few recommendations for future work, which can be performed with this dataset:

- The 3D seismic reflection volume acquired in the DGM was processed by pre-stack time migration algorithm using velocities determined from 3D reflection dataset. Migrating the volume with the high-resolution and accurate the 3D FWI model will re-position the reflections accurately and may image fine-scale features that the migration with multichannel 3Dvelocities was not able to construct.
- Although the 3D FWI model shows good fit with the multichannel images, the resolution of the model can be further improved which can help us in understanding finer processes happening during rifting. In this work, the model was developed using only wide-angle refraction data from the OBSs and was limited to lower frequencies considering large spacing between the OBSs. Performing FWI using the high-frequency reflection data from the 3D pre-stack reflection volume will enhance the resolution of the velocity model derived using the refraction data. Considering elastic and anisotropic approximations of the wave equation will further improve the imaging. However, based on the results of this thesis and previous velocity modelling, it can be inferred that no strong elastic and anisotropic effects are present in this region. Hence, performing acoustic 3D FWI using the multichannel seismic volume should be sufficient to resolve structures accurately to the resolution of the 3D pre-stack migrated seismic images. However, a point to speculate in this study would be the resolution of the velocity model below the S-reflector from where no reflections are seen in the multichannel images.
- Another interesting study would be a high-resolution seismic imaging using the combined data, the multichannel and OBS from the DGM. In general, OBS data do not sample shallow depths just below the seafloor very well due sparse spacing between them, and on the other hand, multichannel seismic fail to image structures below large lithospheric faults like the S-reflector. Hence, combining them into an inversion will resolve structures from the seafloor to the depths

below the S-reflector in the DGM. An additional interesting processing step to include in this exercise would to perform downward continuation of the multichannel data to uncover the turning waves from shallow depths, which are otherwise dominated by high-amplitude direct arrivals. Previously, combined imaging task has been carried out for performing traveltime and full waveform inversions in 2D using real datasets. I believe the Galicia-3D dataset is very well suited to a combined tomography imaging. Hence, I recommend traveltime tomography and FWI using the Galicia-3D dataset in 2D along the OBS lines. 3D tomography of the combined dataset can highly demanding computationally, and it can be very challenging to accurately model the reflections and refractions from both the datasets in 3D, especially the far-offset data.

- The mirror imaging technique has the potential to become a standard processing technique, at least in the studies where there are no multichannel seismic data available. Mirror imaging can supplement traveltime tomography in which the depth (time) of the horizons, like basement, can be incorporated into the inversion to better constrain the inverse problem. It is computationally less demanding than conventional multichannel seismic migration. The 3D OBS dataset of the DGM, acquired in a deep-water environment, is also suitable for testing 3D mirror imaging. Therefore, I recommend performing 3D mirror imaging and establishing it as a standard seismic processing technique.
- In this thesis, interpretations of the 3D FWI model were primarily focused in the crystalline crust and below the S-reflector. However, the model also shows a good match with the multichannel images within the syn- and pre-rift sediments. Hence, it would be interesting to include these sections of the model in the future interpretations to learn more about the fault movements during extension.
- The Galicia 3D experiment was more centred on the multichannel acquisition with a short shot interval (~37.5 m) resulting in the contamination of the wide-angle arrivals by previous-shot multiples at around ~15 km offset in the OBSs. Such a problem in the future surveys can be mitigated by shooting a few shot lines with larger shot interval. The sparse sampling around these large shot interval lines can be compensated by applying an interpolation algorithm between the short interval lines adjacent to the large interval line. This will ensure clearer data at the far-offset in the OBSs at least in a few data profiles.

Appendix A OBS locations and number of shots

Table A- 1 OBS locations used in this thesis in UTM

OBS	Longitude	Latitude
19	672979.6802	4666329.93
20	676162.1579	4666397.554
21	680008.0712	4667694.628
25	692801.4314	4667410.447
26	696838.3345	4668577.651
27	700564.9573	4668693.773
29	706877.7721	4668053.735
30	710502.3294	4668561.09
31	713705.5519	4669313.189
34	724080.4481	4669246.256
35	726979.7182	4669383.457
37	673495.682	4660809.542
38	676875.8488	4661015.535
40	683618.1619	4661476.372
41	686967.2493	4661597.516
43	693642.7293	4662066.2
45	700437.1932	4662122.311
46	703799.8218	4662351.856
47	707156.0159	4662516.14
48	710570.3866	4662672.644
51	720614.3911	4663156.984
52	723996.2082	4663296.753
53	727386.276	4663438.41
54	730717.3383	4663613.12
56	677609.2349	4654878.542
57	681055.5336	4654554.704
59	686977.148	4655897.497
61	693892.6493	4655361.221
62	696742.2911	4656573.3
63	700815.0962	4656098.689
64	704661.7757	4656019.921
66	711547.6591	4657122.562
67	714242.8429	4657314.778
68	717218.3054	4656471.848
70	724921.9652	4656834.695
71	727654.8946	4657922.482
73	615939.4451	4658198.584
74	625589.074	4658663.222
75	635139.5143	4659094.738
76	644672.3215	4659561.043
77	654370.6107	4660010.528
78	663945.2457	4660426.05

79	705554.305	4662369.338
80	708834.4215	4662587.777
81	712180.203	4663098.689
82	715588.3042	4662912.898
83	718894.3542	4663092.364
84	722292.7209	4663231.827
85	725633.5246	4663359.976
86	729031.8561	4663502.689

Table A- 2 Number of shots from each OBS used in 3D FWI

OBS number	Number of shots
56	3917
57	6445
59	6314
61	8193
62	8899
63	3961
64	9835
66	6921
67	5751
68	4899
70	12693
71	6651
37	6930
38	375
40	247
41	6120
43	6129
45	11618
46	12381
47	12659
48	7797
51	8818
52	6924
53	5675
54	4032
19	4237
20	2745
21	10230
25	18881
26	16603
27	4823
29	15640
30	18379
31	6461
34	8566
35	14345

Appendix B Phase plots and comparison of observed and predicted data

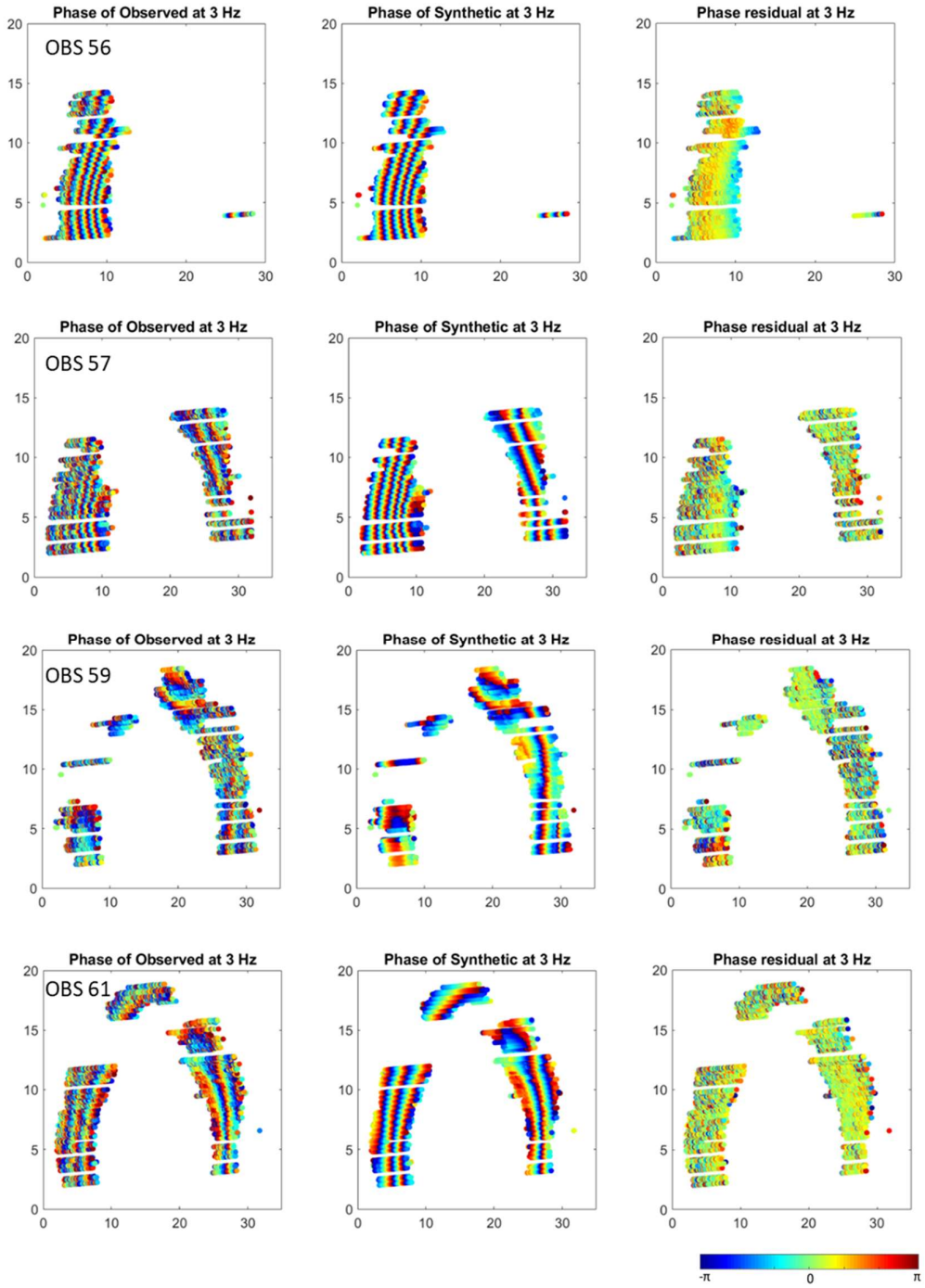

Figure B-1 Phase plots of the observed and synthetic data generated using the FWI model for all instruments along with the phase residuals at 3 Hz. The axes are distances in km. The colour scale is indicated at the bottom of each page of this appendix.

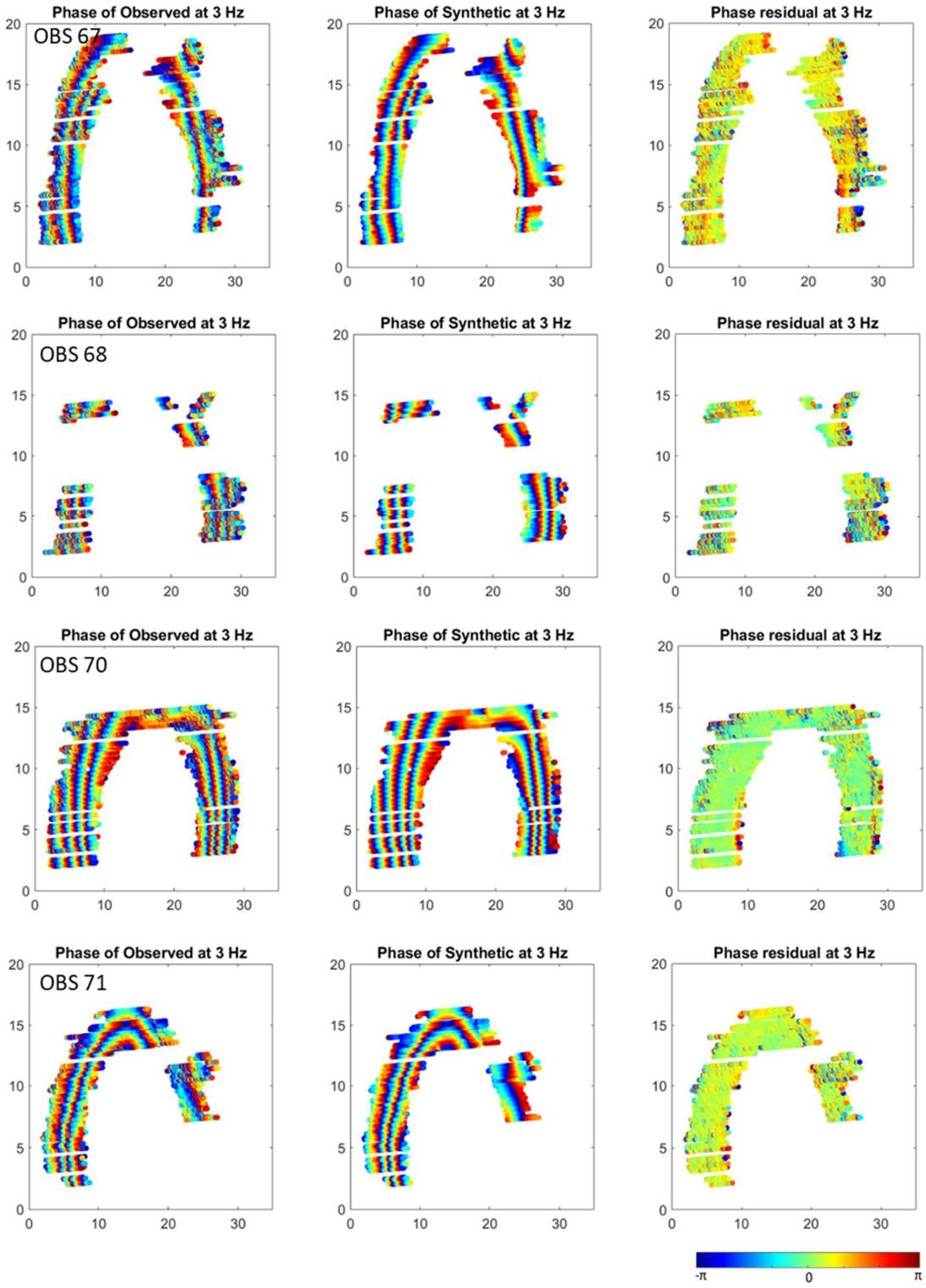

Figure B 1 follow on

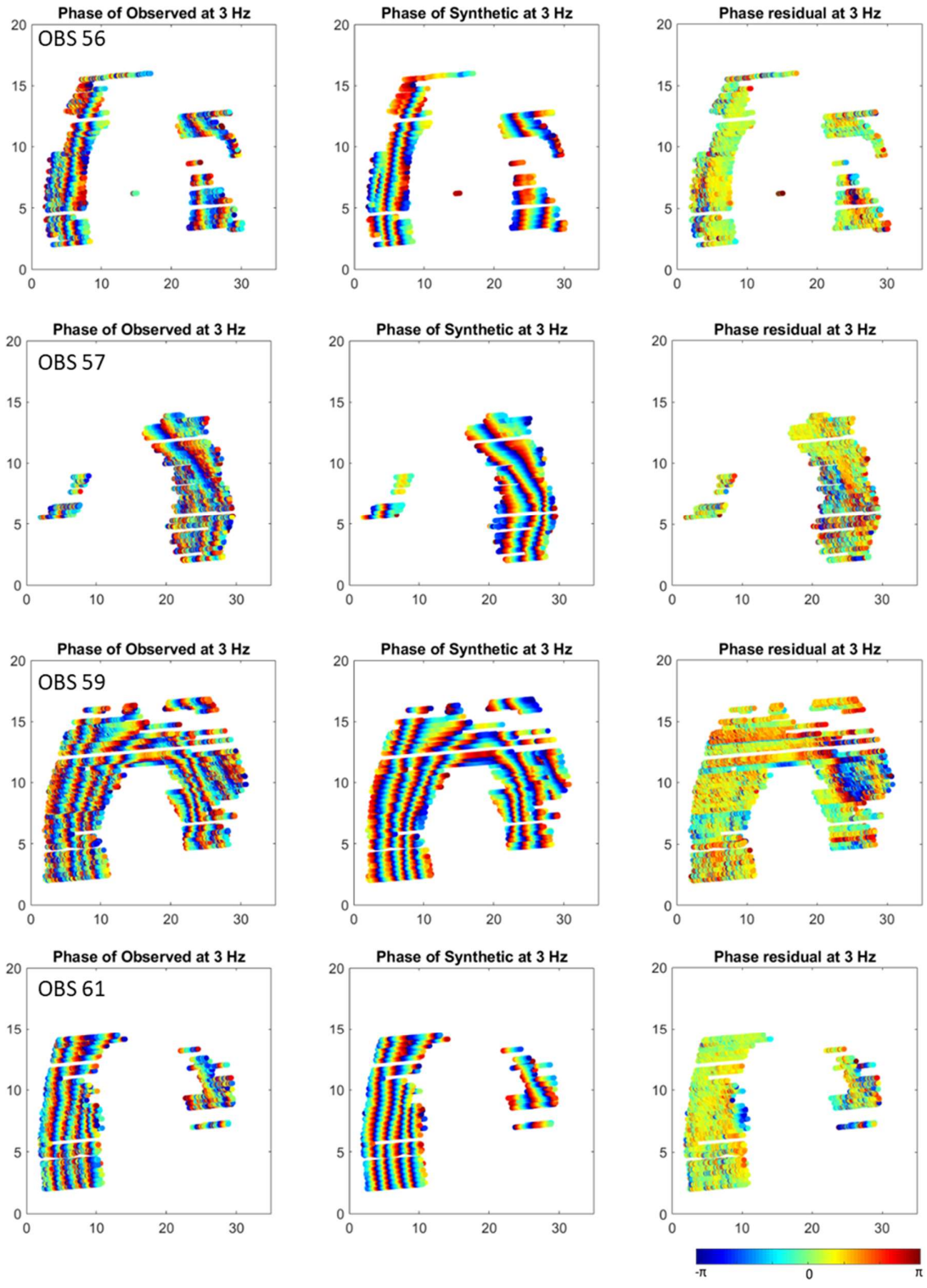

Figure B 1 follow on

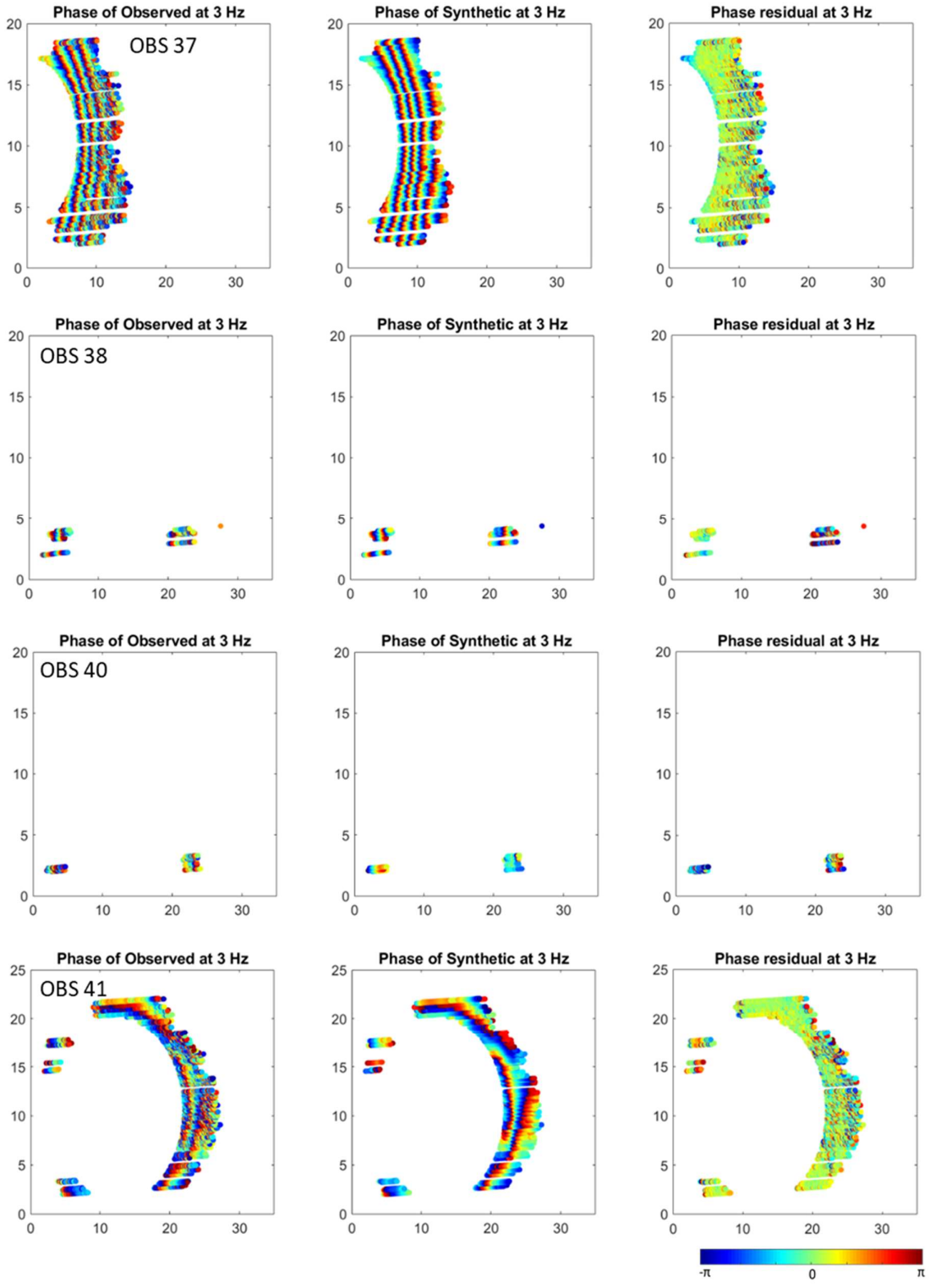

Figure B 1 follow on

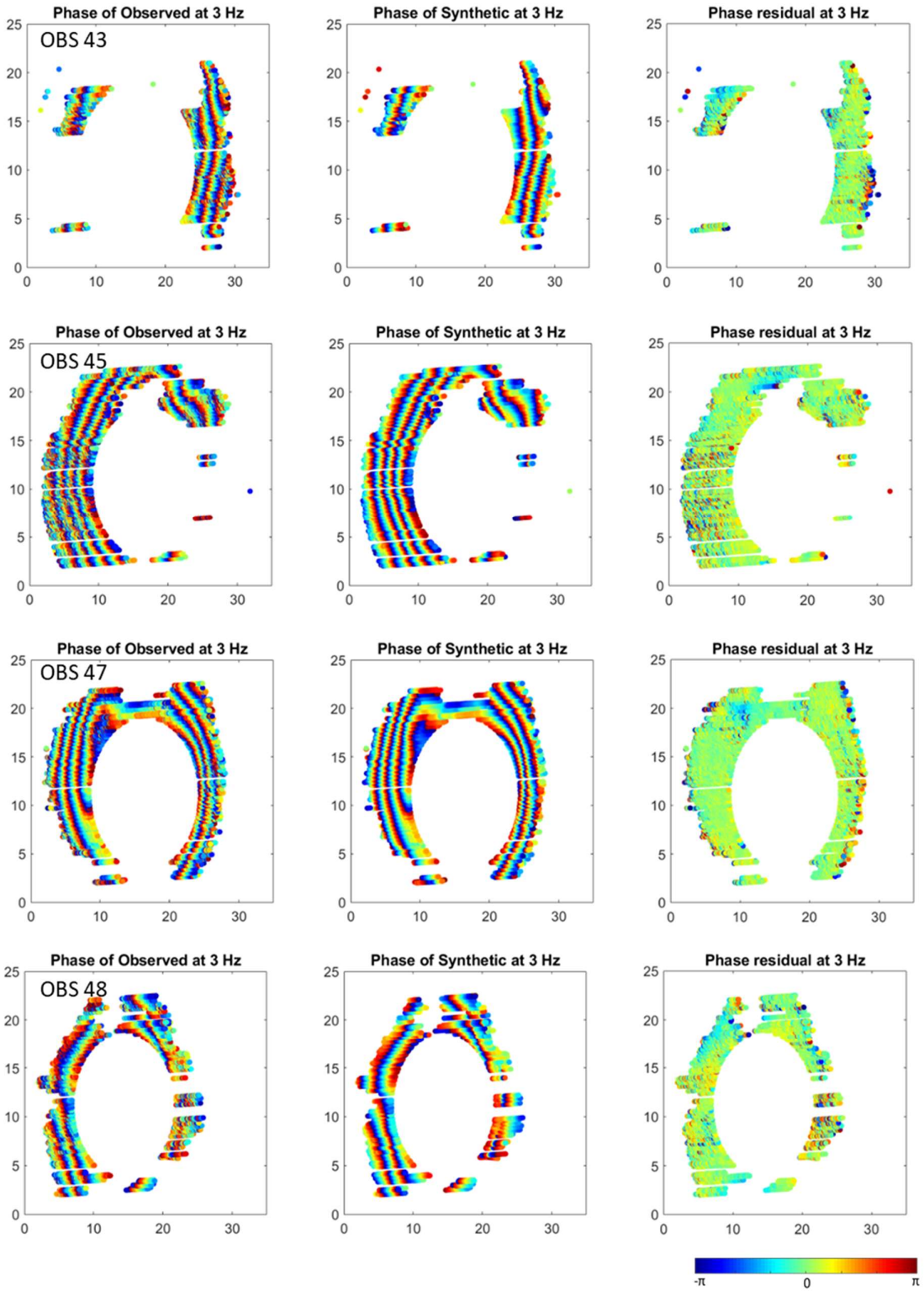

Figure B 1 follow on

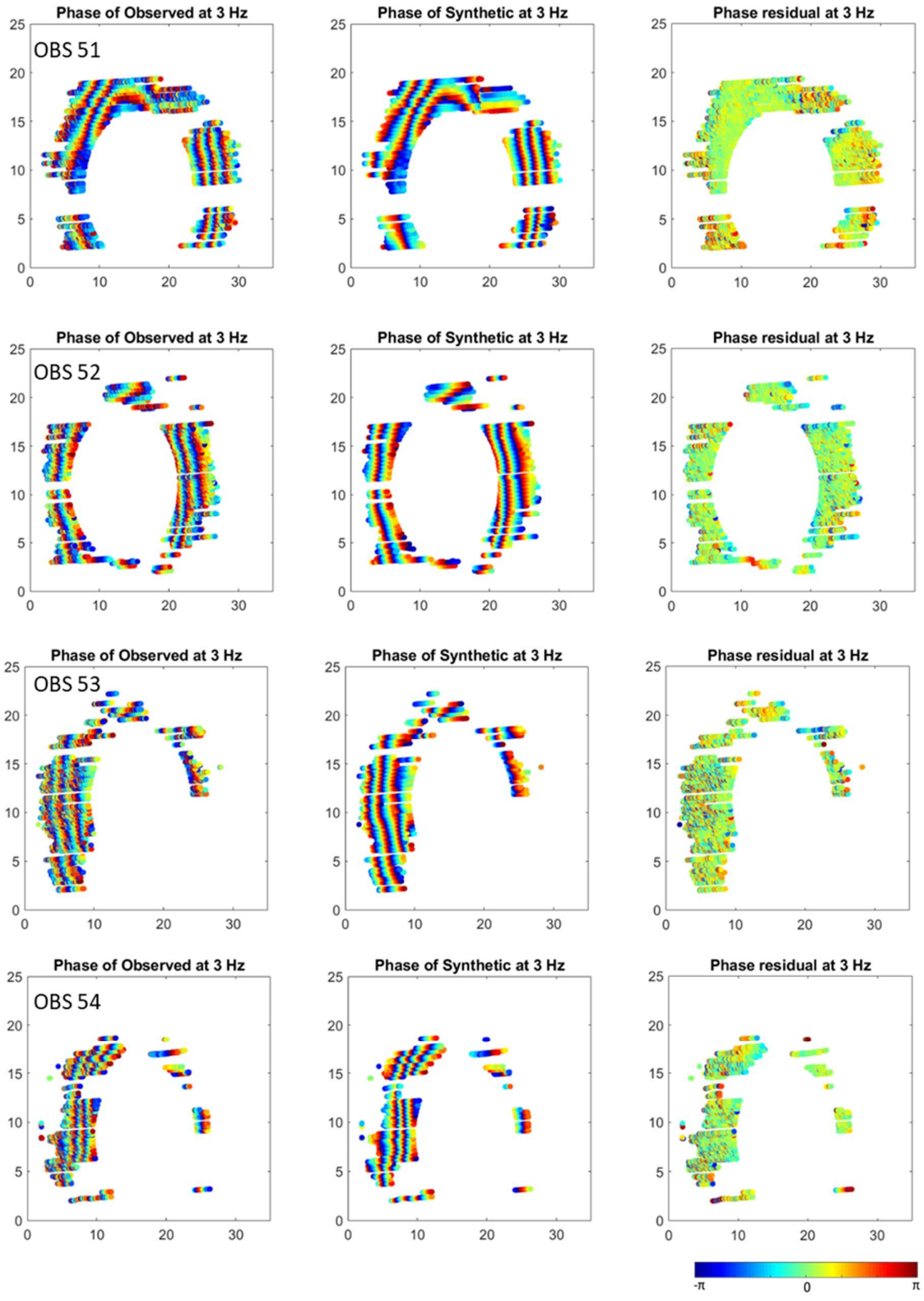

Figure B 1 follow on

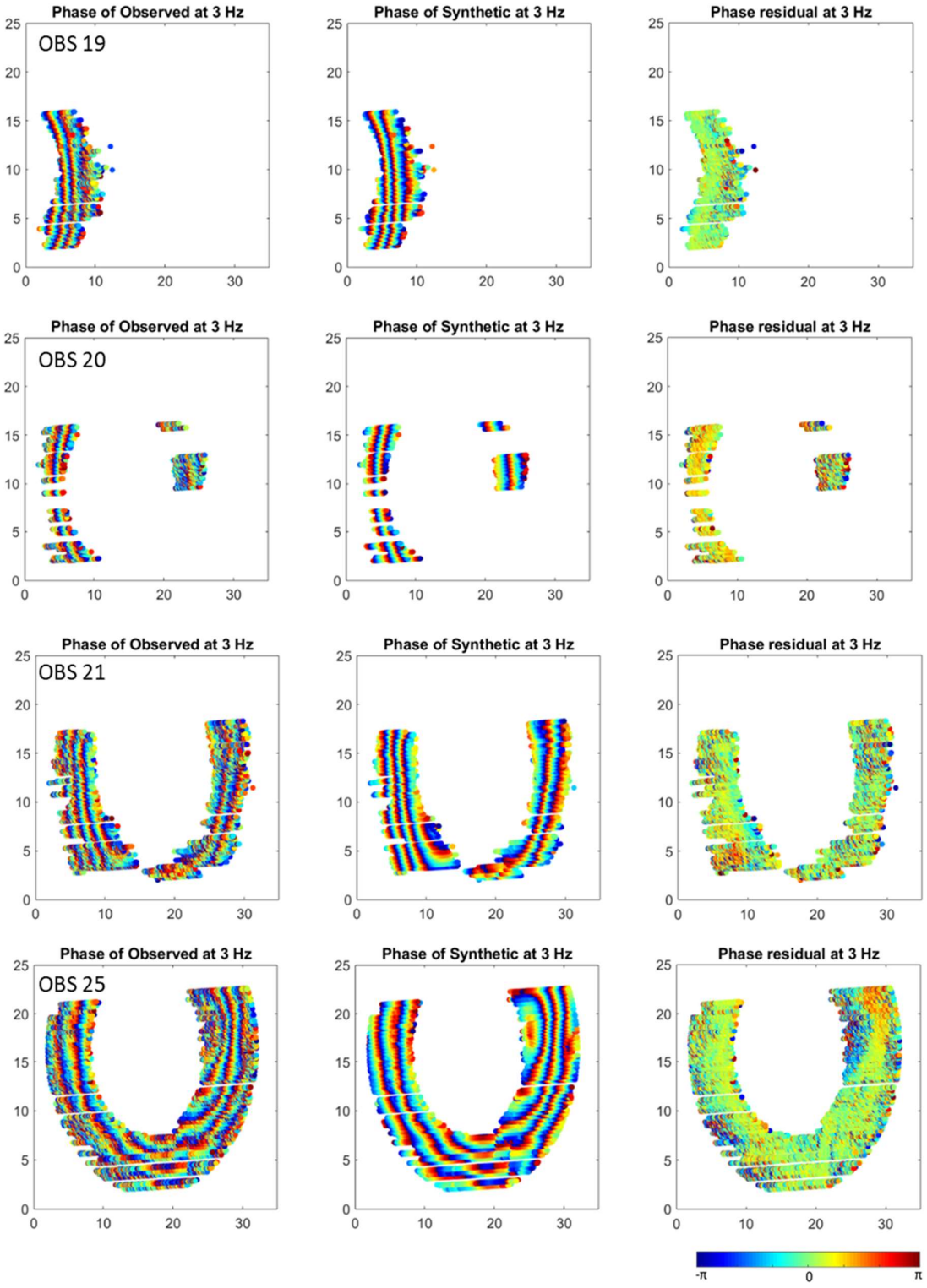

Figure B 1 follow on

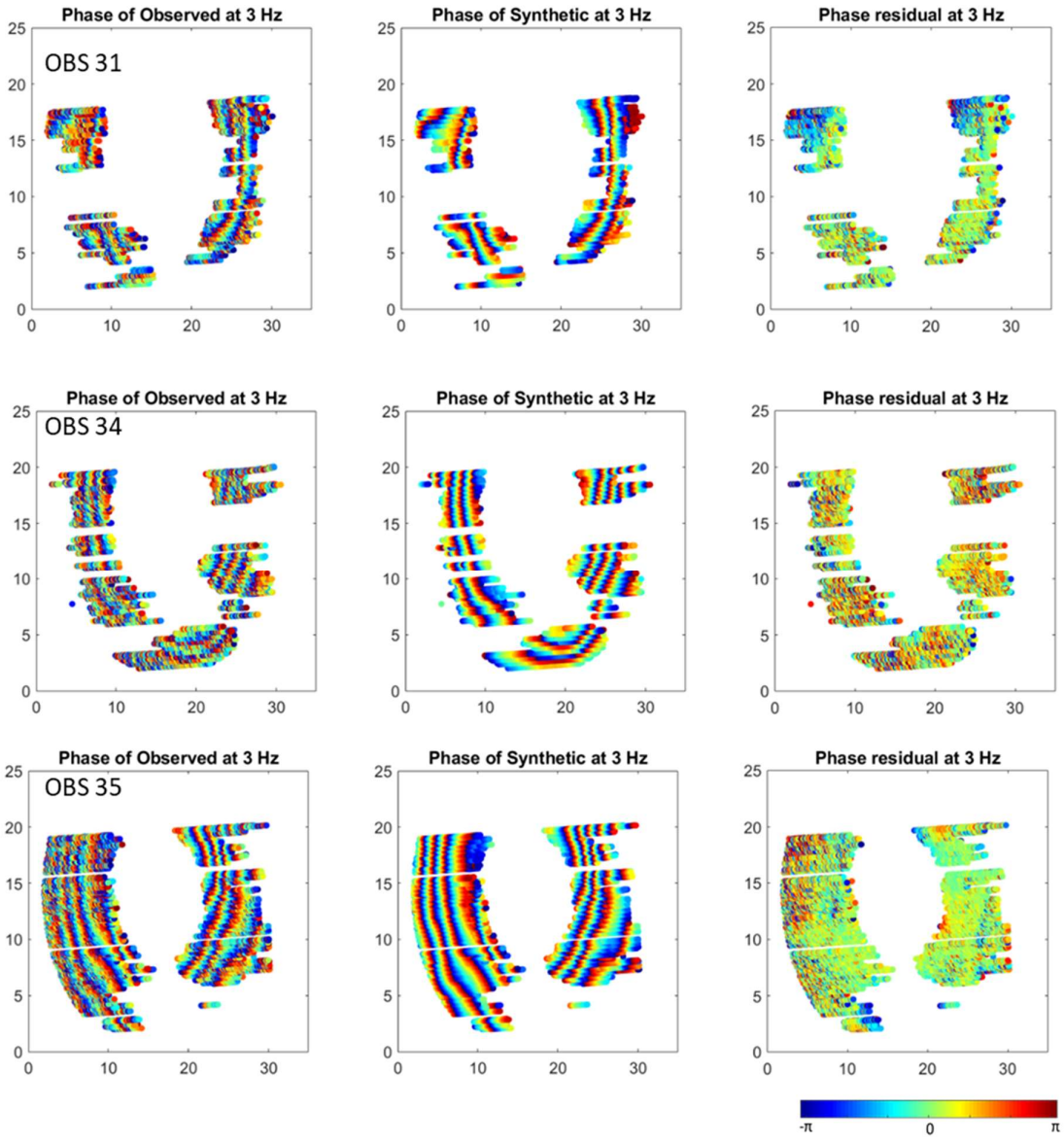

Figure B 1 follow on

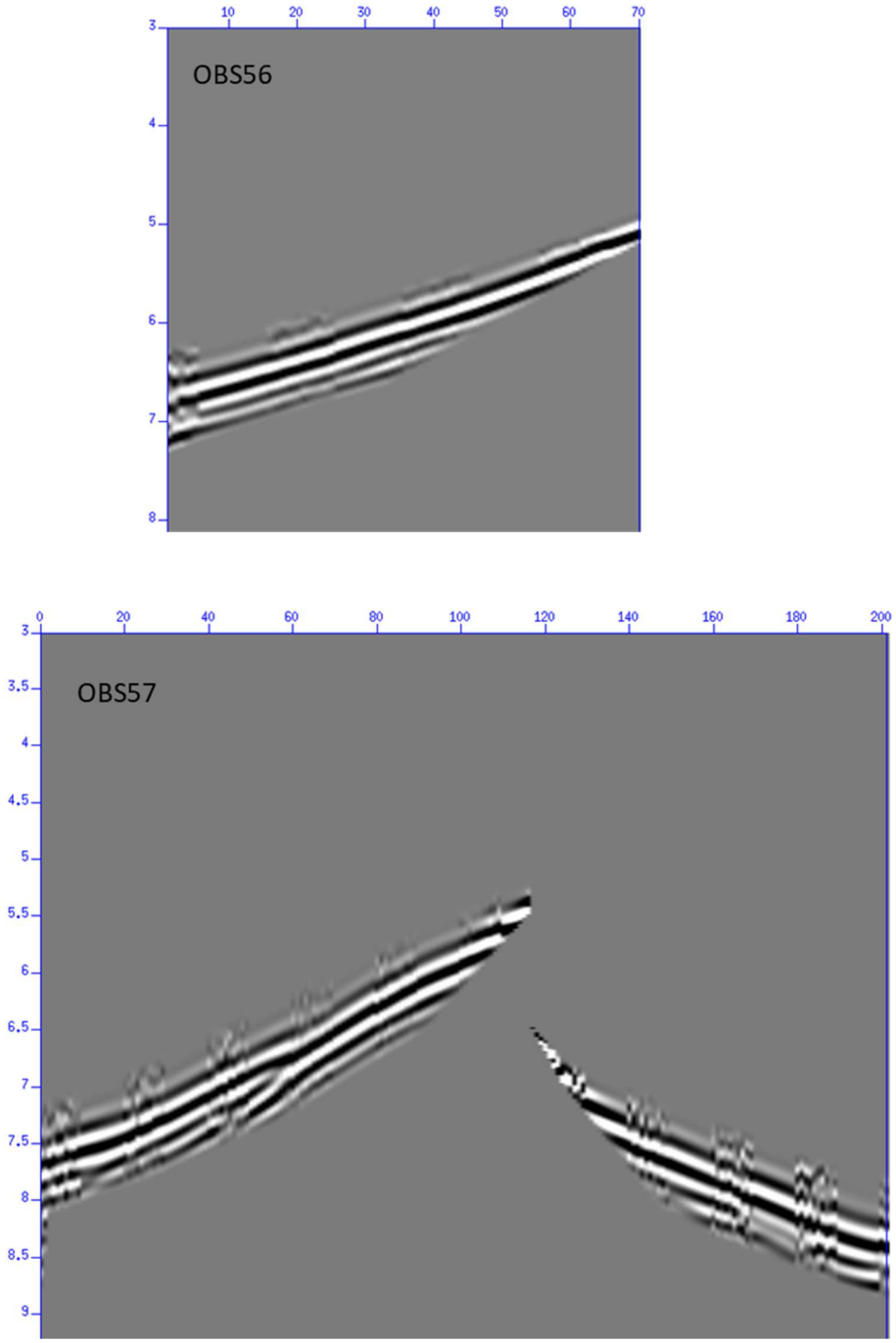

Figure B-2 Observed and FWI model predicted seismic data with ten traces from each dataset alternating along the closest profile to the OBS with OBS number indicated in the top left corner of each profile. The x-axis indicates number of traces and y-axis indicates time (s).

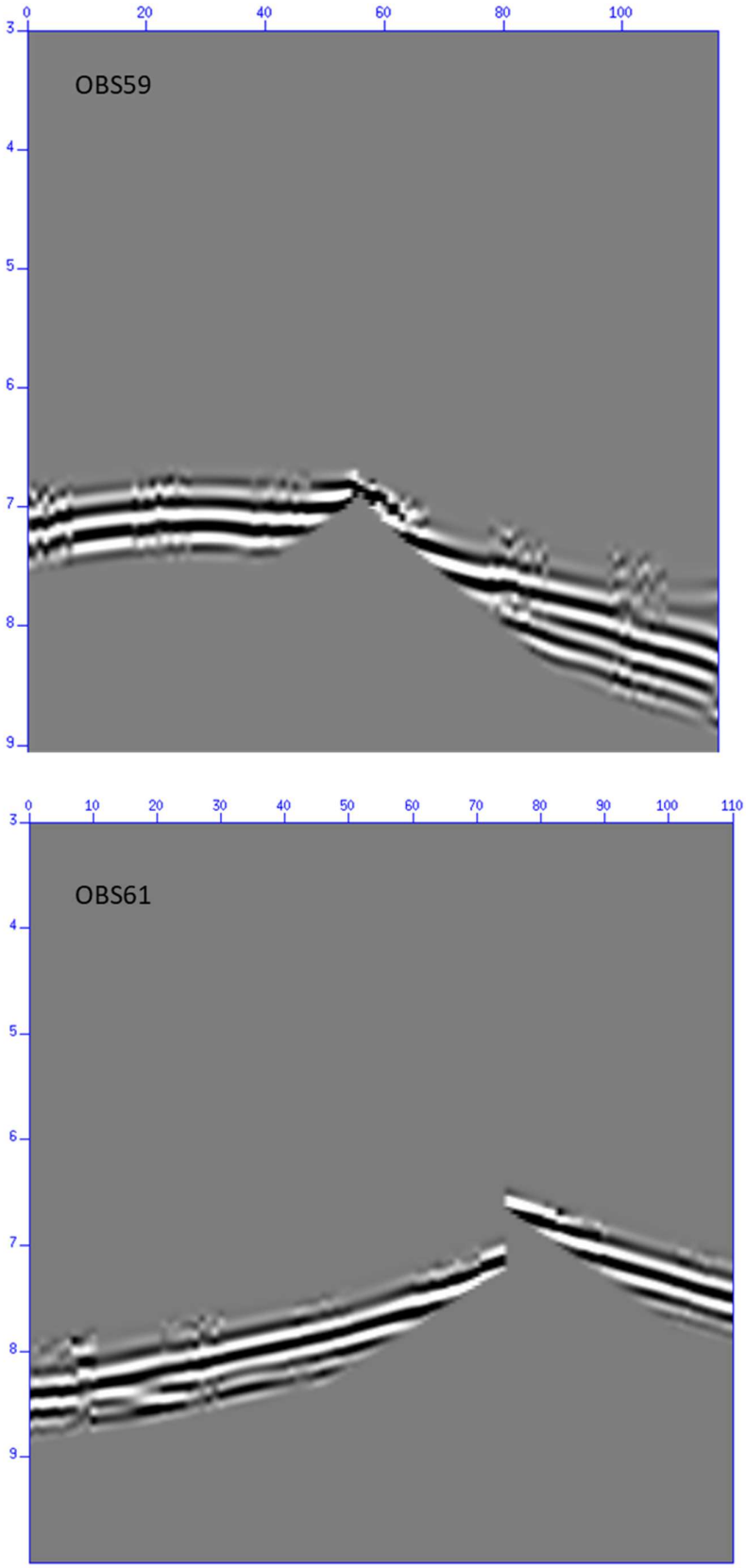

Figure B 2 follow on

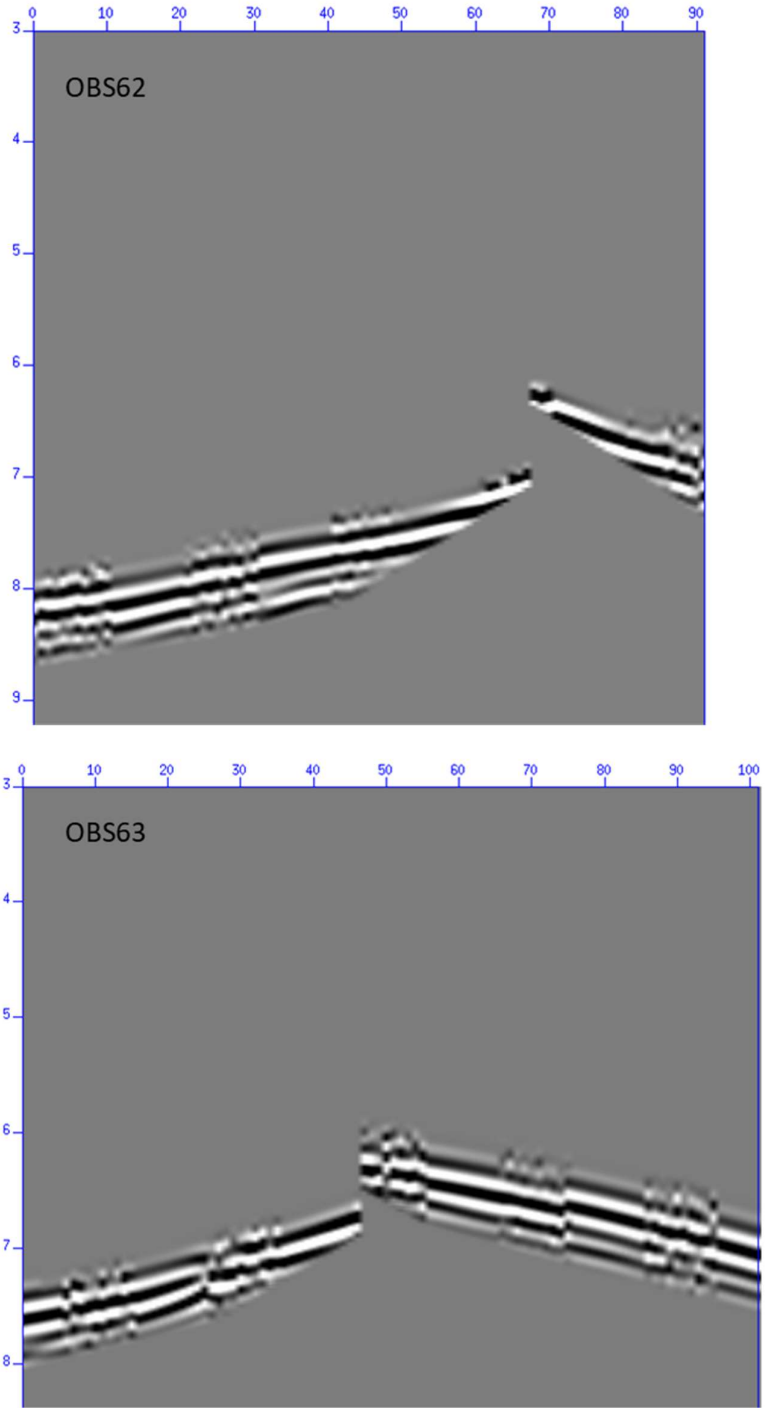

Figure B 2 follow on

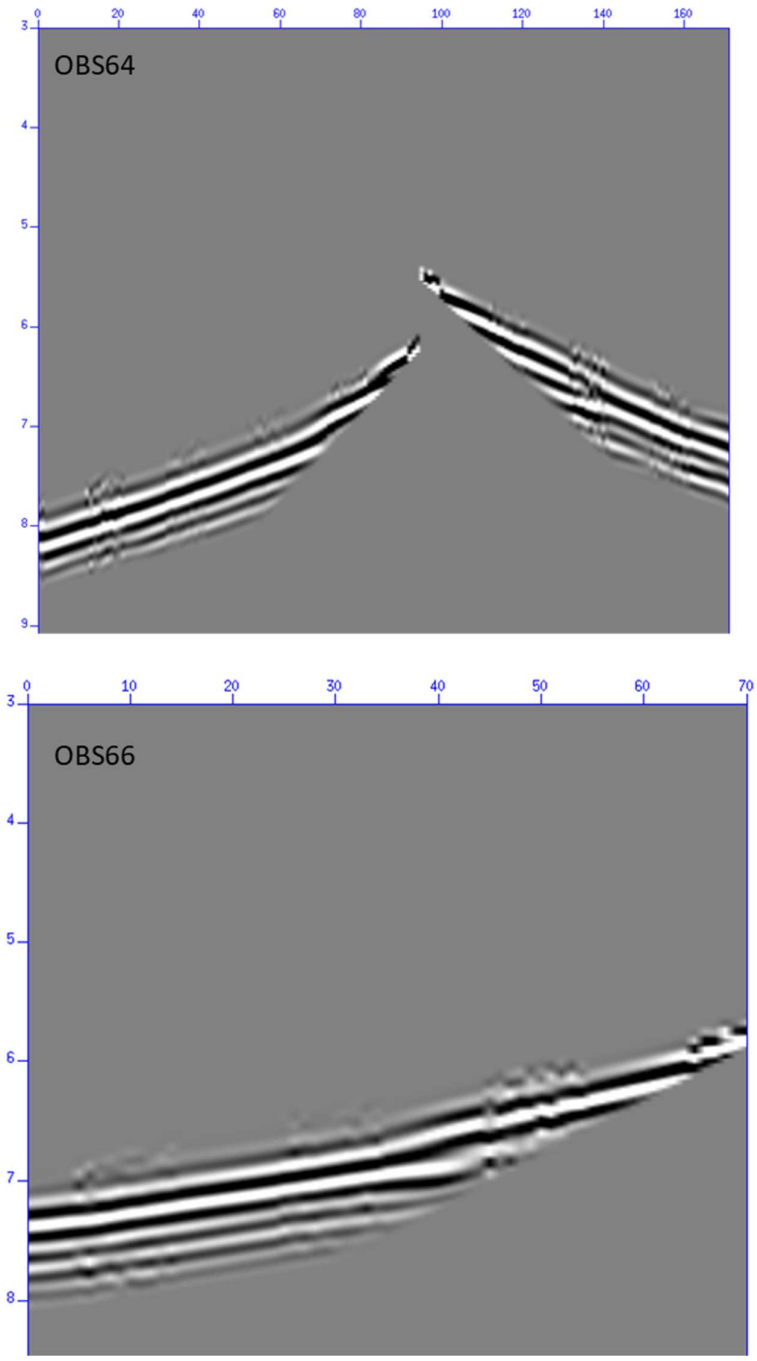

Figure B 2 follow on

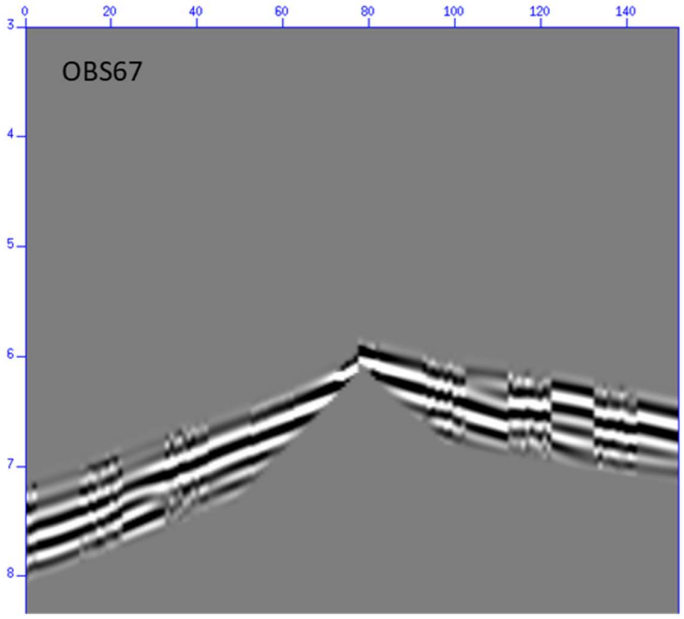

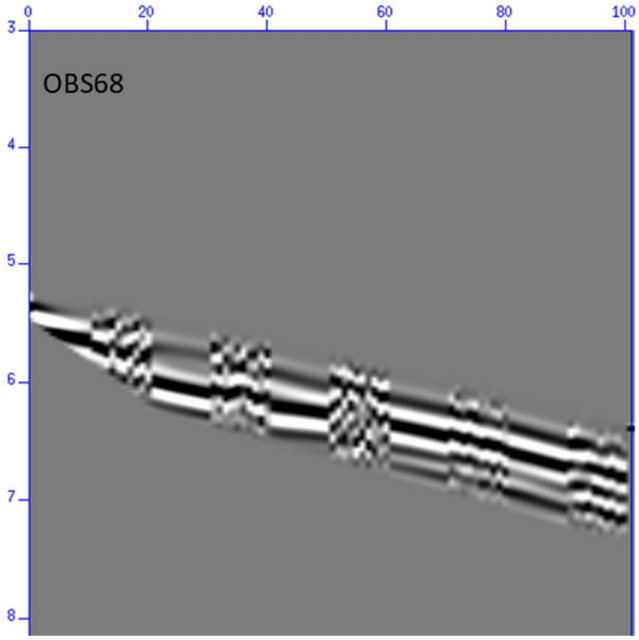

Figure B 2 follow on

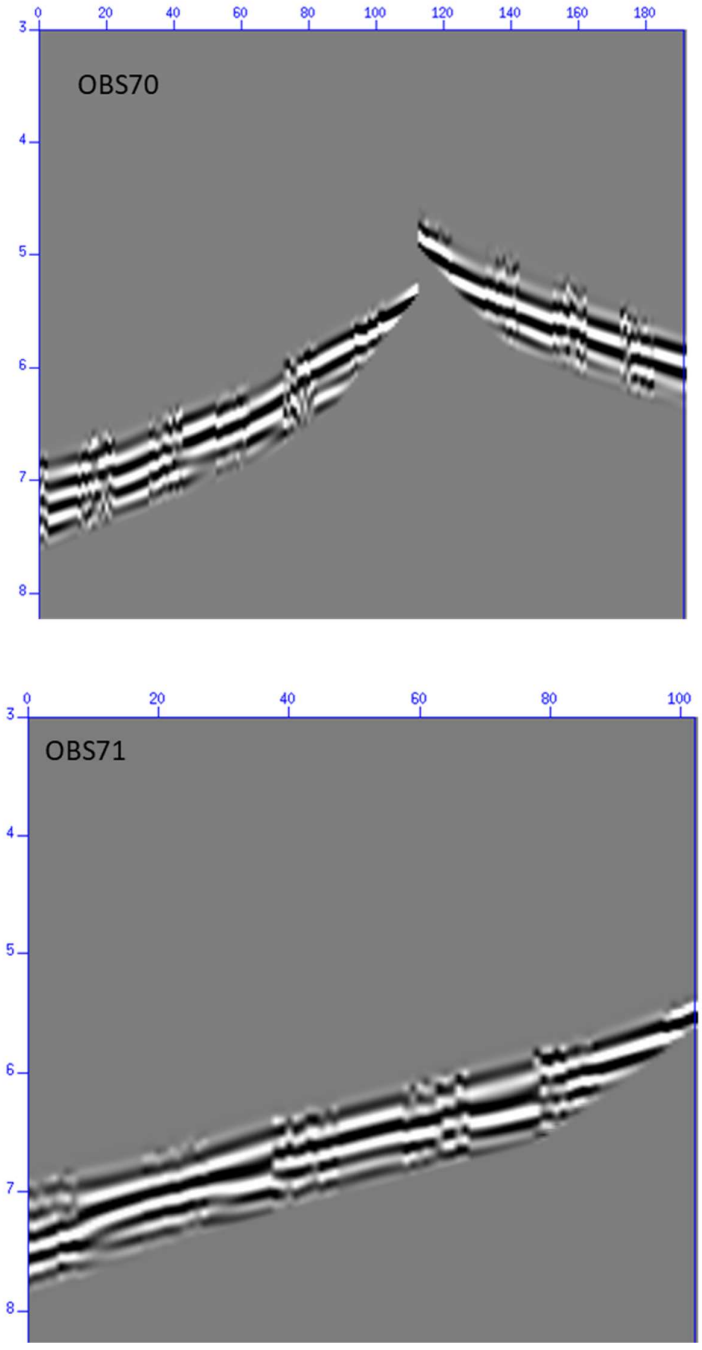

Figure B 2 follow on

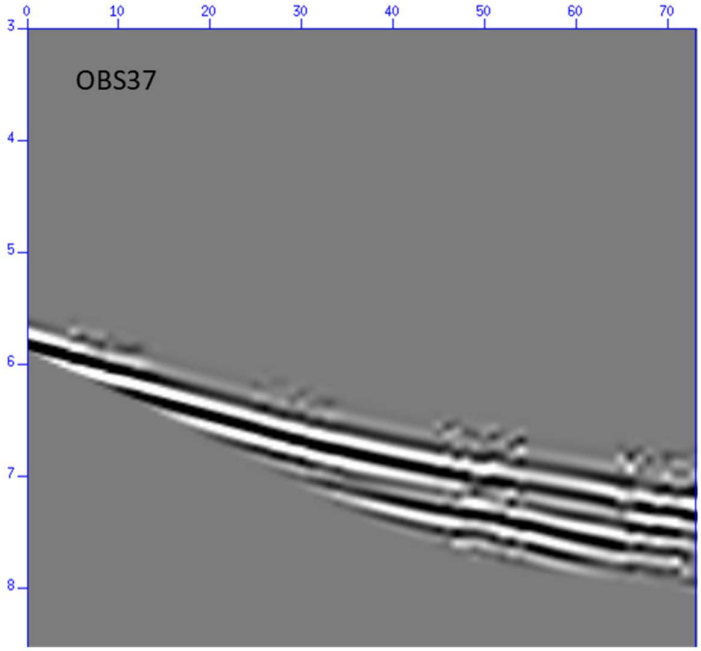

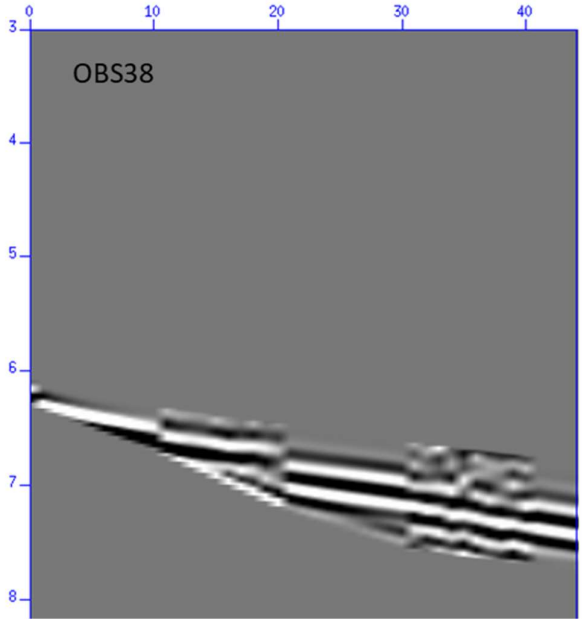

Figure B 2 follow on

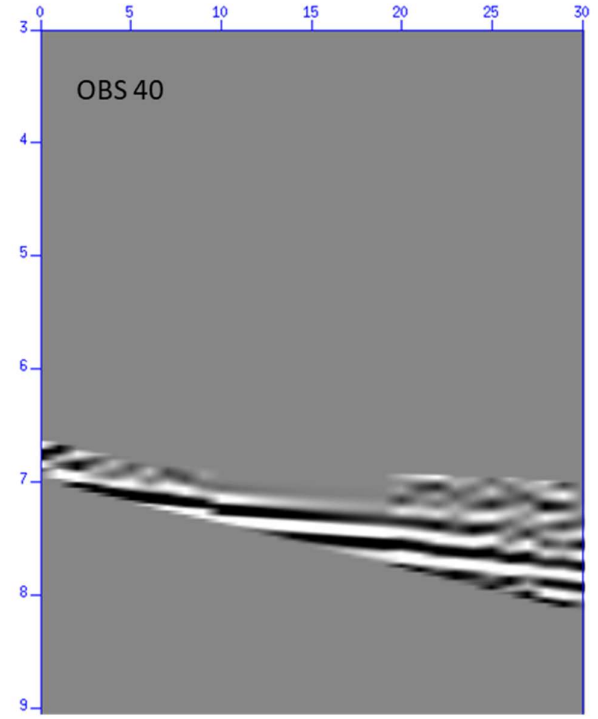

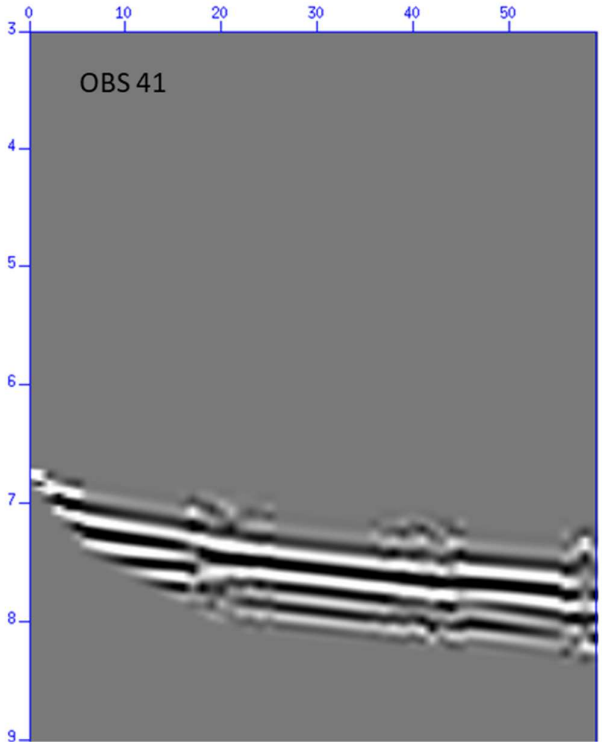

Figure B 2 follow on

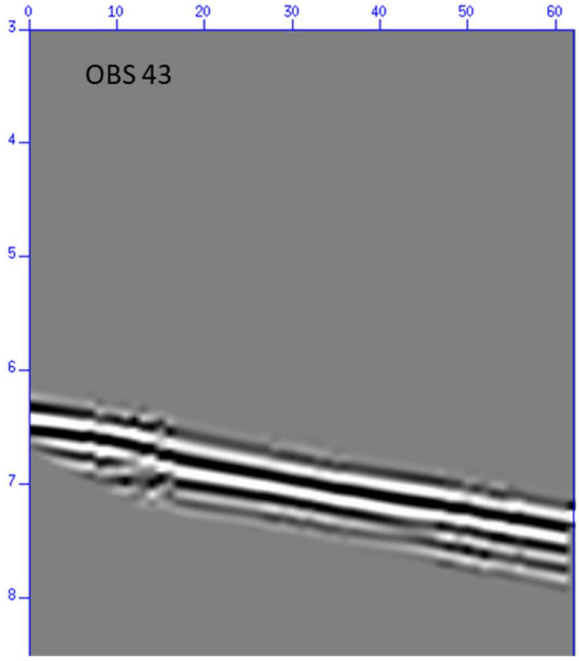

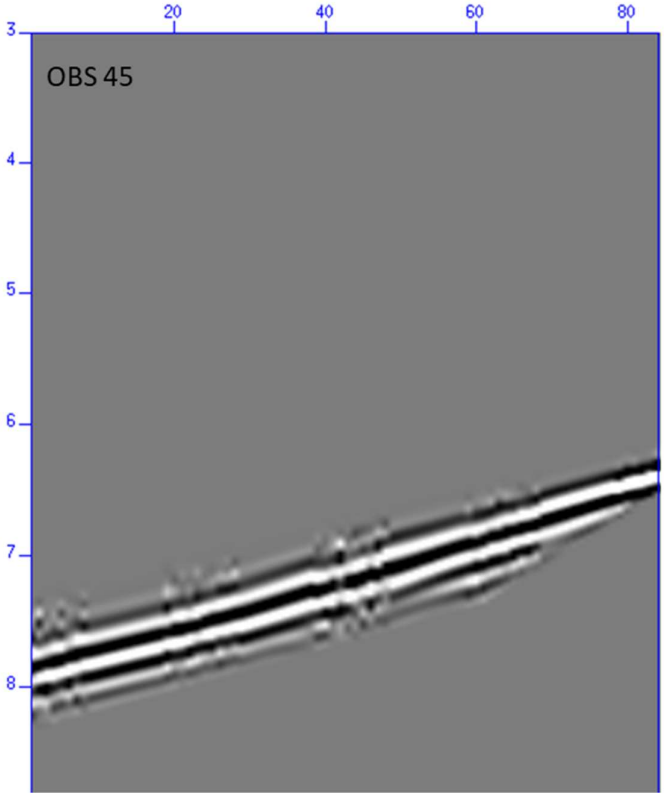

Figure B 2 follow on

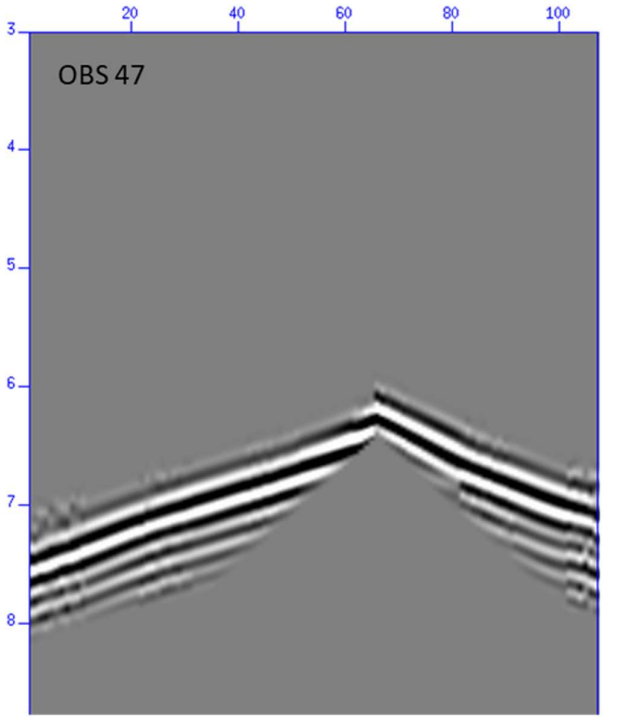

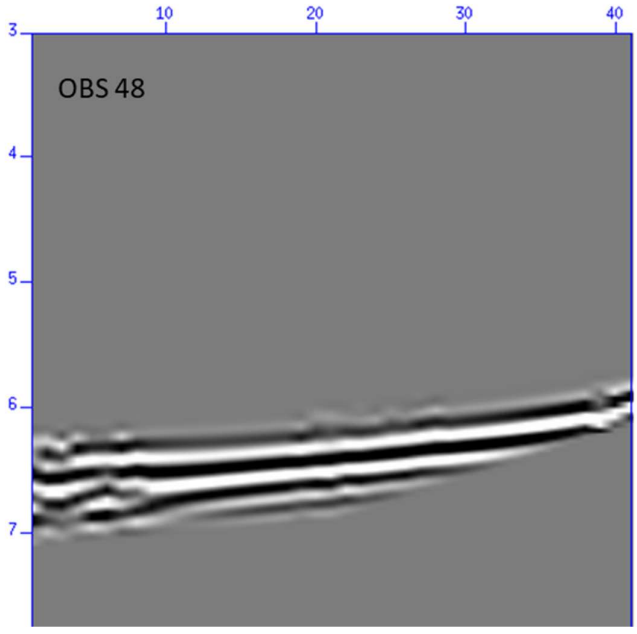

Figure B 2 follow on

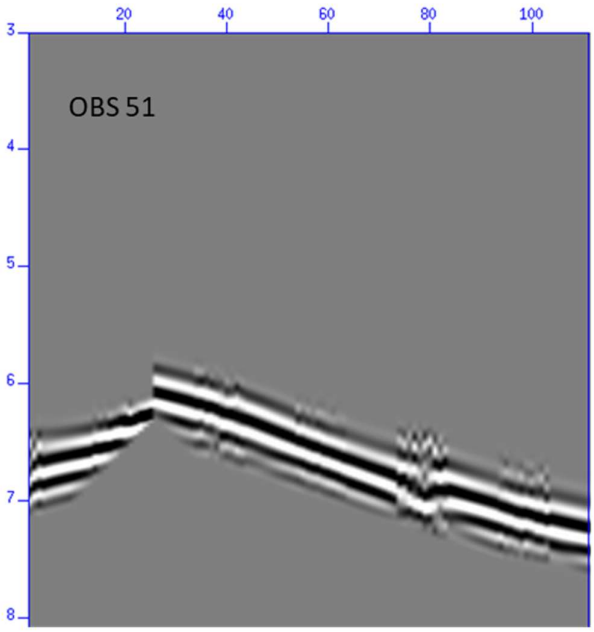

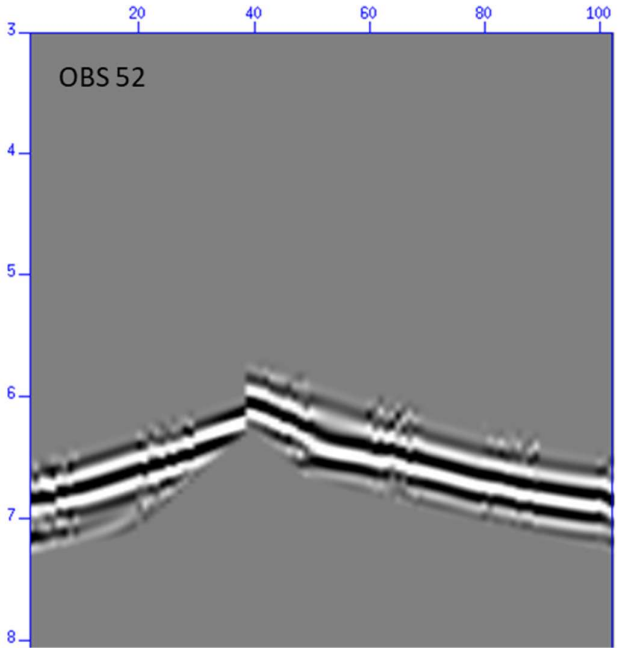

Figure B 2 follow on

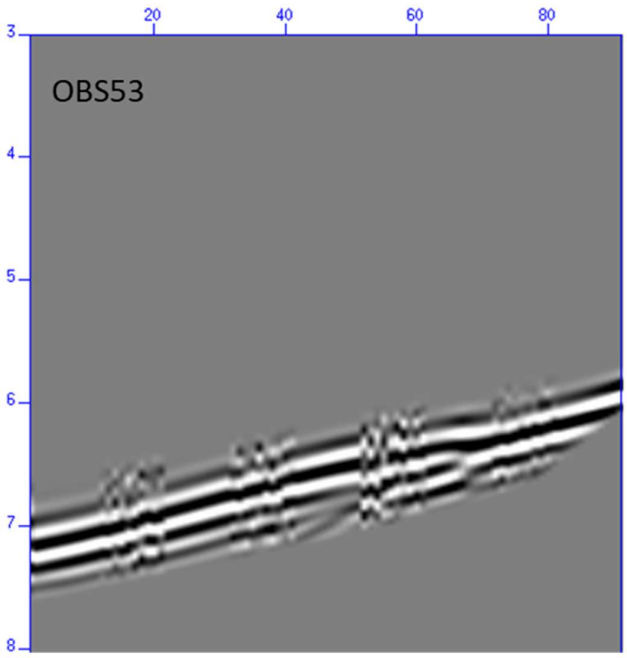

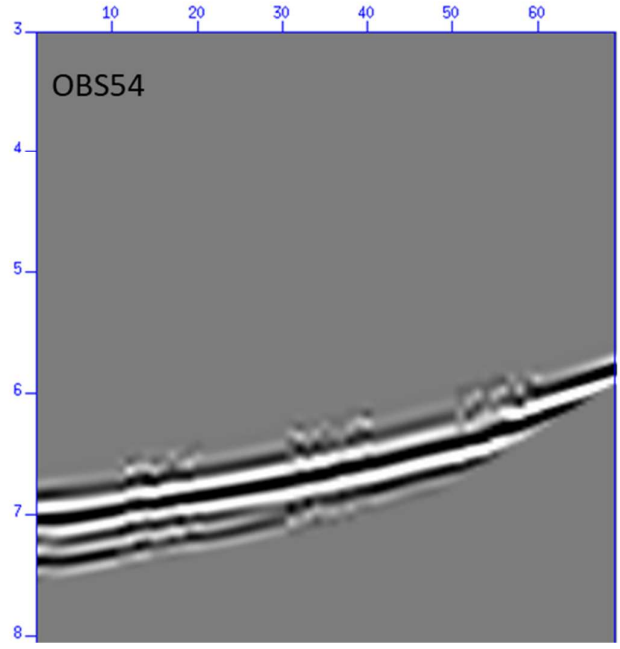

Figure B 2 follow on

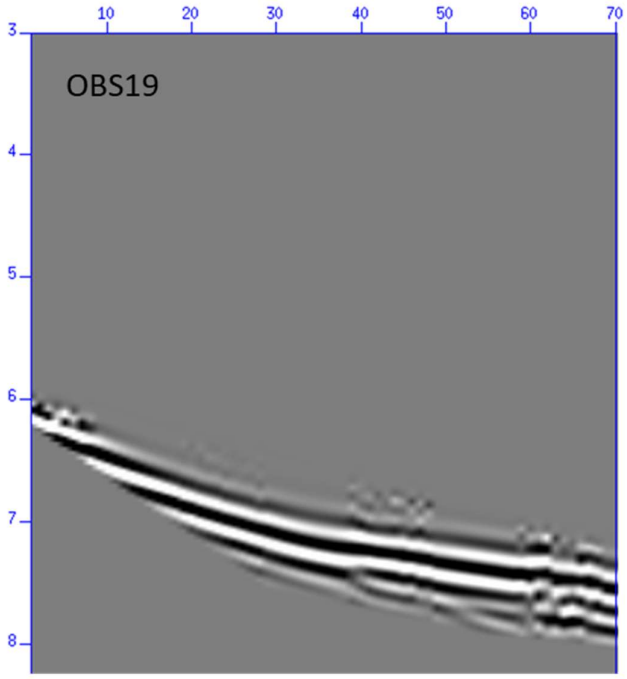

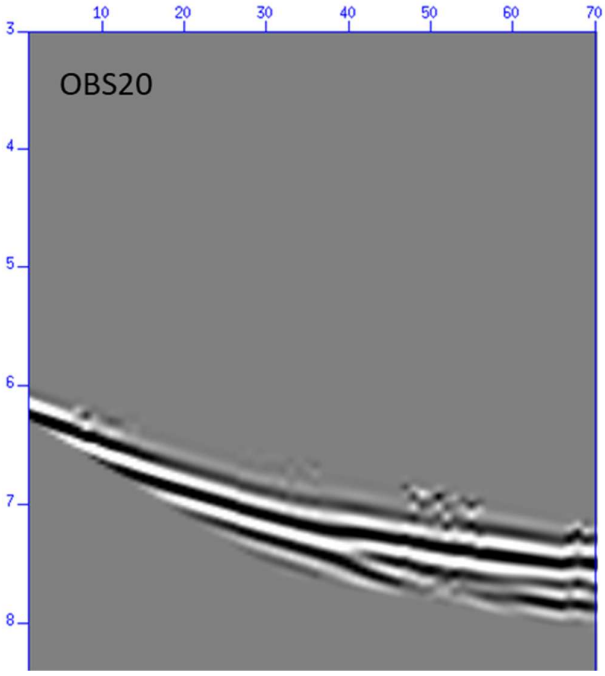

Figure B 2 follow on

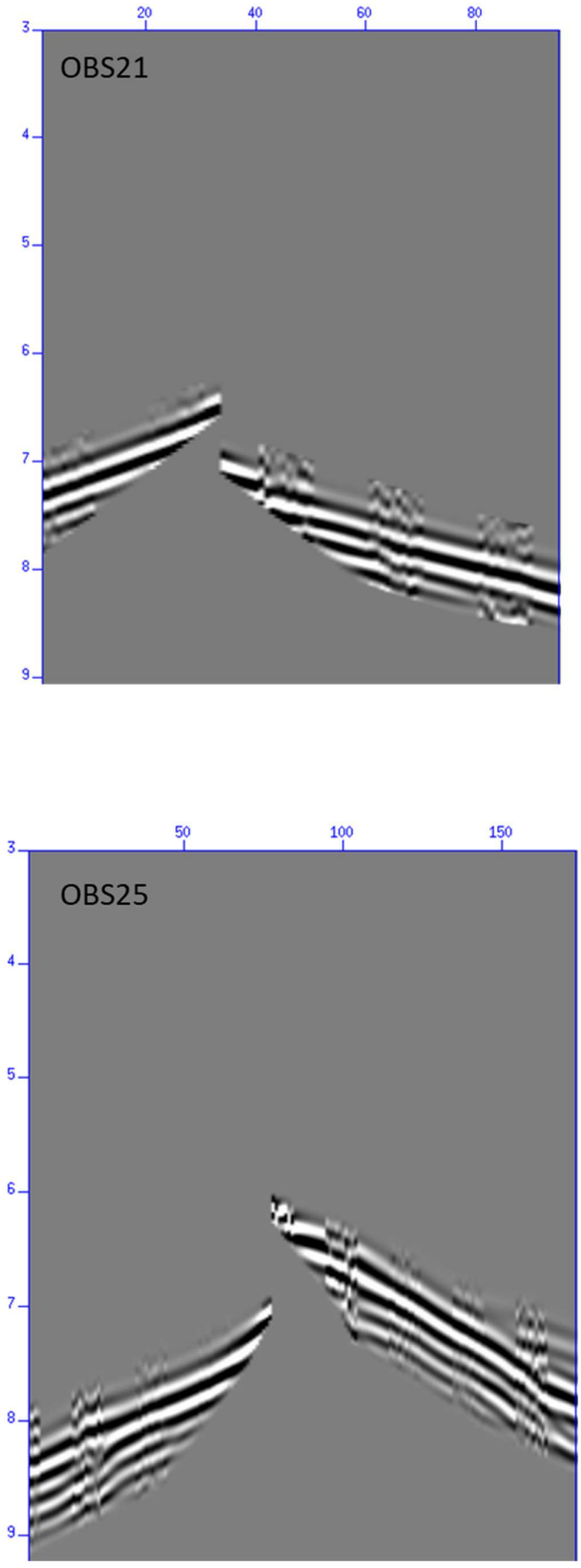

Figure B 2 follow on

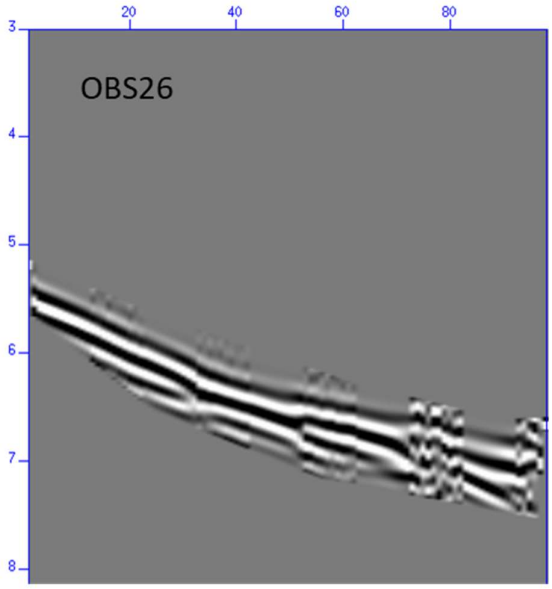

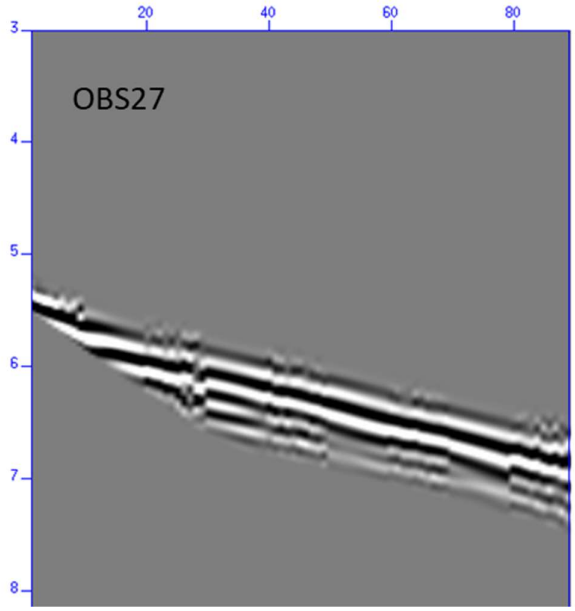

Figure B 2 follow on

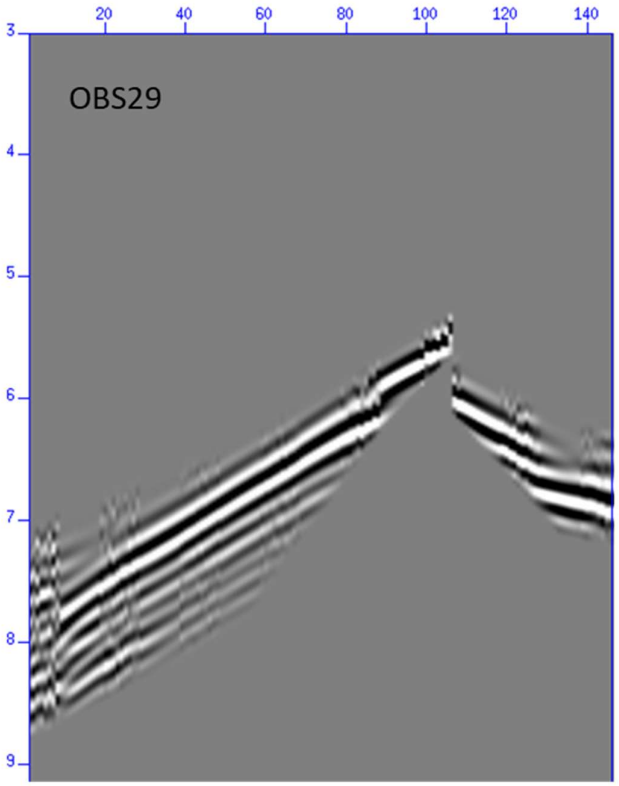

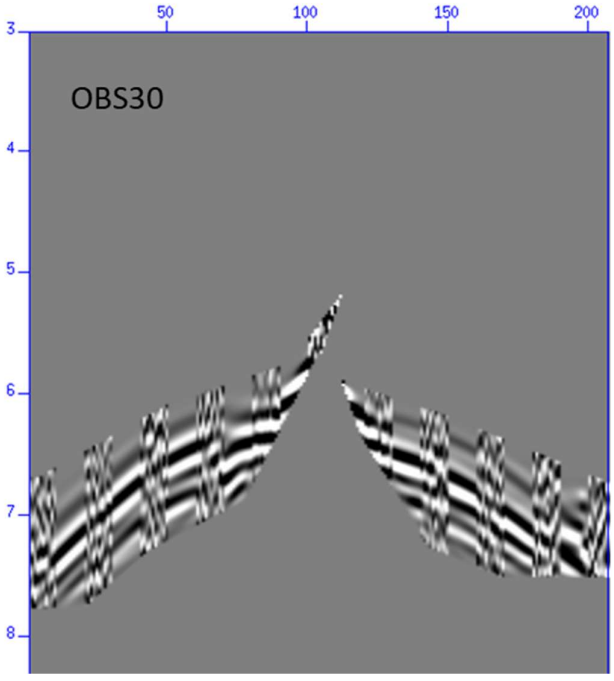

Figure B 2 follow on

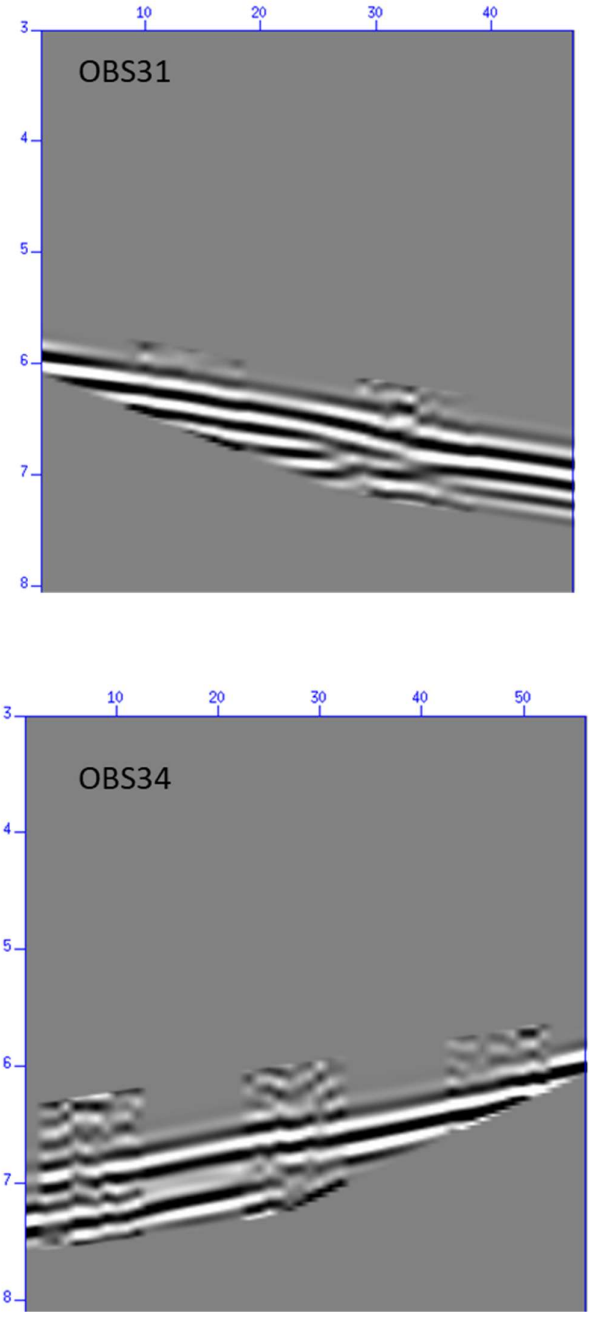

Figure B 2 follow on

Appendix C Distribution of crustal melt bodies at the hotspot-influenced section of the Galápagos Spreading Centre from seismic reflection images

B. Boddupalli[1] and J. P. Canales[2]

[1]National Oceanography Centre Southampton, University of Southampton, Southampton, SO14 3ZH, UK

[2]Department of Geology and Geophysics, Woods Hole Oceanographic Institution, Woods Hole, MA 02543, USA

Key Points

- Seismic images from the hotspot-influenced section of the Galápagos spreading centre reveal a multi-sill magmatic system in the lower crust.
- Spatial correlation between a gap in the axial melt lens and the location of a mature, waning seafloor hydrothermal field suggests magmatic-hydrothermal interactions.
- Evidence for off-axis melt lenses emplaced at the edges of the axial low velocity zone, and weak Moho reflections on the across ridge axis seismic profile, which disappear in the axial zone.

Abstract

Accretion of the lower crust at mid-ocean ridges is a debated topic, with modern seismic observations pointing to a complex magmatic system that includes an axial multi-sill system of mid- and lower-crustal melt lenses, and near- and off-axis melt bodies. Here we revisit the hotspot-influenced section of the western Galápagos Spreading Centre, and re-process multichannel seismic reflection data using a wide-angle seismic tomography model. Our new images show that the magma reservoir in the lower crust at this ridge section is intruded with partially molten melt lenses. The images also show evidence for off-axis melt lenses, magmatic-hydrothermal interactions and Moho reflections in this region. We conclude that the similarities between the axial crustal structure of this hotspot-influenced mid-ocean ridge and the multi-sill magmatic structure imaged at the East Pacific Rise indicate that these features are common along the global mid-ocean ridge system where seafloor spreading is dominated by magmatic accretion.

Plain Language Summary

New oceanic crust forms along mid-ocean ridges from melt extracted from the upwelling mantle. Accretion of the upper crust is well understood, but the process involved in the accretion of the lower crust is still debated. Here we present new seismic images of the crustal magmatic system of the western Galápagos Spreading Centre in the region where the influence of the Galápagos hotspot is largest and ridge magmatism is most robust. Our images show a complex magmatic system that includes lenses of partially molten rock beneath the spreading axis from the mid-crust at 1.5 km and throughout the lower crust down to at least 5.4 km below the seafloor, and off-axis melt bodies. Segmentation of the axial magmatic system correlates with presence of hydrothermal features on the seafloor. This system has characteristics very similar to those recently imaged at the East Pacific Rise, indicating that these features are representative of crustal accretion at mid-ocean ridges where seafloor spreading is dominated by magmatic processes.

1. Introduction

Seismic reflection imaging has been instrumental for the study of the physical structure of magmatic systems beneath intermediate to (ultra)fast-spreading mid-ocean ridges (MORs) where seafloor spreading is magmatically dominated (e.g. Detrick et al., 1987). Studies from the late 1980's through the 2000's showed that the upper oceanic crust is constructed from dyking and sea-floor eruptions from magma that accumulates predominantly within a thin axial melt lens (AML) at ~1-3 km below seafloor (bsf) (e.g. Kent et al., 1993). The AML marks the top of a broad region characterised by low seismic velocities and high attenuation indicative of elevated temperatures and partial melt (e.g. Dunn et al., 2000; Wilcock et al., 1995). However, the absence in those early studies of other crustal reflectors in the axial region, aside from the AML, contributed to the debate of possible models about melt transport from the mantle to the AML and the accretion of the lower crust (e.g. Maclennan et al., 2004).The possible models range from the lower crust crystallizing from the shallow AML (i.e., gabbro glacier model) (Henstock et al., 1993; Quick & Denlinger, 1993) to a dual- or multi-sill models (Boudier et al., 1996; Kelemen et al., 1997). Our understanding about crustal accretion has been changing during the last decade as improved seismic reflection images from different settings provided evidence for more complex crustal magmatic systems. Recent evidence include segmentation of the AML (Carbotte et al., 2013; Marjanović et al., 2018), crustal axial melt sills below the AML (Arnulf et al., 2014; Marjanović et al., 2018), lower crustal sills in the near axis region (Canales et al., 2009), and off-axis magmatic systems (Aghaei et al., 2017; Canales et al., 2012; Han et al., 2014).

The relationship between the recent seismic observations of crustal sills and the axial low velocity zone (LVZ) imaged by seismic tomography is unclear due to the paucity of co-located wide-angle seismic velocity models and modern multichannel seismic (MCS) images. The three-dimensional (3-D) MCS study of the East Pacific Rise (EPR) at 9°38'-57'N (Mutter et al., 2009) indicates that off-axis melt lenses (OAMLs) form close to but outside of the axial LVZ (Canales et al., 2012; Han et al., 2014), based on two-dimensional (2-D) and 3-D wide-angle tomography models from nearby regions (Canales et al., 2012; Dunn et al., 2000). However other features such as sub-axial melt lenses (SAMLs) (Marjanović et al., 2014) lack background P-wave velocity models that would add context and additional constraints to their interpretation.

In this work, we revisit the hotspot-influenced section of the western GSC where coincident 2-D MCS data (Blacic et al., 2004) and 3-D crustal tomography models are available (Canales et al., 2014). Previous studies using the MCS dataset focused on post-stack time-migrated imaging of the Moho ~20-30 km to the north of the ridge axis (Canales et al., 2002), and shallow axial and near-axis structure (layer 2A thickness and depth to the AMLs) (Blacic et al., 2004). However, mid- and lower crustal structure in the near-axis region was not addressed in those studies. Here we use a pre-stack depth migration approach to reprocess the MCS data with the assistance of the tomography-derived P-wave velocity model (Canales et al., 2014). Our new images reveal new features that were not observed in the existing post-stack time-migrated images, which we interpret as OAMLs and SAMLs, in addition to the previously recognized AML and Moho reflectors. We then conduct a joint interpretation of the new observations and the existing 3-D P-wave velocity model that allows us to explore the spatial relationships between the tomography-inferred magma reservoirs and the MCS-imaged melt lenses.

2. Tectonic setting

The GSC forms a divergent plate boundary separating the Cocos plate from the Nazca plate, currently spreading at intermediate rates increasing eastwards from 53 mm/yr at 97° W to 58 mm/yr at 91° W (full rates) (Wilson & Hey, 1995). Seafloor spreading in this region initiated 25 Myr ago with the breakup of the Farallon plate along a fracture zone near the Galápagos hotspot (Hey & Vogt, 1977). The Galápagos hotspot is located ~200 km south of the GSC near 92° W on the western edge of the Galápagos Archipelago. The Galápagos transform fault (TF) located near 90°50' W divides the GSC into two sections: western and eastern (e.g., Christie et al., 2005; Sinton et al., 2003).

Along the western GSC, the influence of the hotspot is most pronounced between 93.25° W and the 90°50' W TF, where the ridge forms a 20-30 km-wide, 400-700 m high axial high with mantle Bouguer anomaly (MBA) and crustal thickness reaching their minimum and maximum, respectively,

along the axis (Canales et al., 2002; Detrick et al., 2002; Ito &Lin, 1995). In this region, complex volcanic lineaments extending between the Galápagos Islands and the GSC are inferred to be a result of the interplay between plume-ridge interactions and lithospheric stresses (Harpp & Geist, 2002; Mittelstaedt et al., 2012). Multibeam bathymetric studies have revealed the fine-scale axial segmentation (<2 km), with right-stepping offsets on the spreading axis attributed to the southward displacement of the axis where volcanic lineaments intersect the ridge (Sinton et al., 2003). An extensive near-bottom hydrographical survey along the GSC between 91°10'W and 94°30'N found evidence for surprisingly scarce high-temperature hydrothermal venting (Baker et al., 2008), with only two confirmed active black smoker fields in the hot-spot influence section of the western GSC near 92°W (Figure C-1) and one near 94°W (Haymon et al., 2008).

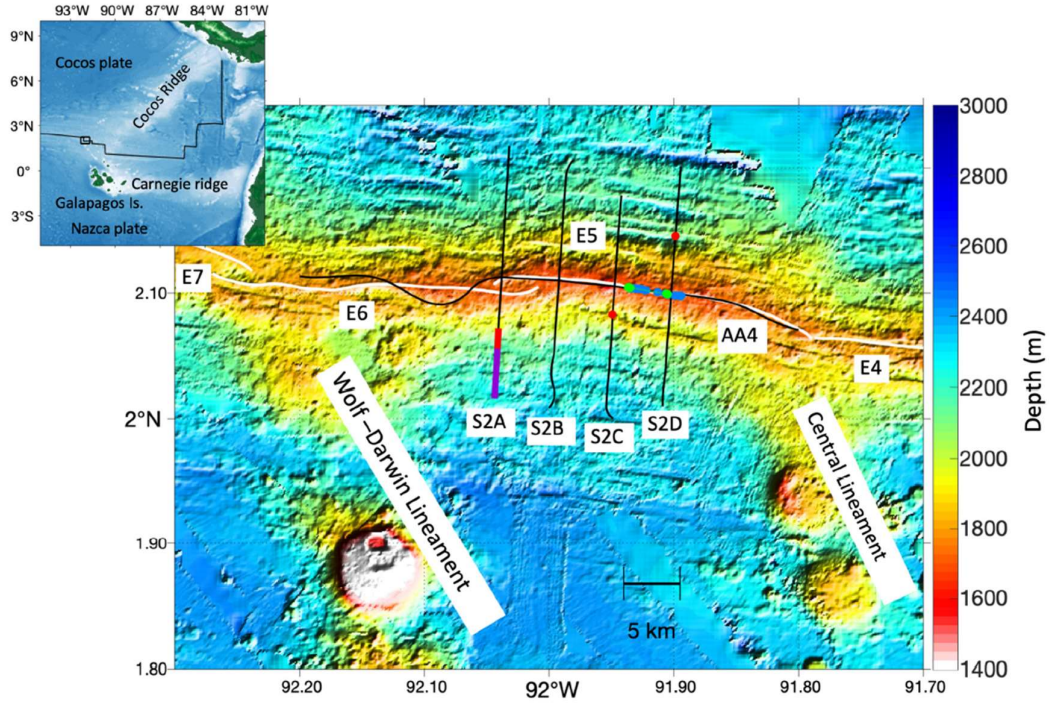

Figure C 1 Bathymetry map of the Eastern Province of the western GSC (following the nomenclature of Sinton et al. (2003)) near the Wolf-Darwin and Central volcanic lineaments (Mittelstaedt et al., 2012). Ridge axis as defined by Sinton et al. (2003) is shown with a white solid line, and EW0004 seismic profiles AA4, S2A, S2B, S2C and S2D used in this study are shown in black bold curves. The location of the OAMLs and the Moho reflections on profiles S2A, S2C and S2D shown in Figures 2 and 3 are highlighted by red and dark violet, respectively. Between the profiles S2C and S2D, we highlight active and inactive black smoker fields in green and blue dots, respectively, along the AA4 profile. The two highlighted active black smoker fields going west to east are the Iguanas and the Pinguinos. Inset shows location of the study area in the eastern Equatorial Pacific.

East of 92.5° W, crustal thickness is 7.5 km (Canales et al., 2002; Canales et al., 2014), and the depth of the ~0.5-1.5-km-wide axial melt lens (AML) as observed in the multichannel seismic reflection imaging is 1.0-2.5 km bsf (Blacic et al., 2004). The variation in the thickness of the layer 2A as observed on the time-migrated seismic sections nearly increases by 150% away from the axis where it is 0.24-0.42 km thick (Blacic et al., 2004). Results from wide-angle seismic tomography predict melt throughout the lower crust with a lower crustal reservoir at 3-4 km bsf containing up to ~2%-7% melt (dependent on melt topology) (Canales et al., 2014). The alignment of these reservoirs with depth is not vertical, but rather shows a gradual shift towards the south flank of the ridge axis (Canales et al., 2014). It is proposed that the Moho reservoir feeds the lower-crustal reservoir which in turn feeds magma to the mid-crustal melt lens (Canales et al., 2014). The high magma supply in the proximity of the hotspot favours the formation of the mid-crustal reservoir, and also imparts greater chemical signature variations to the magma (Rubin & Sinton, 2007).

3. Data and Processing

Multichannel and wide-angle seismic datasets at the GSC were acquired as part of cruise EW00-04 during April-May, 2000, on R/V Maurice Ewing (Detrick & Sinton, 2014). In the reflection survey, ~86% of the length of the ridge axis between ~95.5° W and 91.25° W was surveyed, with nearly 100% coverage east of 94.5° W. Fifteen cross-axis profiles were also acquired, which extended at least 10 km north and south of the ridge. In this study, we have reprocessed five of the EW00-04 seismic profiles located near 92°W between the Central and Wolf-Darwin (WDL) volcanic lineaments: one along the ridge axis and four perpendicular to the ridge axis (Figure C-1). The airgun system was comprised of two arrays of 10 air guns (total volume of 8755 cu in.) towed at a depth of ~8 m. Shooting interval was 15 s with a 50-ms randomization window to minimize noise from previous shots. The shot interval and ship speed of 4.5 kts yielded ~38 m shot spacing. A 6-km-long, 480-channel streamer was used to record 10 s of data at a sampling interval of 4 ms. The 480 channels of the streamer with spacing of 12.5 m resulted in 80-fold common-midpoint (CMP) gathers.

The pre-stack processing sequence consisted of (Figure C-S3A): (1) Common mid-point geometry definition for all seismic data traces. (2) Bandpass filtering (1-6-100-125 Hz). (3) Noise attenuation using the LIFT method, a processing technique that suppresses noise while reconstructing signal to its original form preserving amplitude integrity (Aghaei et al., 2014; Choo et al., 2004; Han et al., 2016) (Figure S3B). (4) Offset-dependent spherical divergence correction to compensate for geometrical spreading. (5) Surface-consistent amplitude balancing to normalize abnormally high/low shot and channel amplitudes. (6) Seafloor primary multiple mute to reduce migration noise.

Following the processing, we applied a pre-stack depth migration (PSDM) algorithm based on decomposition of the wavefield into plane waves and depth imaging using a wave-equation, finite-difference frequency-distance (FX) pre-stack migration of each plane wave (Soubaras, 1996). The 2-D velocity models used for PSDM were extracted from a 3-D velocity model derived from ocean bottom hydrophone (OBH) wide-angle tomography (Canales et al., 2014). For migration of the along-axis profile, a 1-D velocity profile was extracted from the location of intersection of the north-south oriented OBH line with the ridge axis due to limited coverage of the rays along the ridge axis in the OBH survey. This profile was attached to the bottom of the water column velocity profile along the profile AA4 and extrapolated to 15 km depth. For migration of the cross-axis profiles, a 2-D velocity profile was extracted from the 3-D tomography model along the cross-axis OBH line and extrapolated to 15 km depth (Figure C-S1). Then the 2-D model was adjusted to the bathymetry data along each individual cross-axis profile. Post-migration steps included FK enhancement of flat events, lateral mean filter and depth-dependent gain.

4. Results and Discussion

Compared to the previous post-stack time migrated images of Blacic et al. (2004), our new PSDM images show a similar AML distribution, but significant improvement in the imaging of features below the AML and in the near-axis region (Figures C-2, 3). One important difference is our PSDM images do not image the base of Layer 2A, which was well resolved in the Blacic et al. (2004) sections. The reasons for this observation are that the velocity model is poorly constrained at shallow depths, and that the base of Layer 2A is in most cases a high-gradient zone instead of a true reflector that is best imaged by stacking the far-offset retrograde branch of the 2A refraction (Harding et al., 1993). To aid our interpretation, we show our 2-D PSDM sections together with bathymetry and location of the ridge, and with P-wave velocity variations (relative to a 1-D structure, Figure S2) extracted from the 3-D velocity volume to highlight the correlation between LVZs and the identified features. We identify several interesting features in our images: AML, OAMLs, SAMLs and the Moho.

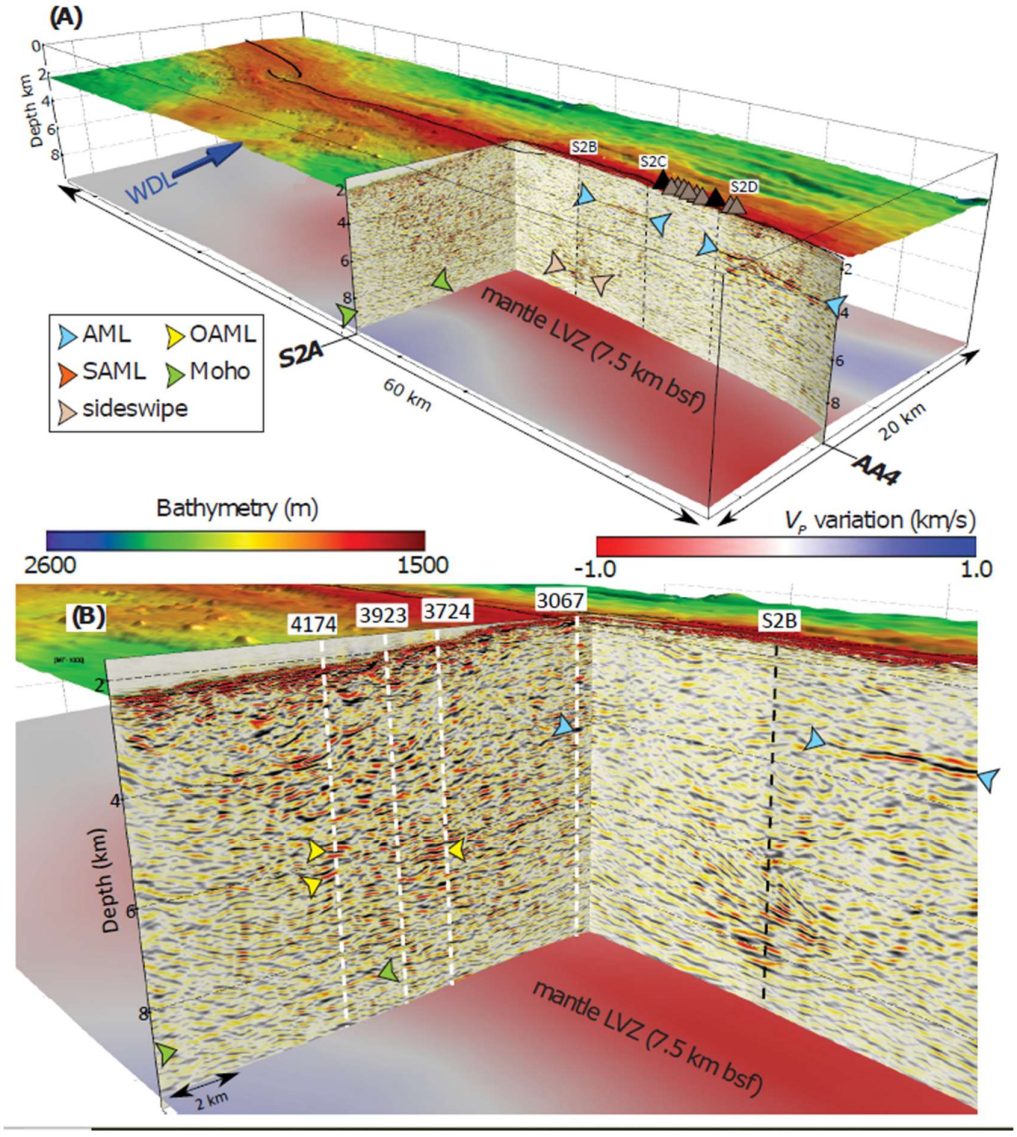

Figure C 2 Three-dimensional perspective of bathymetry, P-wave velocity structure at a depth of 7.5 km below seafloor, and migrated sections for profiles AA4 and S2A. Coloured arrowheads point to the most prominent crustal events interpreted in this study: Axial melt lens (AML), sub-axial melt lens (SAML), off-axis melt lens (OAML), and the Moho. Note Moho reflections are observed away from the mantle low velocity zone (LVZ) but are absent above it within ~3 km of the ridge axis. The dashed vertical lines are the intersection of the profiles S2B, S2C and S2D with profile AA4. Ridge axis is shown with solid lines, and the blue arrow indicates the Wolf-Darwin lineament (WDL). The active and inactive black smoker fields are marked as black and grey triangles, respectively, along the profile AA4. (B). Zoomed-in view of profiles S2A and AA4, with P-wave velocity variation shown at 7.5 km bsf. OAMLs tend to be located at or near the edge of the crustal LVZ, ~3-5 km off axis. P-wave velocity structure is shown as variation relative to a 1-D reference model from the 3-D tomography model of Canales et al. (2014). Labeled dashed vertical white lines locate the CMP supergathers shown in Figures 4 and 5.

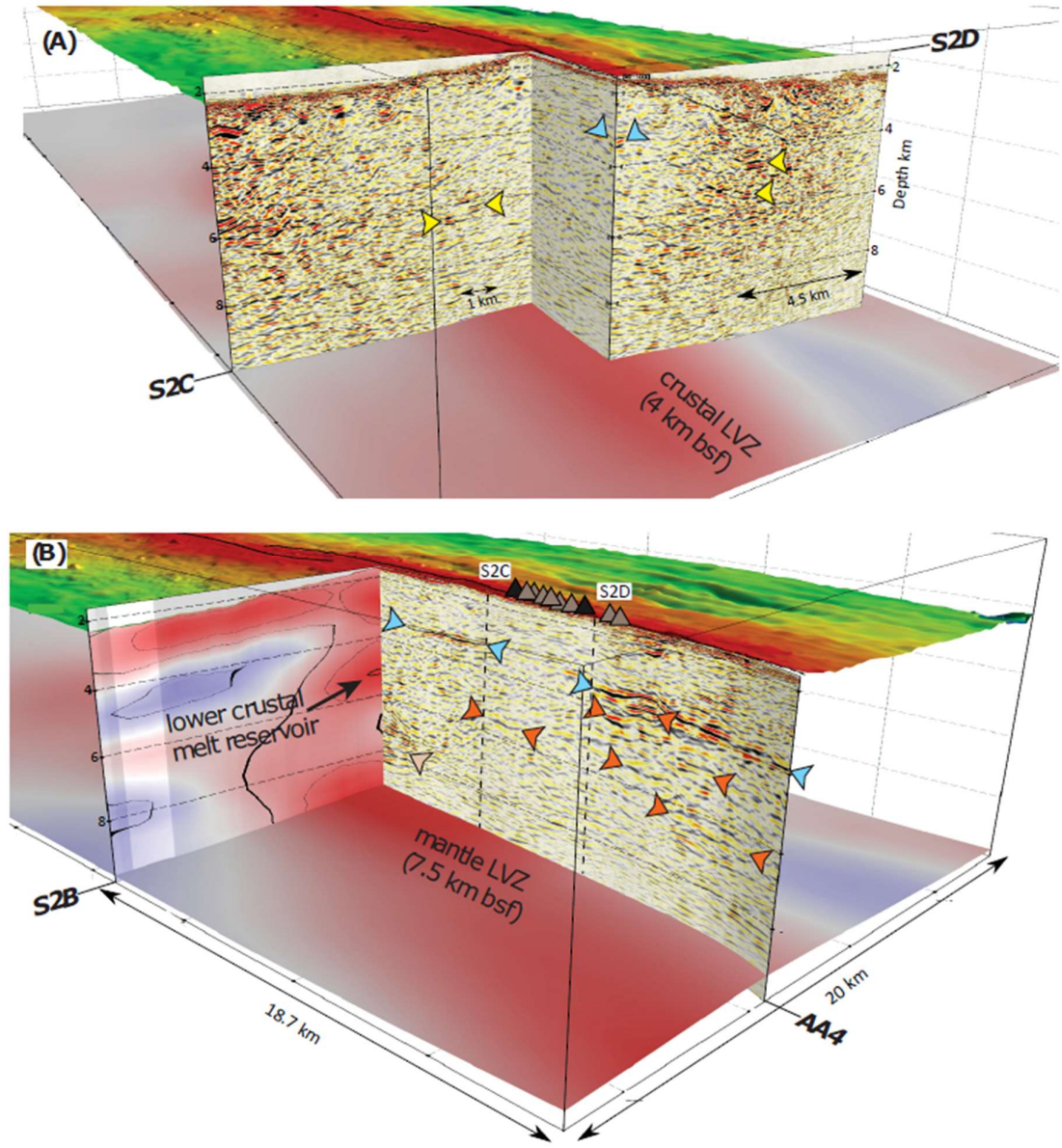

Figure C 3 Three-dimensional perspective of bathymetry, migrated sections for profiles AA4, S2C and S2D, and P-wave velocity structure at the depth of 4 km below the seafloor. Note that the velocity slice is shifted down by 4 km in depth for the sake of visual clarity. OAMLs tend to be located at or near the edge of the crustal LVZ, ~4-5 km off axis. (B) Three-dimensional perspective of bathymetry, P-wave velocity structure at a depth of 7.5 km below seafloor and along profile S2B, and migrated sections for profile AA4. SAMLs are located up to ~2.5 km below the AML within a lower crustal melt reservoir (Canales et al., 2014). P-wave velocity perturbation along S2B is shown with contours every 0.25 km/s (except the 0 km/s contour) to emphasize the lower crustal melt reservoir. Legend for coloured arrowheads and other features as in Fig. 2. The active and inactive black smoker fields are marked as black and grey triangles, respectively, along the profile AA4.

4.1. Axial melt lens (AML)

The AML in our images is a discontinuous feature along the axis of segment E5 at depths of 1.4-2 km bsf. This apparent variability was previously reported by Blacic et al. (2004), and it likely represents true geological small-scale segmentation of the AML, as observed in other similar setting (Carbotte et al., 2016). Although the AML spatial variability could also be an artefact due to data acquisition problems such as streamer feathering or deviations of the profile from the axis, we find this possibility unlikely because maximum deviation of profile AA4 from the morphological axis occurs between profiles S2B and S2C (Figure C-1), where the AML is well imaged (Figure C-2A).

None of our cross-axis profiles cross the ridge in locations where the AML is most prominently imaged on AA4. The intersection of profiles S2A and AA4 occurs at an overlapping spreading centre (OSC) with offset <2 km (Figure C-2), which is a result of the southward displacement of segment E6 due to the influence of the WDL (Sinton et al., 2003). The AML on S2A is identified below the southern limb of the OSC at depth of 2.2-2.4 km bsf (Figure C-2B). Profiles S2B, S2C and S2D are located near the edges of the AML segments (Figure C-2A), although we see clear AML reflection sitting at the top of the LVZ at a depth of 1.5 km bsf at the intersection of profiles S2D and AA4 (Figure C-3A).

A striking feature is the ~4-km-long gap in AML found at the centre of segment E5, roughly between the locations of profiles S2C and S2D (Figure C-2A). Interestingly, this AML gap coincides spatially with the Iguanas-Pinguinos Hydrothermal Field (IPHF) (Haymon et al., 2008) (Figure C-2A, C-3B). This mature and waning field is characterized by clusters of high-temperature active black smoker chimneys that are located over the edges of the AML gap (Figure C-3B): the Iguanas black smokers over the transition between the AML gap and the AML reflector to the west of profile S2C, and the Pinguinos black smokers over the transition between the AML gap and the AML reflector to the east of profile S2D. The IPHF includes scores of recently inactive chimneys and vent biological communities distributed between the active sites over the AML gap (Figure C-3B). Aside from prominent plume anomalies over the IPHF, the hydrographic surveys in this region did not detect significant plume activity anywhere else along segment E5 except weak plume signals further east to 91.8°W (Baker et al., 2008) over the prominent AML section east of profile S2D (Figure C-3B). Based on these observations, we suggest that the current characteristics of the IPHF and the underlying AML segmentation are linked to each other. If AML segmentation is controlled by melt delivery from the mantle and lower crustal melt focusing (Carbotte et al., 2013), then the AML gap represent a decrease in melt delivery from the mantle or the lower crust to the AML at lateral scales of a few km. The decrease of melt influx to the AML and its eventual solidification would then have resulted in waning of hydrothermal activity at the IPHF (i.e., a bottom-up model of magmatic-

hydrothermal interactions), as evidenced by the inactive chimneys. At present, high-temperature circulation is restricted to the edges of the AML gap where fluids can tap heat form the neighbouring, more melt rich AML segments. Alternatively, numerical models indicate that AML segmentation can be influenced by hydrothermal circulation cooling and solidifying the AML (Fontaine et al., 2011). In this case, favourable upper crustal permeability conditions could have led to localization of vigorous hydrothermal activity in the IPHF, as evidenced by the scarce hydrothermal plume activity in the other regions of segment E5. In this top-down model of magmatic-hydrothermal interactions, hydrothermal convection eventually leads to solidification of the AML and formation of the gap under the IPHF. As in the bottom-up scenario, solidification of the AML would lead to waning of hydrothermal activity and focusing of black smoker activity at the edges of the AML gap.

4.2. Sub-axial melt lenses (SAMLs)

On the along-axis seismic section AA4, we observe horizontal, discontinuous reflections below the AML which we interpret as lower-crustal magma sills (Figure C-3), similar to those observed at the EPR (Marjanović et al., 2014). Assuming the dominant data signal frequency of our data is ~10-25 Hz and the background P-wave velocity is 6.5 km/s (Canales et al., 2014), the strongest responses will be from the melt lenses of thickness between ~65-160 m as a single reflector. Lenses with thickness greater than 160 m will be characterized by a pair of opposite polarities from the top and the bottom interface of the lens, which we do not observe in our images.

The identified sills are more prevalent within the depth range where the tomography-derived crustal LVZ is most prominent. Although the 3-D traveltime tomography velocity model does not resolve small-scale structures of the size of a single sill (Canales et al., 2014), the migrated MCS data show that sills form within this crustal section interpreted as a lower-crustal reservoir containing up to 7 % melt (Canales et al., 2014). These authors proposed that the formation of the intermediate crustal reservoir is favoured by a thicker crust due to increased magma supply under the influence of the hotspot. With an increased crustal thickness, the melt extracted from the sub-Moho reservoir travels longer distances towards the AML, thus providing more opportunities for developing permeability barriers within crystallizing gabbros (Kelemen & Aharonov, 1998).

The observation of SAMLs in the region between profiles S2C and S2D where the AML is absent (Figure C-3B) suggests that transfer of melt from the lower crustal reservoir to the shallow crustal reservoir is episodic and requires a melt fraction threshold in the SAML to be exceeded before melt if transferred from the SAML to the overlying AML, probably via hydrofracturing (Korenaga & Kelemen, 1998). Alternatively, if the AML receives melts from the SAML via continuous porous flow

(e.g., Lissenberg et al., 2013), then melt solidification in the AML by hydrothermal cooling in this region has to be more efficient than AML replenishment from below.

4.3. Off-axis melt lenses (OAML)

Along the cross-axis profiles we have identified events located ~4-6 km away from the axial centre and at depths between 3-5 km bsf (Figure C-2, 3) that we interpret as OAMLs. This interpretation is based in part on the character of these events as observed in unmigrated super-CMP gathers, which is similar to the character of the AML event (Figure C-4, 5). In the cross-axis direction, the AML is observed as a near-offset reflection at 0.94 s twtt bsf (Figure C-4A), and the OAMLs are observed also as near-offset reflections at ~1.1-1.6 s bsf (Figure C-4B, C). Most importantly, some of the OAML events have the same waveform polarity as the AML, which is reversed relative to the seafloor reflection polarity (Figure C-5). A reversed polarity is indicative of a velocity inversion, and it has been traditionally used as evidence for the partially molten character of AMLs at MORs (Canales et al., 2012; Collier & Sinha, 1992; Detrick et al., 1987). We cannot however confirm that all of the OAMLs events we have identified have reversed polarity; in many cases steeply dipping diffractions or multiples prevent confident assessment of the OAML polarity (Figure C-4C). However, this does not invalidate our interpretation because apparently normal or ambiguous waveform polarity of partially molten sills is common in MOR seismic reflection studies (e.g., Arnulf et al., 2014; Collier and Sinha, 1992; Detrick et al., 1987).

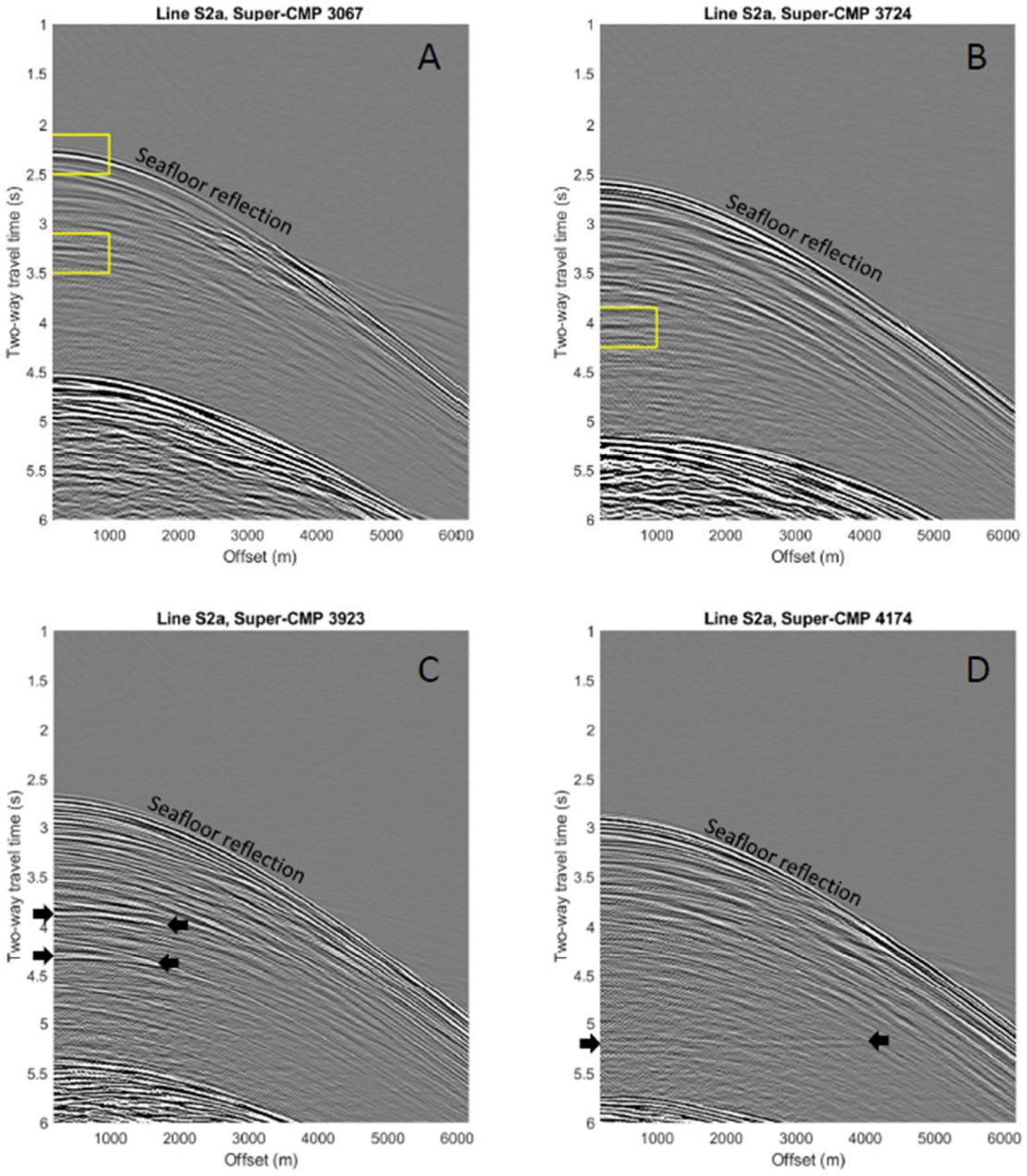

Figure C 4 CMP supergathers from profile S2A. Each supergather is constructed by stacking and gathering 480, 5-fold common-offset gathers from 30 consecutive CMPs. Locations are marked as dashed white lines in the Figure 2B. A) CMP 3067 showing the AML at 3.25s. Data within yellow boxes are shown in Figure 5A, B for seafloor and AML, respectively, to illustrate the reversed polarity of the AML event. B) CMP 3724 showing OAML at ~4s. Data within yellow box are shown in Figure 5C to illustrate the reversed polarity of the OAML event. C) CMP 3923 showing two prominent OAMLs at 3.8s and 4.25s (shown between the black arrows). D) CMP 4174 showing Moho reflections at ~5.15 s extending into the far-offsets (shown between the black arrows).

Under the southern flank of the GSC, the presence of OAMLs could be related to increased magmatism associated to the Wolf-Darwin and Central lineaments (Mittelstaedt et al., 2012; Sinton et al., 2003), which are accompanied by a southward shift of the axial mantle LVZ (Figure 2A). However, OAMLs are also observed beneath the northern ridge flank (Figure C-3A), and in both cases these events tend to be located near the edges of the axial crustal LVZ. This situation is similar to the OAMLs observed off the EPR (Canales et al., 2012), and suggests that these features form in a region of strong thermal and rheological gradients (e.g., Menand, 2011) where crustal cooling may favour the solidification of melt near the edges of the axial crustal melt reservoir. Alternatively, off-axis melt emplacement may be a response to bending stresses that promote vertical melt extraction from a sub-lithospheric melt channel, although this mechanism is more efficient at distances of ~10-20 km from the ridge axis (Sohn & Sims, 2005).

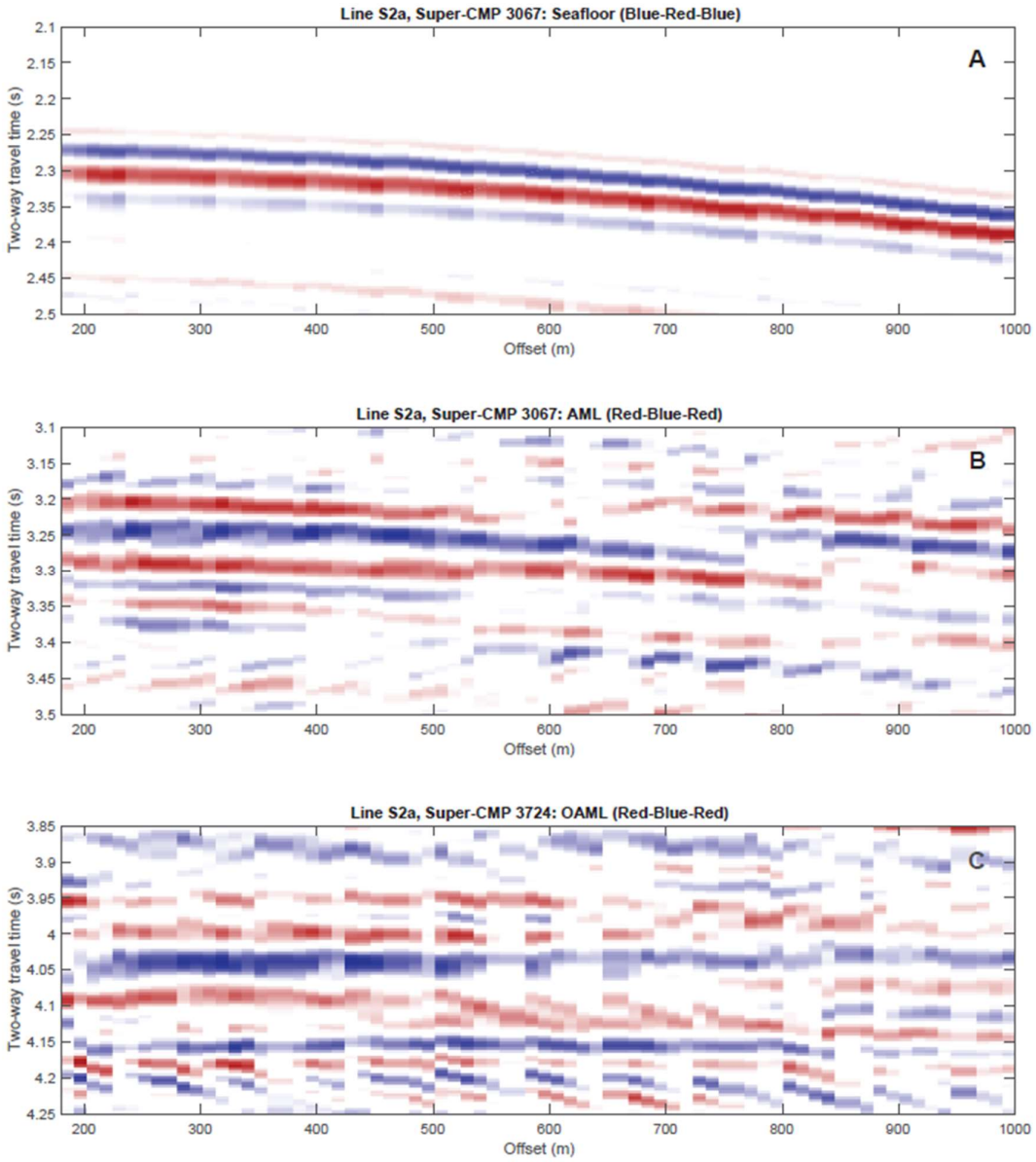

Figure C 5 A) Near-offset seafloor reflections from CMP 3067 (yellow box around 2.3s in Figure 4A) showing normal polarity (blue-red-blue waveforms). B) Near-offset AML reflections from CMP 3067 (yellow box around 3.25 s in Figure 4A) showing reversed polarity (red-blue-red waveforms). C) Near-offset OAML reflections from CMP 3724 (yellow box around 4.05 s in Figure 4B) showing reversed polarity (red-blue-red waveforms).

4.3. Moho

We observe reflections beneath the southern ridge flank along cross-axis profile S2A at 6.7 km depth bsf that we interpret as Moho (Figure C-2). In unmigrated gathers, the Moho is observed as a nearly flat (small moveout) event at ~2.3 s bsf from near to far offsets (Figure 4D), a character typical of Moho events in the vicinity of MORs (e.g., Aghaei et al., 2014; Canales et al., 2009;

Nedimovič et al., 2005). We observe that the polarity of the Moho matches that of the seafloor reflection (Figure C-S4). Our crustal thickness measurement is ~750 m thinner than the 7.45±0.25 km inferred from wide-angle seismic data ~25-30 km to the north of the ridge axis in this region (Canales et al., 2002). This discrepancy could be due to north-south variation in crustal thickness in the study area, and/or due to the different ways that near-vertical and wide-angle seismic data sample a Moho transition zone of finite thickness (e.g., Mutter & Carton, 2013). An important observation is that Moho reflection amplitude diminishes relatively abruptly towards the axial zone, eventually disappearing over the tomographically-inferred mantle LVZ within ~3 km of the ridge axis (Figure C-2). This is most likely due to a combination of attenuation of seismic energy traveling through the axial crustal LVZ (Wilcock et al., 1995), and that Moho across the mantle LVZ may not correspond to a large impedance contrast due to elevated temperatures and presence of melt (13% melt) (Canales et al., 2014). The seismic energy gets significantly attenuated within the axial magma chamber, so a sharp contrast in physical properties is required to be present at the Moho for it to be clearly imaged in a seismic section (Singh et al., 2006; Wilcock et al., 1995).

A short, high amplitude reflection is observed along profile AA4 at its intersection with profile S2B at Moho depths (Figure C-2A, 3B). Although this event could be interpreted as evidence for on-axis Moho or a partially molten sill at or just above the Moho, we prefer to interpret this event as an artefact due to out-of-line side echoes because it is absent on the perpendicular profile S2B and it is accompanied by migration “smiles” characteristic of over-migration, suggesting its origin is somewhere shallower in the system where velocities are lower.

5. Conclusions

In this study, we have performed pre-stack depth migration of 2-D MCS reflection data to provide new constraints on the structure of the axial magma system of the western GSC, using background P-wave velocities previously derived from the 3-D seismic refraction tomography. In our new PSDM images, we observe segmentation of the shallow axial melt lens. A prominent AML gap underlays a mature and waning hydrothermal field, evidencing magmatic-hydrothermal interactions. Here high-temperature hydrothermal activity is restricted to sites over the edges of the AML gap, suggesting that fluids tap heat from the neighbouring AML segments to the west and east of the gap. We also observe sub-axial melt lenses intruding and accreting the lower crust. Some of these SAMLs are present even where the AML is absent, suggesting that melt transfer from the lower crustal reservoir to the shallow AML is episodic. We find evidence for off-axis melt lenses forming at the edges of the tomographically imaged axial low velocity zone, which suggests that off-axis melt lenses form preferentially in a region with large rheological contrasts. Moho reflections are observed at distances larger than ~3 km from the axis, but disappear abruptly across the axial low

velocity zone where elevated temperatures and presence of partial melt increase the attenuation and diminish the impedance contrast across the crust/mantle boundary.

From the above observations, we conclude that the similarities of the GSC magmatic system (i.e., presence of off-axis and lower crustal sills) with that of the EPR support the idea that these are features found along the global mid-ocean ridge system where seafloor spreading is dominated by magmatic accretion.

Acknowledgments

Seismic data used in this study are available at https://doi.org/10.1594/IEDA/314480 (Detrick & Sinton, 2014). Data processing was conducted with Emerson-Paradigm Software package *Echos* licensed to Woods Hole Oceanographic Institution under Paradigm Academic Software Program. B. B. is funded by the Graduate School of the National Oceanography Centre Southampton UK. We thank two anonymous reviewers for their constructive and insightful comments which helped us in improving the manuscript, and A.S. Soule for fruitful discussions.

Supplementary

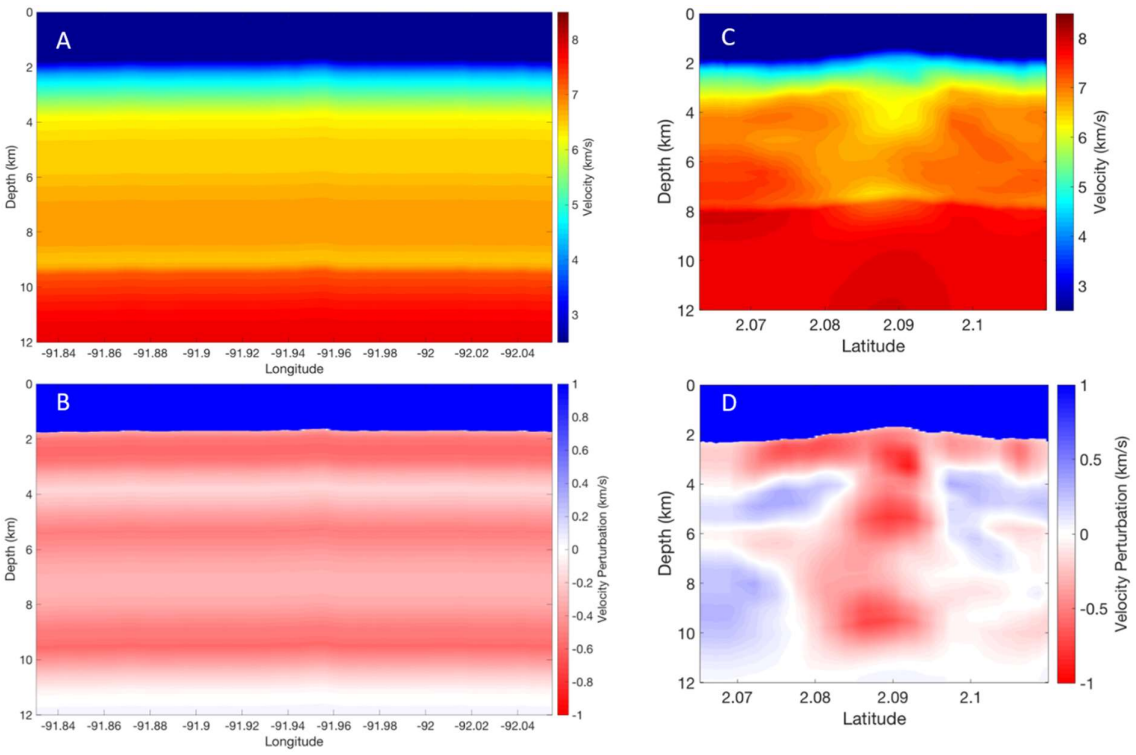

Figure C-S1. Velocity models used for migration along (A) and across axis (C) profiles with their 3 respective velocity perturbations plotted below.

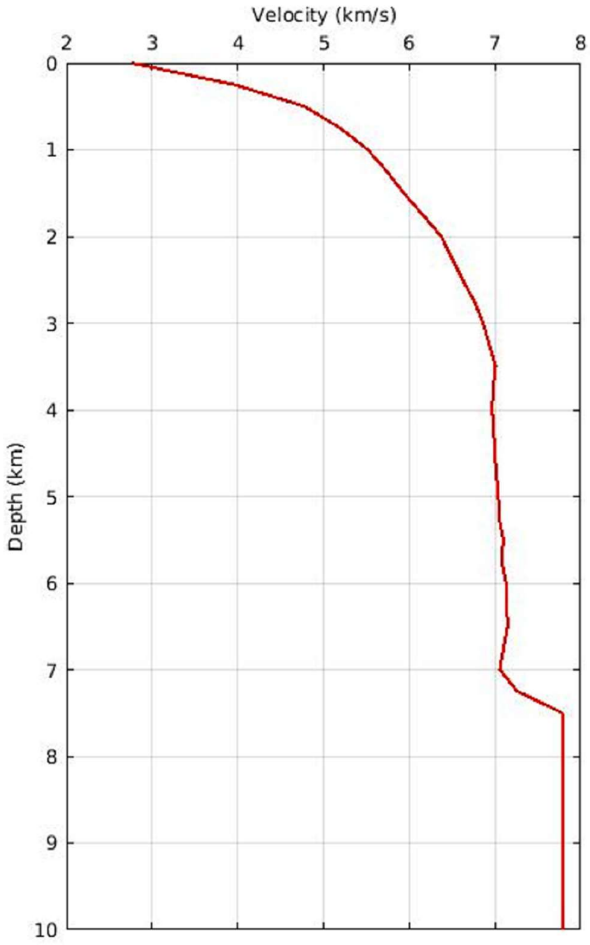

Figure C-S2. Reference velocity model

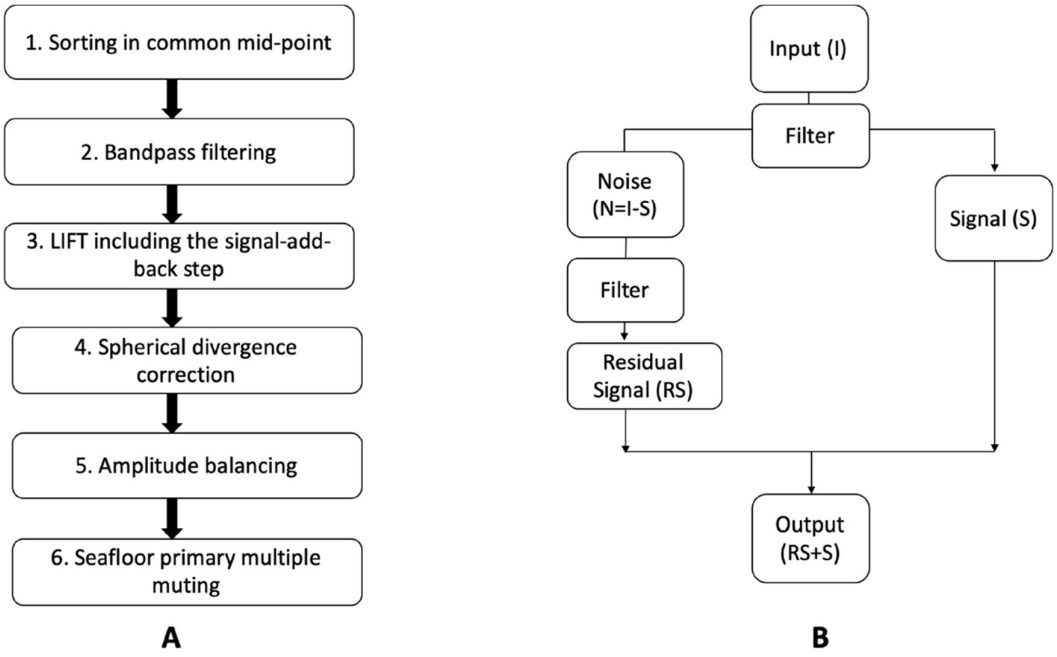

Figure C-S3. A) Seismic data processing flow. B) Flow chart explaining the signal-add-back-step of the LIFT method. In this method the data are divided first into three frequency bands: low-frequency (low-pass filter, passband frequency: 15 Hz, stopband frequency: 20 Hz), high-frequency (high-pass filter, stopband frequency:20 Hz, passband frequency:25 Hz), and intermediate frequency (obtained by subtracting the low-frequency and high-frequency bands from the original data). Then a signal and a noise component are separated for each frequency band using filtering techniques. Optionally, the noise component can be reprocessed to separate a residual signal component, which is then added back to the signal component (i.e., signal-add-back step). Finally, the cleaned signals of the three frequency bands are combined form the LIFT-filtered shot gathers. In our case, low-frequency swell and streamer noise was suppressed in the low-frequency band by applying a frequency-wave number (FK) filter. A median filter was applied to all frequency bands to suppress amplitude spikes. The signal-add-back step was performed for intermediate and high frequency bands.

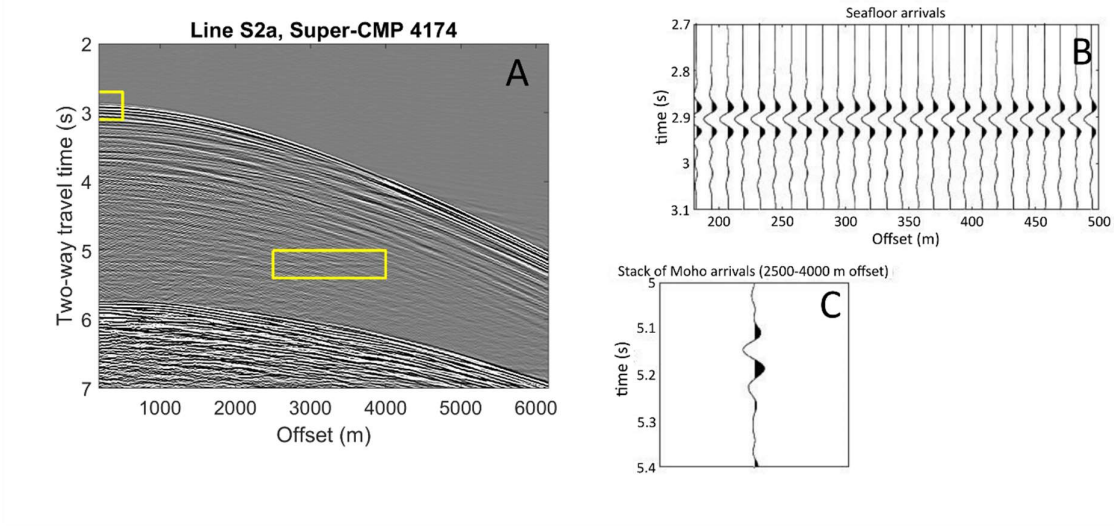

Figure C-S4. A) Representative CMP supergather (4174) showing the Moho reflection at ~2.3 s bsf. Data within yellow boxes is the near offset seafloor reflection shown in B) and the Moho reflections where the signal to noise ratio is high. C) To see the polarity of the Moho we stacked the traces from offsets 2500-4000 m within the yellow box. We observe that the Moho waveform shows same polarity as the seafloor indicating positive impedance contrast at the Moho.

Bibliography

Abma, R., & Claerbout, J. (1995). Lateral prediction for noise attenuation by t-x and f-x techniques. *Geophysics*, *60*(6), 1887–1896. https://doi.org/10.1190/1.1443920

Aghaei, O., Nedimovič, M. R., Carton, H., Carbotte, S. M., Canales, J. P., & Mutter, J. C. (2014). Crustal thickness and Moho character of the fast-spreading East Pacific Rise from 9°42′N to 9°57′N from poststack-migrated 3-D MCS data. *Geochemistry, Geophysics, Geosystems*, *15*(3), 634–657. https://doi.org/10.1002/2013GC005069

Aghaei, O., Nedimović, M. R., Marjanović, M., Carbotte, S. M., Canales, J. P., Carton, H., & Nikić, N. (2017). Constraints on melt content of off-axis magma lenses at the East Pacific Rise from analysis of 3-D seismic amplitude variation with angle of incidence. *Journal of Geophysical Research: Solid Earth*, *122*(6), 4123–4142. https://doi.org/10.1002/2016JB013785

Agudo, O. C. (2018). *Acoustic full-waveform inversion in geophysics and medical imaging*. Imperial College London. https://doi.org/10.25560/62620

Aki, K., & Richards, P. G. (2002). *Quantitative seismology* (Vol. II). W.H. Freeman and Company.

Alford, R. M., Kelly, K. R., & Boore, D. M. (1974). Accuracy of finite-difference modelling of the acoustic wave equation. *Theory and Applications of Transport in Porous Media*, *39*(6), 834–842. https://doi.org/10.1007/978-3-319-61185-3_16

Arnulf, A. F., Singh, S. C., & Pye, J. W. (2014). Seismic evidence of a complex multi-lens melt reservoir beneath the 9° N Overlapping Spreading Center at the East Pacific Rise. *Geophysical Research Letters*, *41*(17), 6109–6115. https://doi.org/10.1002/2014GL060859

Baker, E. T., Haymon, R. M., Resing, J. A., White, S. M., Walker, S. L., Macdonald, K. C., & Nakamura, K. I. (2008). High-resolution surveys along the hot spot-affected Galápagos Spreading Center: 1. Distribution of hydrothermal activity. *Geochemistry, Geophysics, Geosystems*. https://doi.org/10.1029/2008GC002028

Banda, E., & Torne, M. (1995). Iberian Atlantic Margins Group investigates deep structure of ocean margins. *Eos, Transactions American Geophysical Union*, *76*(3), 25–29. https://doi.org/10.1029/EO076i003p00025

Bayrakci, G., Minshull, T. A., Sawyer, D. S., Reston, T. J., Klaeschen, D., Papenberg, C., et al. (2016). Fault-controlled hydration of the upper mantle during continental rifting. *Nature Geoscience*, *9*(5), 384–388. https://doi.org/10.1038/ngeo2671

Berenger, J. P. (1994). A perfectly matched layer for the absorption of electromagnetic waves. *Journal of Computational Physics*, *114*, 185–200.

Beslier, M. O., Ask, M., & Boillot, G. (1993a). Ocean-continent boundary in the Iberia Abyssal Plain from multichannel seismic data. *Tectonophysics*, *218*(4), 383–393. https://doi.org/10.1016/0040-1951(93)90327-G

Beslier, M. O., Ask, M., & Boillot, G. (1993b). Ocean-continent boundary in the Iberia Abyssal Plain from multichannel seismic data. *Tectonophysics*, *218*(4), 383–393. https://doi.org/10.1016/0040-1951(93)90327-G

Blacic, T. M., Ito, G., Canales, J. P., Detrick, R. S., & Sinton, J. (2004). Constructing the crust along the Galapagos Spreading Center 91.3°-95.5°W: Correlation of seismic layer 2A with axial magma lens and topographic characteristics. *Journal of Geophysical Research: Solid Earth*, *109*(B10), 1–22. https://doi.org/10.1029/2004JB003066

Blaich, O. A., Faleide, J. I., & Tsikalas, F. (2011). Crustal breakup and continent-ocean transition at South Atlantic conjugate margins. *Journal of Geophysical Research: Solid Earth*, *116*(1). https://doi.org/10.1029/2010JB007686

Boillot, G., Grimaud, S., Mauffret, A., Mougenot, D., Kornprobst, J., Mergoil-Daniel, J., & Torrent, G. (1980). Ocean-continent boundary off the Iberian margin: A serpentinite diapir west of the Galicia Bank. *Earth and Planetary Science Letters*, *48*(1), 23–34. https://doi.org/10.1016/0012-821X(80)90166-1

Boillot, G., Winterer, E., & Meyer, A. (1987a). Introduction, objectives, and principal results: Ocean Drilling Program Leg 103, west Galicia Margin. *Proc. Ocean Drill. Program, Initial Reports*, *103*, 3–17.

Boillot, G., Winterer, E. L., & Meyer, A. W. (1987b). Ocean Drill. Program Initial Rep.,103. *Ocean Drilling Program, College Station, TX*.

Boillot, Gilbert, & Winterer, E. L. (1988). *DRILLING ON THE GALICIA MARGIN: RETROSPECT AND PROSPECT*. *Proceedings of the Ocean Drilling Program, Scientific Results*.

Boillot, Gilbert, Féraud, G., Recq, M., & Girardeau, J. (1989). Undercrusting by serpentinite beneath rifted margins. *Nature*, *341*(6242), 523–525. https://doi.org/10.1038/341523a0

Boudier, F., Adolphe, N., & Ildefonse, B. (1996). Magma chambers in the Oman ophiolite: fed from the top and the bottom. *Earth and Planetary Science Letters*, *144*(1–2), 239–250. https://doi.org/10.1016/0012-821X(96)00167-7

Bronner, A., Sauter, D., Manatschal, G., Péron-pinvidic, G., & Munschy, M. (2011). Magmatic beakup as an explanaion for magnetic anomalies at magma-poor rifed magins. *Nature Geoscience*, *5*(2), 85–85. https://doi.org/10.1038/nphys1201

Brossier, R., Operto, S., & Virieux, J. (2009). Robust elastic frequency-domain full waveform inversion using the L1 norm. *Geophysical Research Letters*, *36*(L20310).

Brossier, Romain, Operto, S., & Virieux, J. (2010). Which data residual norm for robust elastic frequency-domain full waveform inversion? *Geophysics*, *75*(3). https://doi.org/10.1190/1.3379323

Brun, J. P. (1999). Narrow rifts versus wide rifts: Inferences for the mechanics of rifting from laboratory experiments. *Philosophical Transactions of the Royal Society A: Mathematical, Physical and Engineering Sciences*, *357*(1753), 695–712. https://doi.org/10.1098/rsta.1999.0349

Brun, J. P., & Beslier, M. O. (1996). Mantle exhumation at passive margins. *Earth and Planetary Science Letters*, *142*(1–2), 161–173. https://doi.org/10.1016/0012-821X(96)00080-5

Brune, S., Heine, C., Pérez-Gussinyé, M., & Sobolev, S. V. (2014). Rift migration explains continental margin asymmetry and crustal hyper-extension. *Nature Communications*, *5*, 1–9. https://doi.org/10.1038/ncomms5014

Brune, S., Heine, C., Clift, P. D., & Pérez-Gussinyé, M. (2017). Rifted margin architecture and crustal rheology: Reviewing Iberia-Newfoundland, Central South Atlantic, and South China Sea. *Marine and Petroleum Geology*, *79*, 257–281. https://doi.org/10.1016/j.marpetgeo.2016.10.018

Buck, W. R. (1988). Flexural Rotation of Normal Faults, *7*(5), 959–973.

Bunks, C., Saleck, F. M., Zaleski, S., & Chavent, G. (1995). Multiscale seismic waveform inversion. *Geophysics*, *60*(5), 1457–1473. https://doi.org/10.1190/1.1443880

Canales, J., Ito, G., Detrick, R. S., & Sinton, J. (2002). Crustal thickness along the western Galápagos Spreading Center and the compensation of the Galápagos hotspot swell. *Earth and Planetary Science Letters*, *203*(1), 311–327. https://doi.org/10.1016/S0012-821X(02)00843-9

Canales, J. P., Carton, H., Carbotte, S. M., Mutter, J. C., Nedimović, M. R., Xu, M., et al. (2012). Network of off-axis melt bodies at the East Pacific Rise. *Nature Geoscience*, *5*(4), 279–283. https://doi.org/10.1038/ngeo1377

Canales, Juan Pablo, Nedimovi, M. R., Kent, G. M., Carbotte, S. M., & Detrick, R. S. (2009). Seismic reflection images of a near-axis melt sill within the lower crust at the juan de fuca ridge. *Nature*, *460*(7251), 89–93. https://doi.org/10.1038/nature08095

Canales, Juan Pablo, Dunn, R. A., Ito, G., Detrick, R. S., & Sallarès, V. (2014). Effect of Variations in Magma Supply on the Crustal Structure of Mid-Ocean Ridges: Insights from the Western Galápagos Spreading Center. In *The Galapagos: A Natural Laboratory for the Earth Sciences* (pp. 363–391). https://doi.org/10.1002/9781118852538.ch17

Carbotte, S. M., Marjanović, M., Carton, H., Mutter, J. C., Canales, J. P., Nedimović, M. R., et al. (2013). Fine-scale segmentation of the crustal magma reservoir beneath the East Pacific Rise. *Nature Geoscience*, *6*(10), 866–870. https://doi.org/10.1038/ngeo1933

Carbotte, S. M., Smith, D. K., Cannat, M., & Klein, E. M. (2016). Tectonic and magmatic segmentation of the Global Ocean Ridge System: a synthesis of observations. *Geological Society, London, Special Publications*, *420*(1), 249–295. https://doi.org/10.1144/SP420.5

Carlson, R. L., & Miller, D. J. (2003). Mantle wedge water contents estimated from seismic velocities in partially serpentinized peridotites. *Geophysical Research Letters*, *30*(5), n/a-n/a. https://doi.org/10.1029/2002gl016600

Cerjan, C., Kosloff, D., Kosloff, R., & Reshef, M. (1985). Discrete acoustic and elastic wave equations. *Geophysics*, *50*(4), 705–708. https://doi.org/http://dx.doi.org/10.1190/1.1441945

Chapman, C. (2004). *Fundamentals of seismic wave propagation*. Cambridge University Press.

De Charpal, O., Guennoc, P., Montadert, L., & Roberts, D. G. (1978). Rifting, crustal attenuation and subsidence in the Bay of Biscay. *Nature*, *275*(5682), 706–711. https://doi.org/10.1038/275706a0

Chian, D., Louden, K. E., Minshull, T. A., & Whitmarsh, R. B. (1999). Deep structure of the ocean-continent transition in the southern Iberia Abyssal Plain from seismic refraction profiles: Ocean Drilling Program (Legs 149 and 173) transect. *Journal of Geophysical Research: Solid Earth*, *104*(B4), 7443–7462. https://doi.org/10.1029/1999jb900004

Choo, J., Downton, J., & Dewar, J. (2004). LIFT: A new and practical approach to noise and multiple attenuation. *First Break*, *22*(5), 39–44.

Christensen, N. I., & Mooney, W. D. (1995). Seismic velocity structure and composition of the continental crust: a global view. *Journal of Geophysical Research*, *100*(B6), 9761–9788. https://doi.org/10.1029/95JB00259

Christensen, Nikolas I. (2004). Serpentinites, peridotites, and seismology. *International Geology Review*, *46*(9), 795–816. https://doi.org/10.2747/0020-6814.46.9.795

Christie, D. M., Werner, R., Hauff, F., Hoernle, K., & Hanan, B. B. (2005). Morphological and geochemical variations along the eastern Galápagos Spreading Center. *Geochemistry, Geophysics, Geosystems*, *6*(1), 1–44. https://doi.org/10.1029/2004GC000714

Claerbout, J. F. (1971). Toward a unified theory of reflector mapping. *Geophysics*, *36*(3), 467–481. https://doi.org/10.1190/1.1440185

Clærbout, J. F. (1976). *Fundamentals of Geophysical Data Processing*.

Clayton, R., & Engquist, B. (1977). Absorbing boundary conditions for acoustic and elastic wave equations. *Bulletin of the Seismological Society of America*, *67*(6), 1529–1540. https://doi.org/10.1016/0096-3003(88)90130-0

Collier, J. S., & Sinha, M. C. (1992). Seismic mapping of a magma chamber beneath the Valu Fa Ridge, Lau Basin. *Journal of Geophysical Research*, *97*(B10), 14031. https://doi.org/10.1029/91jb02751

Courant, R., Friedrichs, K., & Lewy, H. (1967). On the partial difference equations of mathematical physics. *IBM Journal of Research and Development*, *11*(2), 215–234.

Dash, R., Spence, G., Hyndman, R., Grion, S., Wang, Y., & Ronen, S. (2009). Wide-area imaging from OBS multiples. *Geophysics*, *74*(6), Q41–Q47. https://doi.org/10.1190/1.3223623

Davis, M., & Kusznir, N. (2004). Depth-Dependent Lithospheric Stretching at Rifted Continental Margins. *Proceedings of NSF Rifted Margins Theoretical Institute*. https://doi.org/10.7312/karn12738-005

Davy, R. G. (2017). *The continent-ocean transition at the Deep Galicia Margin: insights from wide-angle seismic data*. *Thesis*. University of Southampton. https://doi.org/10.1016/j.jsv.2010.04.020

Davy, R. G., Minshull, T. A., Bayrakci, G., Bull, J. M., Klaeschen, D., Papenberg, C., et al. (2016). Continental hyperextension, mantle exhumation, and thin oceanic crust at the continent-ocean transition, West Iberia: New insights from wide-angle seismic. *Journal of Geophysical Research : Solid Earth*, 1–17. https://doi.org/10.1002/2016JB012825.Received

Davy, R. G., Morgan, J. V., Minshull, T. A., Bayrakci, G., Bull, J. M., Klaeschen, D., et al. (2018). Resolving the fine-scale velocity structure of continental hyperextension at the Deep Galicia

Margin using full-waveform inversion. *Geophysical Journal International*, *212*(1), 244–263. https://doi.org/10.1093/gji/ggx415

Dean, S. L., Sawyer, D. S., & Morgan, J. K. (2015). Galicia Bank ocean-continent transition zone: New seismic reflection constraints. *Earth and Planetary Science Letters*, *413*, 197–207. https://doi.org/10.1016/j.epsl.2014.12.045

Dean, S. M., Minshull, T. a., Whitmarsh, R. B., & Louden, K. E. (2000). Deep structure of the ocean-continent transition in the southern Iberia Abyssal Plain from seismic refraction profiles: the IAM-9 transect at 40,20N. *Journal of Geophysical Research*, *104*(B4), 7443–7462. https://doi.org/10.1029/1999JB900301

Dessa, J. X., Operto, S., Kodaira, S., Nakanishi, A., Pascal, G., Virieux, J., & Kaneda, Y. (2004). Multiscale seismic imaging, of the eastern Nankai trough by full waveform inversion. *Geophysical Research Letters*, *31*(18), 2–5. https://doi.org/10.1029/2004GL020453

Detrick, R. S., Buhl, P., Vera, E., Mutter, J., Orcutt, J., Madsen, J., & Brocher, T. (1987). Multi-channel seismic imaging of a crustal magma chamber along the East Pacific Rise. *Nature*, *326*(6108), 35–41. https://doi.org/10.1038/326035a0

Detrick, R. S., Sinton, J. M., Ito, G., Canales, J. P., Behn, M., Blacic, T., et al. (2002). Correlated geophysical, geochemical, and volcanological manifestations of plume-ridge interaction along the Galápagos Spreading Center. *Geochemistry, Geophysics, Geosystems*, *3*(10), 1–14. https://doi.org/10.1029/2002GC000350

Detrick, Robert S., & Sinton, J. M. (2014). *Raw Multi-Channel Seismic Shot Data from the Galapagos Spreading Center acquired during R/V Maurice Ewing expedition EW0004 (2000), Interdisciplinary Earth Data Alliance (IEDA).* https://doi.org/10.1594/IEDA/314480

Dore, T., & Lundin, E. (2015). Hyperextended continental margins—Knowns and unknowns. *Geology*, *43*(1), 95–96.

Driscoll, N., & Karner, G. (1998). Lower crustal extension across the Northern Carnarvon basin, Australia: Evidence for an eastward dipping detachment. *Journal Geophysical Research*, *103*(B3), 4975–4991.

Driscoll, N. W., & Karner, G. D. (1998). Lower crustal extension across the Northern Carnarvon basin, Australia: Evidence for an eastward dipping detachment. *Journal of Geophysical Research: Solid Earth*, *103*(B3), 4975–4991. https://doi.org/10.1029/97jb03295

Dunn, R. A., Toomey, D. R., & Solomon, S. C. (2000). Three-dimensional seismic structure and

physical properties of the crust and shallow mantle beneath the East Pacific Rise at 9 deg 30'N. *Journal of Geophysical Research: Solid Earth*, *105*(B10), 23537–23555. https://doi.org/10.1029/2000JB900210

Emmanuel, S., & Berkowitz, B. (2006). Suppression and stimulation of seafloor hydrothermal convection by exothermic mineral hydration. *Earth and Planetary Science Letters*, *243*(3–4), 657–668. https://doi.org/10.1016/j.epsl.2006.01.028

Evain, M., Afilhado, A., Rigoti, C., Loureiro, A., Alves, D., Klingelhoefer, F., et al. (2015). Deep structure of the Santos Basin-São Paulo Plateau System , SE Brazil Journal of Geophysical Research : Solid Earth, 5401–5431. https://doi.org/10.1002/2014JB011561.Received

Fontaine, F. J., Olive, J. A., Cannat, M., Escartin, J., & Perol, T. (2011). Hydrothermally-induced melt lens cooling and segmentation along the axis of fast-and intermediate-spreading centers. *Geophysical Research Letters*, *38*(14). https://doi.org/10.1029/2011GL047798

Franke, D. (2013, May). Rifting, lithosphere breakup and volcanism: Comparison of magma-poor and volcanic rifted margins. *Marine and Petroleum Geology*. https://doi.org/10.1016/j.marpetgeo.2012.11.003

Franke, D., Savva, D., Pubellier, M., Steuer, S., Mouly, B., Auxietre, J. L., et al. (2014). The final rifting evolution in the South China Sea. *Marine and Petroleum Geology*, *58*(PB), 704–720. https://doi.org/10.1016/j.marpetgeo.2013.11.020

Gardner, G. H. F., Gardner, L. W., & Gregory, A. R. (1974). Formation velocity and density - The diagnostic basics for stratigraphic traps, *39*(6), 770–780.

Gauthier, O., Virieux, J., & Tarantola, A. (1986). Two-dimensional nonlinear inversion of seismic waveforms: numerical results. *Geophysics*, *51*(7), 1387–1403. https://doi.org/10.1190/1.1442188

Gazdag, J. (1978). Wave equation migration with the phase-shift method. *Geophysics*, *43*(7), 1342–1351. https://doi.org/10.1190/1.1440899

Germanovich, L. N., Genc, G., Lowell, R. P., & Rona, P. A. (2012). Deformation and surface uplift associated with serpentinization at mid-ocean ridges and subduction zones. *Journal of Geophysical Research: Solid Earth*, *117*(7), 1–23. https://doi.org/10.1029/2012JB009372

Godfrey, R. J., Kristiansen, P., Armstrong, B., Cooper, M., & Thorogood, E. (1998). Imaging the Foinaven ghost. *SEG Technical Program Expanded Abstracts*, 1333–1335. https://doi.org/10.1190/1.1820147

Górszczyk, A., Operto, S., & Malinowski, M. (2017). Toward a robust workflow for deep crustal imaging by FWI of OBS data: The eastern Nankai Trough revisited. *Journal of Geophysical Research: Solid Earth*, *122*(6), 4601–4630. https://doi.org/10.1002/2016JB013891

Górszczyk, A., Operto, S., Schenini, L., & Yamada, Y. (2019). Crustal-scale depth imaging via joint FWI of OBS data and PSDM of MCS data: a case study from the eastern Nankai Trough. *Solid Earth Discussions*, 1–34. https://doi.org/10.5194/se-2019-33

Gradstein, F. M., Ogg, J. G., Schmitz, M., & Ogg, G. (2012). The geologic time scale 2012. *Elsevier*, *2-volume s*.

Graham, R. P. . (1917). Origin of massive serpentine and chrysotile asbestos, Black Lake-Thetford area, Quebec. *Economic Geology*, *12*(2), 154–202.

Graves, R. W. (1996). Simulating seismic wave propagation in 3D elastic media using staggered-grid finite differences. *Bulletin of the Seismological Society of America*, *86*(4), 1091–1106.

Grion, S., Exley, R., Manin, M., Miao, X. G., Pica, A., Wang, Y., et al. (2007). Mirror imaging of OBS data. *First Break*. https://doi.org/10.3997/1365-2397.2007028

Hammer, P. T. C., Dorman, L. M., Hildebrand, J. A., & Cornuelle, B. D. (1994). Jasper Seamount structure: seafloor seismic refraction tomography. *Journal of Geophysical Research*, *99*(B4), 6731–6752. https://doi.org/10.1029/93JB02170

Han, S, Carbotte, S. M., Canales, J. P., Carton, H., Nedimović, M. R., Gibson, J., & Horning, G. (2016). Seismic reflection imaging of the Juan de Fuca plate from ridge to trench; new constraints on the distribution of faulting and evolution of the crust prior to subduction. *Journal Geophysical Research*, *121*(3), 1849–1872.

Han, Shuoshuo, Carbotte, S. M., Carton, H., Mutter, J. C., Aghaei, O., Nedimović, M. R., & Canales, J. P. (2014). Architecture of on- and off-axis magma bodies at EPR 9°37–40′N and implications for oceanic crustal accretion. *Earth and Planetary Science Letters*, *390*, 31–44. https://doi.org/10.1016/j.epsl.2013.12.040

Harding, A. J., Kent, G. M., & Orcutt, J. A. (1993). A multichannel seismic investigation of upper crustal structure at 9°N on the East Pacific Rise: Implications for crustal accretion. *J. Geophys. Res.*, *98*(B8), 925–13,944. https://doi.org/10.1029/93JB00886

Harpp, K., & Geist, D. (2002). Wolf-Darwin lineament and plume-ridge interaction in northern Galápagos. *Geochemistry, Geophysics, Geosystems*, *3*(11), 1–19. https://doi.org/10.1029/2002GC000370

Haymon, R. M., White, S. M., Baker, E. T., Anderson, P. G., Macdonald, K. C., & Resing, J. A. (2008). High-resolution surveys along the hot spot-affected Galápagos Spreading Center: 3. Black smoker discoveries and the implications for geological controls on hydrothermal activity. *Geochemistry, Geophysics, Geosystems*, *9*(12). https://doi.org/10.1029/2008GC002114

Henning, A. T., Sawyer, D. S., & Templeton, D. C. (2004). Exhumed upper mantle within the ocean-continent transition on the northern West Iberia margin: Evidence from prestack depth migration and total tectonic subsidence analyses. *Journal of Geophysical Research: Solid Earth*, *109*(5), 1–16. https://doi.org/10.1029/2003JB002526

Henstock, T. J., Woods, A. W., & White, R. S. (1993). The accretion of oceanic crust by episodic sill intrusion. *Journal of Geophysical Research*, *98*(B3), 4143–4161. https://doi.org/10.1029/92JB02661

Hey, R., & Vogt, P. (1977). Spreading center jumps and sub-axial asthenosphere flow near the Galapagos hotspot. *Tectonophysics*, *37*(1–3), 41–52. https://doi.org/10.1016/0040-1951(77)90038-5

Hobro, J. W. D., Singh, S. C., & Minshull, T. A. (2003). Three-dimensional tomographic inversion of combined reflection and refraction seismic traveltime data. *Geophysical Journal International*, *152*(1), 79–93. https://doi.org/10.1046/j.1365-246X.2003.01822.x

Hole, J. A. (1992). Nonlinear three dimensional seismic wave travel time tomography. *Journal Geophysical Research*, *97*, 6553–6562.

Huismans, R., & Beaumont, C. (2011). Depth-dependent extension, two-stage breakup and cratonic underplating at rifted margins. *Nature*, *473*(7345), 74–78. https://doi.org/10.1038/nature09988

Ito, G., & J. Lin. (1995). Mantle temperature anomalies along the present and paleoxes of the Galapagos Spreading Center as inferred from gravity analyses. *Journal Geophysical Research: Solid Earth*, *100*(B3), 3733–3745.

Jannane, M., Beydoun, W., Crase, E., Cao, D., Koren, Z., Landa, E., et al. (1989). Wavelengths of earth structures that can be resolved from seismic reflection data (short note). *Geophysics*, *54*(07), 906–910.

Jian, H., Singh, S. C., Chen, Y. J., & Li, J. (2017). Evidence of an axial magma chamber beneath the ultraslowspreading Southwest Indian Ridge. *Geology*, *45*(2), 143–146. https://doi.org/10.1130/G38356.1

Jiang, Z., Yu, J., Schuster, G. T., & Hornby, B. E. (2005). Migration of multiples. *Leading Edge (Tulsa, OK)*, *24*(3), 315–318. https://doi.org/10.1190/1.1895318

Kamei, R., Pratt, R. G., & Tsuji, T. (2013). On acoustic waveform tomography of wide-angle OBS data-strategies for pre-conditioning and inversion. *Geophysical Journal International*, *194*(2), 1250–1280. https://doi.org/10.1093/gji/ggt165

Kelemen, P. B., K. Koga, & N. Shimizu. (1997). Geochemistry of gabbro sills in the crust-mantle transition zone of the Oman ophiolite: Implications of the origin of the oceanic lower crust. *Earth Planetary Science Letters*, *8*(1), 186–188. https://doi.org/10.1093/ilj/8.1.186

Kelemen, Peter B., & Aharonov, E. (1998). Periodic formation of magma fractures and generation of layered gabbros in the lower crust beneath oceanic spreading ridges. In W. R. B. et Al (Ed.), *GEOPHYSICAL MONOGRAPH-AMERICAN GEOPHYSICAL UNION 106* (pp. 267–289). Washington, D.C. https://doi.org/10.1029/GM106p0267

Kent, G. M., Harding, A. J., & Orcutt, J. A. (1993). Distribution of magma beneath the East Pacific Rise between the Clipperton Transform and the 9°17'N Deval from forward modeling of common depth point data. *Journal of Geophysical Research: Solid Earth*, *98*(B8), 13945–13969. https://doi.org/10.1029/93JB00705

Klitgord, K. D., & Schouten, H. (1986). Plate kinematics of the central Atlantic. In *The Western North Atlantic Region* (pp. 351–378). Geology of North America. https://doi.org/10.1130/dnag-gna-m.351

Komatitsch, D., Tsuboi, S., & Tromp, J. (2005). The spectral-element method in seismology. In *Geophysical Monograph Series* (Vol. 157, pp. 205–227). Blackwell Publishing Ltd. https://doi.org/10.1029/156GM13

Korenaga, J., & Kelemen, P. (1998). Melt migration through the oceanic lower crust: a constraint from melt percolation modeling with finite solid diffusion. *Earth and Planetary Science Letters*, *156*(1–2), 1–11. https://doi.org/10.1016/s0012-821x(98)00004-1

Korenaga, J., Holbrook, W. S., Kent, G. M., Kelemen, P. B., Detrick, R. S., Larsen, H.-C., et al. (2000). Crustal structure of the southeast Greenland margin from joint refraction and reflection seismic tomography. *Journal of Geophysical Research: Solid Earth*, *105*(B9), 21591–21614. https://doi.org/10.1029/2000jb900188

Krawczyk, C., Reston, T., Beslier, M., & Boillot, G. (1996). 38. Evidence for detachment tectonics on the Iberia Abyssal Plain rifted margin. *Proceedings-Ocean Drilling Program Scientific Results*,

3–26.

Lailly, P. (1983). The Seismic Inverse Problem as a Sequence of Before Stack Migrations. In *Conference on Inverse Scattering, Theory and Applications, Society for Industrial and Applied Mathematics* (pp. 206–220).

Lavier, L. L., & Manatschal, G. (2006). A mechanism to thin the continental lithosphere at magma-poor margins. *Nature*, *440*(7082), 324–328. https://doi.org/10.1038/nature04608

Levander, A. (1988). Fourth-order finite-difference P-SV seismograms. *Geophysics*, *53*, 1425–1436.

Leythaeuser, T., Reston, T. J., & Minshull, T. A. (2005). Waveform inversion of the S reflector west of Spain: Fine structure of a detachment fault. *Geophysical Research Letters*. https://doi.org/10.1029/2005GL024026

Lindman, E. L. (1975). "Free-space" boundary conditions for the time dependent wave equation. *Journal of Computational Physics*, *18*(1), 66–78.

Lines, L. R., Slawinski, R., & Bording, R. P. (1999). A recipe for stability of finite-difference wave-equation computations. *Geophysics*, *64*(3), 967–969. https://doi.org/10.1190/1.1444605

Lissenberg, C. J., MacLeod, C. J., Howard, K. A., & Godard, M. (2013). Pervasive reactive melt migration through fast-spreading lower oceanic crust (Hess Deep, equatorial Pacific Ocean). *Earth and Planetary Science Letters*, *361*, 436–447. https://doi.org/10.1016/j.epsl.2012.11.012

Lister, C. R. . (1974). On the penetration of water into hot rock. *Geophysical Journal International*, *39*, 465–509.

Lister, G. S., Etheridge, M. A., & Symonds, P. A. (1986). Detachment faulting and the evolution of passive continental margins. *Geology*, *14*(10), 890–891. https://doi.org/10.1130/0091-7613(1986)14<890:CARODF>2.0.CO;2

Lister, G. S., Etheridge, M. A., & Symonds, P. A. (1991). Detachment models for the formation of passive continental margins. *Tectonics*, *10*(5), 1038–1064.

Lymer, G., Cresswell, D. J. F., Reston, T. J., Bull, J. M., Sawyer, D. S., Morgan, J. K., et al. (2019). 3D development of detachment faulting during continental breakup. *Earth and Planetary Science Letters*, *515*, 90–99. https://doi.org/10.1016/j.epsl.2019.03.018

Macdonald, A. H., & Fyfe, W. S. (1985). Rate of serpentinization in seafloor environments. *Tectonophysics*, *116*(1–2), 123–135. https://doi.org/10.1016/0040-1951(85)90225-2

Maclennan, J., Hulme, T., & Singh, S. C. (2004). Thermal models of oceanic crustal accretion: Linking geophysical, geological and petrological observations. *Geochemistry, Geophysics, Geosystems*, *5*(2), 1–32. https://doi.org/10.1029/2003GC000605

Marjanović, M., Carbotte, S. M., Carton, H., Nedimović, M. R., Mutter, J. C., & Canales, J. P. (2014). A multi-sill magma plumbing system beneath the axis of the East Pacific Rise. *Nature Geoscience*, *7*(11), 825–829. https://doi.org/10.1038/ngeo2272

Marjanović, M., Carbotte, S. M., Carton, H. D., Nedimović, M. R., Canales, J. P., & Mutter, J. C. (2018). Crustal Magmatic System Beneath the East Pacific Rise (8°20′ to 10°10′ N): Implications for Tectono-magmatic Segmentation and Crustal Melt Transport at Fast-spreading Ridges. *Geochemistry, Geophysics, Geosystems*, *19*(11), 4584–4611. https://doi.org/10.1029/2018GC007590

Mauffret, A., & Montadert, L. (1987). Rift tectonics on the passive continental margin off Galicia (Spain). *Marine and Petroleum Geology*, *4*(1), 49–70. https://doi.org/10.1016/0264-8172(87)90021-3

Maus, S., Barckhausen, U., Berkenbosch, H., Bournas, N., Brozena, J., Childers, V., et al. (2009). EMAG2: A 2-arc min resolution Earth Magnetic Anomaly Grid compiled from satellite, airborne, and marine magnetic measurements. *Geochemistry, Geophysics, Geosystems*, *10*(8). https://doi.org/10.1029/2009GC002471

McDermott, K., & Reston, T. (2015). To see, or not to see? Rifted margin extension. *Geology*, *43*(11), 967–970. https://doi.org/10.1130/G36982.1

Menand, T. (2011). Physical controls and depth of emplacement of igneous bodies: A review. *Tectonophysics*, *500*(1–4), 11–19. https://doi.org/10.1016/j.tecto.2009.10.016

Menzies, M. A., Klemperer, S. L., Ebinger, C. J., & Baker, J. (2002). Characteristics of volcanic rifted margins. *Special Paper of the Geological Society of America*, *362*, 1–14. https://doi.org/10.1130/0-8137-2362-0.1

Minshull, T. A., Dean, S. M., Whitmarsh, R. B., Russell, S. M., Louden, K. E., & Chian, D. (1998). Deep structured the vicinity of the ocean-continent transition zone under the southern Iberia Abyssal Plain Discovery 215 Working Group. *Geology*, *26*(8), 743–746. https://doi.org/10.1130/0091-7613(1998)026<0743:dsitvo>2.3.co;2

Minshull, T.A., Dean, S. M., & Whitmarsh, R. B. (2014). The peridotite ridge province in the southern Iberia Abyssal Plain: Seismic constraints revisited. *Journal of Geophysical Research : Solid*

Earth, (Figure 1), 1–14. https://doi.org/10.1002/2014JB011281.Received

Minshull, Timothy A. (2009). Geophysical characterisation of the ocean-continent transition at magma-poor rifted margins. *Comptes Rendus - Geoscience*. https://doi.org/10.1016/j.crte.2008.09.003

Mittelstaedt, E., Soule, S., Harpp, K., Fornari, D., McKee, C., Tivey, M., et al. (2012). Multiple expressions of plume-ridge interaction in the Galápagos: Volcanic lineaments and ridge jumps. *Geochemistry, Geophysics, Geosystems*, *13*(5), 1–31. https://doi.org/10.1029/2012GC004093

Mora, P. (1987). NONLINEAR TWO-DIMENSIONAL ELASTIC INVERSION OF MULTIOFFSET SEISMIC DATA. *Geophysics*, *52*(9), 1211–1228. https://doi.org/10.1190/1.1442384

Mora, P. (1988). Elastic wave-field inversion of re ection and transmission data. *Geophysics*, *53*(6), 750–759. https://doi.org/10.1088/0031-9155/54/11/004.Exact

Morgan, J., Warner, M., Arnoux, G., Hooft, E., Toomey, D., VanderBeek, B., & Wilcock, W. (2016). Next-generation seismic experiments - II: Wide-angle, multi-azimuth, 3-D, full-waveform inversion of sparse field data. *Geophysical Journal International*, *204*(2), 1342–1363. https://doi.org/10.1093/gji/ggv513

Mufti, I. R. (1990). Large-scale three-dimensional seismic models and their interpretive significance. *Geophysics*, *55*(9), 1166–1182. https://doi.org/10.1190/1.1442933

Murillas, J., Mougenot, D., Boulot, G., Comas, M. C., Banda, E., & Mauffret, A. (1990). Structure and evolution of the Galicia Interior Basin (Atlantic western Iberian continental margin). *Tectonophysics*, *184*(3–4). https://doi.org/10.1016/0040-1951(90)90445-E

Mutter, J. C., & Carton, H. D. (2013). The mohorovicic discontinuity in ocean basins: Some observations from seismic data. *Tectonophysics*, *609*, 314–330. https://doi.org/10.1016/j.tecto.2013.02.018

Mutter, John C. (1993). Margins declassified. *Nature*. https://doi.org/10.1038/364393a0

Mutter, John C., Carbotte, S., Nedimovic, M., Canales, J. P., & Carton, H. (2009). Seismic imaging in three dimensions on the east pacific rise. *Eos, Transactions American Geophysical Union*, *90*(42), 374–375. https://doi.org/10.1029/2009EO420002

Nedimović, M. R., Carbotte, S. M., Harding, A. J., Detrick, R. S., Canales, J. P., Diebold, J. B., et al. (2005). Frozen magma lenses below the oceanic crust. *Nature*, *436*(7054), 1149–1152. https://doi.org/10.1038/nature03944

Nirrengarten, M., Manatschal, G., Tugend, J., Kusznir, N. J., & Sauter, D. (2017). Nature and origin of the J-magnetic anomaly offshore Iberia–Newfoundland: implications for plate reconstructions. *Terra Nova*, *29*(1), 20–28. https://doi.org/10.1111/ter.12240

Operto, S., Virieux, J., Dessa, J. X., & Pascal, G. (2006). Crustal seismic imaging from multifold ocean bottom seismometer data by frequency domain full waveform tomography: Application to the eastern Nankai trough. *Journal of Geophysical Research: Solid Earth*, *111*(9), 1–33. https://doi.org/10.1029/2005JB003835

Paige, C. C., & Saunders, M. A. (1982). LSQR: An Algorithm for Sparse Linear Equations and Sparse Least Squares. *ACM Transactions on Mathematical Software (TOMS)*, *8*(2), 195–209. https://doi.org/10.1145/355993.356000

Pérez-Gussinye, M. (2013). A tectonic model for hyperextension at magma-poor rifted margins: An example from the west iberia-newfoundland conjugate margins. *Geological Society Special Publication*, *369*(1), 403–427. https://doi.org/10.1144/SP369.19

Pérez-Gussinyé, M., Ranero, C. R., Reston, T. J., & Sawyer, D. (2003). Mechanisms of extension at nonvolcanic margins: Evidence from the Galicia interior basin, west of Iberia. *Journal of Geophysical Research: Solid Earth*, *108*(B5), 1–19. https://doi.org/10.1029/2001JB000901

Pérez-Gussinyé, Marta, & Reston, T. J. (2001). Rheological evolution during extension at nonvolcanic rifted margins: Onset of serpentinization and development of detachments leading to continental breakup. *Journal of Geophysical Research: Solid Earth*, *106*(B3), 3961–3975. https://doi.org/10.1029/2000jb900325

Peron-Pinvidic, G., Manatschal, G., & Osmundsen, P. T. (2013). Structural comparison of archetypal Atlantic rifted margins: A review of observations and concepts. *Marine and Petroleum Geology*, *43*, 21–47. https://doi.org/10.1016/j.marpetgeo.2013.02.002

Péron-Pinvidic, G., Manatschal, G., Minshull, T. A., & Sawyer, D. S. (2007). Tectonosedimentary evolution of the deep Iberia-Newfoundland margins: Evidence for a complex breakup history. *Tectonics*, *26*(2), 1–19. https://doi.org/10.1029/2006TC001970

Pickup, S. L. B., Whitmarsh, R. B., Fowler, C. M. R., & Reston, T. J. (1996). Insight into the nature of the ocean-continent transition off West-Iberia from a deep-multichannel seismic reflection profile. *Geology*, *24*(12), 1079–1082. https://doi.org/10.1130/0091-7613(1996)024<1079

Plessix, R. È., & Perkins, C. (2010). Full waveform inversion of a deep water ocean bottom seismometer dataset. *First Break*, *28*(4), 71–78. https://doi.org/10.3997/1365-2397.2010013

Pratt, G., & Worthington, M. H. (1990). Inverse theory applied to multi-source cross-hole tomography, Part 1: Acoustic wave-equation method. *Geophysical Prospecting*, *38*, 287–310.

Pratt, G., Shin, C., & Hicks. (1998). Gauss-Newton and full Newton methods in frequency-space seismic waveform inversion. *Geophysical Journal International*, *133*(2), 341–362. https://doi.org/10.1046/j.1365-246X.1998.00498.x

Pratt, R. G., Song, Z. M., Williamson, P., & Warner, M. (1996). Two-dimensional velocity models from wide-angle seismic data by wavefield inversion. *Geophysical Journal International*, *124*(2), 323–340. https://doi.org/10.1111/j.1365-246X.1996.tb07023.x

Pratt, R. Gerhard. (1999). Seismic waveform inversion in the frequency domain, Part 1: Theory and verification in a physical scale model. *Geophysics*, *64*(3), 888–901. https://doi.org/10.1190/1.1444597

Quick, J. E., & Denlinger, R. P. (1993). Ductile deformation and the origin of layered gabbro in ophiolites. *Journal of Geophysical Research*, *98*(B8), 14015–14027.

Ranero, C. R., & Pérez-Gussinyé, M. (2010). Sequential faulting explains the asymmetry and extension discrepancy of conjugate margins. *Nature*, *468*(7321), 294–299. https://doi.org/10.1038/nature09520

Reiter, E. C., Toksöz, M. N., Keho, T. H., & Purdy, G. M. (1991). Imaging with deep-water multiples. *Geophysics*, *56*(7), 1081–1086. https://doi.org/10.1190/1.1443119

Reston, T. J. (2005). Polyphase faulting during the development of the west Galicia rifted margin. *Earth and Planetary Science Letters*, *237*(3–4), 561–576. https://doi.org/10.1016/j.epsl.2005.06.019

Reston, T. J. (2007). The formation of non-volcanic rifted margins by the progressive extension of the lithosphere: the example of the West Iberian margin. *Geological Society, London, Special Publications*, *282*(1), 77–110. https://doi.org/10.1144/SP282.5

Reston, T. J. (2009a). The extension discrepancy and syn-rift subsidence deficit at rifted margins. *Petroleum Geoscience*, *15*(3), 217–237. https://doi.org/10.1144/1354-079309-845

Reston, T. J. (2009b). The structure, evolution and symmetry of the magma-poor rifted margins of the North and Central Atlantic: A synthesis. *Tectonophysics*, *468*(1–4), 6–27. https://doi.org/10.1016/j.tecto.2008.09.002

Reston, T. J., Krawczyk, C. M., & Klaeschen, D. (1996). The S reflector west of Galicia (Spain):

Evidence from prestack depth migration for detachment faulting during continental breakup. *Journal of Geophysical Research: Solid Earth*, *101*(B4), 8075–8091. https://doi.org/10.1029/95JB03466

Reston, T. J., Pennell, J., Stubenrauch, A., Walker, I., & Pérez-Gussinyé, M. (2001). Detachment faulting, mantle serpentinization and serpentinite mud volcanism beneath the Porcupine Basin SW Ireland. *Geology*, *29*, 587–590.

Reston, T. J., Booth-Rea, G., Leythaeuser, T., Sawyer, D., Klaeschen, D., & Long, C. (2007). Movement along a low-angle normal fault: The S reflector west of Spain. *Geochemistry, Geophysics, Geosystems*, *8*(6), 1–14. https://doi.org/10.1029/2006GC001437

Ronen, S., Comeaux, L., & Miao, X. (2005). Imaging downgoing waves from ocean bottom stations. In *SEG Annual Meeting* (pp. 963–967). https://doi.org/10.1901/jaba.1992.25-341

Rubin, K. H., & Sinton, J. M. (2007). Inferences on mid-ocean ridge thermal and magmatic structure from MORB compositions. *Earth and Planetary Science Letters*, *260*(1–2), 257–276. https://doi.org/10.1016/j.epsl.2007.05.035

Russell, S. M., & Whitmarsh, R. B. (2003). Magmatism at the west Iberia non-volcanic rifted continental margin: Evidence from analyses of magnetic anomalies. *Geophysical Journal International*, *154*(3), 706–730. https://doi.org/10.1046/j.1365-246X.2003.01999.x

Sawyer, D. S., Coffin, M. F., Reston, T. J., Stock, J. M., & Hopper, J. R. (2007). COBBOOM: The Continental Breakup and Birth of Oceans Mission. *Scientific Drilling*, *5*(5), 13–25. https://doi.org/10.2204/iodp.sd.02.2007

Sawyer, Dale S., Coffin, M. F., Reston, T. J., Stock, J. M., & Hopper, J. R. (2007). COBBOOM: The Continental Breakup and Birth of Oceans Mission. *Scientific Drilling*, (5), 13–25. https://doi.org/10.2204/iodp.sd.5.02.2007

Schuba, C. N., Gray, G. G., Morgan, J. K., Schuba, J. P., & Sawyer, D. S. (2019). Origin of Serpentinization Patterns Beneath the S-Reflector Detachment Fault in the Galicia Margin, Offshore Spain. *Geochemistry, Geophysics, Geosystems*, *20*(8), 3971–3984. https://doi.org/10.1029/2019GC008400

Schuba, C. Nur, Schuba, J. P., Gray, G. G., & Davy, R. G. (2019). Interface-targeted seismic velocity estimation using machine learning. *Geophysical Journal International*, *218*(1), 45–56. https://doi.org/10.1093/gji/ggz142

Schuba, C Nur, Gray, G. G., Morgan, J. K., Sawyer, D. S., Shillington, D. J., Reston, T. J., et al. (2018).

A low-angle detachment fault revealed: Three-dimensional images of the S-reflector fault zone along the Galicia passive margin. *Earth and Planetary Science Letters*, *492*, 232–238. https://doi.org/10.1016/j.epsl.2018.04.012

Shah, N., Warner, M., Nangoo, T., Umpleby, A., Stekl, I., Morgan, J., & Guasch, L. (2012). Quality assured full-waveform inversion: Ensuring starting model adequacy. In *81st Annual International Meeting, SEG, Expanded abstract, SI3.5.* (pp. 1–5).

Shin, C., Jang, S., & Min, D. J. (2001). Improved amplitude preservation for prestack depth migration by inverse scattering theory. *Geophysical Prospecting*, *49*(5), 592–606. https://doi.org/10.1046/j.1365-2478.2001.00279.x

Shipboard Scientific Party ODP Leg 149. (1993). ODP drills the West Iberia rifted margin. *Eos*, *74*, 454–455.

Shipboard Scientific Party ODP Leg 173. (1998). Drilling reveals transition from continental breakup to early magmatic crust. *Eos*, *79*(173), 180–181.

Shipp, R. M., & Singh, S. C. (2002). Two-dimensional full wavefield inversion of wide-aperture marine seismic streamer data. *Geophysical Journal International*, *151*(2), 325–344. https://doi.org/10.1046/j.1365-246X.2002.01645.x

Sibuet, J.-C. (1992). New constraints on the formation of the non-volcanic continental Galicia-Flemish Cap conjugate margins. *Journal of the Geological Society*, *149*(5), 829–840. https://doi.org/10.1144/gsjgs.149.5.0829

Sibuet, J. C., Srivastava, S., & Manatschal, G. (2007). Exhumed mantle-forming transitional crust in the Newfoundland-Iberia rift and associated magnetic anomalies. *Journal of Geophysical Research: Solid Earth*, *112*(6), 1–23. https://doi.org/10.1029/2005JB003856

Sibuet, Jean-Claude, Louvel, V., Whitmarsh, R. B., White, R. S., Horsefield, S. J., Sichler, B., et al. (1995). Constraints on Rifting Processes from Refraction and Deep-Tow Magnetic Data: The Example of the Galicia Continental Margin (West Iberia). In *Rifted Ocean-Continent Boundaries* (pp. 197–217). Springer Netherlands. https://doi.org/10.1007/978-94-011-0043-4_11

Singh, S. C., Harding, A. J., Kent, G. M., Sinha, M. C., Combier, V., Bazin, S., et al. (2006). Seismic reflection images of the Moho underlying melt sills at the East Pacific Rise. *Nature*, *442*(7100), 287–290. https://doi.org/10.1038/nature04939

Sinton, J., Detrick, R., Canales, J. P., Ito, G., & Behn, M. (2003). Morphology and segmentation of the western Galápagos spreading center, 90.5°-98°W: Plume-ridge interaction at an

intermediate spreading ridge. *Geochemistry, Geophysics, Geosystems*, *4*(12), 1–26. https://doi.org/10.1029/2003GC000609

Sirgue, L. (2006). The importance of low frequency and large offset in waveform inversion. In *68th EAGE Conference and Exhibition incorporating SPE EUROPEC 2006*.

Sirgue, L., Barkved, O. I., Dellinger, J., Etgen, J., Albertin, U., & Kommedal, J. H. (2010). Full waveform inversion: The next leap forward in imaging at Valhall. *First Break*, *28*(4), 65–70. https://doi.org/10.3997/1365-2397.2010012

Skogseid, J. (2001). Volcanic margins: Geodynamic and exploration aspects. *Marine and Petroleum Geology*, *18*(4), 457–461. https://doi.org/10.1016/S0264-8172(00)00070-2

Sohn, R. A., & Sims, K. W. W. (2005). Bending as a mechanism for triggering off-axis volcanism on the East Pacific Rise. *Geology*, *33*(2), 93–96. https://doi.org/10.1130/G21116.1

Soubaras, R. (1996). Explicit 3-D migration using equiripple polynomial expansion and Laplacian synthesis. *Geophysics*, *61*(5), 1386–1393. https://doi.org/10.1190/1.1444062

Srivastava, S. P., Sibuet, J. C., Cande, S., Roest, W. R., & Reid, I. D. (2000). Magnetic evidence for slow seafloor spreading during the formation of the Newfoundland and Iberian margins. *Earth and Planetary Science Letters*, *182*(1), 61–76. https://doi.org/10.1016/S0012-821X(00)00231-4

Sutra, E., & Manatschal, G. (2012). How does the continental crust thin in a hyperextended rifted margin? Insights from the iberia margin. *Geology*, *40*(2), 139–142. https://doi.org/10.1130/G32786.1

Taillandier, C., Noble, M., Chauris, H., & Calandra, H. (2009). First-arrival traveltime tomography based on the adjoint-state method. *Geophysics*, *74*(6). https://doi.org/10.1190/1.3250266

Tarantola, A. (1986). A strategy for nonlinear elastic inversion of seismic reflection data. *Geophysics*, *51*(10), 1893–1903. https://doi.org/10.1190/1.1442046

Tarantola, Albert. (1984). Inversion of seismic reflection data in the acoustic approximation. *Geophysics*, *49*(8), 1259–1266. https://doi.org/10.1190/1.1441754

Tucholke, B. E., & Sibuet, J.-C. (2007). Leg 210 synthesis: tectonic, magmatic, and sedimentary evolution of the Newfoundland-Iberia rift. *Proceedings of the Ocean Drilling Program, Scientific Reports*, *210*, 1–56.

Tucholke, B. E., Sawyer, D. S., & Sibuet, J.-C. (2007). Breakup of the Newfoundland Iberia rift.

Geological Society, London, Special Publications, *282*(1), 9–46. https://doi.org/10.1144/SP282.2

Tucholke, Brian E., & Sibuet, J. C. (2012, October). Problematic plate reconstruction. *Nature Geoscience*. https://doi.org/10.1038/ngeo1596

Virieux, J., & Operto, S. (2009). An overview of full-waveform inversion in exploration geophysics. *Geophysics*, *74*(6), WCC1–WCC26. https://doi.org/10.1190/1.3238367

Warner, M., Morgan, J., Umpleby, A., Stekl, I., & Guasch, L. (2012). Which physics for full-wavefield seismic inversion? In *74th European Association of Geoscientists and Engineers Conference and Exhibition 2012 Incorporating SPE EUROPEC 2012: Responsibly Securing Natural Resources* (pp. 2994–2998). European Association of Geoscientists and Engineers, EAGE.

Warner, Michael, Ratcliffe, A., Nangoo, T., Morgan, J., Umpleby, A., Shah, N., et al. (2013). Anisotropic 3D full-waveform inversion. *Geophysics*, *78*(2), R59–R80. https://doi.org/10.1190/geo2012-0338.1

Watremez, L., Prada, M., Minshull, T., O'Reilly, B., Chen, C., Reston, T., et al. (2018). Deep structure of the Porcupine Basin from wide-angle seismic data. *Petroleum Geology Conference Proceedings*, *8*(1), 199–209. https://doi.org/10.1144/PGC8.26

Weinberg, R. F., Regenauer-Lieb, K., & Rosenbaum, G. (2007). Mantle detachment faults and the breakup of cold continental lithosphere. *Geology*, *35*(11), 1035–1038. https://doi.org/10.1130/G23918A.1

Wernicke, B. (1985). Uniform-sense normal simple shear of the continental lithosphere. *Canadian Journal of Earth Sciences*, *22*(1), 108–125. https://doi.org/10.1139/e85-009

Whitmarsh, R. B., Manatschal, G., & Minshull, T. A. (2001). Evolution of magma-poor continental margins from rifting to seafloor spreading. *Nature*, *413*(6852), 150–154. https://doi.org/10.1038/35093085

Whitmarsh, R B, & Miles, P. R. (1995). Models of the development of West Iberia rifted continental margin at 40 degrees 30' N deduced from surface and deep-tow magnetic anomalies. *Journal Geophysical Research*, *100*, 3789–3806.

Whitmarsh, Robert B., White, R. S., Horsefield, S. J., Sibuet, J.-C., Recq, M., & Louvel, V. (1996). The ocean-continent boundary off the western continental margin of Iberia: Crustal structure west of Galicia Bank. *Journal of Geophysical Research*, *101*(B12), 28291. https://doi.org/10.1029/96JB02579

Wilcock, W. S. D., Solomon, S. C., Purdy, G. M., & Toomey, D. R. (1995). Seismic attenuation structure of the East Pacific Rise near 9°30'N. *Journal of Geophysical Research: Solid Earth*, *100*(B12), 24147–24165. https://doi.org/10.1029/95JB02280

Wilson, D. S., & Hey, R. N. (1995). History of rift propagation and magnetization intensity for the Cocos-Nazca spreading Center. *Journal of Geophysical Research*, *100*(B6), 10041–10056. https://doi.org/10.1029/95JB00762

Zelt, C. A., & Smith, R. B. (1992). Seismic traveltime inversion for 2-D crustal velocity structure. *Geophysical Journal International*, *108*(1), 16–34. https://doi.org/10.1111/j.1365-246X.1992.tb00836.x

Zelt, C A, & Barton, P. J. (1998). Three-dimensional seismic refraction tomography: A comparison of two methods applied to data from the Faraoe Basin. *J. Geophys. Res.*, *103*(B4), 7187–7210.

Zelt, Colin A., Sain, K., Naumenko, J. V., & Sawyer, D. S. (2003). Assessment of crustal velocity models using seismic refraction and reflection tomography. *Geophysical Journal International*, *153*(3), 609–626. https://doi.org/10.1046/j.1365-246X.2003.01919.x